



**Politecnico
di Torino**

POLITECNICO DI TORINO

Department of Mechanical and Aerospace Engineering

Master of Science in Automotive Engineering

Academic Year 2020/2021

July 2021

**Rotary Regenerative Shock Absorber
for Automotive Applications:
Control Strategies
and
Hardware-In-the-Loop Implementation**

Supervisor: **Prof. Nicola Amati**

Co-supervisor: **Prof. Andrea Tonoli**

Prof. Renato Galluzzi

Dr. Salvatore Circosta

Candidate:

Manfredi Tornabene

*To my uncle Saro
who continues to observe me
while I am pursuing my passions*

Acknowledgements

This thesis work has been developed at the Laboratorio Interdisciplinare di Meccatronica (Polytechnic of Turin).

I am very grateful to Prof. Amati for the opportunity he gave to me to approach the world of mechatronics, entirely new for me, with this work about an interesting topic of the automotive field.

I am also very thankful to Prof. Tonoli, for his trust in making me start this project. Special thanks to Salvo, always available to have a chat and give me a hand. You provided me with the tools to tackle the job when I was not too sure, I learned a lot of valuable notions from your many tips which helped me in finding the right path. I really enjoyed our days in the laboratory in Verrès.

I would like to thank Renato Galluzzi, for his support during these months in solving different issues. Our virtual meetings have always provided me much interesting food for thought.

Finally, I am very grateful to my family, my mother Maria, my father Dario and my sister Francesca, for their support and for having allowed me to take this path.

Abstract

Active and semi-active suspensions are devices designed to improve comfort and road-holding performance of the vehicle. Considered as one of the most advanced technologies in the automotive field, they allow to control the suspension motion by acting on its damping characteristics (semi-active and active), to perform energy recovery functions (active) and to provide active forces to the suspension (active). The *semi-active* device can induce a variable damping without requiring high energy levels and with reduced costs. The *active* system, instead, needs more supplied energy, higher costs and produces an overall actuation force for controlling the suspension motion. In the last years both solutions have been studied and developed in different forms with peculiar features, with the common purpose of enhancing the performance of a conventional fixed-damping suspension system.

One of these active technologies is the subject of this Thesis Work: a *Rotary Regenerative Shock Absorber* (RRSA) for automotive application. This prototype has been designed as a pure electro-mechanical active device installed in the vehicle suspension to replace the traditional passive damper. By means of a properly designed linkage system, the forces exchanged between ground and tire are transmitted to the RRSA device, which in turns is able to provide *active* and *passive* forces, with potential energy recovering capacity in the second case.

This study, in particular, has focused on the RRSA prototype introduced in a physical Hardware-In-the-Loop (HIL) installation. The active device has been connected to an actuation testbench and simulated in different conditions imposed by a Quarter Car SimulinkTM Model implemented in a *dSpace*TM Unit.

First, the entire HIL system has been modelled in *MATLAB/Simulink*TM. Then, the limited testbench-bandwidth has been extended by using properly designed *Compensation Methods*, experimentally validated in actual HIL Testing. After that, simulations and tests have been conducted to the HIL Model to prove its robustness. Finally, specific analyses have been carried out to the RRSA Model for evaluating the most suitable control strategy for optimizing the performance of the Quarter Car Model.

Contents

1	Introduction	1
1.1	Active and semi-active suspensions	1
1.1.1	Suspension technologies	1
1.1.2	Rotary Regenerative system	3
1.2	Hardware-In-the-Loop testing	4
1.3	Thesis Motivation	7
1.4	Thesis Outline	7
2	Rotary Regenerative Shock Absorber and HIL Test Bench	9
2.1	RRSA Prototype	9
2.1.1	RRSA design	9
2.1.2	Electric machine design	11
2.1.3	Gearbox design	11
2.1.4	Linkage placement	12
2.2	HIL Testing	14
2.2.1	Test Bench and HIL Components	14
2.2.2	Working Principle	15
3	Hardware-In-the-Loop System: Numerical Modelling	21
3.1	HIL Simulink TM representation: Block Model	21
3.1.1	Quarter Car Model	22
3.1.2	Testbench Model	25
3.1.3	RRSA Controller and System	30
3.1.4	Transmission system to QCM	32
3.2	Equivalent Modelling Implementations	32
3.2.1	State Space Model	32
3.2.2	Transfer Function Model	34
3.3	HIL State Space Model Simulation	35
3.3.1	Methodology	35
3.3.2	Analysis of the results: Instability	36
3.4	Inverse Compensation Method	42
3.4.1	Theory	42

3.4.2	Compensation Procedure	43
3.4.3	HIL Simulation Results	51
3.5	Model Following Compensation Method	92
3.5.1	Methodology	92
3.5.2	HIL Simulation Results	95
3.5.3	Final considerations	100
4	RRSA Control Strategy: Numerical Modelling	101
4.1	Sky-Hook Control	101
4.1.1	Sky-Hook Theory	101
4.1.2	QC and Sky-Hook Control Model	107
4.1.3	Methodology	111
4.1.4	QCM Results	115
4.2	Spring-Negation Control	151
4.2.1	Methodology	151
4.2.2	QCM results	153
4.3	Final considerations	160
5	Experimental Tests	163
5.1	HIL Testing: Model-Following Compensation	163
5.1.1	Methodology	163
5.1.2	Results	164
6	Conclusions and future developments	177
	List of Figures	181
	List of Tables	188
	Bibliography	189

Introduction

1.1 Active and semi-active suspensions

1.1.1 Suspension technologies

In the last years, advanced vehicle suspension systems with *adaptive*, *semi-active*, and *active* devices have attracted interest in the field of the engineering research and development.

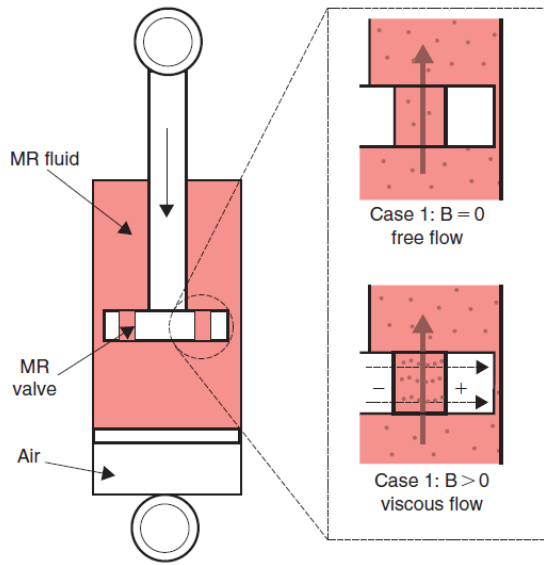
According to their capacity for adjusting the damping force, automobile suspensions can be classified as passive, active or semi active (SA). *Passive suspensions* are generally found in most vehicles and consist of a spring, used to store energy for some time segment of a suspension cycle, in parallel with a passive shock absorber used to dissipate this energy. Thus, they are able only to dissipate energy. Their damping characteristics are set to be time invariant, but they are dependent on ageing and wear. Their damping capabilities are set mechanically by an a priori choice of a particular level of compromise between *comfort* and *road-holding performance*.

Vehicle suspensions with active components improve the comprehensive performances of vehicles. *Active suspensions* are able to store, dissipate and generate energy to control the chassis motion by using a fully active actuator. Thus, an external power supply is necessary to operate this mechatronic control system. They can influence both the steady state as well as the transient behaviour of the suspension deflection;

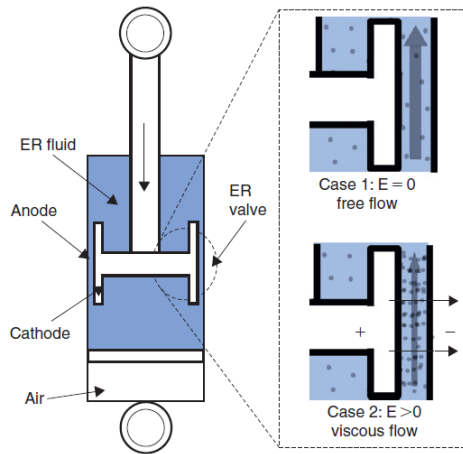
thus, theoretically, the compromise in conventional passive suspensions is eliminated. Because the power demand of active suspensions in luxury and/or heavy vehicles is too large to meet using standard vehicle supplies, SA suspensions have gained importance for car manufacturers during the last few decades. In addition, SA control has recently been an area of much interest because it provides similar performances of active actuators without requiring a significant external power supply for the dampers. *SA suspensions* consist of a spring and a damping component with a continuously variable damping coefficient adjusted through external control signals along a road profile, which offers much better comfort and road-holding performances with respect to those provided by passive suspensions. The most fundamental advantage is its cost benefit in comparison with those of active suspensions, i.e. a SA suspension is much less complex than an active suspension and may be manufactured at a lower cost. However, this technology does not allow to operate in *active mode*, i.e providing power to the suspension system, differently from the active devices, but just to dissipate energy with a variable controlled damping system. Overall, the economical feasibility and the reduced complexity of the SA technology has led the engineering research towards them, despite the active technologies can offer a wider range of operating conditions.

In the following are grouped some options for adaptable damping technologies: *electro-hydraulic (EH) technology* in which the valve holes dimensions are varied; *pneumatic damper* which varies the pressure in the damper camera; *Magneto-Rheological Damper (MR)* which varies the oil viscosity using a magnetic field; *electrorheological damper* where the viscosity of the oil varies according to the applied voltage. Their fundamental working principle are briefly explained in the schemes in Figure 1.1 a) and Figure 1.1 b).

Some applications, instead, are characterized by the use of *electro-magnetic* and *electro-mechanical* based systems, for providing an overall force depending on the current level applied by the ECU. Furthermore, more advanced solutions have being studied and analized in order to improve the efficiency and the control capabilities and, on the other hand, the economical aspect of the entire project.



(a) Magneto-Rheological Damper



(b) Electro-Rheological Damper

Figure 1.1: Examples of semi-active damper with variable controlled damping

1.1.2 Rotary Regenerative system

In the automotive field, new worldwide regulations are driving the change for a always cleaner environment. Thanks to the constantly increasing electrification of the implemented systems, the tendency nowadays is to spread the usage of mechatronics devices. Such systems, indeed, are the favoured ones due to their energy harvesting features, improving efficiency and overall achieved CO₂ emissions.

Among the different mechatronic technologies, *regenerative shock absorbers* are one of the most interesting. These systems are able to change the damping characteristics or

even to provide *active forces* to the vehicle suspension, while also recovering part of the energy, otherwise dissipated as heat. In order to perform this dual behaviour, they employ an electric machine controlled as a generator (damper) or motor (actuator), as described in [2].

Considering the type of suspension motion, linear electric machines could seem the best choice to be implemented in a regenerative damper. Their limited force density, however, has suggested the use of rotary electric motors combined with a properly designed linear-to-rotary motion conversion system, such as ball screw, rack pinion and electro-hydrostatic systems, the most diffused examples in literature, [2].

In 2016, Audi AG developed and introduced *eROT*, a new concept of regenerative suspension based on a rotary drive line, composed by an electric machine and a gearbox. Differently from traditional dampers, such system is connected to the suspension itself through a linkage and it can work as full active damper. For this technology it has been specified an overall harvesting output from four corners in the range of 100-150W on average, during testing on German roads, with different power transients according to the road roughness. Under customer driving conditions, all of this results in a CO₂ savings up to 3g/km [2].

The latest developments from the German group has shown a similar device with additional features for further improving comfort and safety. By implementing a predictive control strategy with cameras, the system can scan the road and regulate consequently the active force provided to the suspension system. The overall result is a smoother cruise and a higher level of perceived comfort for the passengers, with reduced acceleration feelings obtained by tilting the vehicle body.

Together with Audi AG, also other manufacturers like Toyota, Honda and Hyundai are studying and developing the rotary technology, a topic of great interest in the modern automotive industry.

1.2 Hardware-In-the-Loop testing

“*Hardware-in-the-loop (HIL)* is a type of component testing method in which the physical component to be tested communicates with the numerical model of the rest of

components” [4].

HIL represents one of the available procedures to be applied whenever is required a component testing, together with the most common *in-field* technique and the *simulated* one. Differently from the “in-field” testing method, the HIL type provides a wider range of possible working conditions and a more accurate and precise control level, improving the repeatability and the stability of the test.

The simulation testing method, instead, provides the whole system under testing in a simulated form and can not properly replicate the dynamic characteristics of many dynamic systems. Dynamic models, in fact, are very often implemented as resulting from simplifying assumptions, due to the uncertainty of the dynamic parameters of the system.

Hence, by applying the HIL technique, a certain component of a system can be tested physically in almost real conditions. Not only this type of test saves time and cost, but also there are no concerns about the test safety.

The tested component is often an electronic control unit (ECU), since most dynamic systems, especially in aerospace and the automobile industry, have a main controller (ECU). Sometimes, instead, HIL is an area of interest for evaluating the performance of other mechanical/electro-mechanical components in a system. As visible in Figure 1.3, in literature this type of testing is quite diffused, for example, for Magneto-Rheological dampers. To link the tested component to the numerical model, a transfer system is required, for properly communicating the input signals representing the actual working conditions. Without reference to the specific application, the typical transfer system is usually composed by a set of actuators, sensors and valves for correctly transmitting the input signal (displacement, force etc) to the tested component. Figure 1.2 shows an example of a HIL layout for testing semi-active suspension, where the three different parts characterizing this type of simulation are separately distinguished.

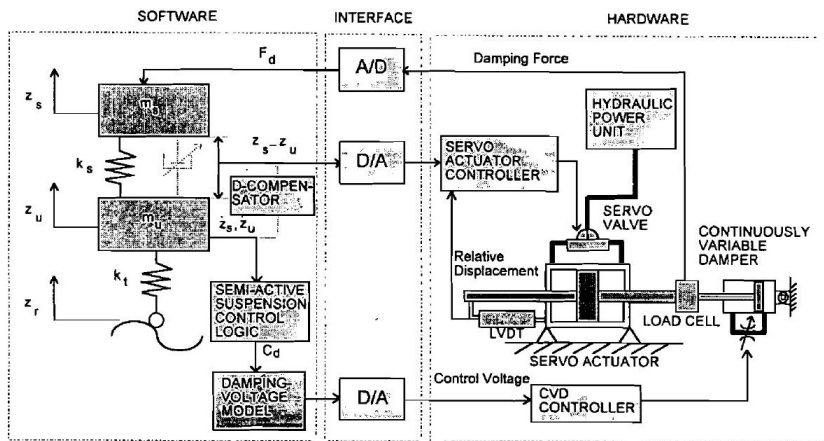


Figure 1.2: Example: Hardware-In-the-Loop with semi-active suspension [5]

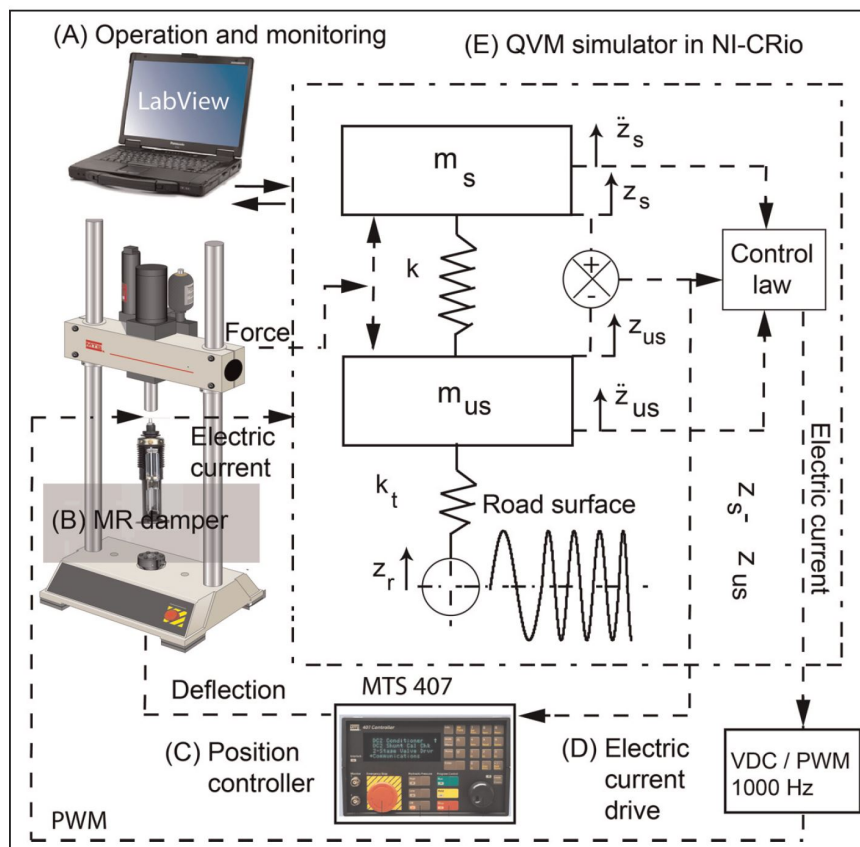


Figure 1.3: Example: Hardware-In-the-Loop with MR damper [7]

1.3 Thesis Motivation

The motivation of this project is to design a MATLAB/SimulinkTM model of a *Rotary-Regenerative-Shock-Absorber* (RRSA) mounted in a HIL installation. A proper *Compensation Scheme* capable of extending the limited testbench-bandwidth must be designed and implemented, to stabilize the entire HIL physical system.

Starting from the basic modelling of the testbench, this Thesis first focuses on the fully-simulated analysis of the Hardware-In-the-Loop system and then on the experimental validation of the obtained *compensated results*, directly on the real bench. After that, numerical analyses are performed on the RRSA prototype model, evaluating the most suitable control strategies for enhancing the Quarter Car Model (QCM) performance.

1.4 Thesis Outline

This Thesis Work is organized as follows:

- *Chapter 2*: It describes the Rotary Regenerative Shock Absorber prototype under testing, highlights the main features and briefly explains the design methodology. Then, the actual *Test Bench* and the HIL main components characterizing this Thesis Work, are described. Furthermore, the HIL Testing Procedure is briefly explained.
- *Chapter 3*: First, the numerical representation of the whole HIL system in MATLAB/SimulinkTM is described, highlighting each implemented component. Then, it is described the instability issue of the simulation with related results, and it is introduced and described the followed procedure for stabilizing the simulation. After that, compensated numerical results are acquired and further robustness tests are performed. Finally, another compensation method is proposed.
- *Chapter 4*: It takes into account, among the available strategies capable of controlling the Rotary Regenerative Shock Absorber, the *Sky-Hook* (SH) and the

Spring-Negation (SN) Control. Tests and numerical analyses are performed in MATLAB/Simulink™ Model, first considering a simplified RRSA model, and then evaluating the SH results with a more complex model affected by the active damper *energy conversion efficiency* map.

- *Chapter 5*: The physical HIL Testing is performed with the designed compensation method, and the resulting outputs are measured and acquired. The validation of the designed *Controller* is overall achieved and further analyses are performed for describing the experimental test results.
- *Conclusions and future developments*: It presents the conclusions and some possible future works of this Thesis.

Rotary Regenerative Shock Absorber and HIL Test Bench

2.1 RRSA Prototype

2.1.1 RRSA design

The Rotary Regenerative Shock Absorber (RRSA) analyzed in this study finds its fundamentals on the usage of a controlled electric machine.

Such device is able to provide an active force that can aid or counteract the suspension linear motion. In particular, in the first case, the machine works as a motor, drawing electrical power from the supply (the car battery pack) and providing it in the form of mechanical one. In the second case, instead, the machine performs mechanical-to-electrical power conversion, hence storing in the battery the kinetic energy from road irregularities as electricity.

Due to the nature of the suspension motion, a *linkage* is required, to operate the conversion of the linear motion into angular displacement of the electric machine (and viceversa). As shown in the scheme in Figure 2.1, the wheel upright linear speed v , belonging to the wheel hub, is converted into rotary motion ω through the linkage itself. This connecting element is characterized by a transmission ratio equal to $\tau = v/\omega$, being ω the angular velocity of the output shaft of the linkage, i.e the input shaft of the RRSA.

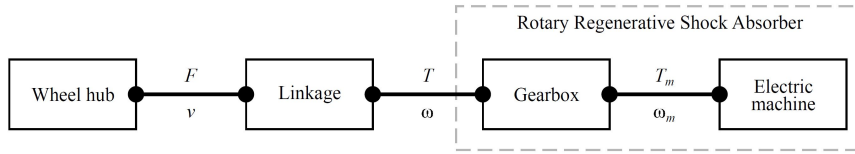


Figure 2.1: Rotary Regenerative Shock Absorber working principle diagram

Then, passing through the linkage, the transmission of motion continues in the RRSA component. First of all, the rotary displacement is applied directly from the linkage to the gearbox, integrated part of the *RRSA*, and consequently to the *RRSA electric machine*. The used gearbox has its low-speed high-torque shaft receiving the angular speed from the linkage, while its high-speed low-torque shaft is directly coupled to the rotor of the electric machine.

Consequently, the gearbox operates as a speed multiplier with a transmission ratio $\tau_g = \omega / \omega_m$, being ω_m the angular speed of the electric machine itself [2]. In Figure 2.2 can be observed the actual Rotary Regenerative Shock Absorber prototype used in the HIL Installation and considered in this Thesis Work.

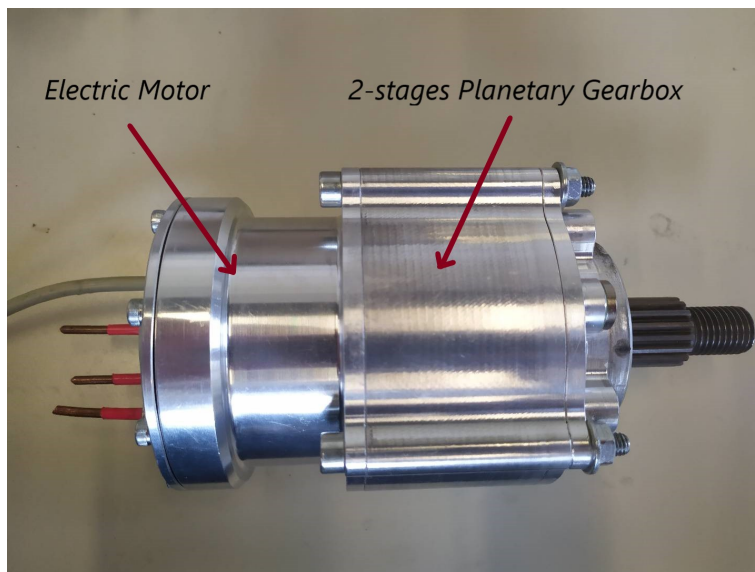


Figure 2.2: RRSA prototype

2.1.2 Electric machine design

The electric machine technology and its design were defined by operating conditions considering different physical domains, i.e. mechanical (level of vibrations), electrical (voltage and current limits) and thermal (temperature), [2].

Since the volume reduction is crucial in this application, the permanent-magnet synchronous machine was selected because it offers the highest torque-to-mass ratio among different available electric motors.

The sizing of the electric machine is strictly related to the definition of the overall transmission ratio, which allows to convert the requirements at the wheel upright into the input of the electric machine.

2.1.3 Gearbox design

The selection of this prototype gearbox architecture was driven by some envelope constraints, as described in detail in [2]. Fixed-axis and planetary configurations were compared and, although the first achieves slightly better performance in terms of overall efficiency and noise level, the planetary architecture provides relevant compactness and mass reduction. Hence, a planetary gearbox was the preferred solution. The selected configuration is composed by two stages that share the same fixed ring, as depicted in Figure 2.3. Each stage has one planet carrier, three planet gears and one sun gear. For each of both stages, the input is fixed to the planet carrier, whereas the sun gear represents the output. The output of the second stage drives the electric machine shaft. In [2] the design goal was the optimization of the selected configuration by trying to minimize mass and overall dimensions, as well as the gearbox inertia at the input shaft. Gearbox components were sized for facing overloads and fatigue. The operating conditions are defined at the suspension level, hence the *linkage transmission ratio* τ_{QC} is used to convert them to the gearbox input shaft.

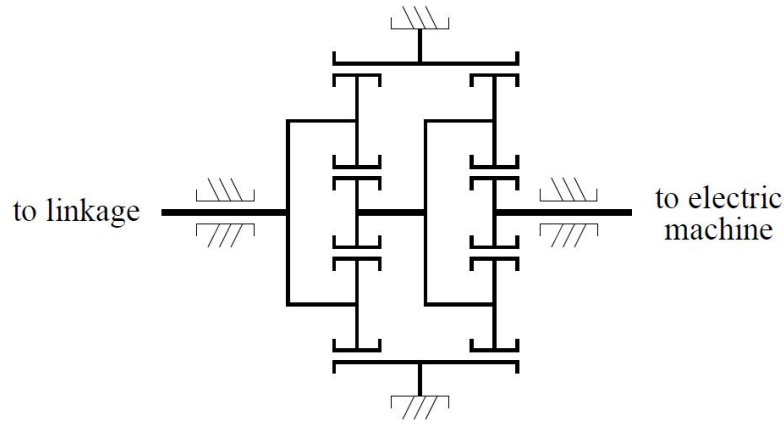


Figure 2.3: *RRSA gearbox scheme*

2.1.4 Linkage placement

The linkage design, which is discussed in [2], was heavily decided by the reference vehicle suspension layout. The suspension kinematics was initially simplified into a 2D representation and the linkages were studied with the mechanism synthesis approach, as seen in Figure 2.4. The lever transmission ratio and the transmission angle were the performance parameters taken into account in the definition of the linkage. The lever transmission ratio converts the linear speed applied at the upright (v) into an angular speed at the gearbox input shaft (ω). Corresponding to this, the electric machine reacts by producing a torque T at the gearbox input shaft, which will be converted into a force F at the upright. The leverage transmission ratio τ_{QC} must be minimized so that, according to Equation 2.1, the overall transmission ratio τ_t can be achieved with a lower gearbox contribution τ_{gb} .

$$\tau_l = \tau_{QC} \longrightarrow \text{Leverage Transmission Ratio} \tag{2.1}$$

$$\tau_t = \tau_l \tau_{gb} = \frac{v}{\omega_m}$$

In these conditions, in fact, both the compactness and the efficiency of the gearbox can be improved.

For what concerns the transmission angle, it defines the achieved quality of the linkage transmission. In the case of a four-bar linkage, it is defined as the angle between the

coupler and the follower. It varies throughout the range of operation and it is most favorable when equal to 90° . Therefore, the design aims to limit the transmission angle in the range between 40° and 140° , as accurately recommended in the literature [2].

The fulfillment of performance and packaging criteria led to the four layouts illustrated in 2.4. Layouts (a) and (b) place the RRSA in the pivot point of the lower and the upper suspension arm, respectively. In this case no additional levers are required, since the suspension arms themselves are used as connecting links. Both layouts provide a simple solution since the suspension architecture remains unchanged. However, the resulting nominal linkage transmission ratio is 346mm/rad for Layout (a) and 251mm/rad for Layout (b). Layout (c) decreases the linkage transmission ratio through a fourbar-linkage constituted by the lower suspension arm and two additional links, achieving a nominal leverage transmission ratio of 100mm/rad . Layout (d) uses two links, where the longest one is hinged on the damper tube. The RRSA is placed at the pivot point of the lower arm, thus producing a nominal leverage transmission ratio of 115mm/rad . Among the investigated configurations, Layout (c) achieves the lowest τ_{QC} and, therefore, represented a promising candidate in the case of a total redesign of the suspension architecture. Layout (d), on the other hand, features a slightly larger transmission ratio than (c), but does not require significant changes in the existing suspension assembly. Therefore, Layout (d) was taken as reference setup for the design of the gearbox. This layout could achieve a smaller ratio by reaching transmission angles outside the specified range. However, this choice would have a negative impact on the achieved transmission quality. Hence, this application addresses an RRSA design based on a linkage system which is able to accomplish a nominal leverage transmission ratio of 115mm/rad . Moreover, the layout of this mechanism is constrained by the suspension architecture, that must be accounted for the proper design.

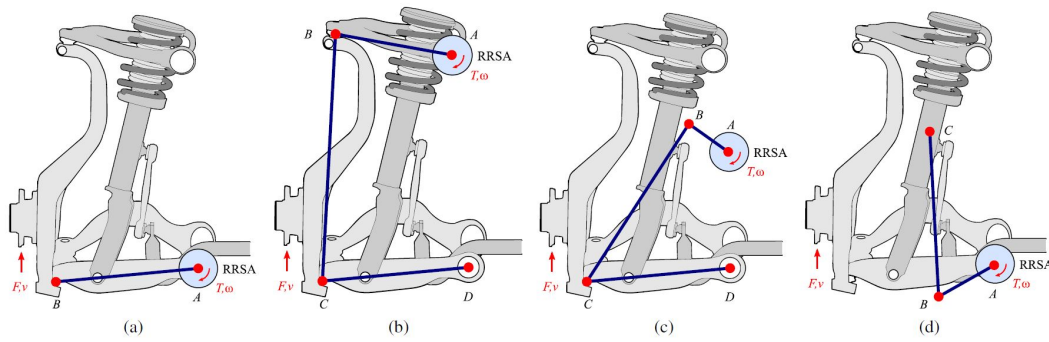


Figure 2.4: RRSA linkage position

2.2 HIL Testing

2.2.1 Test Bench and HIL Components

The entire installation for performing HIL Testing is mainly composed by the actual Testbench, with its hydraulic actuation group, and by the HIL Components required for connecting the *hardware part* of the system to the *software part*, considering the description in Chapter 1. All the components are grouped together and briefly described in the following:

- **Kollmorgen Unit:** It is the electric motor driving the Hydraulic Pump for providing actuation.
- **Hydraulic Pump:** It is a *Gerotor Pump*, driven by the Kollmorgen Motor, used for supplying pressurized oil to the actuation circuit, which in turn acts on the rotary damper.
- **Driving Actuator:** It is the hydraulic piston, powered by the pump, which provides the actuation force to rotary damper.
- **Transmission lever:** It is the connecting link between the piston head and the RRSA prototype. It is used to convert the linear motion of the piston into a rotational motion at the input shaft of the RRSA gearbox.

- **Rotary Regenerative Shock Absorber (RRSA):** It is the prototype *rotary damper*, object of this Thesis Work. It is rigidly connected to the Testbench structure and receives the actuation force through the transmission lever. Its three phases can be connected to the MPPM Unit for providing specific levels of current to the electric machine (EM) and obtaining desired damping conditions.
- **Sensors:** Two *pressure sensors* are used for monitoring both sides of the Hydraulic Pump (*left* and *right* side) and one *position sensor* is used for measuring the linear piston displacement. Then, a *Load Cell* is mounted at the end of the hydraulic actuator. It measures the dynamic force resulting from the piston-RRSA interface and transfers this signal to the QCM implemented in the dSpaceTM, for providing the QC damping force and closing the HIL Testing procedure.
- **Battery Management System (BMS):** It is the battery pack system receiving and providing the electric power to the RRSA prototype.
- **MPPM Unit:** It is the electronic unit, called Multi-Purpose Power Module (MPPM), mainly used for setting the damping levels of the RRSA.
- **dSpaceTM Unit:** It is a MicroLabBox Unit, an all-in-one development system for the laboratory that combines compact size and reduced system costs with high performance and versatility. It provides dedicated electric motor control features and interfaces for Ethernet and CAN bus.

2.2.2 Working Principle

Considering the described parts of the installation, the overall working principle characterizing the Hardware-In-the-Loop operations can be illustrated.

Once defined the desired testing conditions, the QCM is implemented in SimulinkTM with the proper MATLABTM code, running in the considered PC with the User-interface. Actually, the simulated QCM is loaded from the Control PC to the *dSpace*, the Control Unit shown in Figure 2.10 b), devoted to perform the real QCM simulations on the physical Testbench, with sensors and electrical connections to it. When running the HIL Test from the user-interface (connected to the dSpaceTM Unit), the

Testbench, powered by the inverter shown in Figure 2.5, starts to operate. Despite the actual working conditions could include also a simple sinewave input-displacement to the bench (i.e, without QCM implemented and no HIL Test), this description regards the most complete and articulated HIL Testing. In the simulated QCM, the *relative displacement* between the masses is used for computing the corresponding *RRSA rotation*, main input of the Testbench.

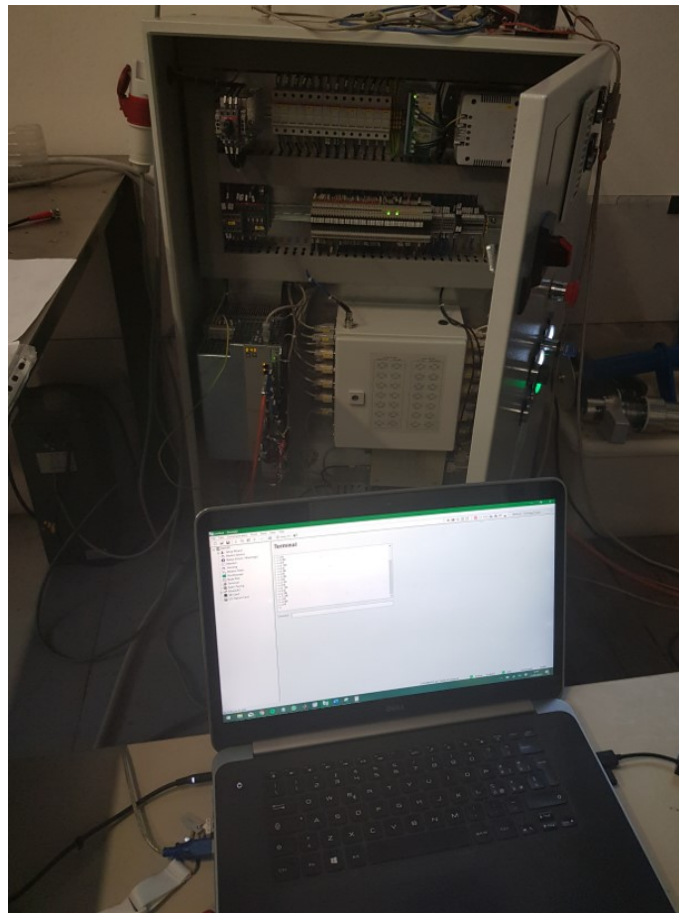


Figure 2.5: *Inverter and Control PC with User-Interface for HIL Testing*

This angular displacement is passed through a numerical controller (in this case a PID Controller) implemented in the *software* part, for evaluating the current to be required from the Kollmorgen Motor to drive the Hydraulic Pump, shown in Figure 2.6.

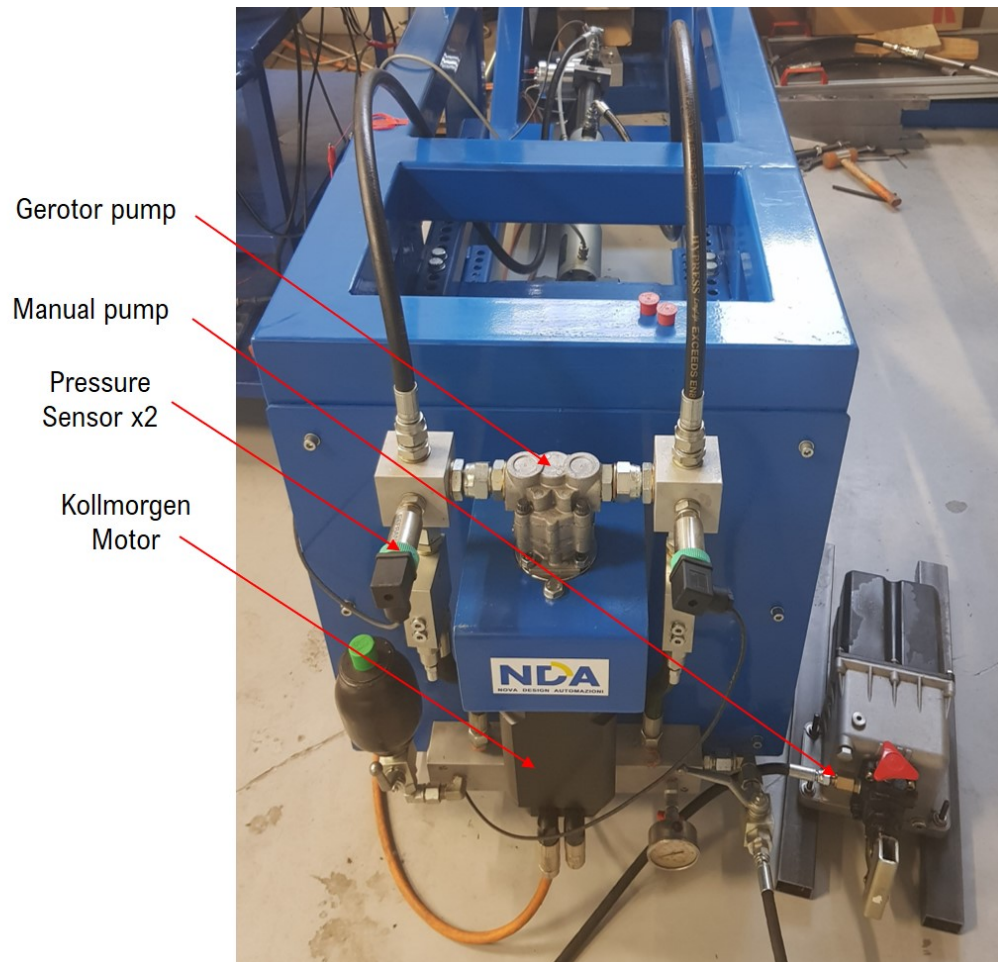


Figure 2.6: Hydraulic Pump and Kollmorgen Motor

Hence, the Gerotor Pump is activated and starts pressurizing the oil in the hydraulic circuit, producing the consequent movement of the hydraulic piston/driving actuator, visible in Figure 2.7. The hydraulic piston is equipped with a *Load Cell* (LC) between the piston head itself and the connecting lever to the RRSA. This Load Cell plays a fundamental role: it transfers in real time the perceived dynamic force to the QCM. Its signal, in fact, is read by the corresponding sensor and passed through the dSpace™ Unit, hence to the simulated QC. As a consequence, the HIL Testing loop is closed, since the force measured by the Load Cell is introduced in the QCM as a suspension damping force. Such force, in particular, strictly depends on the imposed damping to the rotary damper prototype (RRSA), properly set in the User-Interface by manually operating on the MPPM settings.

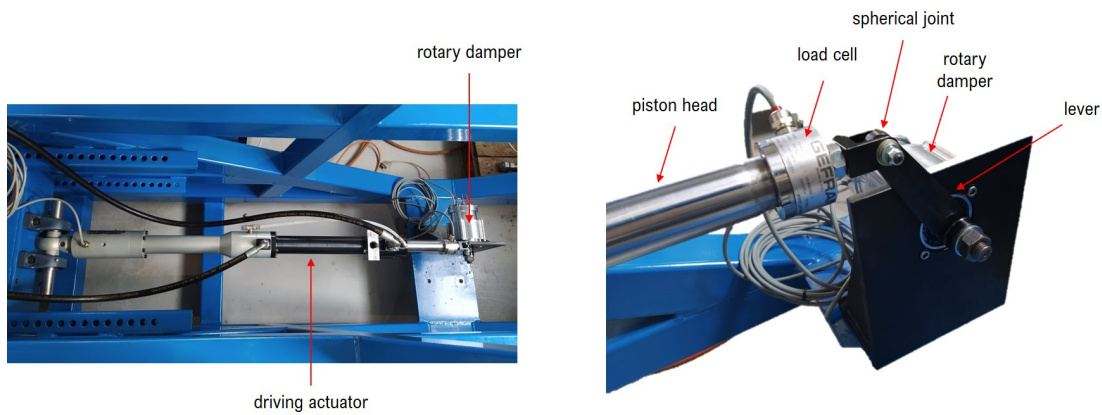


Figure 2.7: Driving actuator with Load Cell and connection to the rotary damper

The MPPM Unit, shown in Figure 2.10 a), is connected to the three phases of the RRSA electric machine, clearly observable in Figure 2.8. Consequently, by connecting the driving actuator to the rotary damper through the transmission lever, the imposed damping coefficient (related to the current level circulating in the rotary three-phases) significantly affects the dynamic force measured by the Load Cell sensor.

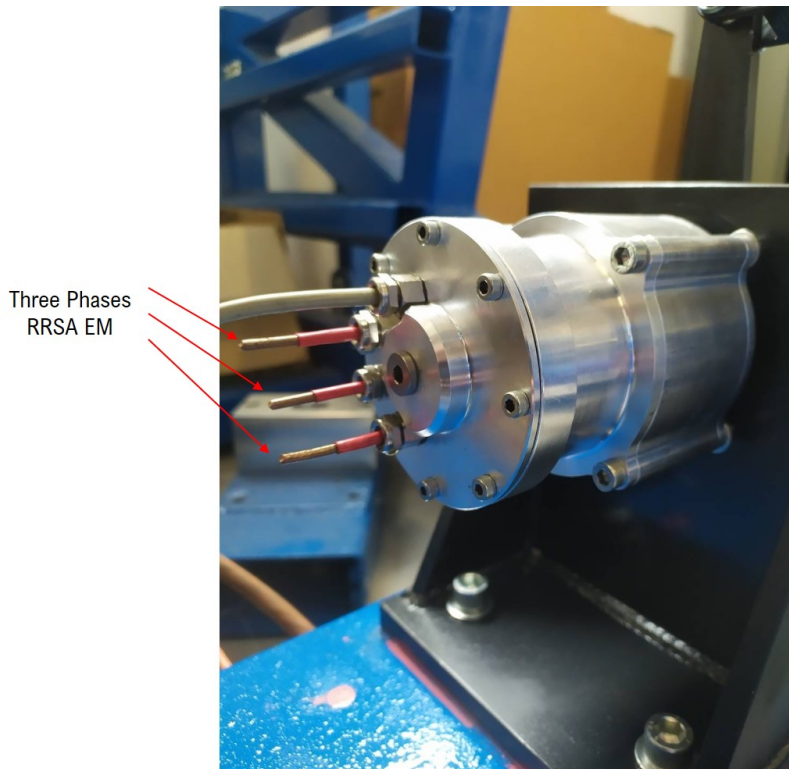


Figure 2.8: RRSA Prototype installed in the Testbench (without electric connections to the phases)

2.2. HIL Testing

During the HIL Test, the Mechanical Power dissipated in the QCM (expressed as $P_{mech} = F_{damp} * Speed_{rel}$, in which F_{damp} is the Load Cell Force introduced in the QCM and acting on the sprung mass, while $Speed_{rel}$ is the relative speed between sprung and unsprung masses) is numerically computed and monitored. On the other hand, since the regenerative capacity offered by the rotary damper, a certain Electric Power is acquired, representing the RRSA *regenerated power*. The corresponding energy content, over the entire test duration, is stored in the BMS unit shown in Figure 2.9.

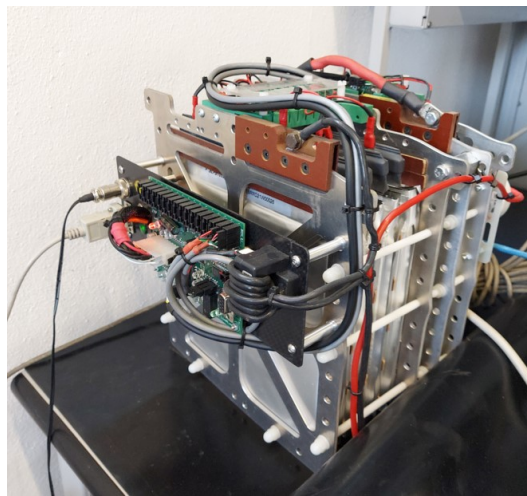


Figure 2.9: Battery Management System



(a) MPPM



(b) dSpace™

Figure 2.10: MPPM and dSpace™

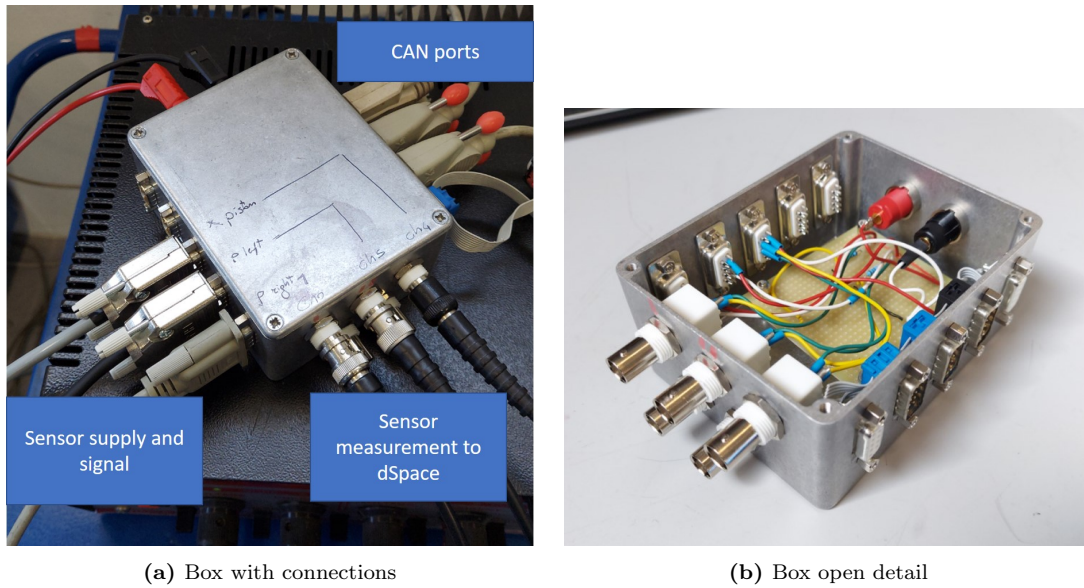


Figure 2.11: *Dedicated box for sensor supply*

Finally, in order to improve the organization level of the whole bench with the related hardware connections, a *dedicated box* has been properly modified and used, obtaining the resulting object shown in Figure 2.11. In a unique component, sensor and signal supply, CANbus connections and Testbench sensor measurements to the dSpaceTM are provided, with great achieved compactness and handling capacity of the interested links.

By introducing the Load Cell signal in the simulated QCM, the overall HIL Testing Procedure is complete and the output results can be acquired and analyzed.

Hardware-In-the-Loop System: Numerical Modelling

3.1 HIL SimulinkTM representation: Block Model

The first model that has been implemented is the *block representation*, which finds its roots on the initial schemes that were provided for starting the overall study.

The SimulinkTM Space is organized in macro-blocks using the *Subsystem* command and each of them includes specific components of the Hardware-In-the-Loop installation, shown in Figure 3.1. During the modelling process, one of the main driving purposes has been the modularity of the representation, in order to directly provide an easier access to all the parameters of interest.

Overall, the HIL modelling process has generated four main subsystems, that will be described in detail in the following Sections:

- *Quarter Car Model*
- *Testbench Model*
- *RRSA Controller and System Model*
- *Transmission system to QCM*

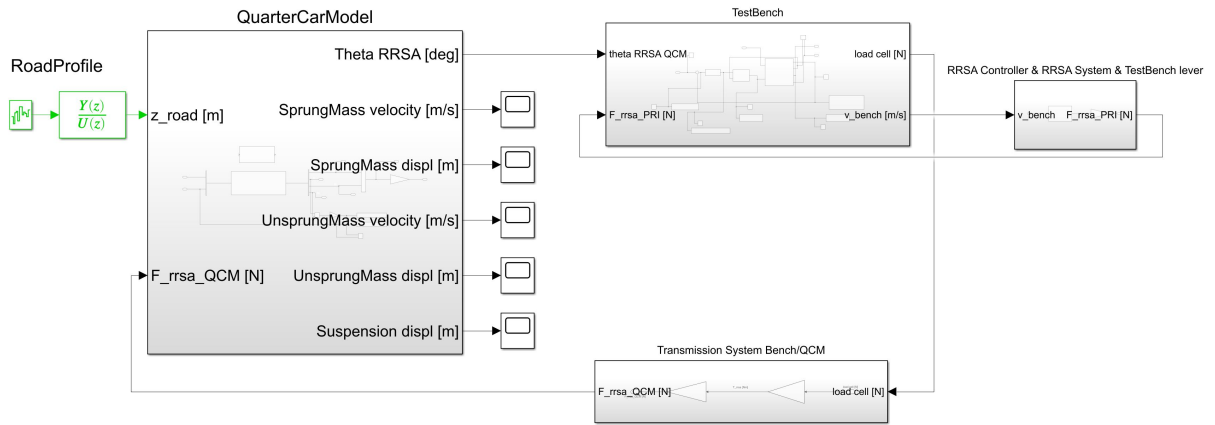


Figure 3.1: HIL block model

3.1.1 Quarter Car Model

The considered Quarter Car is a standard two degrees of freedom model, whose scheme is depicted in Figure 3.3. In this system there are two received inputs: the *ground vertical displacement* and the *active damping force*.

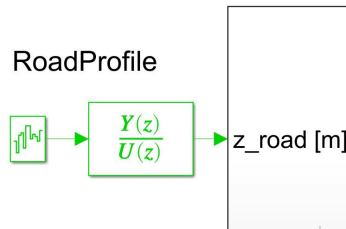


Figure 3.2: Road Profile White Noise

The former is generated by the *Road Profile block*, shown in Figure 3.2, according to the data set in the MATLABTM code regarding the type of ISO-profiles, while the latter is introduced in the model directly from the testbench block.

In this representation the sprung and the unsprung masses are connected by means of three elements in a parallel arrangement: *suspension stiffness* (spring), *suspension passive damper* (shock absorber) and *active damper* (RRSA). Then, the tire-ground contact is modelled with a parallel system including the *tire stiffness* and the *tire damping*.

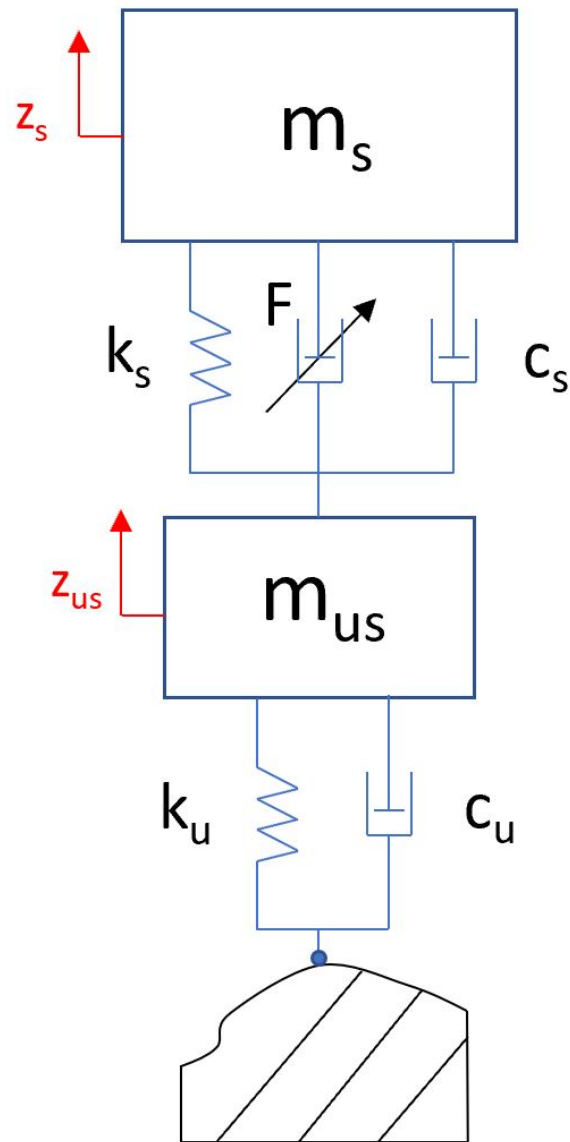


Figure 3.3: Quarter Car with two degrees of freedom

With reference to the acting forces on the overall system, two force diagrams are obtained and used for computing the overall dynamic's law of the Quarter Car, shown in Figure 3.4. In these schemes, directions and verses of the involved forces are properly considered for achieving the overall balance.

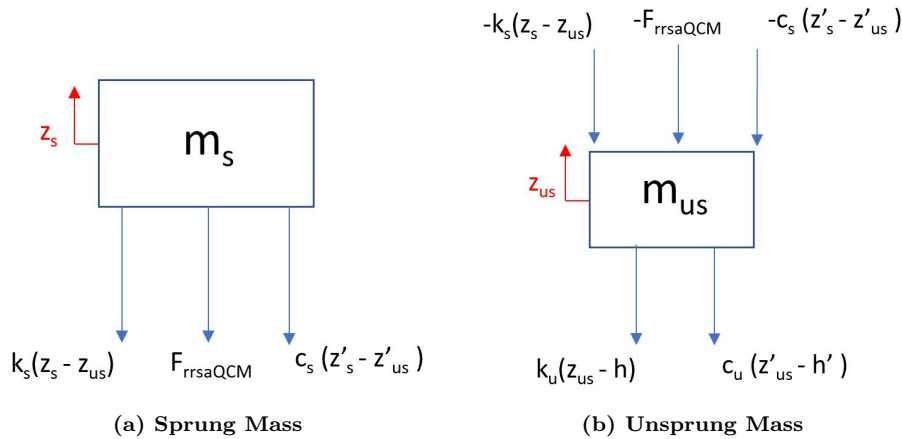


Figure 3.4: QCM force diagrams

Once arranged the dynamic system of the Quarter Car Model, its equations are implemented in the SimulinkTM Space with block representation. *Add blocks, integral operators* and *static gains* are the easiest and most used elements in this step. The overall scheme is then included in a single *Subsystem block*, visible in Figure 3.1, and some key outputs are considered. Despite some of them are necessarily always required, their overall number is changed in the next implementations, in order to provide a more detailed analysis on some achievable data. Moreover, Table 3.1 provides all fundamental parameters of the implemented QCM, referred to a JeepTM Renegade vehicle model.

Sprung Mass [kg] $\rightarrow m_s$	416.5
Unsprung Mass [kg] $\rightarrow m_{us}$	40
Susp.Stiffness [N/m] $\rightarrow k_s$	23256
Susp.Passive damping [Ns/m] $\rightarrow c_s$	0
Tire Stiffness [N/m] $\rightarrow k_u$	$223e3$
Tire Damping [Ns/m] $\rightarrow c_u$	0
QC Linkage [m/rad] $\rightarrow \tau_{QC}$	0.115

Table 3.1: Quarter Car Model Data (Jeep Renegade)

3.1.2 Testbench Model

Once described the numerical modelling of the Quarter Car, taking into account the chain of events occurring in the HIL procedure, is fundamental to model the overall testbench. As described in Chapter 2, it receives the information about the angular displacement of the RRSA from the QCM for producing an overall force read by the *Load Cell sensor*, main output of the Hydraulic group within the testbench. However, in order to provide the force that will be introduced in the QCM to simulate the active shock absorber, a certain number of interactions are required between the different components to elaborate this information.

To better understand the working sequence occurring within the testbench, the overall *SimulinkTM Subsystem* is internally divided in multiple block models, as can be seen in Figure 3.5, each corresponding to a specific subsystem of the actual testbench, described in 2.2:

- *Kollmorgen Controller (KC)*
- *Kollmorgen-Pump Group (KPG)*
- *Piston-RRSA Interface (PRI)*

With all these parts, the obtained model replicates the working principle characterizing the physical installation. The angular displacement of the RRSA coming from the QCM, in fact, enters in the testbench and is compared to the signal elaborated by the PRI model. The resulting *error* is used by the Controller of the Kollmorgen Unit to provide the useful current and it drives the motor itself. As a consequence, the hydraulic piston produces an actuation force to be transmitted directly to the RRSA prototype, by means of the transmission lever.

Stricly speaking, the latter description regards all the sequences that are included in this Testbench block model. However, as can be seen from Figure 3.5, additional signals are present in this representation, not provided by the described subsystems. This is true since the modelled testbench interacts with a separate block representing the RRSA System (and Control), which in turns provides the Active force, generated by the RRSA EM itself, to the testbench.

It is fundamental to highlight that, at this stage of the *block representation* analysis, the described division is just performed for facilitating the analysis of each single component. The actual testbench must always be intended not only with the included subsystems but also with the RRSA prototype model.

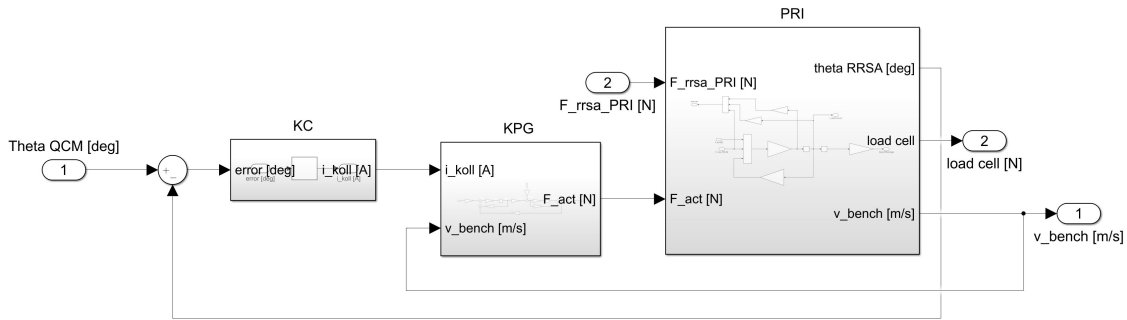


Figure 3.5: Testbench block model

Kollmorgen Controller: PID

The Kollmorgen electric motor, designed to drive the hydraulic pump of the testbench, must be powered by a current according to the *tracking level* of the angular displacement of the RRSA. With this latter term is intended the *difference between the RRSA rotation computed directly in the QCM and the one generated by the testbench*, passing through the actuation line. The lower the difference between these two signals, the better is the *tracking capacity* of the testbench, i.e the testbench can replicate the simulated rotation of the RRSA received as input with good approximation.

In this case, considering the feedback of the RRSA angular displacement from the bench model, the *error signal* introduced in the Kollmorgen Controller block, gives an idea about the tracking level itself, being very small when the tracking capacity is high and viceversa.

This error signal is elaborated by a *PID Controller*, which in turns provides the *Kollmorgen Current signal* to drive the Kollmorgen Unit. The PID Controller is optimized by considering the parameters grouped in Table 3.2.

P	I	D	N
3	0.1	0.03	600

Table 3.2: PID coefficients

Kollmorgen-Pump Group

Once computed the control current for the Kollmorgen electric motor, this signal is sent directly to the Kollmorgen itself. It is modelled and included in the second main block composing the Testbench system, the *Kollmorgen-Pump Group* block.

This *Subsystem* contains the whole electro-hydraulic part of the testbench, i.e the Kollmorgen electric motor driving the Hydraulic pump connected to it. As can be seen in Figure 3.5, together with the control current there is also a second input signal, the *piston speed*, which is taken from the PRI Subsystem for being used here in the dynamic's law of the hydraulic system. Once elaborated the two input signals, the *KPG Subsystem* provides the hydraulic-actuation force to be applied directly to the hydraulic piston.

Also in this modelling process, for describing each sequence of the output signal computation, just static gains and integral-operators are used and combined, as can be seen in Figure 3.6, while all the fundamental parameters are summed up in Table 3.3.

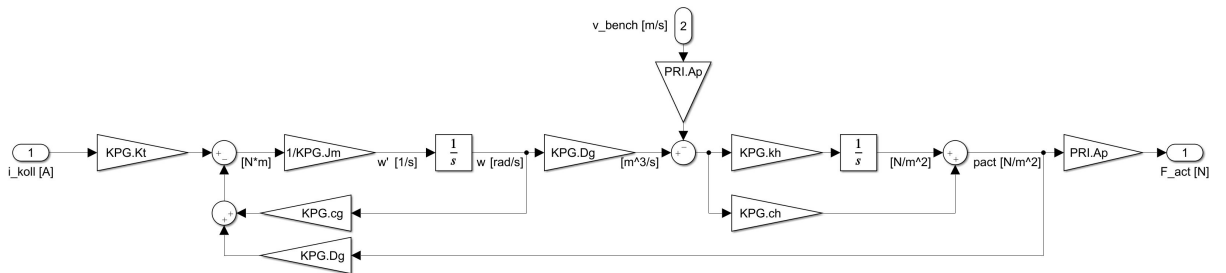


Figure 3.6: KPG model

KollMorgen Torque Constant [Nm/A] \longrightarrow Kt	0.92
KollMorgen Inertia [kgm^2] \longrightarrow Jm	40
KollMorgen Dissipation [Nms/rad] \longrightarrow cg	0.01
Angular Volume displaced [m^3/rad] \longrightarrow Dg	$3.3617e - 7$
KollMorgen Saturation Current [A]	90

Table 3.3: *KollMorgen Pump Group Data*

Piston-RRSA Interface

The third and last Subsystem implemented in this block representation is the *PRI*, always visible in Figure 3.5. After having obtained the hydraulic actuation force in the KPG, it is introduced as one of the two inputs of the interface model between Piston and RRSA prototype.

As described in 2.2, the role played by the hydraulic piston, within the testbench, is to drive the rotary damper by receiving specific input from the Hydraulic Pump.

In order to numerically describe this mechanism, the Piston-RRSA Interface is modelled as a 1 dof system. The Hydraulic Piston and the RRSA are modelled as two masses, and are connected by means of a rigid lever, whose rigidity and damping coefficients are assumed infinitely large. This assumption, not far from the physical reality, implies that both masses are included in a *1 degree-of-freedom system*, where both of them move as a unique rigid body.

In this model, both masses are subjected to the same number of forces. The Hydraulic Piston receives the actuation force from the KPG Subsystem and must face its inertial effects and the corresponding dissipative contributions. The equivalent mass representing the RRSA prototype, instead, receives the force computed by the electric machine of the active damper itself, coming from the *RRSA Controller and System block*, and is subjected to the dissipative and inertial contribution too, as the Hydraulic Piston. The whole system, together with the acting forces, can be seen in Figure 3.7.

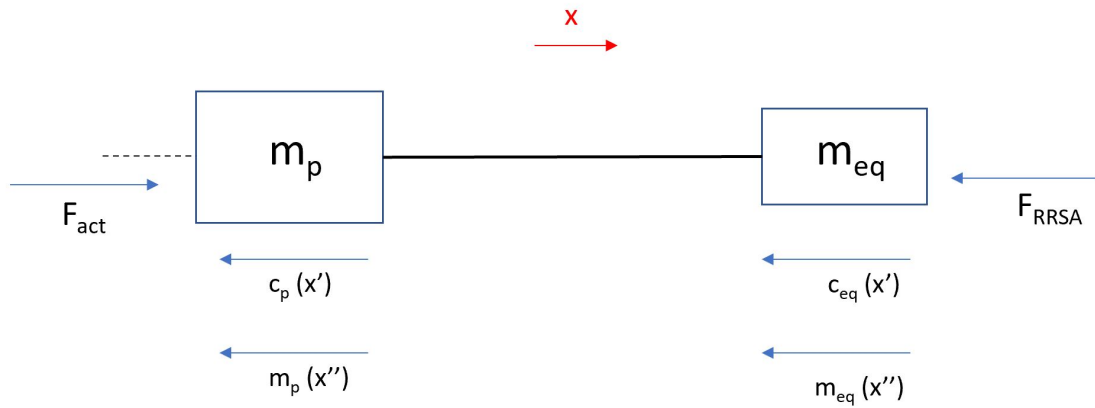


Figure 3.7: Piston-RRSA Interface model with 1 degree of freedom

This model is not concerning the possible linear displacement of the rotary damper, which is obviously axially fixed and can only rotate, but it is just modelling the overall assembly as rigidly connected. The unique linear displacement, in fact, is then converted into a rotational motion, passing through the transmission lever ratio, for obtaining the corresponding RRSA angular displacement. This linear-to-rotational conversion is clearly visible inside the PRI Subsystem, in Figure 3.8, together with the whole scheme representing the block model of the Piston-RRSA Interface.

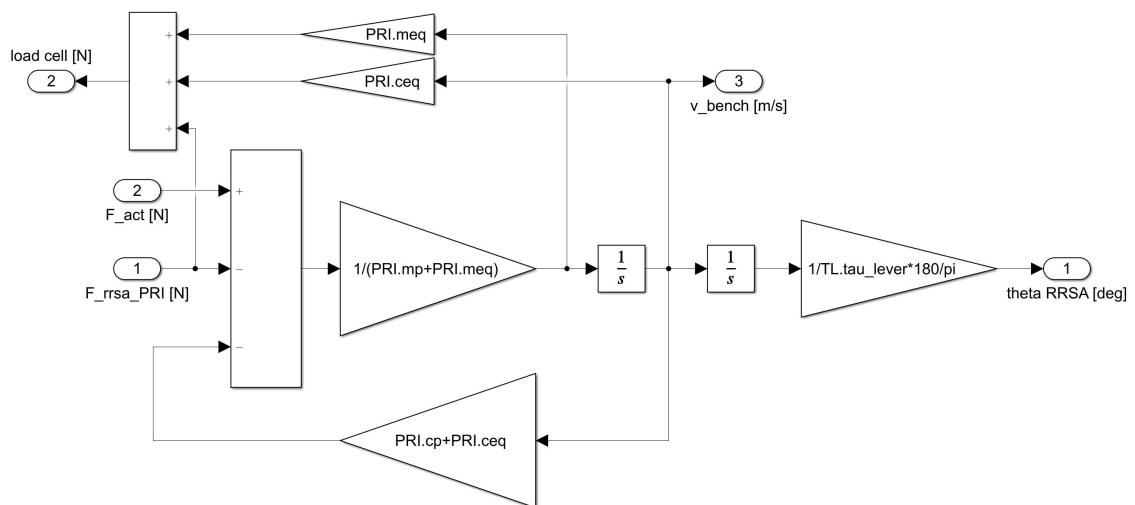


Figure 3.8: PRI block model

Piston Area [m^2] \longrightarrow Ap	0.92
Piston Mass [kg] \longrightarrow mp	12.76
Piston Dissipative Coefficient \longrightarrow cp	1000
RRSA Equivalent Mass [kg] \longrightarrow meq	5.58
RRSA Dissipative Coefficient \longrightarrow ceq	250

Table 3.4: *Piston-RRSA-Interface Data*

3.1.3 RRSA Controller and System

As mentioned in 3.1.2, even though the active damper RRSA physically belongs to the testbench itself, at this stage of the description it is considered in a separate Simulink™ Subsystem, for better visualizing its system and controller.

The implemented block model, visible in Figure 3.5, includes not only the RRSA Controller and System but also the *transmission ratio of the testbench lever*. Implemented in the form of a simple gain, this block is required anytime is needed the conversion of the *Torque* at the output of the *planetary gearbox* of the RRSA into the corresponding *Force*, to be introduced in the previously described PRI Subsystem.

The active damper and its controller, included in this unique Subsystem, are further distinguished within the block itself, as showed in Figure 3.9, where each of them is individually identified. First considering the *RRSA Control Current* block, it receives as input the *testbench speed*, i.e the *piston speed*, and provides the control current to be delivered to the RRSA System. This process follows the mathematical relations expressed in Equation 3.1 (in which, c is the imposed RRSA damping, v_{QC} is the relative speed between sprung and unsprung mass, v_{bench} is the piston speed, τ_{bench} is the transmission lever ratio and K_T is the torque constant of the RRSA EM).

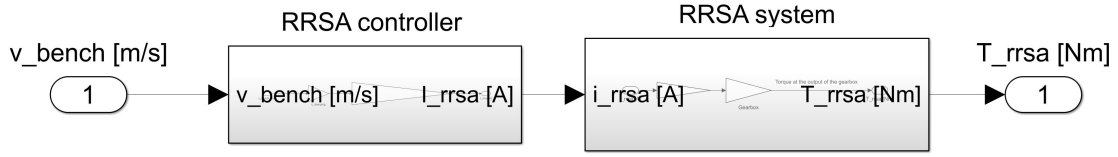


Figure 3.9: RRSA Controller and System model

$$F_{QC} = \frac{T_{RRSA}}{\tau_{QC}} = cv_{QC}$$

Where

$$\begin{aligned} v_{QC} &= \dot{\theta}_{RRSA} \tau_{QC} \\ \dot{\theta}_{RRSA} &= \frac{1}{\tau_{bench}} v_{bench} \\ \Rightarrow v_{QC} &= v_{bench} \frac{\tau_{QC}}{\tau_{bench}} \end{aligned}$$

From the first equation: (3.1)

$$T_{RRSA} = c \frac{\tau_{QC}^2}{\tau_{bench}} v_{bench}$$

But it is valid:

$$T_{RRSA} = \tau_{gb} K_T i_{RRSA}$$

Hence:

$$\Rightarrow i_{RRSA} = c \frac{\tau_{QC}^2}{K_T \tau_{bench} \tau_{gb}} v_{bench}$$

Once computed the RRSA control current, it is finally introduced in the subsystem representing the Rotary Damper itself. The *RRSA System* block, visible in Figure 3.9, receives the current as unique input and must convert it into a torque. This transformation is permitted by modelling the overall system with a simple static gain containing the information about *torque constant* K_T , following the mathematical relations shown in Equation 3.2, which in turns is transformed in Equation 3.3 for computing the resulting force. Moreover, the two fundamental implemented data are summed up in Table 3.5.

$$T_{RRSA} = \tau_{gb} K_T i_{RRSA} \quad (3.2)$$

$$F_{RRSA} = \frac{T_{RRSA}}{\tau_{bench}} \quad (3.3)$$

RRSA Torque Constant [Nm/A] \longrightarrow k_T	0.0493
RRSA Planetary Gearbox \longrightarrow τ_{gb}	87.35

Table 3.5: *RRSA Data*

3.1.4 Transmission system to QCM

The last Subsystem to be analyzed is the one which allows the *conversion* of the *Load Cell Force*, measured in the PRI Block, into the actual damping force acting on the Quarter Car Model. This Subsystem is called *Transmission System Bench/QCM* and it is shown in Figure 3.1.

Considering in detail, it is simply composed by a series connection of the two static gains representing the transmission ratios required, where the τ_{QC} has been introduced in Table 3.1 while the τ_{bench} is the bench lever transmission ratio and it is equal to 0.125. The Load Cell signal passes through the testbench transmission lever and is converted into the RRSA Torque (always at the output of the gearbox), which in turns is converted into the damping force acting in the QCM, passing through the transmission lever of the QCM itself, as expressed in Equation 3.4.

Performing this last conversion, all blocks characterizing the system are described and the overall *HIL* Modelling process is complete.

$$F_{QCM} = \frac{F_{LoadCell}\tau_{bench}}{\tau_{QC}} \quad (3.4)$$

3.2 Equivalent Modelling Implementations

3.2.1 State Space Model

Before starting with the actual simulation of the designed system, additional modelling processes are performed. Due to the extremely dispersive layout provided by the *block model representation*, this study requires a more compact model in order to facilitate

calculations and further analyses.

Starting from the Simulink™ model described in 3.1.2, the entire system is rearranged in State Space form. For each considered part of the HIL model, the corresponding equations are re-formulated and organized according to the designed states of the system, with the overall result shown in Figure 3.10.

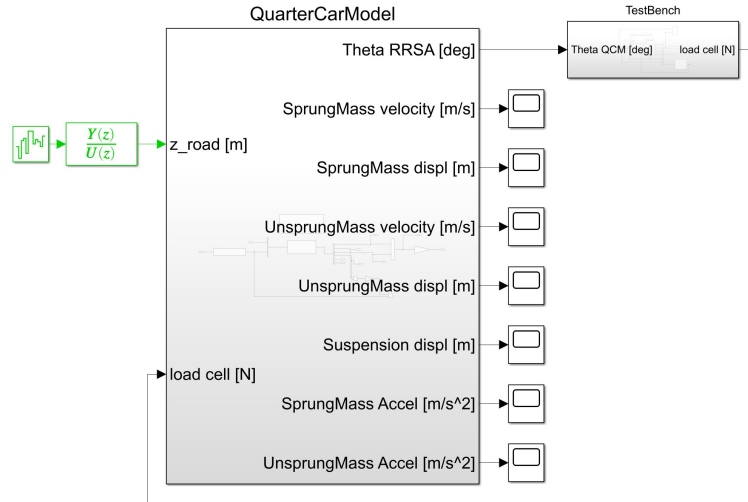


Figure 3.10: HIL State Space Model: overall layout

With respect to the layout shown in Figure 3.1, the components characterizing the TestBench are here grouped in a single *Subsystem* called *Testbench*. The QCM Subsystem, shown in detail in Figure 3.11, is much more compact than the block model, since the whole dynamic system is contained in the *SS block*, providing the same desired outputs. The transmission system to the QC, instead, is kept with its original form, since no State Space would be significant.

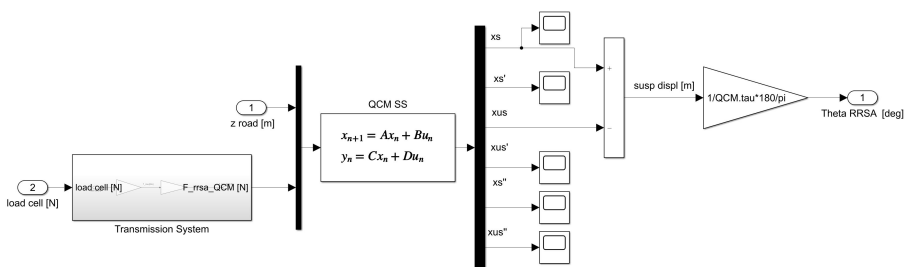


Figure 3.11: HIL State Space Model: QCM layout

By replacing the block model representation with the State Space one, certainly the Testbench is the most affected part of the HIL Model. As can be observed in Figure 3.12, in fact, the whole complex and particularly articulated system described in 3.1.2 is now composed by two main SS Systems, i.e the KPG and the PRI, and by the PID Controller and the RRSA System, both of them unchanged with respect to the *block model*. The overall result is extremely easier to be analyzed, showing very clearly every connection between the different components of the Bench model.

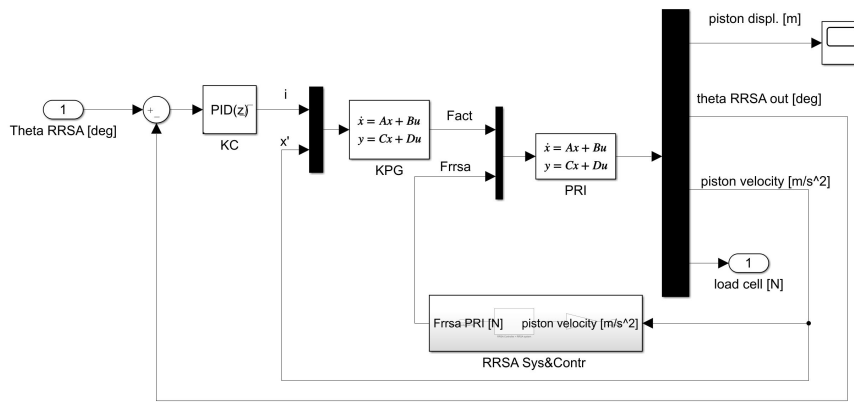


Figure 3.12: *HIL State Space Model: Testbench layout*

3.2.2 Transfer Function Model

In parallel to the development of the HIL *State Space* model, a third modelling procedure has been performed, in order to further reduce the complexity level of the system. This implementation is called *Transfer Function representation*, since the key components are reduced to their specific transfer functions.

Starting from the *SS model* described in 3.2.1, the designed SS components are characterized by a certain number of transfer functions, depending on their input and output signals.

Once considered all the transfer functions, it has been required to mathematically perform accurate *hand-made* analytical calculations for obtaining the overall Transfer Function, combining between each other the individual functions. By means of this computation, the overall TestBench is reduced to just one *Transfer Function*, visible

in Figure 3.13, providing the Load Cell signal from the input RRSA rotation coming from the QCM, with the possibility of including or not the RRSA damping effects, according to the implemented Transfer Function features.

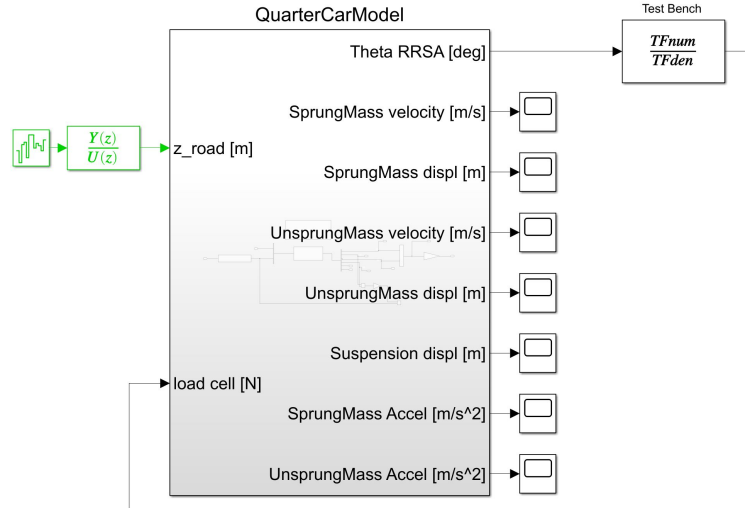


Figure 3.13: HIL Transfer Function Model: overall layout

3.3 HIL State Space Model Simulation

3.3.1 Methodology

Once modelled each single component of the HIL System, in order to start the simulation process is required to assign specific values to the parameters of every subsystem. For what concerns the QCM, its characteristic data have been shown in 3.1.1 in Table 3.1 with reference to a JeepTM Renegade vehicle model, while the remaining parameters are provided directly from the datasheet of each component, as summed up in Tables 3.1 - 3.3 - 3.4 in 3.1.1 and in 3.1.2.

The SimulinkTM model is the one shown in figure 3.10, with all components implemented in the State Space form, to make it easier the evaluation of the results.

Moreover, the reference model itself is simulated in two different forms, depending on the continuous or discrete SimulinkTM implementation of some parts, and the results are constantly compared.

The discretization is applied to all those parts that are actually simulated in the physical HIL application, hence loaded in the dSpaceTM Unit: *Quarter Car Model* and *PID Kollmorgen Controller*. Both systems are characterized by a discretization frequency equal to 4kHz, specified both in the MATLABTM script and in the SimulinkTM space. The continuous implementation, instead, is typical to all those State Spaces that represent a physical component in the real HIL system: Kollmorgen-Pump Group, Piston-RRSA Interface and RRSA system.

Finally, the Quarter Car Model, is here actually implemented without accounting for the tire damping c_u , negligible with respect to the other parameters and consequently set equal to zero.

3.3.2 Analysis of the results: Instability

The first analysis that has been conducted focuses on the frequency domain of the system, since its stability is the fundamental starting condition. Hence, the testbench is reduced to just one *Transfer Function*, providing the output RRSA angle over the input reference one coming from the QCM. Of the resulting transfer function, analytically obtained and validated, is computed the RootLocus and the Bode Diagram, shown in Figure 3.14. In this case the RRSA damping is not affecting the FRF of the testbench, since it is set equal to zero, and the overall bench shows a stable behaviour, with no poles with positive real part. However, as can be observed, the Bode Diagram shows a certain peak around 15Hz, after which the overall response tends to attenuate the input signal.

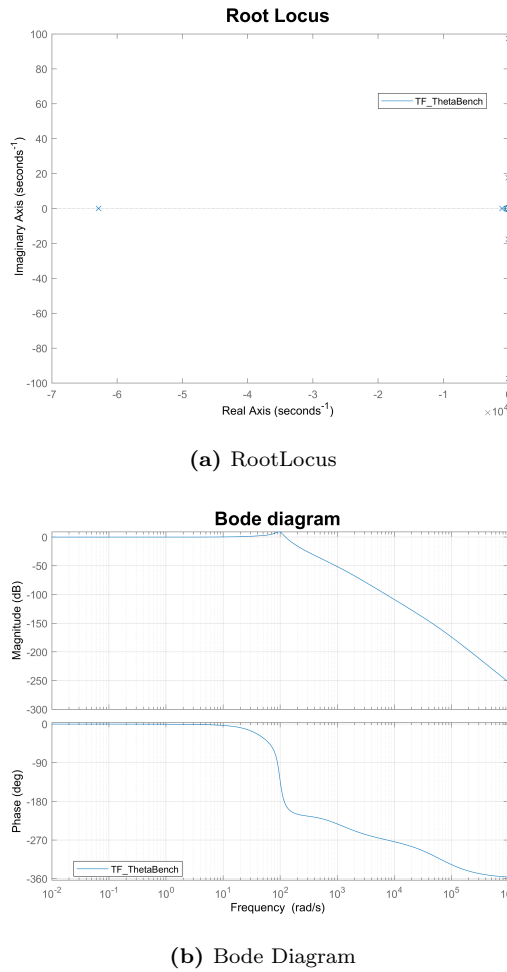
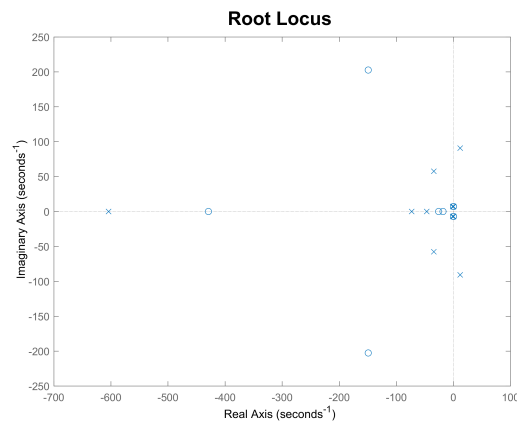


Figure 3.14: *TestBench* frequency response without RRSA damping

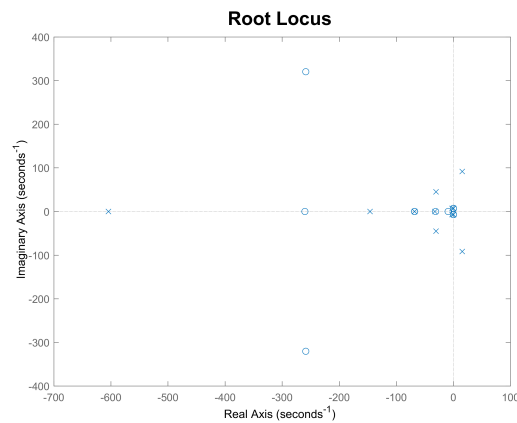
The increase of this frequency, i.e its shift towards higher values, is *one of the main goal* of this study, since it is not feasible to work with a real testbench having such characteristic frequencies: once implemented the ISO road profile, in fact, the signal frequencies entering in the TestBench will be variable and of different entities, inevitably causing relevant and several problems in the results evaluation.

Once evaluated the frequency response of the TestBench, the study can proceed with the frequency analysis of the whole HIL Model. In order to consider the effective stability/instability of the system, the overall HIL system has been reduced to a single TF, having the *input* given by the *road profile* and the *output* defined by the *sprung mass displacement* (any other QCM output signal could have been chosen, it was just required for studying the stability of the system). Starting from the Transfer Function representation of the test bench shown in Figure 3.13, it has been combined

with the corresponding transfer functions of the Quarter Car Model for performing the analytical resolution into just one *overall transfer*. Once reached this function, first of all, it has been validated with the State Space representation of the HIL system, positively demonstrating the correct followed procedure for computing numerically (and logically) its expression. After that, it has been extracted the RootLocus of the obtained Transfer Function, shown in Figure 3.15, for RRSA damping set equal to 1kNs/m and 2kNs/m.



(a) RRSA $c=1\text{kNs/m}$



(b) RRSA $c=2\text{kNs/m}$

Figure 3.15: *HIL Model: HIL RootLocus (sprung mass displacement=output, road profile=input)*

It can be observed that the overall HIL Simulation is characterized by an unstable behaviour, proved by the presence of positive-real part poles for both RRSA damping. Such considerations have been validated by the results in time domain, taking into account a sinewave road-input signal of 1Hz/0.01m and obtaining the *sprung mass displacement* directly from the overall Transfer Function, visible in Figure 3.16.

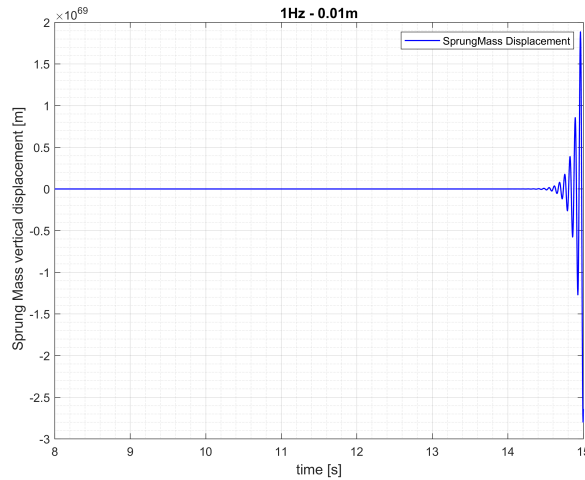


Figure 3.16: HIL Model: Instability results with Sinewave input=1Hz/0.01m and RRSA damping=1kNs/m

The HIL System, with this modelling features, seems to have an unstable behaviour caused by some intrinsic limitations, as was expected based on the analyses carried out before this Thesis Work: hence, the instability has been correctly demonstrated from the numerical point of view.

Considering, then, that the Testbench system has proved to be individually stable, even with the limited bandwidth available, and that the observed instability appears when all systems are connected with each other, i.e when the Hardware-In-the-Loop is correctly implemented, the root cause of the unstable behaviour must be searched in some of the key parameters.

In order to find out the real cause of this behaviour, the simulation has been run with modified parameters. First of all, a *tire damping* value equal to 100Ns/m has been tested, resulting in a non-diverging theta QCM but equally to a saturated Kollmorgen current: consequently, by removing these saturation limits, the overall simulation is still diverging and the whole HIL system is unstable.

Secondly, the *unsprung mass* of the QCM has been modified. From the starting value of 40kg, it has been increased progressively looking at the frequency domain results, up to a value of 320kg. In this condition the simulation largely reaches a stable behaviour and none of the signal is diverging. As shown in Figure 3.17, in fact, the

RootLocus of the overall TF does not show anymore real-part positive poles, meaning that the *instability has been cancelled*. This fact has been proved by the sprung mass displacement in time domain, visible in Figure 3.18, which is no more a divergent signal.

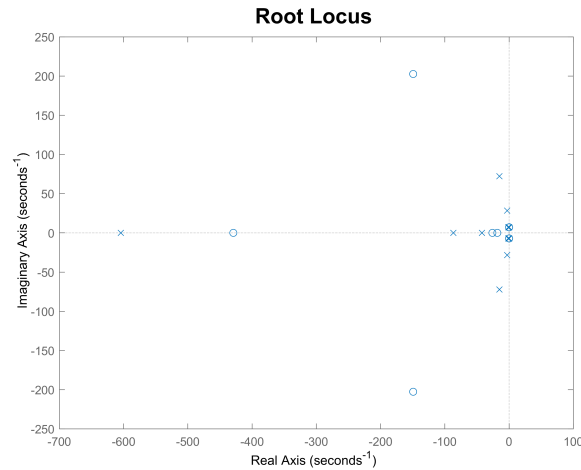


Figure 3.17: *HIL Model: Rootlocus Stable results with unsprung mass=320kg and RRSA damping=1000Ns/m*

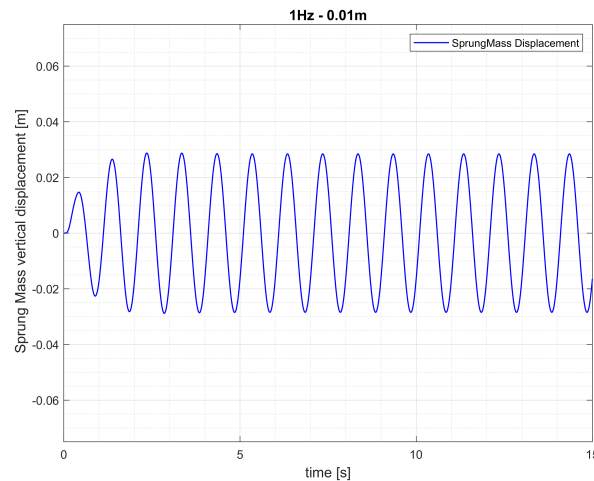


Figure 3.18: *HIL Model: Stable results with unsprung mass=320kg and RRSA damping=1000Ns/m*

These results have highlighted the main cause of the instability of the HIL system: the *limited frequency bandwidth of the test bench*.

The test bench used in this HIL simulation, modelled as described in 3.1.2, has a

frequency bandwidth which is not wide enough for including also the highest frequency characterizing the QCM, identified by the *unsprung mass* of the Quarter Car Model itself. Considering the modelled two degrees of freedom QC, belonging to the JeepTM Renegade (front axle), according to [3], the characteristic frequencies of an *undamped QC with 2 degrees of freedom* are provided by the Equation 3.5:

$$f(\omega) = m_s m_u \omega^4 - [P m_s + K(m_s + m_u)] \omega^2 + KP \quad (3.5)$$

in which, m_s and m_u are, respectively the sprung and the unsprung mass, P is the tire stiffness, K is the suspension stiffness and ω is the frequency (in rad/s).

By introducing the proper values in Equation 3.5, presented in 3.1, the following characteristic frequencies are obtained:

$$\begin{aligned} \text{Sprung Mass frequency} &\longrightarrow \omega_s = 1.132Hz \\ \text{Unsprung Mass frequency} &\longrightarrow \omega_u = 12.6Hz \end{aligned} \quad (3.6)$$

The experienced instability, hence, is due to the fact that the *unsprung mass* frequency ω_u is higher than the available bandwidth of the modelled Testbench. Consequently, by increasing the unsprung mass value, the corresponding frequency is reduced up to the point in which it falls within the frequency bandwidth of the test bench, and no instability occurs. In particular, repeating the calculation with the increased unsprung mass of 320kg, these are the new frequencies of the QC:

$$\begin{aligned} \text{Sprung Mass frequency} &\longrightarrow \omega_s = 1.128Hz \\ \text{Unsprung Mass frequency} &\longrightarrow \omega_u = 4.46Hz \end{aligned} \quad (3.7)$$

In conclusion, proved that the frequency bandwidth of the test bench is not capable of including the highest nominal frequency of the QCM, the next step has the purpose of widening the frequency bandwidth of the test bench under analysis, by following a proper compensation procedure, in order to completely delete the unstable behaviour that occurs with nominal parameters.

3.4 Inverse Compensation Method

The first followed approach for stabilizing the HIL System is defined as *Inverse Compensation Method*. In literature this kind of method has been followed for compensating actuator delay within the simulation, as described in [1] - [4], in order to provide reliable results not affected by the actuator dynamics. With the same purpose, this approach has been used here for properly compensating the dynamic effects of the modelled TestBench in the whole HIL System.

3.4.1 Theory

The *Inverse Compensation Method* is used for solving potential undesired effects caused by a particular component of the installation. From the numerical point of view, this approach implies the inversion of a certain *Transfer Function* (TF), representing the interested component of the simulation, and the application of such resulting TF within the overall system.

By performing these calculations, the input signal that should be applied directly to the interested component, i.e to its corresponding model, is instead passed through the obtained inverted transfer function, whose output is then directed to the main TF. This sequence of passages is summed up in Figure 3.19.

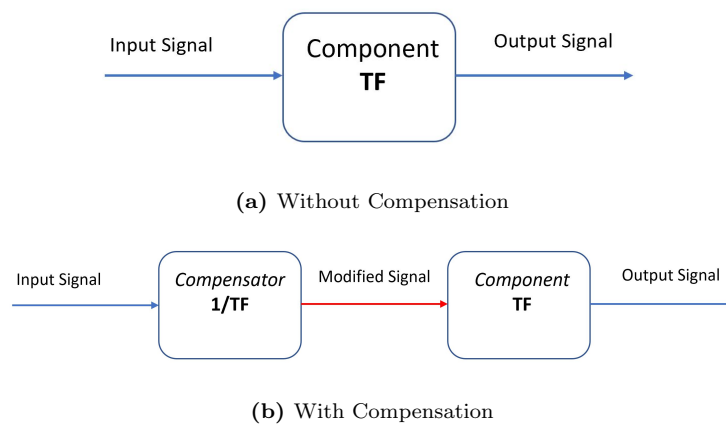


Figure 3.19: Application scheme of Inverse Compensation Method

Consequently, by introducing the Compensator Transfer Function between the input signal and the actual component model, all possible dynamic effects of the latter can be solved, at least from the numerical point of view. The Compensator, in fact, must be properly set in order to decide the interested frequency range for which is required the compensation procedure itself, i.e ensuring desired results on a specific frequency window.

3.4.2 Compensation Procedure

Methodology

Once described the reference Theory, it must be practically applied to the designed numerical model. The implementation procedure can be defined in the following consequent steps:

1. Compute the *TestBench Transfer Function* ($\theta_{\text{Out}} / \theta_{\text{QCM}}$)
2. Compute the *inverse* of the TestBench Transfer Function
3. Define the *cut-off frequency* and the required amount of closure poles to allow the SimulinkTM implementation
4. Introduce the resulting *Compensator* in the overall model

In order to follow these passages is required to work with the *State Space Model* of the HIL System, described in 3.2.1, since the *first* step needs to be accomplished with mathematical calculations based on some available results. The starting phase, in fact, concerns the computation of the *Testbench TF* between the RRSA Output Rotation, directly taken from the *PRI Subsystem*, analyzed in 3.1.2, and the RRSA Input Rotation, coming from the *QCM Block*, in the overall HIL implementation.

Since the focus, for the Compensator computation, is completely related to the Testbench Subsystem, each component here included is defined according to its corresponding transfer functions, i.e the transfer functions related to the *KPG State Space* and to the *PRI State Space*.

It is important to highlight the fact that the Compensator has been considered as the inverse TF of the Testbench (computed between the input and output RRSA rotation), i.e including the *PID* information, but without considering the influence of the RRSA in terms of electrical current. This fact implies that the starting step considers the Testbench model with *RRSA damping* set to θ , hence not affecting the dynamics of the system with its produced force but only with its mechanical connection to the piston (hence, affecting the system with its inertial and dissipative contributions).

Once identified the required transfer functions with the aim of computing the overall $\theta_{\text{Out}}/\theta_{\text{QCM}}$, the mathematical computation has been started, following an *hand-made* analytical approach similar to the one mentioned in 3.3.

By solving the overall circuit, composed by all the fundamental and required transfer functions, the target function between the reference input rotation θ_{QCM} and the output rotation θ_{Out} is obtained. This transfer function has been positively validated by implementing it in SimulinkTM and by comparing its output (θ_{Out}) with the one produced by the used State Space Model.

After that, the obtained TF has been inverted in MATLABTM and 4 *closure poles* have been added in order to allow its implementation in SimulinkTM, since the inverted TF has clearly a higher grade at the numerator than at the denominator (the opposite of the requirement for implementing a proper TF).

The starting value for the *cut-off frequency* f_{cut} has been set to 500Hz, and the application to the inverse of the Testbench TF has been developed as follows:

$$\tau = \frac{1}{2\pi f_{\text{cut}}} \quad (3.8)$$

$$TF_{\text{Inverse}} = TF_{\text{Bench}}^{-1} \quad (3.9)$$

$$TF_{\text{Compensator}} = TF_{\text{Inverse}} \left(\frac{1}{\tau s + 1} \right)^4 \quad (3.10)$$

At the end of Eq. 3.10 the *Compensator* Transfer Function is finally obtained, and in Figure 3.20 is visible its Bode Diagram.

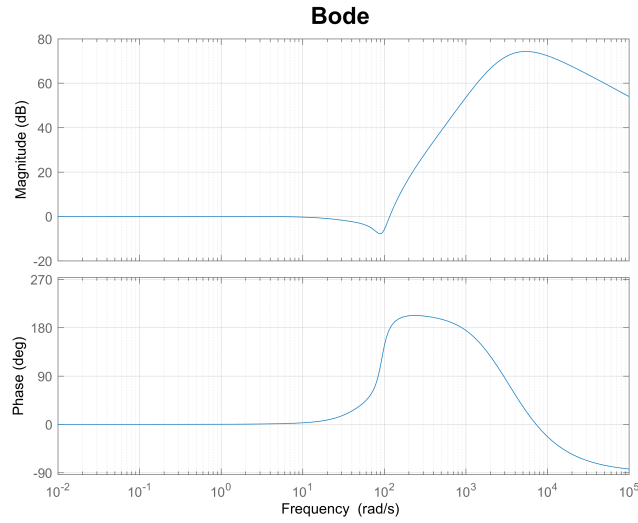


Figure 3.20: Bode Diagram of Compensator Transfer Function with cut-off frequency=500Hz

At this point the compensation procedure requires to combine the information related to the Testbench *without* Compensation, with the Compensator itself, in order to judge the validity of the followed method and of the performed calculations. For this reason, it is computed the *overall* TF between reference rotation and output rotation, with the Compensator model placed before the Testbench, as shown in Figure 3.19, performing the following calculation in MATLABTM:

$$TF_{CompBench} = TF_{Compensator}TF_{Bench} \quad (3.11)$$

Consequently, the overall frequency response of the combined system of Compensator and Testbench is obtained, i.e the *Compensated Testbench*, whose Bode Diagram is represented in Figure 3.21. The Testbench has been first considered, as mentioned before, without RRSA Current contribution, i.e with RRSA damping = 0Ns/m, obtaining quite good compensating performance compared to the case without Compensator, 3.14(b) in 3.3.2. Without Inverse Compensation Method, in fact, the Testbench has shown a limited bandwidth around 15Hz, while with its application the overall system allows to keep very poor attenuation level (looking at the magnitude level in bode representation in 3.21) up to more than 150Hz.

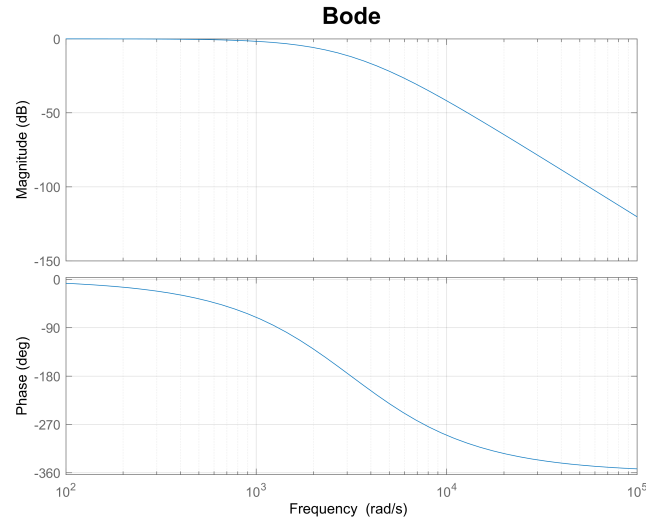


Figure 3.21: Bode Diagram of Compensated Testbench TF with cut-off frequency=500Hz and with testbench RRSA damping=0kNs/m

Finally, the Compensation effects have been evaluated in the case in which the RRSA Current is not 0, hence the *active damper is working* and its contribution in produced force is not null. The Testbench model is now affected by the RRSA damping, which is set to 1kNs/m, while the Compensator is still the same, since, as previously described, it is designed with no RRSA damping. Performing the same procedure of the case without it, is obtained the overall TF with the imposed RRSA damping, whose Bode Diagram is shown in Figure 3.22. As can be observed, the introduced damping in the testbench causes some modifications in the overall frequency response of the system, both in phase-shift and magnitude, with respect to the case without it. This phenomenon was certainly expected, since the considered mathematical formulation takes into account a Compensator TF which is not depending on the damping of the actuator.

The inverted testbench function, which defines the Compensator, is always referred to the case without RRSA damping, since the compensation procedure must be obtained without real-time updating the Compensator itself, which is designed in fixed conditions. As inevitable consequence, hence, the product defined in Eq. 3.11 provides a frequency response function that clearly shows the effects of the introduced damping,

since the Compensator is not directly derived from the considered Testbench TF.

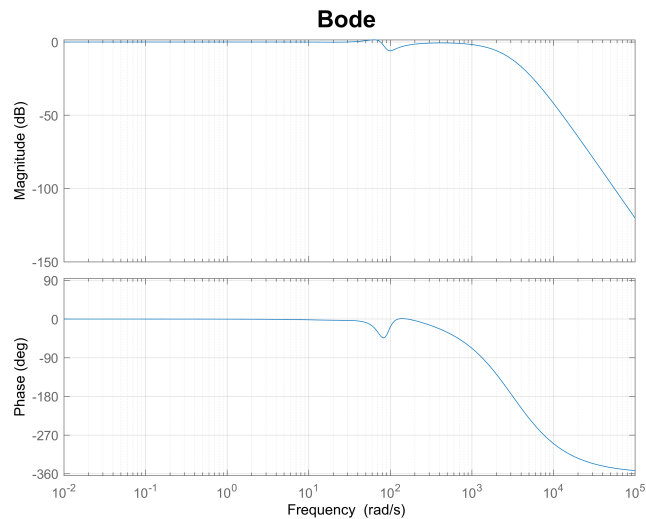


Figure 3.22: Bode Diagram of Compensated Testbench TF with cut-off frequency=500Hz and with testbench RRSA damping=1kNs/m

Time domain results

Once defined the Compensation procedure and having obtained the Compensator Transfer Function frequency response, the overall system can be analyzed also in time domain, to provide graphical results based on the obtained Bode diagrams.

Hence, the Testbench State Space Model, described in 3.2.1, is implemented in SimulinkTM together with the *Compensator TF*, characterized by the common discretization frequency of 4kHz, used for all models that will be loaded in the dSpaceTM Unit. The input signal is a sinewave representing the *RRSA Rotation* that, in the final HIL System, will be provided directly by the QCM. This periodic signal has been set with a frequency of 10Hz, close to the observed critical region without Compensation, and with an amplitude of 2deg. The whole described SimulinkTM implementation is shown in Figure 3.23.

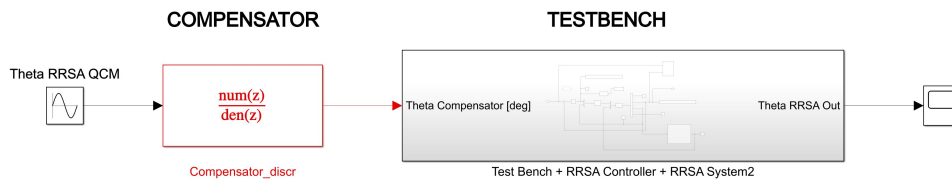
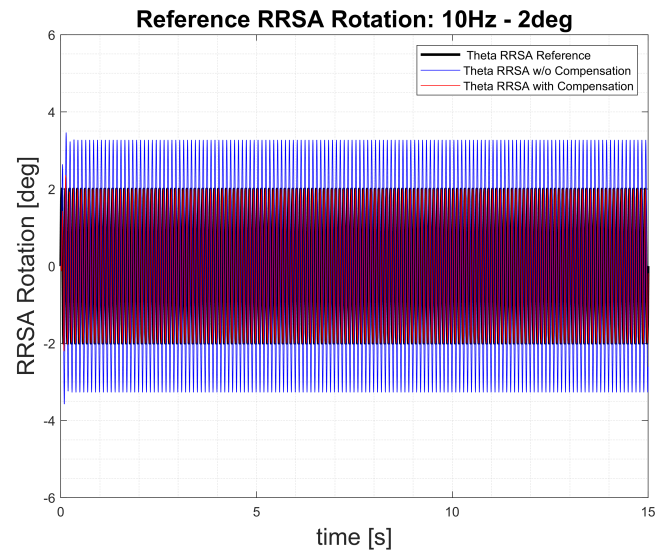
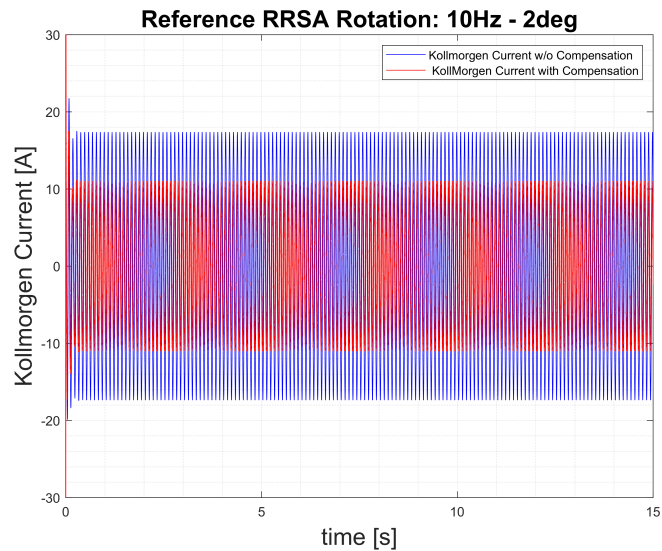


Figure 3.23: SimulinkTM Model of Compensated Testbench



(a) RRSA Tracking



(b) Kollmorgen Current

Figure 3.24: Compensated Testbench results with no damping and input rotation of 10Hz-2deg

For this analysis, the main output of the *Compensated Testbench* is the RRSA Rotation obtained by the PRI Subsystem, which is considered to evaluate the tracking

capability of the Bench with the applied compensation procedure. The other output taken into account is the KollMorgen Current, the fundamental electric parameter used for judging the simulated performance of the electric motor driving the pump, always considering a saturation level of 90A.

As it has been done in 3.4.2, the first considered configuration of the Testbench does not include the effects of the RRSA damping, i.e its value is set equal to zero, obtaining the simulation results shown in Figure 3.24. Considering the frequency response function in 3.21, these results validate the expected behaviour of the simulation. With an imposed testbench RRSA damping equal to zero, in fact, the frequency response of the combined Compensator-Testbench has shown no magnitude attenuation/amplification for a wide frequency range, since the Compensator itself is "perfectly coupled" with the modelled Testbench (both of them are not affected by RRSA damping). The tracking of the RRSA Rotation, hence, shows perfectly overlapped curves between Reference signal and Output signal *with Compensation*, while the *absence of the Compensation procedure* implies a significant amplification of the input signal, as can be seen in 3.24 a).

Due to this difference between the two configurations (with/without Compensation), also the current level characterizing the KollMorgen Unit is visibly different, meaning that the Testbench not compensated is closer to the saturation level than the compensated one, being anyway inside the characteristic limits.

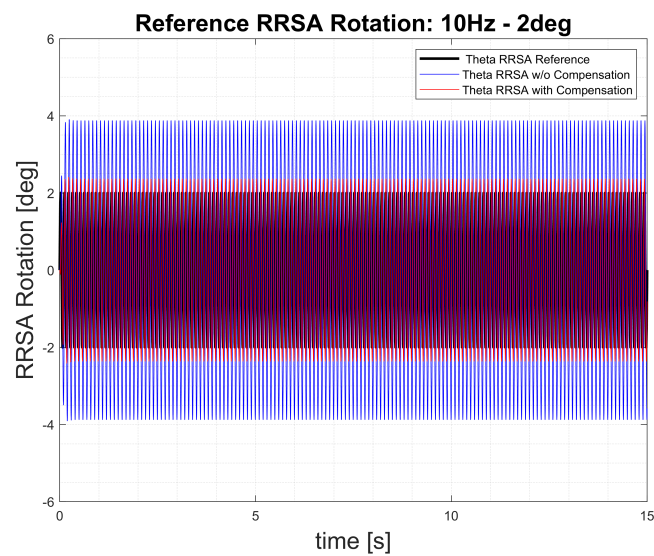
Overall, the obtained results with no RRSA damping imposed at the Testbench have proved the expected satisfying results, thanks to the mathematical coupling behaviour between the Compensator and the bench itself.

However, the same output signals have been acquired also for the *damping configuration*, in which the RRSA damping in the bench is set equal to 1000Ns/m. The resulting signals can be observed in Figure 3.25.

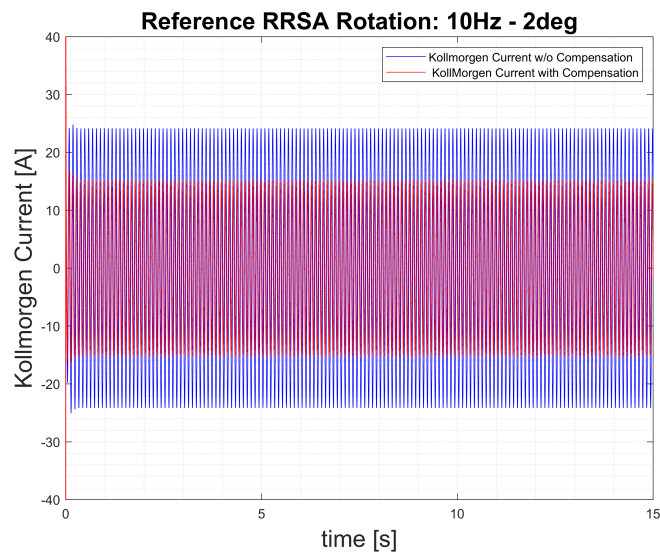
The frequency domain analysis performed for this configuration is here validated by the time domain results. As expected, in fact, the RRSA damping affects the Testbench Model with no modifications on the Compensator, which instead is defined with no damping. The Bode Diagram in Figure 3.22 has shown the effects of such difference in the Compensator-Bench combination, with not negligible magnitude and phase modi-

fications around 100 rad/s (15Hz).

The time domain analysis has proved the whole phenomenon. The RRSA Tracking, in Figure 3.25 a), clearly shows the small difference between reference signal and output rotation, which does not exist at all in Figure 3.24 a) due to the absence of damping. As inevitable consequence, also the Kollmorgen current is affected by this different behaviour, showing a slightly higher steady state value when the Compensation is applied.



(a) RRSA Tracking



(b) Kollmorgen Current

Figure 3.25: Compensated Testbench results with testbench RRSA damping=1kNs/m and input rotation of 10Hz-2deg

Despite the effects caused by the imposed RRSA damping, at the considered input frequency (10Hz) the amplification factor does not provide dramatic increase in steady state values, for what concerns the RRSA tracking capabilities of the system. Even the electric current characterizing the RRSA is not subjected to extremely high increase, keeping its steady state value always below the saturation limits. Most important, both signals do not show bad results as with the Bench without Compensation, hence further validating the Compensation procedure with these acceptable numerical results.

3.4.3 HIL Simulation Results

Once evaluated the Compensation effects on the Testbench model with a cut-off frequency of 500Hz, the study focuses now on the complete HIL Model, with the comparison between the two reference standardized road profiles, *ISO-B* and *ISO-C*, with a reduced *cut-off* frequency of 250Hz. By separately performing additional analyses on the compensating performance, in fact, the reduction of f_{cut} has numerically provided lower values of KollMorgen current, even further from the saturation level with respect to the results obtained with 500Hz.

The ISO-B road profile is characterized by a speed of $70km/h$, while the ISO-C profile is combined with a speed of $35km/h$, since its higher roughness with respect to the previous one, as can be seen in the summing up Table 3.6.

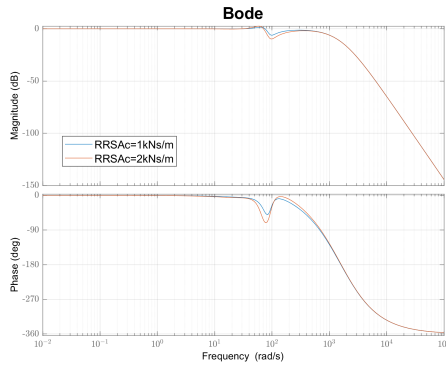
The simulations are moreover performed for both damping values of RRSA.

Road Profile	ISO-B (ISO-C)
Road Profile Roughness	$6.4e - 7(25.6e - 7)$
Speed [km/h]	70(35)
RRSA damping [Ns/m]	1000, 2000
Simulating time [s]	15
Cut-Off Frequency [Hz]	250

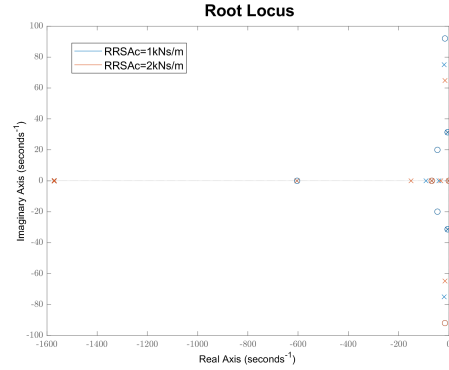
Table 3.6: Simulation Data of Compensation Analysis

Frequency domain results

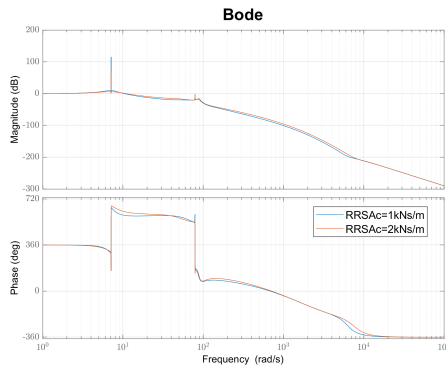
This section sums up the obtained MATLABTM results concerning the performed frequency domain analysis, for both RRSA damping values. In Figure 3.26 can be observed the main considered representations: the Bode and Rootlocus of the *Compensated Testbench*, and the Bode and Rootlocus of the *overall HIL model*.



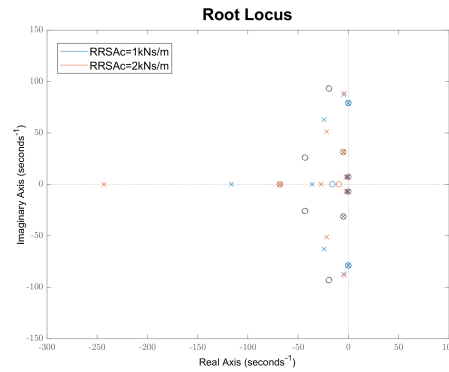
(a) Bode: Compensated Testbench



(b) Rootlocus: Compensated Testbench



(c) Bode: HIL Compensated System



(d) Rootlocus: HIL Compensated System

Figure 3.26: Frequency Domain results of HIL with Compensation and $f_{cut}=250\text{Hz}$

By comparing Figure 3.26 a) with 3.22, is clearly visible the effect caused by the reduced cut-off frequency, since the Compensated-Testbench shows an earlier attenuation level, both in Magnitude and in Phase, due to the frequency defining the Compensator that is now decreased from 500Hz to 250Hz. The stability of the Compensated Testbench, instead, is basically unchanged.

For what concerns the HIL Model, represented by the overall transfer function $\frac{z_s}{z_{road}}$, in the Bode Diagram can be observed two local peaks corresponding to the quarter car model masses (around 1Hz and 13Hz), and a certain attenuation level depending on the

imposed cut-off frequency. Considering the corresponding Rootlocus, the whole model appears to be stable, since no positive-real-part poles are present, hence validating the followed Compensation procedure at the HIL macro level.

With this brief frequency domain analysis on the numerical model, the Inverse Compensation Method has proved to properly stabilize the entire HIL System for both considered damping values, while keeping a faster attenuation level due to the decreased cut-off frequency.

Time domain results

Once obtained and analyzed the results in the frequency domain, the study proceeds with the time domain signals. The reference SimulinkTM Model is the one shown in Figure 3.27, implemented with *SS Models* both in continuous and in discrete form.

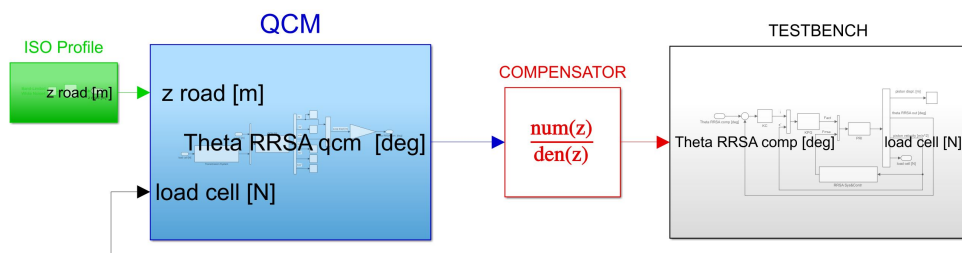


Figure 3.27: HIL Compensated SimulinkTM Model

In this analysis, five main outputs are monitored from the HIL Simulated System:

- Tracking of the RRSA Rotation
- Load Cell Force
- KollMorgen Current
- Unsprung Mass Vertical Acceleration
- Sprung Mass Vertical Acceleration

Each of them is constantly considered both in the Continuous and in the Discrete Model, just to monitor the actual equivalence between the two implementations. Moreover, they will be taken into account in the analyses in the following Chapters.

As can be noted, three of the considered outputs regard, strictly speaking, the Testbench measurements, while the last two are related to the QCM system, clearly affected by the overall HIL System performance.

For what concerns the *Tracking*, it is based on the comparison between the RRSA rotation computed in the QCM and the obtained value in Testbench, as main output of the whole system. It is a measure of the good (or poor) performance of the overall HIL System implemented with the designed Compensator, according to tracking level reached by the system. Moreover, the RRSA damping effects can be evaluated by considering the amplitude of the signal itself.

The second main output, the *Load Cell Force*, represents the actual signal measured by the physical sensor installed in the Testbench. As mentioned in Chapter 2, the Load Cell Sensor is capable of measuring forces up to 5kN and it is placed just at the end of the driving actuator (hydraulic piston).

The KollMorgen Unit, then, is mainly characterized by its current, which represents an important indicator of the actual state of the system. Its upper limit, defined as *saturation limit*, is set to 90A and, in order to accurately emulate the real system, is imposed inside the PID KollMorgen Controller, in the Simulink™ model. By inserting this information in the model, in fact, the temporal signal at the output of the PID Block can not overcome 90A and the signal can be saturated.

The remaining considered outputs, instead, focus on the dynamics of the two masses of the QC, evaluating their vertical acceleration during the whole duration of the test. Starting from the Tracking of the RRSA rotation, the resulting signal can be observed in Figure 3.28. As can be seen, the tracking performance are quite satisfactory for both considered road profiles, providing the ISO-C results with slightly amplified rotation due to the more demanding conditions of the road.

However, for both of them, the increase in RRSA damping implies a significant amplitude reduction of the whole signal, since the RRSA angle is derived from the relative displacement between the QCM masses, strictly dependent on the imposed damping

3.4. Inverse Compensation Method

value (the higher the damping, the lower the relative displacement).

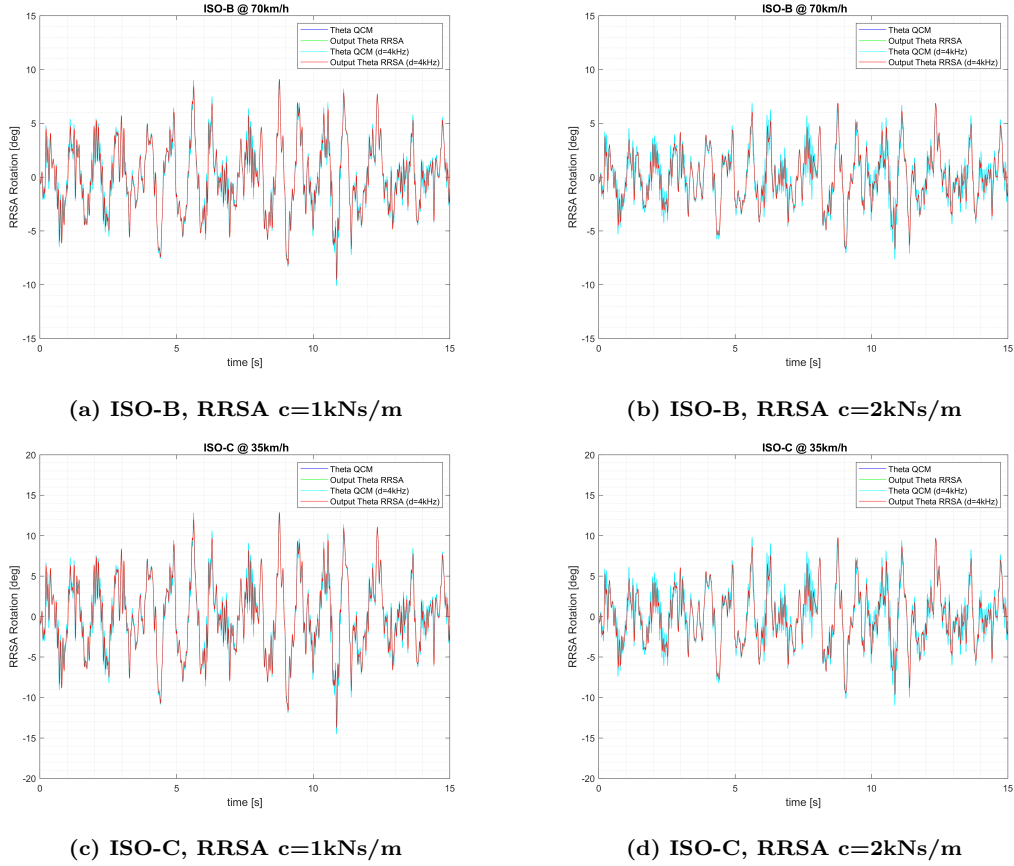


Figure 3.28: Compensation Results with ISO-B and ISO-C inputs and $f_{cut}=250\text{Hz}$: Tracking of RRSA rotation

Similar considerations can be extended to the case of the simulated signal coming from the Load Cell Sensor, shown in Figure 3.29. As expected, in fact, the Load Cell Force is generally higher in the case of ISO-C profile and experiences a further increase when doubling the RRSA damping, reaching in this way the highest peaks for any simulated *nominal conditions*. However, even in this really demanding condition, the overall signal does not come any closer to the sensor end-scale, i.e 5kN, hence further proving the complete validity of the overall HIL simulation.

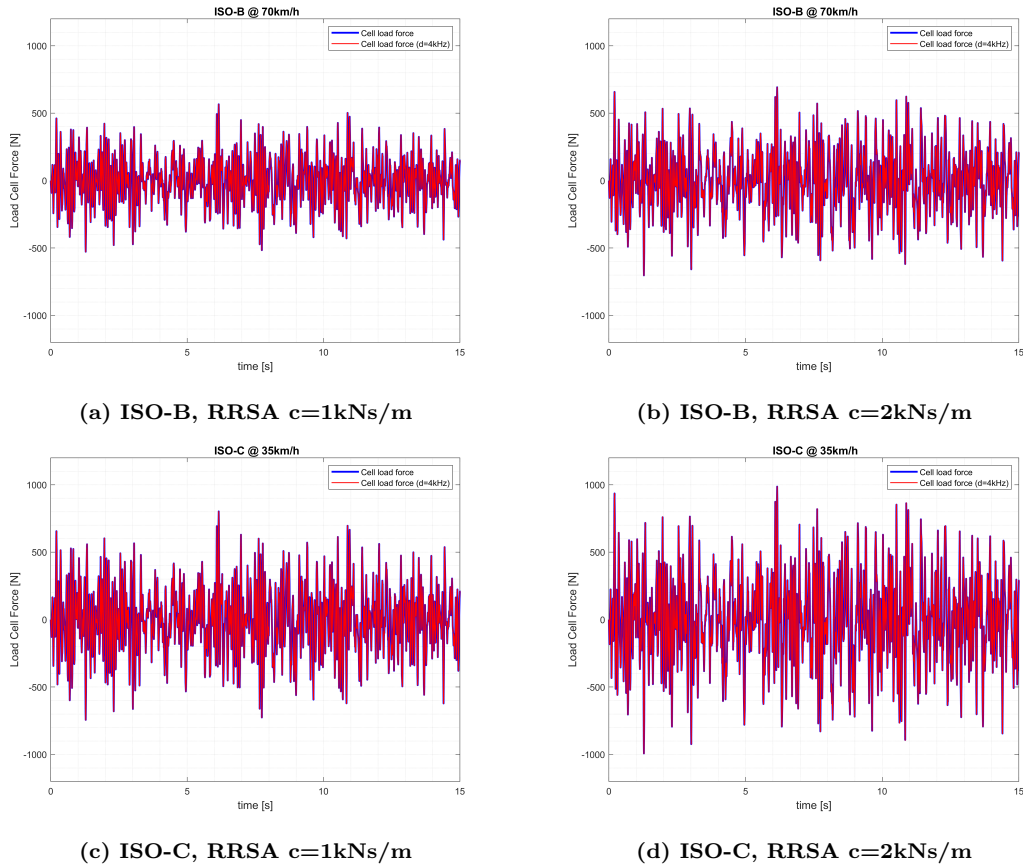


Figure 3.29: Compensation Results with ISO-B and ISO-C inputs and $f_{cut}=250\text{Hz}$: Load Cell Force

A more detailed analysis is required in taking into account the KollMorgen Current, shown in Figure 3.30. First considering the time-history of the ISO-B road profile, whose RMS is summed up in Table 3.7, the signal never reaches the saturation value of 90A, differently from the additional test performed with $f_{cut}=500\text{Hz}$ in which the overall rms value was higher. This difference, in fact, as previously mentioned, has led to choose the decreased value of 250Hz to perform the HIL simulation, as evident from the the RMS value comparison described in Table 3.8. The reduction in cut-off frequency, characterizing just the *Compensator*, in fact, implies a relevant reduction in the RMS value with both simulated damping values, of nearly 30%.

This phenomenon, to be validated by the experimental results, is of great importance, since the resulting current required from the KollMorgen Unit is heavily reduced and far more distant from the saturation level.

In addition to these considerations, also the ISO-C road profile is evaluated and its RMS results are summed up in Table 3.9. As expected, the more demanding characteris-

3.4. Inverse Compensation Method

tics of the input road profile (together with the reduced speed) generate a significant increase in the overall signal, which locally reaches the saturation limit of the electric motor driving the pump. However, despite the increase of more than 40% with respect to the corresponding ISO-B simulations, the resulting RMS values are perfectly feasible with the general characteristics of the machine, hence providing reliable results even with this input road profile.

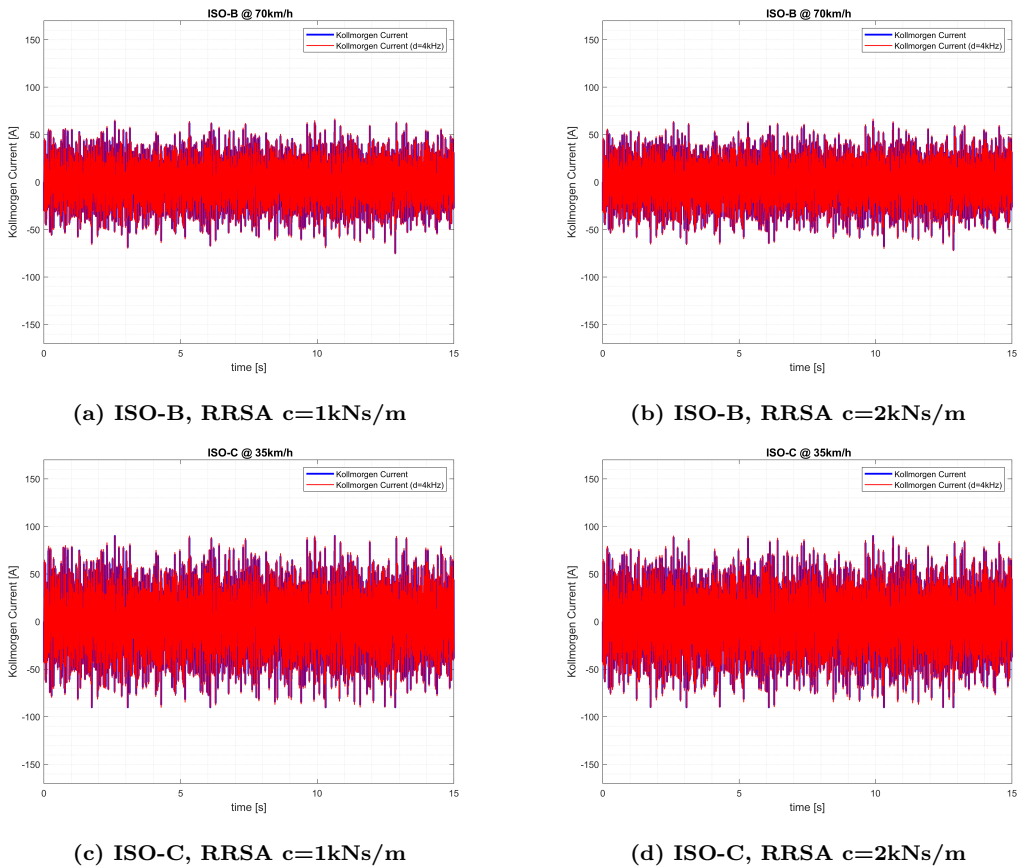


Figure 3.30: Compensation Results with ISO-B and ISO-C inputs and $f_{cut}=250\text{Hz}$: KollMorgen Current

RRSA damping [Ns/m]	Discr. Model RMS [A]	Cont. Model RMS [A]
1000	19.33	18.9
2000	19	18.5

Table 3.7: Compensation Results ISO-B with $f_{cut}=250\text{Hz}$: Kollmorgen Current RMS

RRSA damping	rel.dev (wrt ISO-B/500Hz)
[Ns/m]	[%]
1000	-27.3
2000	-28.1

Table 3.8: *Compensation Results ISO-B with $f_{cut}=250\text{Hz}$ with relative deviation: Kollmorgen Current RMS*

RRSA damping	Discr.Model RMS	rel.dev. (wrt ISO-B/250Hz)
[Ns/m]	[A]	[%]
1000	27.33	+41.4
2000	26.85	+41.3

Table 3.9: *Compensation Results ISO-C with $f_{cut}=250\text{Hz}$ with relative deviation: KollMorgen Current RMS*

Finally, the analysis can move on the last two measured outputs, related to the QC performance. Starting from the Unsprung Mass acceleration, its time-histories are shown in Figure 3.31 for both road profiles. The ISO-B input signal, as evident from Tables 3.10 and 3.11, provides a slight increase in the computed RMS value for both damping configurations, with respect to the performance of the 500Hz cut-off frequency model. This increase, even if lower than 10%, is clearly in opposition to the evaluated results for the KollMorgen Current, in which case the cut-off frequency set to 250Hz implies a general improvement of the current signal.

For what concerns, instead, the ISO-C input profile, as visible in Figure 3.41, its corresponding signal has a significantly increased amplitude along the whole simulation, as expected. This observation is validated by the RMS values, shown in Table 3.12, which are subjected to similar percentage-increase experienced by the KollMorgen Current.

3.4. Inverse Compensation Method

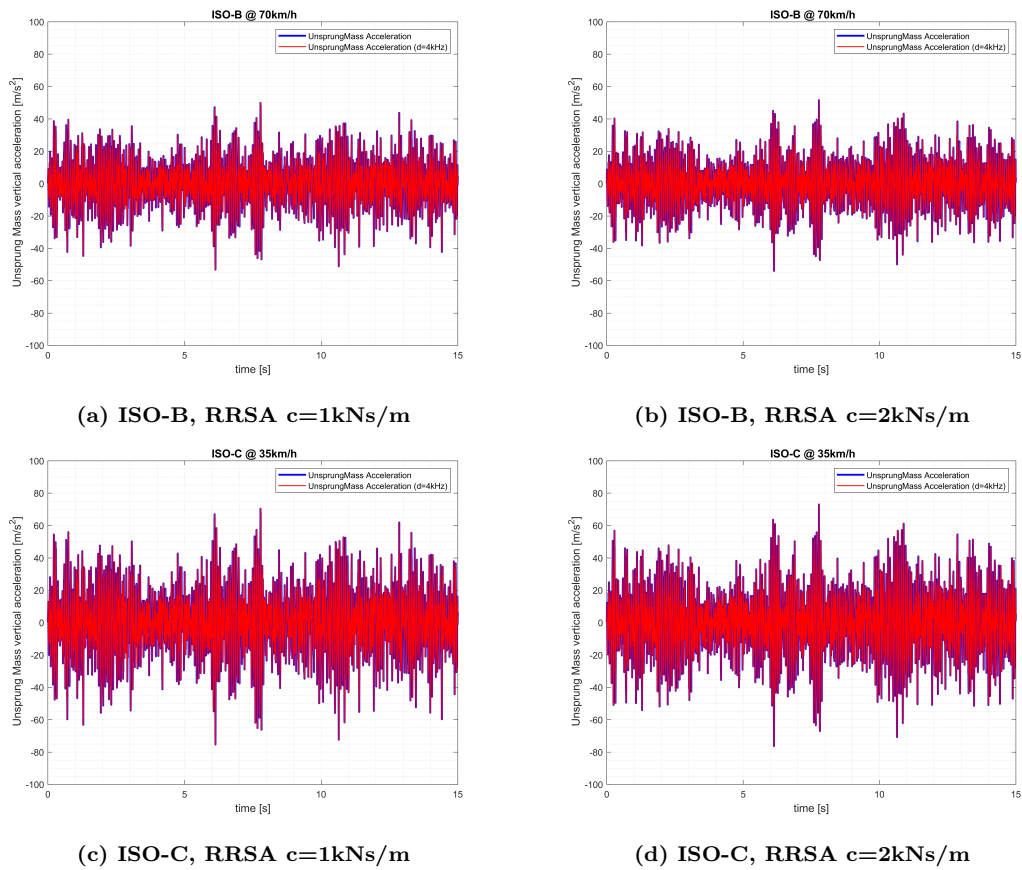


Figure 3.31: Compensation Results with ISO-B and ISO-C inputs and $f_{cut}=250\text{Hz}$: Unsprung Mass Acceleration

RRSA damping [Ns/m]	Discr.Model RMS [m/s ²]	Cont.Model RMS [m/s ²]
1000	14.1	14.06
2000	13.95	13.9

Table 3.10: Compensation Results ISO-B with $f_{cut}=250\text{Hz}$: Unsprung Mass Acceleration RMS

RRSA damping [Ns/m]	rel.dev. (wrt ISO-B/500Hz) [%]
1000	+6
2000	+8.3

Table 3.11: Compensation Results ISO-B with $f_{cut}=250\text{Hz}$ with relative deviation: Unsprung Mass Acceleration RMS

RRSA damping [Ns/m]	Discr.Model RMS [m/s ²]	rel.dev. (wrt ISO-B/250Hz) [%]
1000	19.96	+41.6
2000	19.74	+41.5

Table 3.12: *Compensation Results ISO-C with $f_{cut}=250\text{Hz}$ with relative deviation: Unsprung Mass Acceleration RMS*

Last signal to be analyzed is the *vertical acceleration of the Sprung Mass*, represented in Figure 3.32 for both damping values. As can be observed, by doubling the RRSA damping coefficient the resulting signal is generally amplified. In Table 3.13 are summed up the RMS results for the ISO-B road input, while in Table 3.14 is shown the comparison with the 500Hz cut-off frequency configuration. Following the same trend of the Unsprung Mass, the applied reduction of cut-off frequency implies a slight increase in the corresponding RMS values, with respect to the case at 500Hz. Anyway, if this could be seen as a relevant drawback, as happens for the Unsprung Mass, the entity of such increases is quite low (being in this case lower than 3%), i.e not leading to any particular problems neither in simulation nor, possibly, in the practical implementation of the model.

Considering, then, the ISO-C road profile, its time evolution shows the expected amplitude increase due to the more demanding characteristics of the input signal, better described in Table 3.15 considering the corresponding RMS values. Furthermore, the relative increase with respect to the ISO-B profile is still in the order of 40%, hence sharing this trend with the previous analyzed resulting signals.

3.4. Inverse Compensation Method

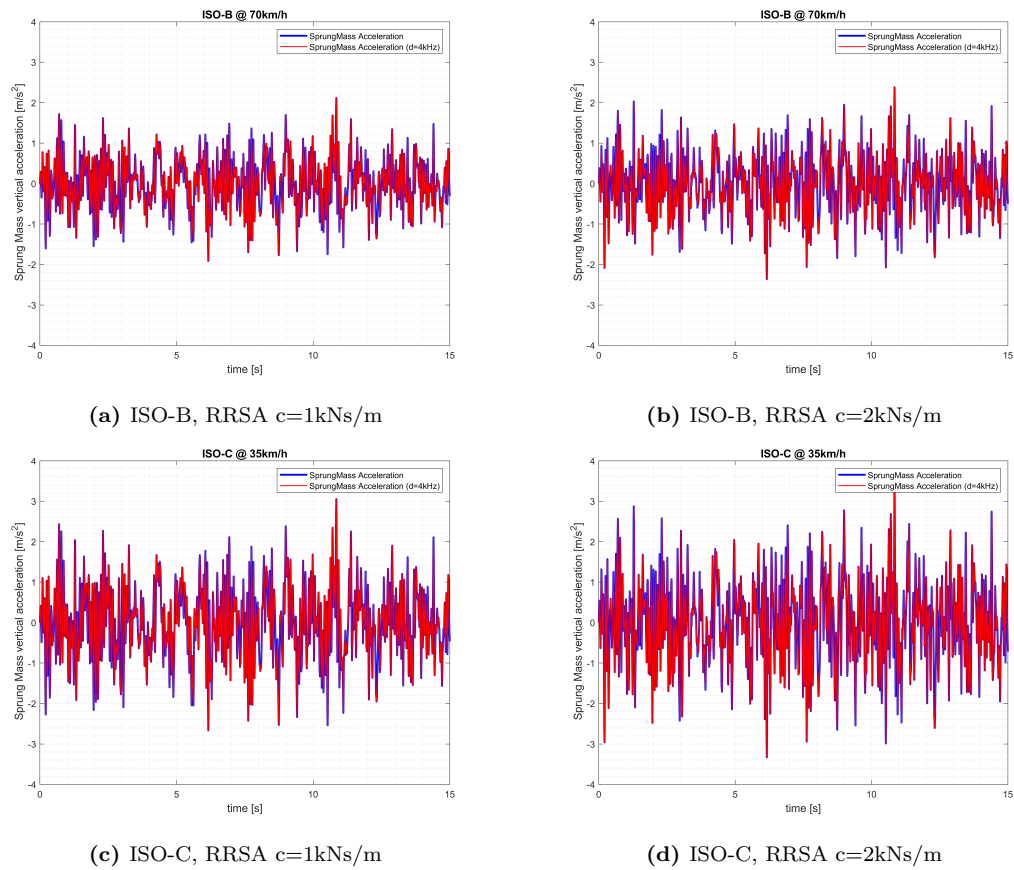


Figure 3.32: Compensation Results with ISO-B and ISO-C inputs and $f_{cut}=250\text{Hz}$: Sprung Mass Acceleration

RRSA damping [Ns/m]	Discr.Model RMS [m/s ²]	Cont.Model RMS [m/s ²]
1000	0.615	0.615
2000	0.71	0.71

Table 3.13: Compensation Results ISO-B with $f_{cut}=250\text{Hz}$: Sprung Mass Acceleration RMS

RRSA damping [Ns/m]	rel.dev. (wrt ISO-B/500Hz) [%]
1000	+2.5
2000	+2.9

Table 3.14: Compensation Results ISO-B with $f_{cut}=250\text{Hz}$ with relative deviation: Sprung Mass Acceleration RMS

RRSA damping [Ns/m]	Discr.Model RMS [m/s ²]	rel.dev. (wrt ISO-B/250Hz) [%]
1000	0.874	+42.1
2000	1.004	+41.4

Table 3.15: *Compensation Results ISO-C with $f_{cut}=250\text{Hz}$ with relative deviation: Sprung Mass Acceleration RMS*

Final considerations

The followed compensation procedure has shown satisfying results in terms of stability of the whole Hardware-In-The-Loop Simulated System, the first important target of this Thesis Work. Once evaluated the causes of the instability, i.e the limited frequency bandwidth of the testbench, the application of the *Inverse Compensation Method* to the whole simulation has provided significant results. The frequency domain analysis has provided the frequency response of the designed *Compensator* and its positive contribution within the simulated system. Such study, hence, has demonstrated the achievement of the desired goal, i.e the stability of the whole System in nominal conditions, while the time-domain analysis has allowed to individually evaluate the effects on the measured significant outputs.

The reduction of the cut-off frequency from 500Hz to 250Hz has provided significant improvements in simulation. As it has been described, the frequency analysis has not been heavily affected by the new imposed frequency characterizing the Compensator. As a matter of fact, the most evident modifications have occurred exactly on its frequency response, combined with the testbench. Despite this difference, the overall HIL Simulation has maintained its stability.

With the analysis in time domain, instead, it has been possible to highlight some major peculiarities depending on the cut-off frequency. The reduction up to 250Hz, in fact, has mainly affected the KollMorgen Current signal, decreasing its saturation level and providing definitely lower RMS values, with a reduction of almost 30% with respect to the case at 500Hz: a significant improvement in achieving the best possible *Compensating Performance* in the HIL Simulated System. Despite the decrease in cut-off frequency has, oppositely, implied a slight increment in the RMS values characterizing

the outputs of the QCM, the entity of such variations is still low (around 7% for the Unsprung Mass and lower than 3% for the Sprung Mass) and allows to accept the cut-off frequency at 250Hz as the target one for some of the following analyses.

Finally, with the same frequency, the ISO-C input road profile has provided relevant but expected results. Since its different characteristics with respect to the ISO-B signal, in fact, the obtained outputs have experienced an overall increase which, anyway, does not change the success of the designed compensation model. As a matter of fact, each monitored signal is still inside the possible operative window of each modelled component, without generating any criticalities even in this more demanding simulated conditions.

All the considered outcomes have provided feasible values according to the limits imposed by the physical mechanical components installed in the actual Testbench and, considering the satisfying obtained results, the compensation method can be assessed to have properly solved the bench instability in the HIL numerical configuration.

Comparison between different implemented compensated models: SS, TF and block model

With reference to 3.2, and with the introduced Compensation Method, for providing reliable results on the developed additional models, this section briefly describes the performed comparison between the three developed implementations of HIL Compensated System in Simulink™ space: the *block model*, the *state space model* and the *transfer function model*. The tested conditions are shared with the analysis carried out in the previous Subsection but with only one input road profile, *ISO-B @ 70km/h*, and one RRSA damping value, i.e 1000Ns/m, keeping the initial cut-off frequency of the Compensator of 500Hz.

In order to simply validate the modelled systems, just three signals have been monitored: *RRSA Rotation from QCM*, *Load Cell force* and *Kollmorgen Current* from the Testbench, all of them shown in Figure 3.33.

As can be observed, all of developed models have been correctly structured and implemented, since perfect overlapped curves can be appreciated. Only the block model

representation, with respect to the State-Space and Transfer Function (directly derived from the State-Space model), shows some very negligible differences in the Load Cell signal, solely caused by software numerical errors and by SimulinkTM simulation settings.

Overall, the three developed representations of the *HIL Compensated System* are perfectly validated between each other, demonstrating the positively performed analytical calculation and modelling process.

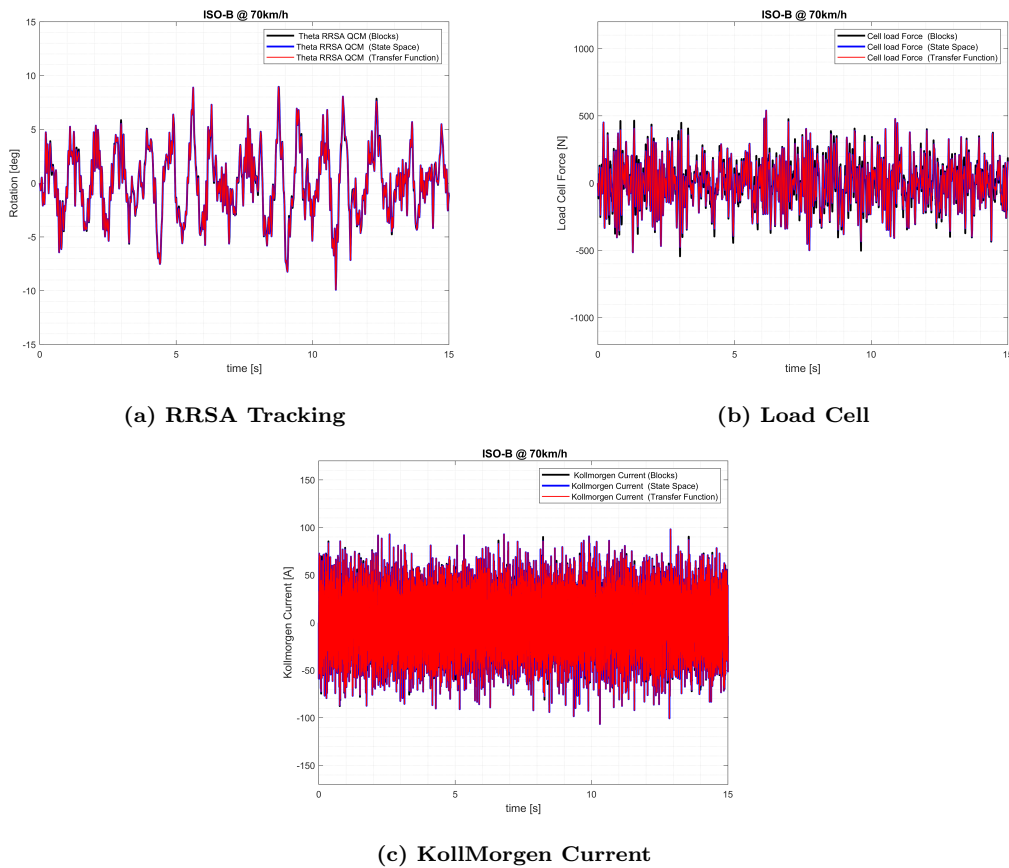


Figure 3.33: *HIL Compensation Results with ISO-B input, $f_{cut}=500\text{Hz}$ and RRSA damping= 1kNs/m : comparison between different implementations*

Robustness Tests

In this Section the study proceeds with some tests concerning the *robustness* modelling process of the overall HIL System. These checks have the general purpose of validating the obtained MATLABTM/SimulinkTM Model, by properly modifying some key parameters in order to evaluate the consequent effects. In the physical HIL Installation, in fact, some not-modelled factors like *noise*, *measuring system off-sets*, *sensor*

drift and *dissipative contributions* can certainly affect its overall working conditions. Consequently, the designed Robustness Tests have the aim of increasing the accuracy level of the Model by simulating more *realistic* conditions. In particular, two different kinds of analyses have been carried out to test the model robustness:

- The *OFAT* Test
- The *Noise Disturbance* Test

Robustness test: OFAT

Methodology

Before proceeding with the experimental tests on the actual Testbench, a robustness analysis of the whole HIL system is performed. The main purpose of this procedure is to simulate some possible disturbances affecting the real HIL testing and to evaluate the consequent possible deviations of some key parameters of the simulation itself.

In order to perform such tests, three important data are alternatively modified:

- The *unsprung mass* of the QCM
- The *piston mass* of the TestBench
- The *dissipative coefficients* of the TestBench

These robustness tests are performed by changing *OFAT* (one factor at time), in order to judge the effects of each single variation on the whole HIL system with a good accuracy. Each factor is deviated from its nominal value of a fixed percentage, equal to +/- 10% , and for each conducted test the frequency domain and the time domain results are analyzed. Moreover, to sum up the robustness test into the most significant cases, only the ISO-C road profile at 35km/h is considered, being the most critical condition faced by the QC, with a fixed RRSA damping of 1kNs/m and a cut-off frequency of 250Hz.

Frequency domain results

The robustness test main purpose is to evaluate the effects of the three modified-key-factors on the whole HIL simulation. Starting from their variations, the frequency domain is inspected and some detectable differences are noted.

Since the dissipative-coefficients and the piston mass are factors characterizing the

testbench, the first followed step has been to evaluate its different frequency response function and rootlocus, always referring to the TF previously obtained ($\frac{\theta_{out}}{\theta_{ref}}$, with RRSA damping=0). As it is visible in Figure 3.34, however, neither their positive nor their negative variations cause significant differences in the Testbench frequency response, which keeps substantially its nominal trend.

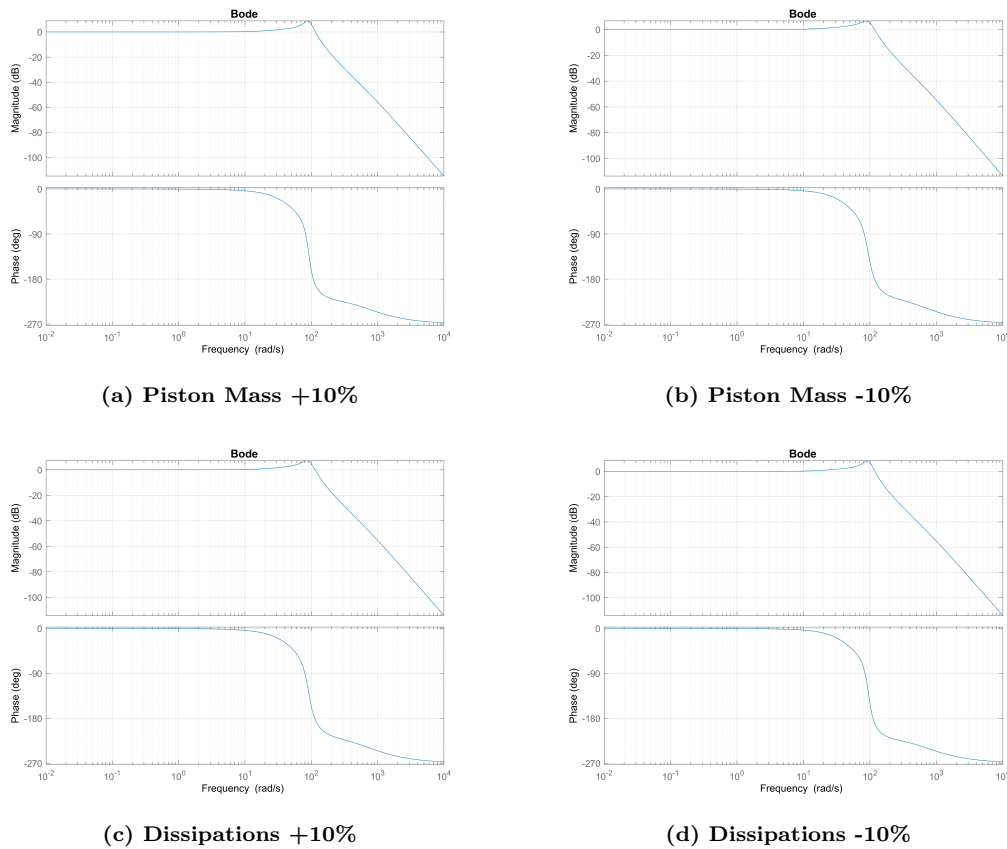


Figure 3.34: *Piston Mass and Dissipation Robustness Test: Testbench Bode Diagram ($\frac{\theta_{out}}{\theta_{ref}}$).*

The frequency response function obtained, instead, by varying the unsprung mass value is obviously unchanged with respect to the nominal one, being this parameter not affecting it (hence, it not included in the plot). Also the stability of the testbench has been taken into account, as a function of the performed robustness tests. In Figure 3.35, in fact, are visible the Root Loci of the Testbench transfer function corresponding to the *Piston Mass* and *Dissipative Coefficients* sensitivity. As can be seen, negligible differences can be observed in the location of some poles, zeros and couples of poles and zeros.

3.4. Inverse Compensation Method

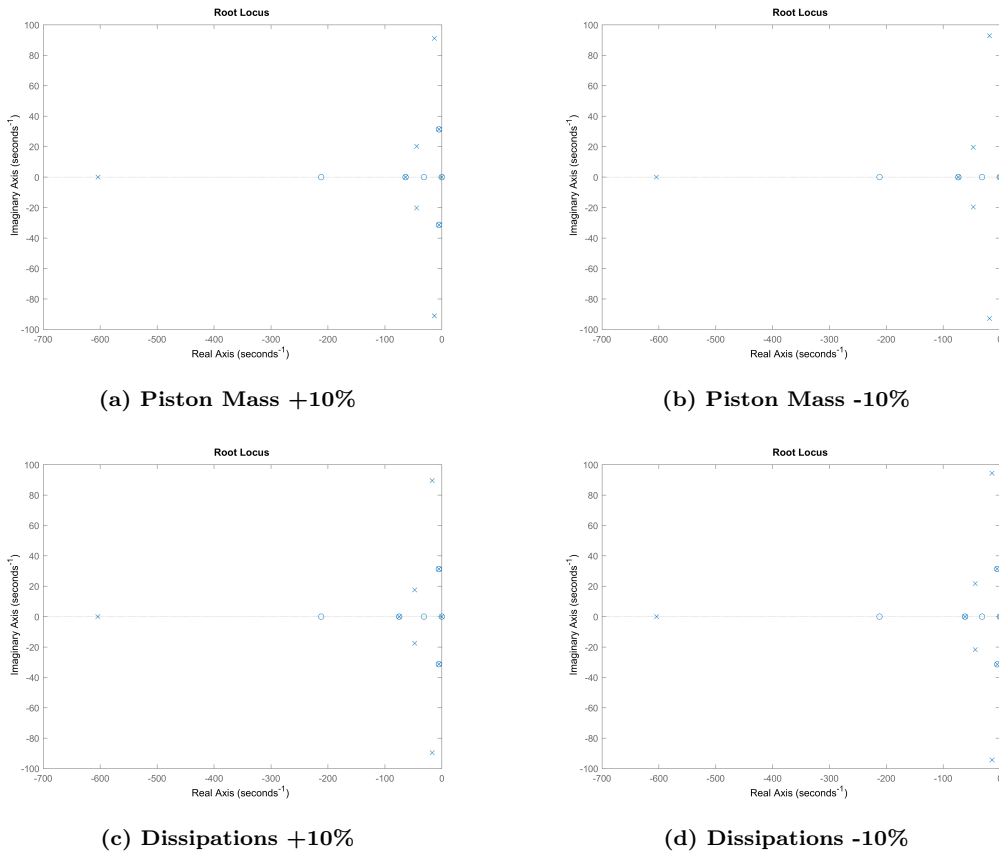


Figure 3.35: Piston Mass and Dissipation Robustness Test: Testbench Root Locus ($\frac{\theta_{out}}{\theta_{ref}}$)

Once analyzed the frequency response of the Testbench Model, the study proceeds passing to the *instability* of the overall *HIL simulation without Compensation*, to observe if the involved factors can affect it. In this analysis, together with the variation of the Piston Mass and the Dissipative Coefficients of the testbench, also the Unsprung Mass effect is considered, since it affects the QCM which is now part of the system. Even in this case, however, the frequency domain results are not significantly different with respect to the nominal conditions. In Figure 3.36, in fact, are grouped together just the results containing negative variations of the key parameters, since no visible differences have been noted in all the other cases. The Root Locus shows the expected HIL instability, with just some couples of poles and zeros moved along the chart. Up to this moment, the RRSA damping has not been involved in the analyses, since the Testbench TF, as previously explained, is computed without considering the force gen-

erated by the RRSA. In this second step, instead, the HIL simulation takes into account the *actuation effect* of the active damper, i.e a current flows in the electric machine of the RRSA and a force is generated, numerically speaking.

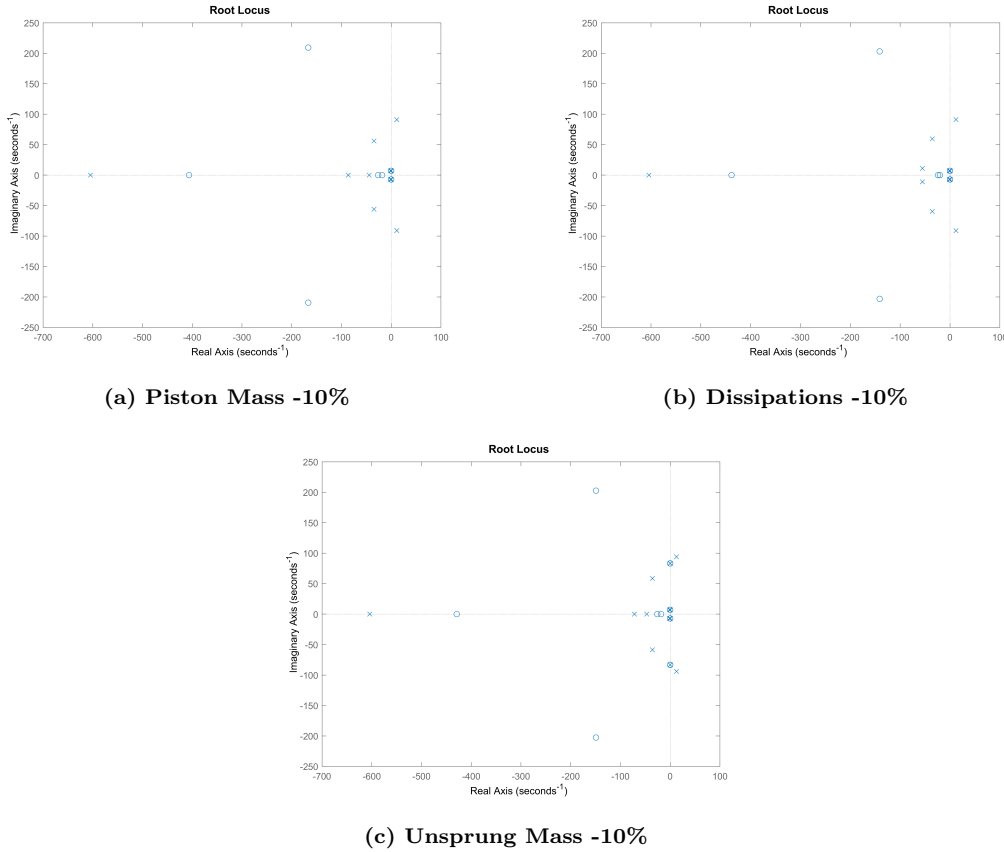


Figure 3.36: *OFAT Robustness Test: HIL Root Locus without Compensation* (Sprung Mass displacement =output, road displacement=input)

The study focuses now on the Compensation effects, starting from the evaluation of the new frequency response function between *Compensator* and *Testbench*, even though the Compensator can not be affected by the parameters involved in the robustness test. In fact, as it was previously described, the Compensator is designed as the inverse transfer function of the testbench, computed as function of θ_{RRSA} , without RRSA current contribution and, most important, in nominal conditions. Consequently, the Compensator can be affected only by the imposed cut-off frequency, which in this case has been definitely fixed to 250Hz, since the better obtained results. Hence, the overall frequency response function of the assembly *Compensator-Testbench* can be affected only by the differences spotted in the TestBench bode diagram, shown in Figure 3.34,

3.4. Inverse Compensation Method

since the Compensator itself is a constant transfer function in all the performed robustness tests, and can not be affected by the Unsprung Mass variation, being the QCM not included in this assembly. All these considerations are demonstrated by the results shown in Figure 3.37, to be properly compared with the ones in Figure 3.35

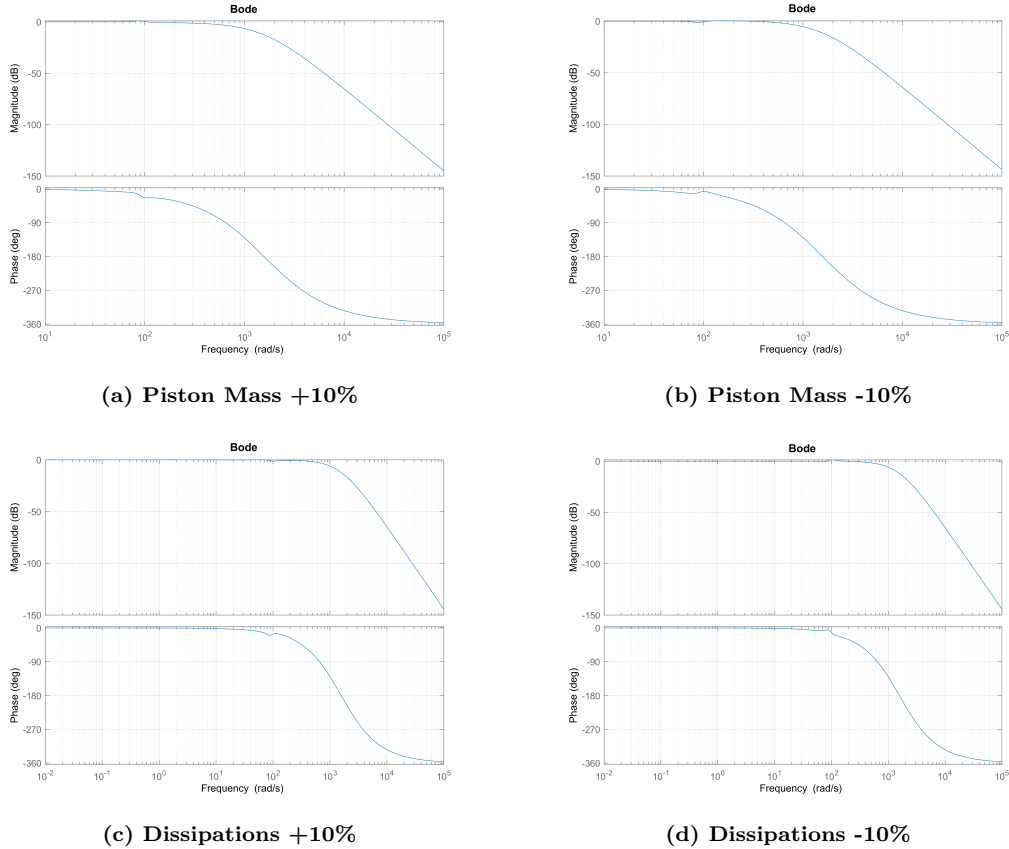


Figure 3.37: *Piston Mass and Dissipations Robustness Test: Compensator-Testbench Bode Diagram ($\frac{\theta_{out}}{\theta_{ref}}$, with RRSA current=0)*

With respect to the nominal frequency response, every computed Bode diagram shows just a slight deviation around 100 rad/s, both in the amplitude and in the phase response. Such short irregularities, anyway, consist in very few dB in Magnitude and just slightly more in Phase, which allows to state that the overall response is maintained constant in all the performed robustness tests. Most important, the designed Compensator demonstrates to be able to properly work even with modified key parameters, offering basically the same frequency response in all conditions.

However, in order to complete the frequency analysis of the *Compensated-Testbench*,

the RRSA current must be taken into account in the model and in the robustness test, as shown in Figure 3.38. Particularly now than any other previous case, the robustness tests results show no perceivable differences with respect to the nominal condition set up. For this reason, as it has been done in Figure 3.36, only the negative variations have represented, since no relevant differences have been noted. Even considering the short and negligible irregularities observed in Figure 3.37, now with the introduction of the force provided by the active damper (hence, with a damping coefficient of 1kN-s/m, an electric current is flowing in the electric machine) such observable differences basically disappear.

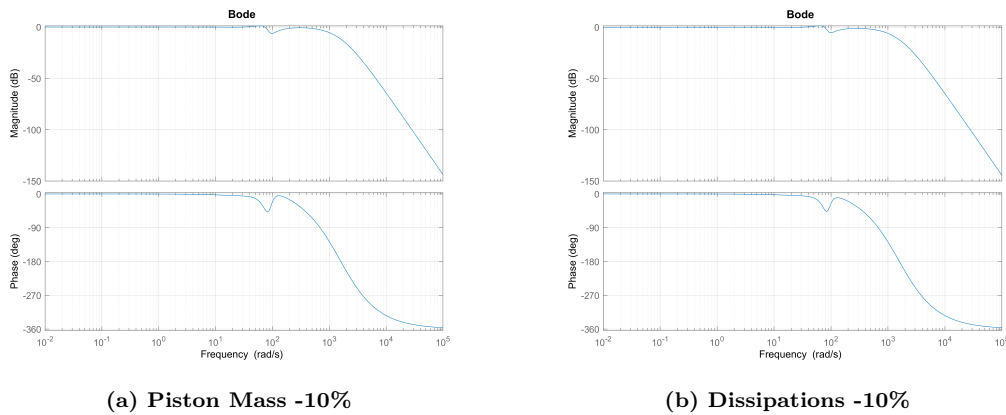


Figure 3.38: *Piston Mass and Dissipations Robustness Test: Compensator-Testbench Bode Diagram ($\frac{\theta_{out}}{\theta_{ref}}$) with RRSA current ($c=1kNs/m$)*

Finally, the overall *HIL Compensated System* frequency response is evaluated for all performed robustness tests, together with their corresponding Root Loci. Also in this case, the results do not provide significant differences with respect to the reference model, again showing in Figure 3.39 just the negative variations of the involved parameters (since no visible deviations can be appreciated with the positive ones).

3.4. Inverse Compensation Method

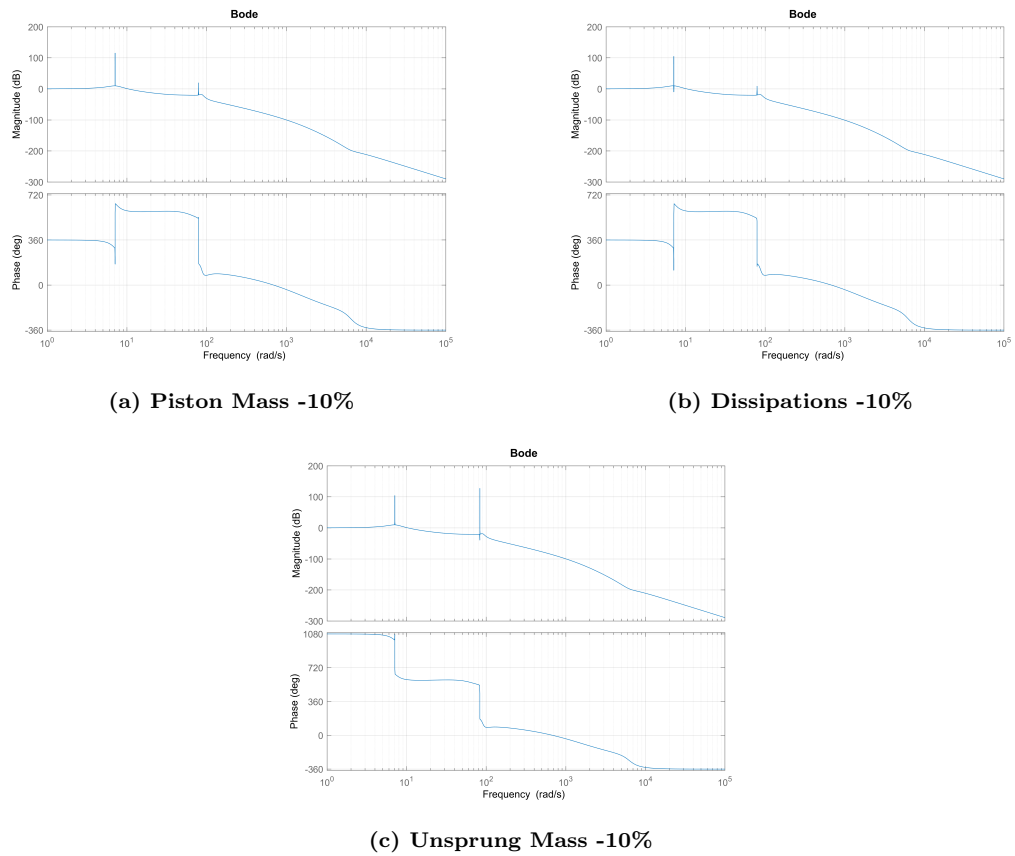


Figure 3.39: OFAT Robustness Test: HIL Compensated Bode Diagram (Sprung Mass displacement =output, Road displacement=input) with RRSA current ($c=1\text{kNs/m}$)

The bode diagrams, related to the TF between *Sprung Mass Displacement* and *Road profile displacement*, in fact, basically remain unchanged, with just some negligible differences in the Magnitude response (in the reached peaks) and more evident deviations in the Phase response. However, can be comfortably assessed that the Magnitude response keeps its nominal trend in all the considered robustness tests, proving one more time the capability of the designed Compensator to work properly in conditions different from the nominal ones.

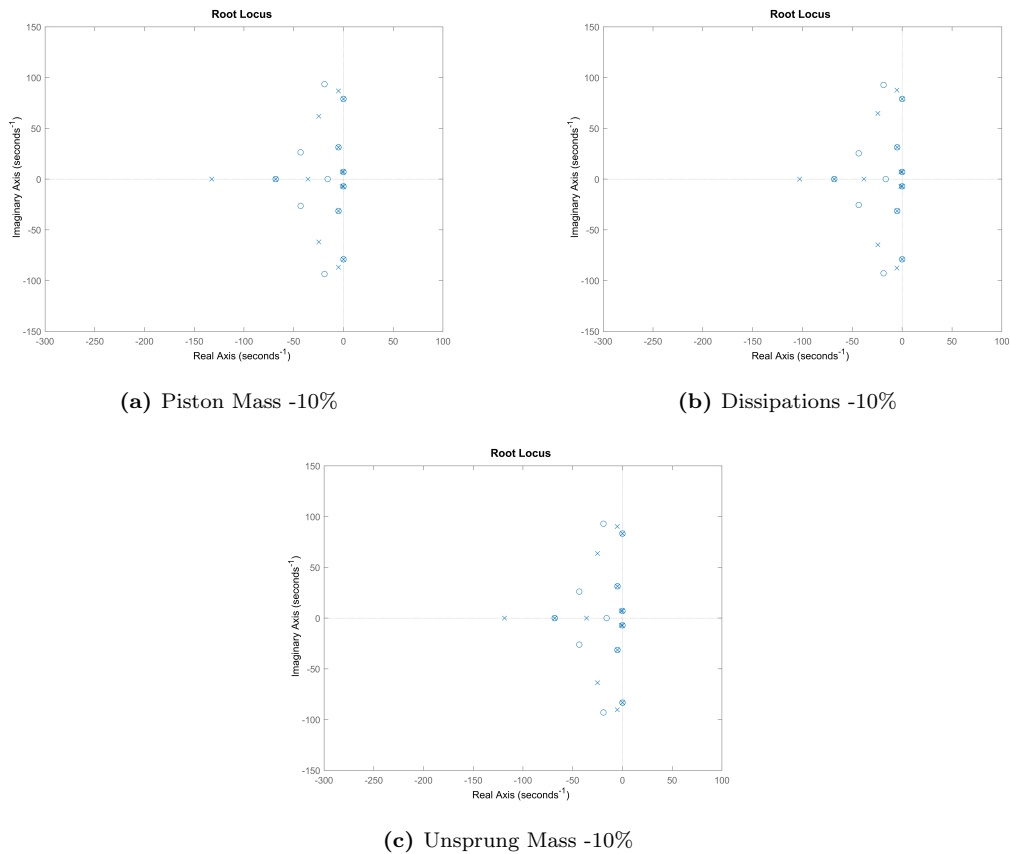


Figure 3.40: *OFAT Robustness Test: HIL Compensated Root Locus* (Sprung Mass displacement =output, Road displacement=input) with *RRSA current* ($c=1\text{kNs/m}$)

The stability analysis represented by the Root Locus, in Figure 3.40, concludes the frequency domain analysis of OFAT robustness tests. One more time, just the negative variations are considered, since the positive one provide very similar results.

As can be seen, no relevant differences can be appreciated with respect to the nominal conditions, with just some displaced location of poles, zeros and couples of poles and zeros. Most important, none of the performed analyses contains positive-real-part poles, hence further demonstrating the stability of the *HIL Compensated simulation* in frequency domain even with the considered deviated key parameters.

Road Profile	ISO-C
Road Profile Roughness	$25.6e - 7$
Road Profile Speed [km/h]	35
RRSA damping [Ns/m]	1000
Time duration [s]	15
Cut-Off Frequency [Hz]	250

Table 3.16: *Simulation Data*

Time domain results

The performed frequency domain analysis has proved the stability of the *HIL system with inverse compensation method* with the designed robustness test. Now, the required step is to analyze the time domain of each test, by evaluating the same output signals obtained in 3.4.

As previously described, the simulation is performed with a standard *ISO-C road profile at 35km/h*, for an overall duration of 15s, as reassumed in Table 3.16. Similarly to what has been done in 3.4, moreover, each measured output constantly contains the comparison between the continuous and discrete Simulink Model. The latter, as described in the previous sections, is obtained with a discretization frequency of 4kHz. Starting from the *RRSA tracking*, Figure 3.41 provides an overall view of the time-histories of the performed robustness test, with just negative 10% variation of the considered parameters, since no considerable differences can be appreciated.

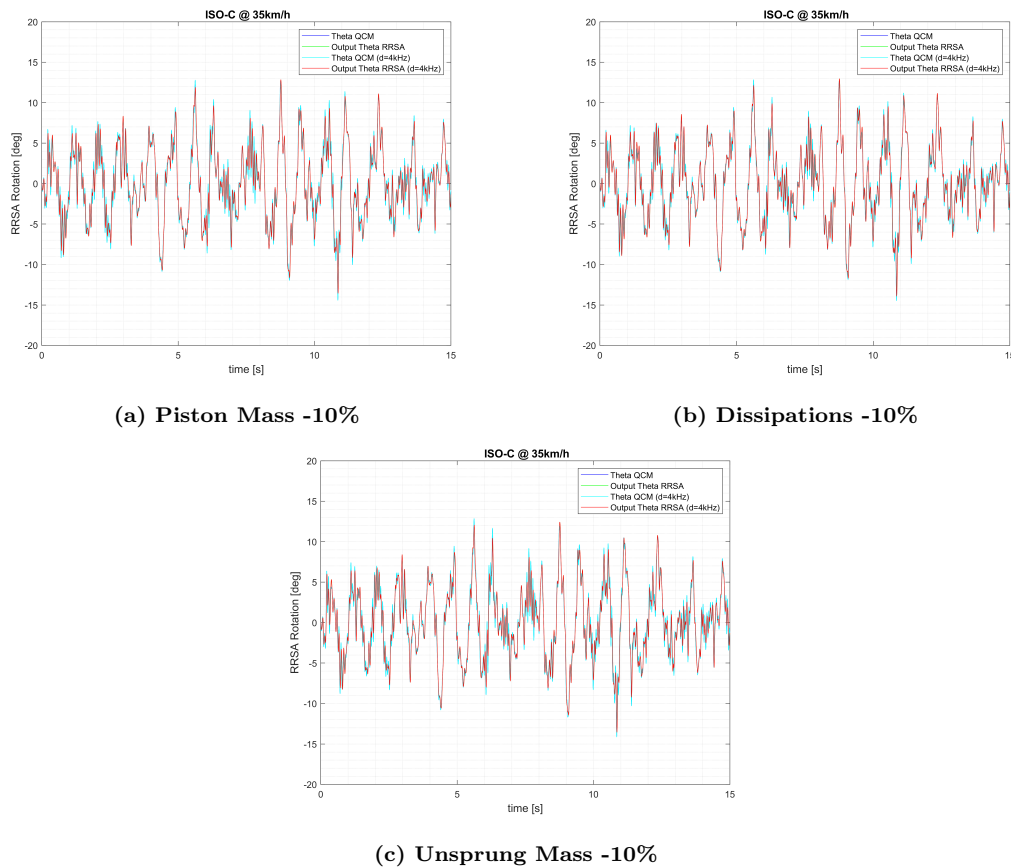


Figure 3.41: OFAT Robustness Test: Tracking of RRSA rotation

Each plot contains 4 different representations, as described in previous analysis, showing the time-tracking of the RRSA rotation between QCM and Testbench for both continuous and discrete models. All of the tested configurations show basically the same tracking level with respect to the nominal conditions, with no relevant differences. Similar considerations can be done for the Load Cell results, shown in Figure 3.42, in which, with just some local different peaks in amplitude, each measured signal keeps the overall course followed by the nominal configuration.

3.4. Inverse Compensation Method

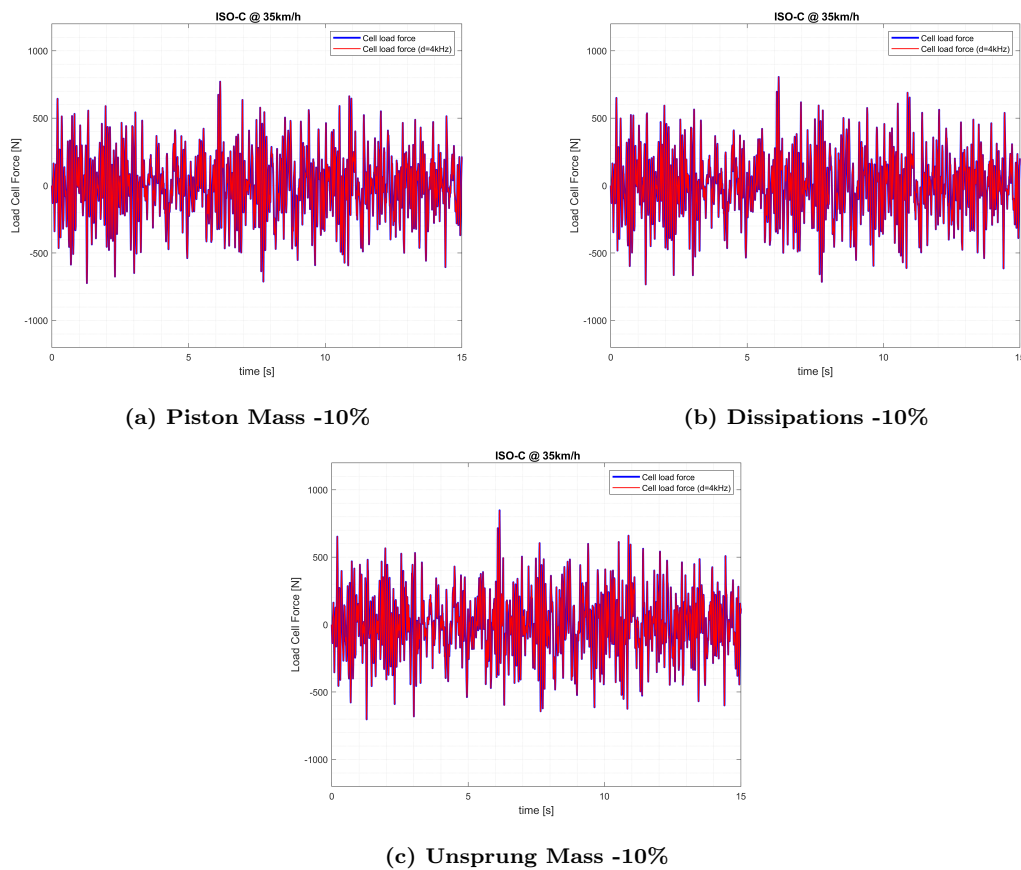


Figure 3.42: OFAT Robustness Test: Load Cell Force

Once evaluated the first two signals of the time-domain analysis, the study requires to focus on the remaining three fundamental signals: the *current of the KollMorgen*, the *Sprung Mass vertical acceleration* and the *Unsprung Mass vertical acceleration*. For these outputs, together with their simulated time-histories, it is added the *root mean square value* of the signals (RMS), in order to efficiently sum up their course and to highlight the deviations between each of the simulated conditions.

For each measured output, the time-results are grouped just for the negative variation of the involved parameters (-10%), as it has been done in the previous sections, while the obtained RMS values have been collected in the following tables for both variations (-10% and +10%), to provide the overall results in a simpler way. Starting with the *Kollmorgen Current*, in Figure 3.43 can be observed the time-evolution of the signal, for both the continuous and the discrete implementation and for both tested deviations. Looking at the Sum-Up Tables 3.19 and 3.17, some relevant details are noted. Combining the information retrieved by the RMS values, in fact, it is evident that the

whole system shows a reduced sensitivity towards two of the considered Robustness Tested Parameters, i.e the *Piston Mass* and the *Dissipative coefficients*, providing a relevant dependency only on the *Unsprung Mass*.

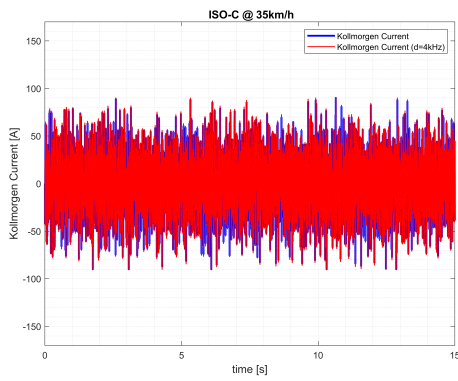
Without focusing on the yet discussed small differences between discrete and continuous model, and taking into account the Discrete Model (previously reasoned), the deviation of +10% of these two parameteres (*Piston Mass* and *Dissipative coefficients*) implies very reduced changes with respect to the nominal configuration, leading to a KollMorgen Current relative variation of 0.44% (in case of Piston Mass) and 0.3% (in case of Dissipative Contribution). The same deviation of +10% for the Unsprung Mass, instead, leads to a KollMorgen Current relative variation of 7.8%, with negative sign in this case. All these results are summarized in Table 3.20.

This first analysis suggests that the overall *HIL Simulated System* seems to be more sensitive to the Unsprung Mass value introduced in the QCM, rather than to the other considered parameters. This fact can be stricly correlated to the Instability Analysis discussed in 3.3.2, in which the Unsprung Mass has shown its critical importance. In this case, the increase of 10% of the Unsprung Mass leads to a reduction of the KollMorgen Current RMS, i.e a decreased amount of current is required from the PID control system. This result is a further demonstration that a heavier Unsprung Mass can lead to a more stable overall HIL system, since the *saturation limit* of the KollMorgen Unit is further than in nominal conditions.

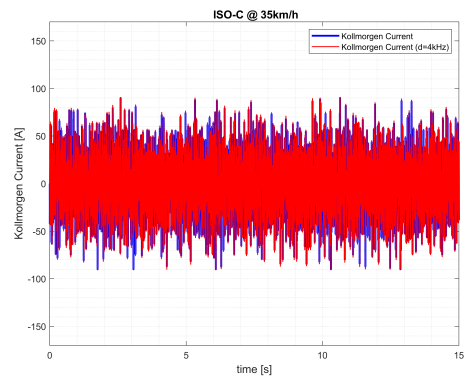
Equivalent but opposite considerations are valid looking at Table 3.18. By decreasing the consired parameters of the same 10%, in fact, for all tested conditions quite similar relative deviations are obtained, with respect to the positive variation, and the Unsprung Mass test results in an increase of almost 10% in KollMorgen Current RMS. Hence, opposite to the previous case, the lighter Unsprung Mass leads to an overall condition *closer* to the saturation limit of the KollMorgen Unit and, consequently, *closer* to the instability, as expected.

In both cases, Dissipative Coefficients and Piston Mass do not show great impact on the KollMorgen Current signal, with relative deviations in anycase lower than 1%.

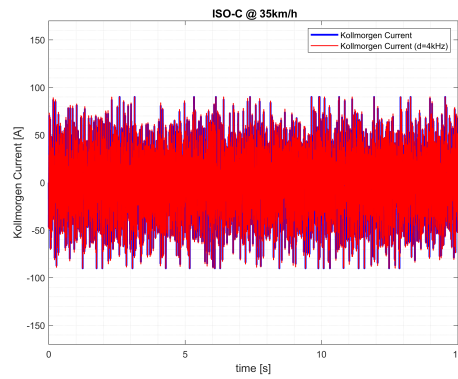
3.4. Inverse Compensation Method



(a) Piston Mass -10%



(b) Dissipations -10%



(c) Unsprung Mass -10%

Figure 3.43: OFAT Robustness Test (-10%): KollMorgen Current

Test Condition	Discr. Model RMS	Cont. Model RMS
	[A]	[A]
Piston Mass -10%	27.25	26.65
Unsprung Mass -10%	29.97	29.30
Dissipation -10%	27.26	26.60
Nominal Condition	27.33	26.68

Table 3.17: *OFAT Robustness Test (-10%): Kollmorgen Current RMS*

Test Condition	Discr. Model RMS	rel.dev (wrt Nom.Cond.)
	[A]	[%]
Piston Mass -10%	27.25	-0.3
Unsprung Mass -10%	29.97	+9.7
Dissipation -10%	27.26	-0.26

Table 3.18: *OFAT Robustness Test (-10%) relative deviation: Kollmorgen Current RMS*

Test Condition	Discr. Model RMS	Cont. Model RMS
	[A]	[A]
Piston Mass +10%	27.45	27.21
Unsprung Mass +10%	25.19	24.55
Dissipation +10%	27.41	26.75
Nominal Condition	27.33	26.68

Table 3.19: *OFAT Robustness Test (+10%): Kollmorgen Current RMS*

Test Condition	Discr. Model RMS	rel.dev (wrt Nom.Cond.)
	[A]	[%]
Piston Mass +10%	27.45	+0.44
Unsprung Mass +10%	25.19	-7.8
Dissipation +10%	27.41	+0.3

Table 3.20: *OFAT Robustness Test (+10%) relative deviation: Kollmorgen Current RMS*

3.4. Inverse Compensation Method

The fourth important considered output is the *Unsprung Mass vertical acceleration*, obtained within the QCM block. As well as the Sprung Mass Acceleration, it is here introduced to provide an idea about its entity, as shown in Figures 3.44 and in Tables 3.23 - 3.21, for better evaluating the performed analyses in the following Chapters.

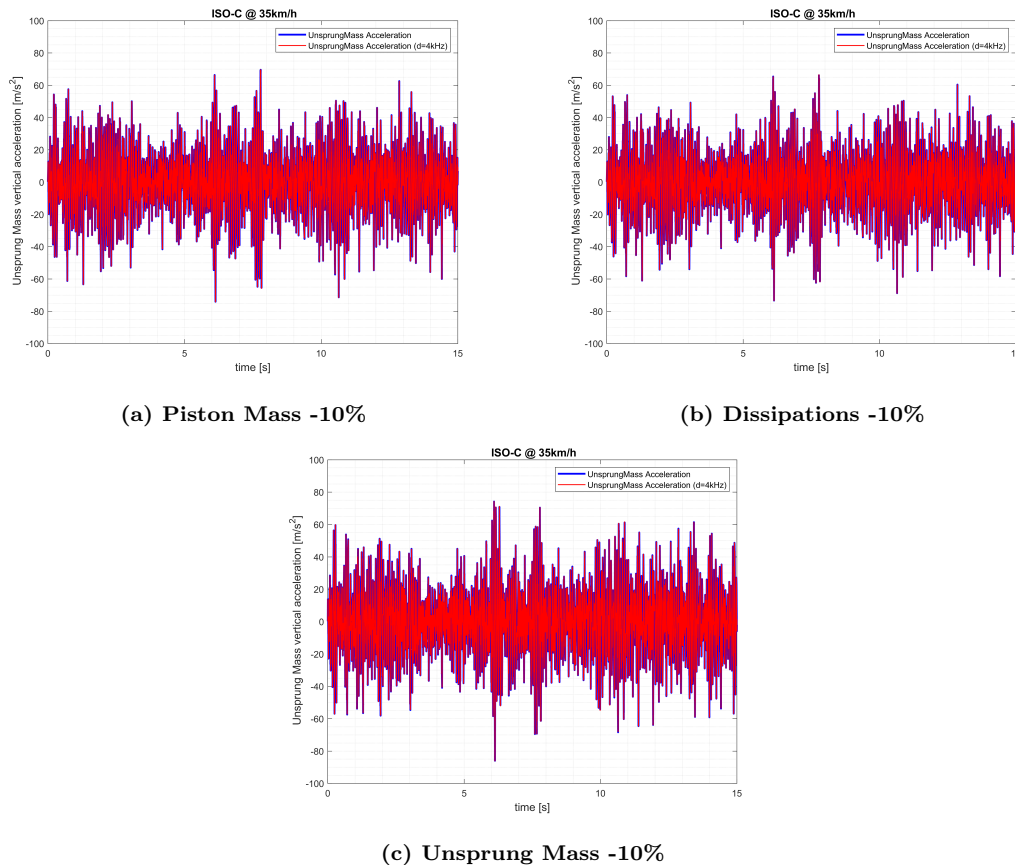


Figure 3.44: OFAT Robustness Test (-10%): Unsprung Mass Acceleration

In this case, as can be observed, the relative impact provided by the Unsprung Mass variation is reduced with respect to the KollMorgen Current case, but also the trends are opposite. By increasing of 10% the unsprung mass, in fact, is obtained a decrease of more than 6% in the Unsprung Mass Acceleration, while the same increase applied to the Piston Mass and to the Dissipative Coefficients lead to positive deviations, i.e. *increase of Unsprung Mass Acceleration*. In particular, if the Piston Mass contribution is limited to low percentages, the Dissipative Contribution has the same order of the Unsprung Mass one, providing an increase of 4% of the Unsprung Mass acceleration. By evaluating the negative variation of 10%, Figure 3.22, the trend is opposite but the order of magnitude of the relative deviation is basically the same. This double analysis

allows to state that both the Dissipative Coefficients and the Unsprung Mass itself have a non-negligible impact on the Unsprung Mass vertical acceleration, differently from the Kollmorgen analysis (in which only the Unsprung Mass is the main affecting parameter). Moreover, as expected, lighter values of Unsprung Mass provides higher vertical acceleration of the same mass.

Test Condition	Discr. Model RMS [m/s ²]	Cont. Model RMS [m/s ²]
Piston Mass -10%	19.3	19.45
Unsprung Mass -10%	21.14	21.07
Dissipation -10%	19.16	19.12
Nominal condition	19.96	19.90

Table 3.21: *OFAT Robustness Test (-10%): Unsprung Mass Acceleration RMS*

Test Condition	Discr. Model RMS [m/s ²]	rel.dev (wrt Nom.Cond.) [%]
Piston Mass -10%	19.45	-2.5%
Unsprung Mass -10%	21.14	+6
Dissipation -10%	19.16	-4

Table 3.22: *OFAT Robustness Test (-10%) relative deviation: Unsprung Mass Acceleration RMS*

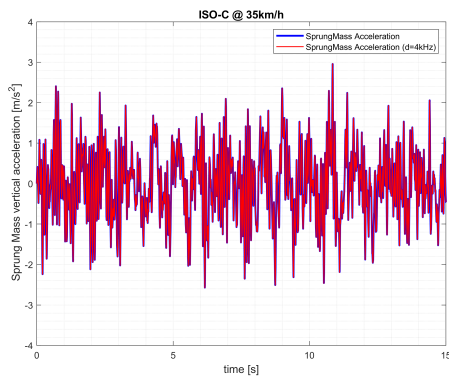
Test Condition	Discr. Model RMS [m/s ²]	Cont. Model RMS [m/s ²]
Piston Mass +10%	20.16	20.11
Unsprung Mass +10%	18.69	18.63
Dissipation +10%	20.81	20.74
Nominal condition	19.96	19.90

Table 3.23: OFAT Robustness Test (+10%): Unsprung Mass Acceleration RMS

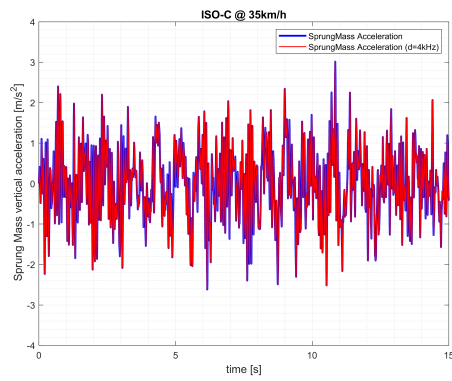
Test Condition	Discr. Model RMS [m/s ²]	rel.dev (wrt Nom.Cond.) [%]
Piston Mass +10%	20.16	+1
Unsprung Mass +10%	18.69	-6.4
Dissipation +10%	20.81	+4.3

Table 3.24: OFAT Robustness Test (+10%) relative deviation: Unsprung Mass Acceleration RMS

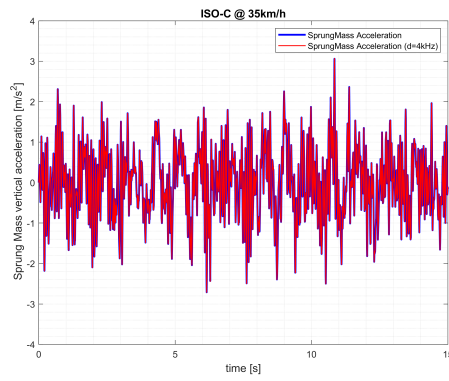
Finally, the vertical acceleration of the Sprung Mass of the QCM is considered, represented in Figure 3.45 and Tables 3.27-3.25. This measurement, as previously mentioned, will be fundamental for the next analyses, in particular for defining the *Comfort Coefficient* in 4.1.4, one of the two key parameters in the QC performance analysis. The performed robustness tests, summed up in Tables 3.28 and 3.26, do not show a single-particularly relevant dependency on any of the tested parameters. In fact, the positive variation of 10% provides an increase of 1-2% of the Sprung Mass vertical acceleration for all three parameters, while a negative variation provides decreases of the same entities. Hence, it can be assessed that the vertical acceleration of the sprung mass is not significantly affected by any particular tested data.



(a) Piston Mass -10%



(b) Dissipations -10%



(c) Unsprung Mass -10%

Figure 3.45: OFAT Robustness Test (-10%): Sprung Mass Acceleration

Test Condition	Discr.Model RMS [m/s ²]	Cont.Model RMS [m/s ²]
Piston Mass -10%	0.861	0.860
Unsprung Mass -10%	0.847	0.846
Dissipation -10%	0.864	0.863
Nominal condition	0.874	0.873

Table 3.25: OFAT Robustness Test (-10%): Sprung Mass Acceleration RMS

Test Condition	Discr.Model RMS [m/s ²]	rel.dev (wrt Nom.Cond.) [%]
Piston Mass -10%	0.861	-1.5%
Unsprung Mass -10%	0.847	-3%
Dissipation -10%	0.864	-1.14%

Table 3.26: OFAT Robustness Test (-10%) with relative deviation: Sprung Mass Acceleration RMS

Test Condition	Discr. Model RMS [m/s ²]	Cont. Model RMS [m/s ²]
Piston Mass +10%	0.888	0.886
Unsprung Mass +10%	0.892	0.891
Dissipation +10%	0.884	0.883
Nominal condition	0.874	0.873

Table 3.27: OFAT Robustness Test (+10%): Sprung Mass Acceleration RMS

Test Condition	Discr. Model RMS [m/s ²]	rel.dev (wrt Nom.Cond.) [%]
Piston Mass +10%	0.888	+1.6%
Unsprung Mass +10%	0.892	+2%
Dissipation +10%	0.884	+1.1%

Table 3.28: OFAT Robustness Test (+10%) with relative deviation: Sprung Mass Acceleration RMS

Final considerations

The overall results obtained from this OFAT robustness test have shown that the HIL system keeps its stability, even considering some deviated key factors. The stable behaviour has been proved first in the frequency domain, considering all the possible differences from the nominal model, and then in time domain, in order to evaluate the reached working conditions with respect to the designed limits. In all performed tests the significant outcomes have provided satisfactory results and the prefixed target of this study has been successfully achieved.

Robustness test: Noise Disturbance

Methodology

The actual HIL System, as it was described in Chapter 2.2, is equipped with two fundamental sensors in the testbench for evaluating two key parameters: the *Load Cell force* and the *Piston Position* in the test bench. These two sensors, as every measuring devices, introduce some errors in the actual signal and, up to this point, this phenomenon has been neglected.

Hence, for simulating the presence of the sensors in the layout of the HIL system, and for evaluating their effects in the interested outputs, this additional analysis is conducted. This Section, in fact, has the purpose of modelling in the Simulink™ Space the potential effects of some noise sources, that could occur in the physical installation.

The disturbing noises are added in the Simulink™ Model by means of the *Uniform Random Number block*, capable of providing a signal normally distributed between two chosen limits. For what concerns the Load Cell measurement, the noise is set equal to 5% of the maximum readable value from the Load Cell itself, i.e 5000N, the end-scale; consequently, this noise signal max amplitude is fixed to 250N. The noise related to the Piston Position, instead, is set to 5% of the maximum peak reached by the model in its nominal conditions and, as a consequence, its maximum amplitude is equal to 0.0015m (1.5mm).

From the point of view of the implementation, quite a standard procedure has been followed. The noise affecting the Load Cell measurement is introduced at the output

of the TestBench, here inserting the Uniform Random Number block and adding consequently this signal to the reference one. Instead, in order to account for the noise affecting the Piston Position measurement, the Uniform Random Number block is introduced inside the Testbench, at the output of the PRI block. Here, in fact, one of the outputs is the computed RRSA angle, then sent in feedback to the PID controller of the Kollmorgen. From the moment that the RRSA rotation is obtained directly from the piston position, the θ_{RRSA} , output of the PRI, is converted first into the Piston Position signal, adding in this way the noise disturbance generated by the Uniform Random Number block, and the resulting *new* Piston Position is re-converted into RRSA rotation, finally feedback in the PID controller. Both the described schemes can be observed respectively in Figure 3.46 and in Figure 3.48, with the additional plot of the noise affecting the Load Cell signal and the Piston Position measurements, in Figure 3.47 and 3.49.

For this last simulation analysis of robustness, the starting MATLAB/Simulink™ model is the original one, with all parameters implemented in their *nominal conditions*. As for the OFAT analysis, also in this case only the most stressed condition is tested, hence the ISO-C profile is the only considered road input, and all the remaining Simulation Data are summed up in Table 3.29.

Road Profile	ISO-C
Road Profile Roughness	$25.6e - 7$
Road Profile Speed [km/h]	35
RRSA damping [Ns/m]	1000
Time duration [s]	15
Cut-Off Frequency [Hz]	250
Max ampl. Load Cell Noise [N]	250
Max ampl. Piston Position Noise [mm]	1.5

Table 3.29: Noise Disturbance Testing: Simulation Data

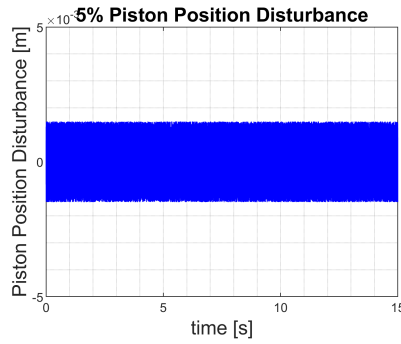


Figure 3.49: *Piston Position Noise signal*

Time domain results

As it was performed in the OFAT Robustness Test analysis, the first two outputs to be analyzed are the Tracking of the RRSA angle and the force measured by the Load Cell Sensor.

Moreover, since the RRSA rotation intrinsically contains information about the piston axial displacement, i.e one of the two noise-affected quantities of the test, it assumes, particularly here, a fundamental importance.

For what concerns the tracking capability of the testbench, shown in Figure 3.50, it is maintained substantially unchanged with respect to the nominal configuration, demonstrating the quality of the designed control system. This result can also be assessed to the fact that the introduced Piston Position Noise, which is added in the Model right before completing the feedback line towards the PID Controller, has a very reduced entity even if referred to the peak nominal value, hence its effect can be positively compensated by the control system.

The Load Cell signal, instead, represented in Figure 3.51, appears clearly modified. The introduced noise, in fact, reaching a maximum amplitude of 250N, is perfectly comparable with the nominal signal and, as a consequence, the resulting signal is heavily amplified. However, even if the locally reached peaks overcome 1kN, the whole signal time-history does not minimally come close to the end-scale of the Load Cell Sensor, i.e 5kN, and the system can be assessed to be able to properly compensate even with so critical conditions. It is important to highlight, with these considerations, that the performed Noise Disturbance Robustness Test represents a case of *particularly stressed conditions*, since the *Piston Position noise signal* is referred to the maximum

reached peak in nominal conditions (with a percentage of 5%), while, most relevant, the Load Cell noise signal is referred to the end-scale of the sensor itself, translating this information into a signal with maximum amplitude of 250N, i.e quite a *significant disturbance*. Hence, taking into account these considerations, the results obtained with this second type of Robustness Test assume an increased importance.

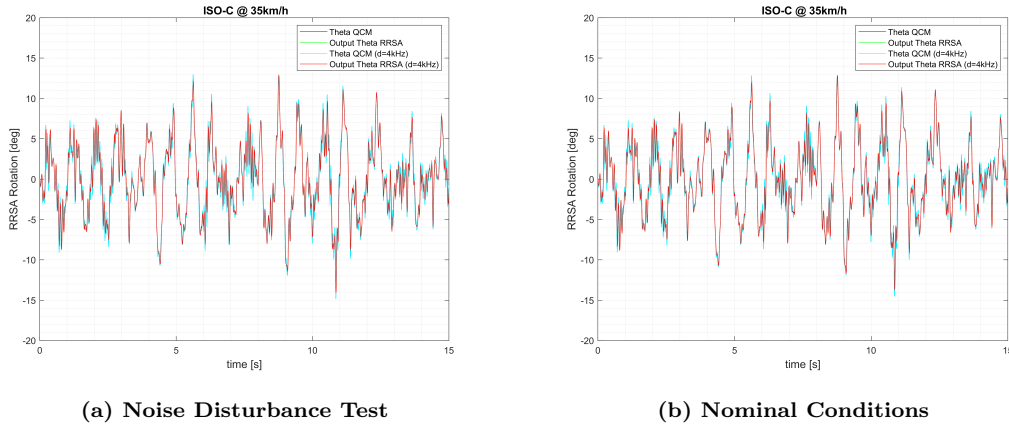


Figure 3.50: *Noise Disturbance Robustness Test: Tracking of RRSA rotation*

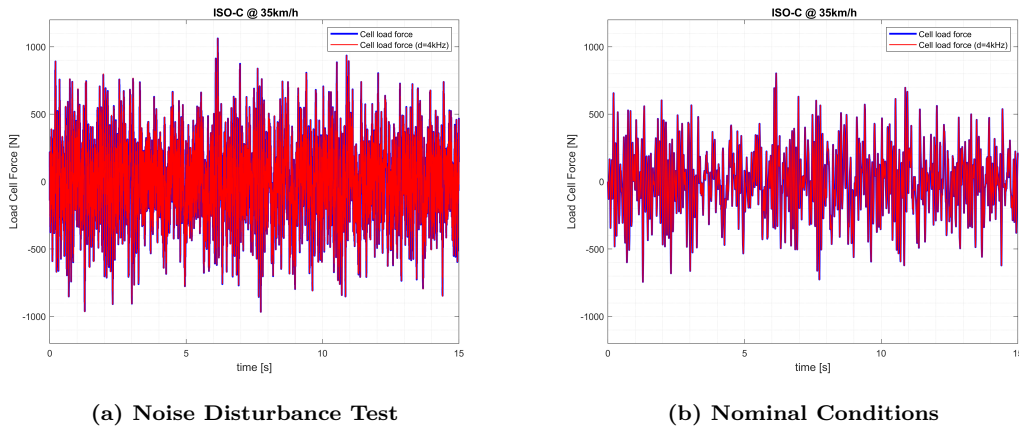


Figure 3.51: *Noise Disturbance Robustness Test: Load Cell Force*

As well as the Load Cell Force, also the KollMorgen Unit is significantly affected by the added noise signals in the simulation. As shown in Figure 3.52 and in Table 3.30, the signal time-history is locally highly truncated at the saturation level of the electric motor, i.e 90A, much more than the nominal configuration. Looking at the corresponding RMS values, in fact, the introduction of the disturbance signals cause an increase of more than 20% with respect to the starting condition, visible in Table

3.31, i.e the *largest measured increase* in all performed robustness test.

However, even in these conditions, the overall Simulated system is still stable. If on one side the signal representing the current flowing in the KollMorgen Unit is clearly truncated at the saturation level, on the other one the RMS resulting value is still not close to the maximum limit sustainable by the KollMorgen itself.

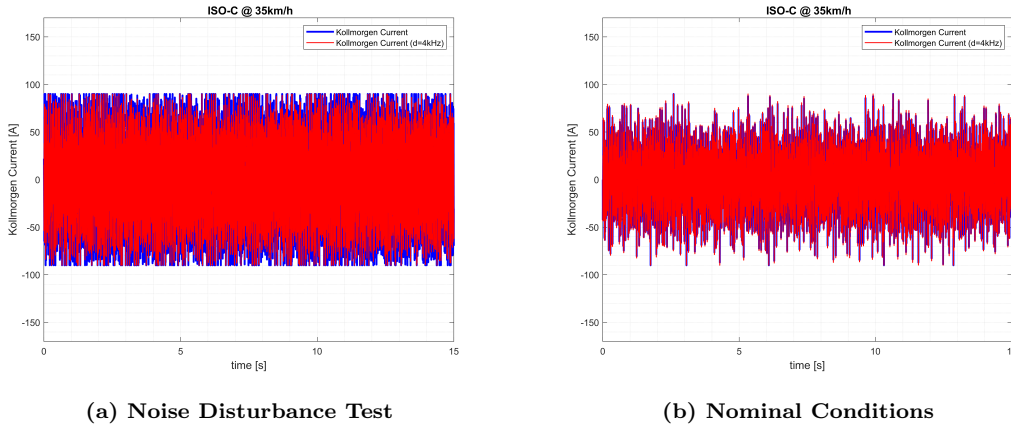


Figure 3.52: Noise Disturbance Robustness Test: KollMorgen Current

Test Condition	Discr. Model RMS [A]	Cont. Model RMS [A]
Noise Disturbance Test	33.1	34.5
Nominal condition	27.33	26.68

Table 3.30: Noise Disturbance Robustness Test: Kollmorgen Current RMS

Test Condition	Discr. Model RMS [A]	Relative deviation
Noise Disturbance Test	33.1	+21.1%
Nominal condition	27.33	0%

Table 3.31: Noise Disturbance Robustness Test with relative deviation: Kollmorgen Current RMS

The Noise Disturbance Robustness Test affects, differently, also the output of the QCM. The Unsprung Mass vertical acceleration, shown in Figure 3.53, experiences a relative increase of its RMS value of slightly more than 3%, visible in Table 3.33. The Sprung Mass vertical acceleration, instead, is more affected by the introduced disturbances, as can be seen in its time-history in Figure 3.54. In this case, the increase with

respect to the nominal condition is higher than 9%, shown in Table 3.35, proving that the dynamics of the QC Sprung Mass are more sensitive to the sensor measurements.

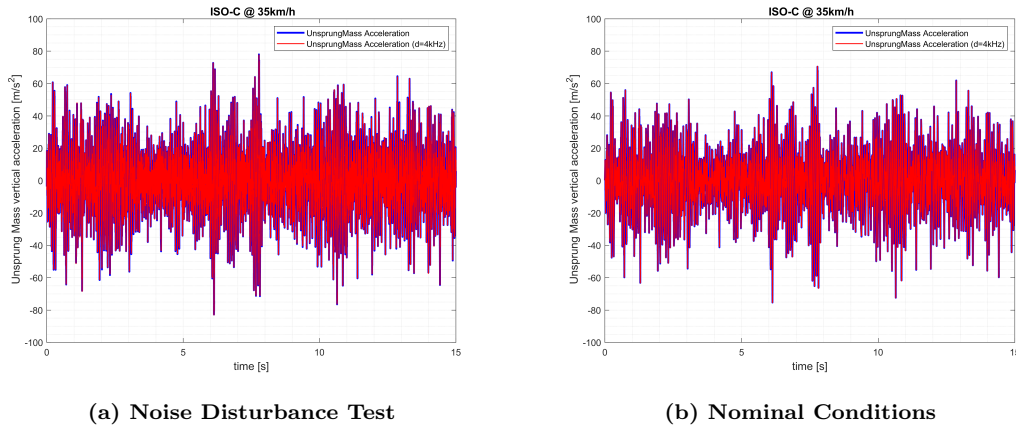


Figure 3.53: *Noise Disturbance Robustness Test: Unsprung Mass Acceleration*

Test Condition	Discr. Model RMS [m/s ²]	Cont. Model RMS [m/s ²]
Noise Disturbance Test	20.60	20.64
Nominal condition	19.96	19.90

Table 3.32: *Noise Disturbance Robustness Test: Unsprung Mass Acceleration RMS*

Test Condition	Discr. Model RMS [m/s ²]	Relative Deviation
Noise Disturbance Test	20.60	+3.2%
Nominal condition	19.96	0%

Table 3.33: *Noise Disturbance Robustness Test with relative deviation: Unsprung Mass Acceleration RMS*

3.4. Inverse Compensation Method

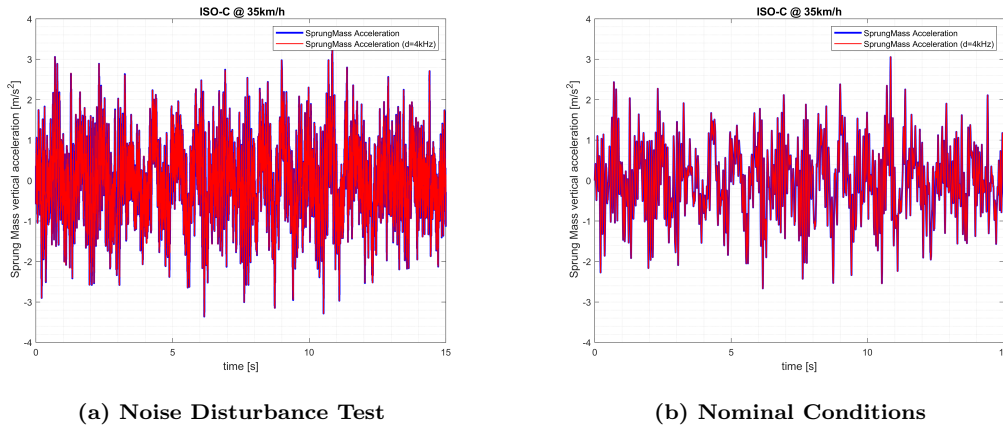


Figure 3.54: Noise Disturbance Robustness Test: Sprung Mass Acceleration

Test Condition	Discr. Model RMS [m/s ²]	Cont. Model RMS [m/s ²]
Noise Disturbance Test	0.956	0.957
Nominal condition	0.874	0.873

Table 3.34: Noise Disturbance Robustness Test: Sprung Mass Acceleration RMS

Test Condition	Discr. Model RMS [m/s ²]	Cont. Model RMS [m/s ²]
Noise Disturbance Test	0.956	+9.4%
Nominal condition	0.874	0%

Table 3.35: Noise Disturbance Robustness Test with relative deviation: Sprung Mass Acceleration RMS

Final considerations

The purpose of this additional simulation was to prove the stability of the whole HIL system by trying to model it in a more realistic way, introducing some noise disturbances in correspondence of the measurement devices: with this target in mind, the test can be considered quite *successful*. The addition of the two noise signals to the Simulink™ Model, based on the nominal configurations, have clearly shown their effects, providing significant results in the time domain. The monitored outputs have shown different levels of sensitivity to the sensor measured signals. The tracking capabilities of the testbench, containing information about the Piston Position, have not significantly changed, showing further good compensation performances of the control

system. The Load Cell signal has experienced higher modifications, due to the higher absolute entity of its modifications, remaining in any case far below the sensor measurement *end-scale*. The current characterizing the KollMorgen Unit, even if experiencing the largest increase, has been kept below the critical limits of the electric machine. Finally, the QC outputs have shown different behaviours towards the system modification, with relative increases always under control.

Considering the particularly demanding characteristics of the ISO-C road profile and the extremely stressed designed test conditions, the robustness test with Simulated Noise Disturbance can be considered successfully performed.

3.5 Model Following Compensation Method

Once described and analyzed the numerical results obtained with the *Inverse Compensation Method*, this Thesis Work proposes another compensation method in order to solve the testbench-bandwidth-caused instability: the *Model Following Approach*.

3.5.1 Methodology

This compensation method is based on the scheme shown in Figure 3.56, in which the control scheme is applied to the bench model. The testbench SimulinkTM Model is summed up by the Transfer Function G_p , that has been computed following an analytical approach similar to the one described in 3.4. It provides the RRSA Output rotation receiving the Kollmorgen current signal as unique input (hence, $\frac{\theta_{out}}{i_{Koll}}$), taking into account the RRSA installation (with its mechanical connection to the hydraulic piston) and, according to the tested condition, even its damping value.

The actual *Compensation Scheme*, instead, is composed by two transfer functions: TF_{des} and $TF_{following}$.

The first one represents the *desired behaviour* requested by the Testbench, and it is numerically implemented with a *Bessel Filter* with a filter order n_{des} equal to 4 and a cut-off frequency f_{cut} equal to 500Hz. The Bessel filter is a type of analog linear filter with a maximally flat group/phase delay (maximally linear phase response), which

maintains the wave shape of filtered signals in the passband. In MATLABTM it is obtained with the *mkfilter* command, that with the code:

$$TF_{des} = mkfilter(f_{cut}, n_{des}, 'bessel') \quad (3.12)$$

returns a single-input, single-output analog low pass filter, whose frequency response function is shown in Figure 3.55.

Once defined the desired Testbench transfer function, the $TF_{following}$ is computed as the ratio between the TF_{des} and the Testbench G_p , i.e performing the *inversion* of this last transfer function. Concerning this calculation, it is important to highlight the fact that the *filter order* imposed to the expression 3.12 has been properly set to make possible the SimulinkTM implementation of the Control Scheme, since it allows to obtain the same order on both numerator and denominator of $TF_{following}$ (the equivalent procedure has been followed for the *Inverse Compensation Method* by introducing the closure poles).

At this point the Compensation Scheme is ready to be implemented following the layout described in Figure 3.56, as can be observed in the SimulinkTM detail in Figure 3.57.

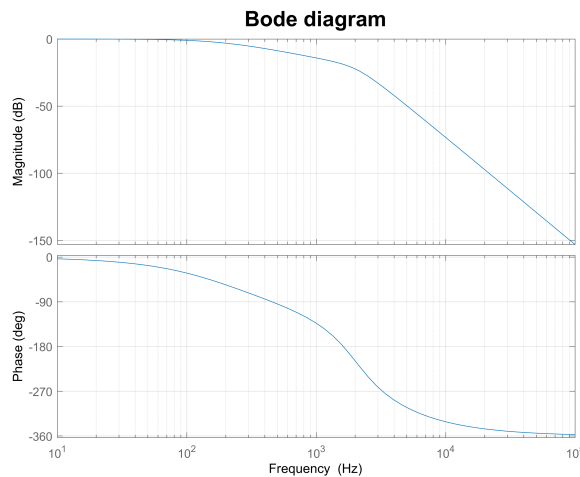


Figure 3.55: Bode Diagram of TF_{des} (Bessel filter)

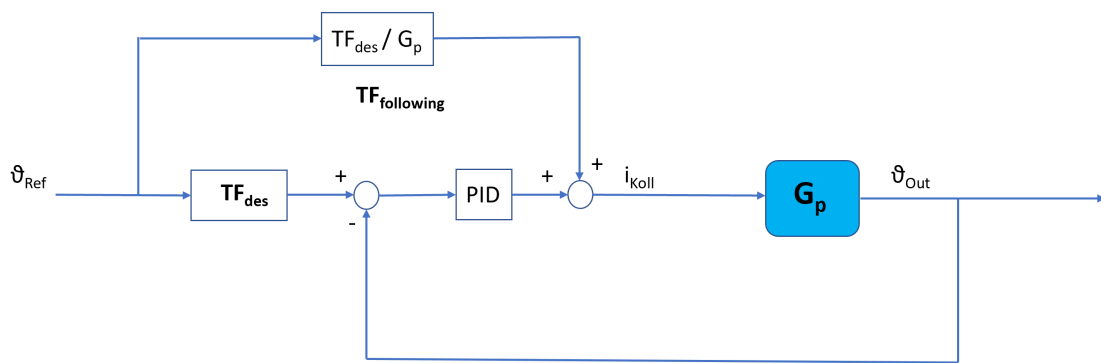


Figure 3.56: Model Following Scheme applied to the Testbench system.

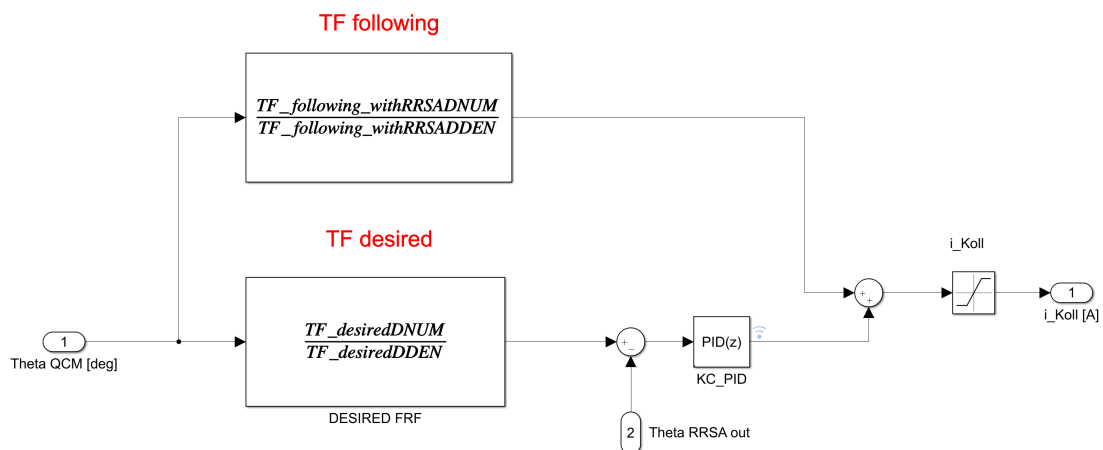


Figure 3.57: Model Following Control Scheme implemented in SimulinkTM

Once applied to the single Testbench, the *Model Following Compensation Scheme* is linked to the QCM for evaluating its performance at the overall level of HIL System, producing the general layout shown in Figure 3.58. In this final step the *Testbench Block* clearly includes all the components previously described, including the RRSA model with all the corresponding contributions, providing both the *RRSA Output Rotation* and the *Load Cell Force*, to be introduced in the QCM.

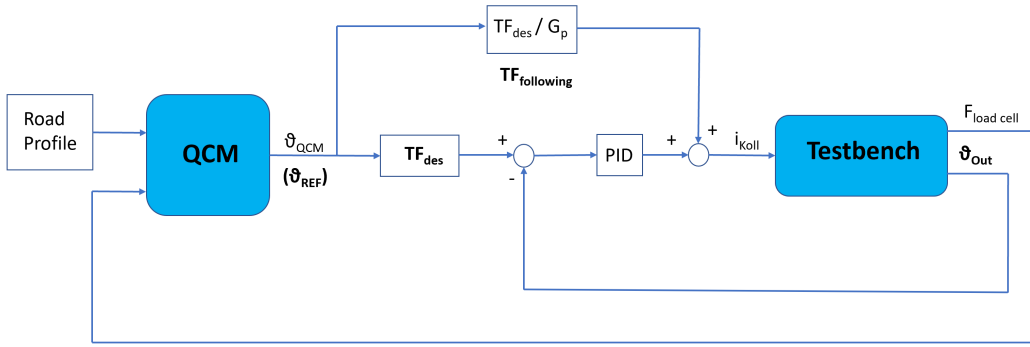


Figure 3.58: Model Following Scheme applied to the HIL system.

3.5.2 HIL Simulation Results

Frequency domain results

The first analyses that are carried out concern the frequency domain of the modelled system. In particular, the first considered condition does not include any RRSA damping value, setting it equal to 0Ns/m; hence, the RRSA is still present in the model of the State Space system but no current is flowing in its simulated electric machine, since the damping value is null, and no consequent force is generated (it affects the system with its inertial and dissipative contribution).

By performing analytical calculations equivalent to the ones described in 3.4.2, the *Compensated-Testbench Transfer Function* is obtained, i.e. $\frac{\vartheta_{out}}{\vartheta_{QCM}}$, and its Bode diagram is compared with the *Bessel Filter*, shown in Figure 3.59. As can be seen, the two frequency responses are perfectly overlapped, as expected, since the Compensation Scheme is acting on the Testbench with the same damping parameters. The $TF_{following}$, in fact, is referred to the Testbench without RRSA damping and, in this specific configuration, the Testbench model is actually without RRSA damping, i.e the compensation is *mathematically* ensured.

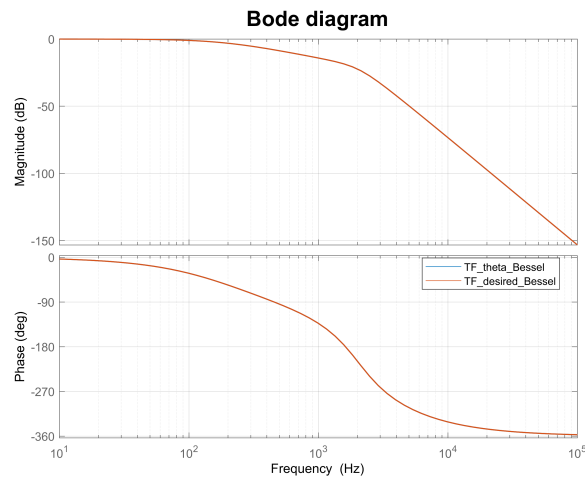


Figure 3.59: Bode Diagram comparison between **Bench TF with Compensation** and **Desired TF (Bessel Filter)**, with Testbench&Compensator **RRSA damping=0Ns/m**

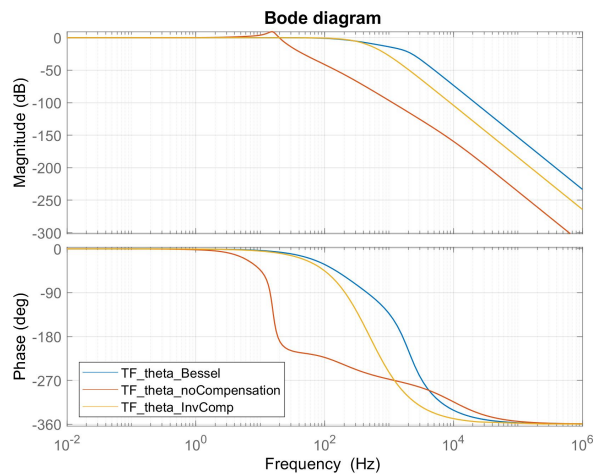


Figure 3.60: Bode Diagram comparison between **Model Following Method** (with Bessel filter and $f_{cut}=500\text{Hz}$), **Inverse Compensation Method** (with $f_{cut}=500\text{Hz}$) and **Bench without Compensation**, with Testbench&Compensator **RRSA damping=0Ns/m**

With the same configuration, moreover, the *Model Following Method* is compared with the corresponding *Inverse Compensation Method* and with the Testbench Bode diagram without any kind of compensation, visible in Figure 3.60. Considering this plot, it is clear that the *Model Following Compensation* allows to obtain a further increased Testbench bandwidth with significantly reduced attenuations both in Mag-

nitide and in Phase, as can be seen from the differences between the *blue* and *yellow* curve. With this important observation regarding the Bench bandwidth improvement, the *Model Following Method* appears to be likely the best choice with respect to the *Inverse Compensation Method*.

However, as previously described, the optimal behaviour observed in Figure 3.59 is substantially derived from the mathematical relations that link the Compensation Scheme with the Testbench, being defined both of them with reference to the same damping value.

At this point, in fact, the study proceeds by simulating a Testbench RRSA damping equal to 1000Ns/m (hence, the RRSA model is providing a force and is characterized by a current) while keeping the $TF_{following}$ referred to the case with *no damping*, i.e 0Ns/m. This comparison is performed in the Bode Diagram in Figure 3.61. As expected, the actual Testbench frequency response (with Model Following, the blue line) and the desired frequency response (red line) are no longer overlapped, since the $TF_{following}$ is not mathematically linked to the simulated testbench. Moreover, this behaviour has been previously described also for the *Compensation Method* in 3.4.2 in Figure 3.22, here replicated in Figure 3.62 in comparison with the *Model Following Method*. Overall, the performed frequency domain analysis has demonstrated that this last compensation approach appears to be able to further increase the Bench bandwidth and to provide better results in terms of *phase* and *magnitude* response, with respect to the previously implemented *Inverse Compensation Method*.

However, the model mismatch occurring when a certain damping difference is imposed between the Compensation Scheme and the Modelled Testbench, still exists. As described for the *Inverse Compensation Method*, in fact, the Compensator can not perfectly operate when its reference RRSA damping is quite different from the Testbench one, as visible in Figure 3.61.

These considerations must be taken into account with the actual HIL physical implementation of this Compensation Method, for evaluating the effective compensating performance.

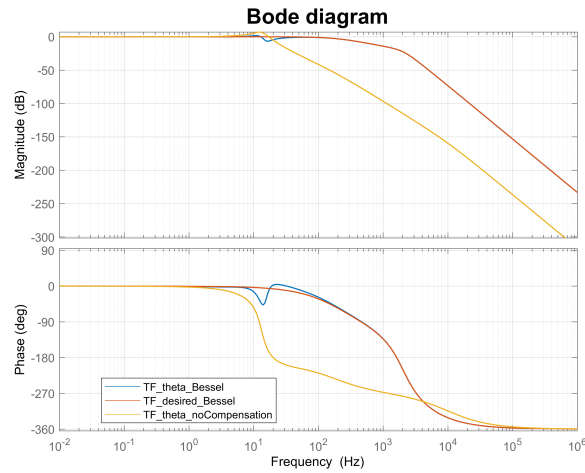


Figure 3.61: Bode Diagram comparison between **Bench TF with Model Following Method** (with Bessel Filter and $f_{cut}=500\text{Hz}$), **Desired TF** (Bessel Filter) and **Bench TF without Compensation**, with Testbench **RRSA damping=1000Ns/m** and Compensator **RRSA damping=0Ns/m**

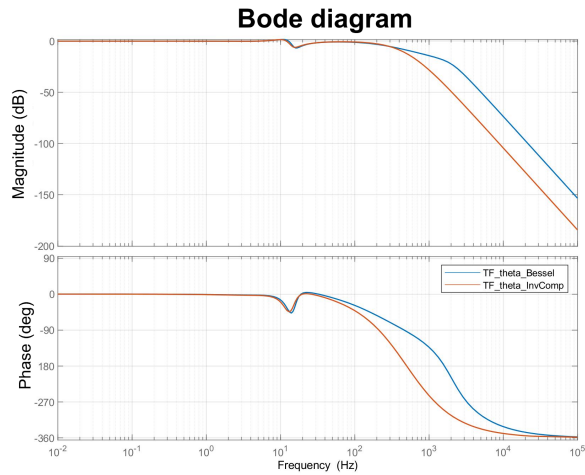


Figure 3.62: Bode Diagram comparison between **Bench TF with Model Following Method** (with Bessel Filter and $f_{cut}=500\text{Hz}$) and **Bench TF with Inverse Compensation** (with $f_{cut}=500\text{Hz}$), with Testbench **RRSA damping=1000Ns/m** and Compensator **RRSA damping=0Ns/m**

Time domain results

Once described and examined the frequency domain results about the *Model Following Method*, this Section completes the Compensation analysis by evaluating also the

3.5. Model Following Compensation Method

time domain results.

The QCM input is the ISO-B @ 70km/h and the Testbench is characterized by a RRSA damping of 1000Ns/m, while the $TF_{following}$ of the Compensation Scheme is maintained in nominal conditions (with 0Ns/m, as previously described).

Considering the equivalent analysis performed in the former sections, the monitored signals are four:

- RRSA Tracking Angle (Testbench performance)
- Kollmorgen Current (Testbench performance)
- Sprung Mass Vertical Acceleration (QC performance)
- Unsprung Mass Vertical Acceleration (QC performance)

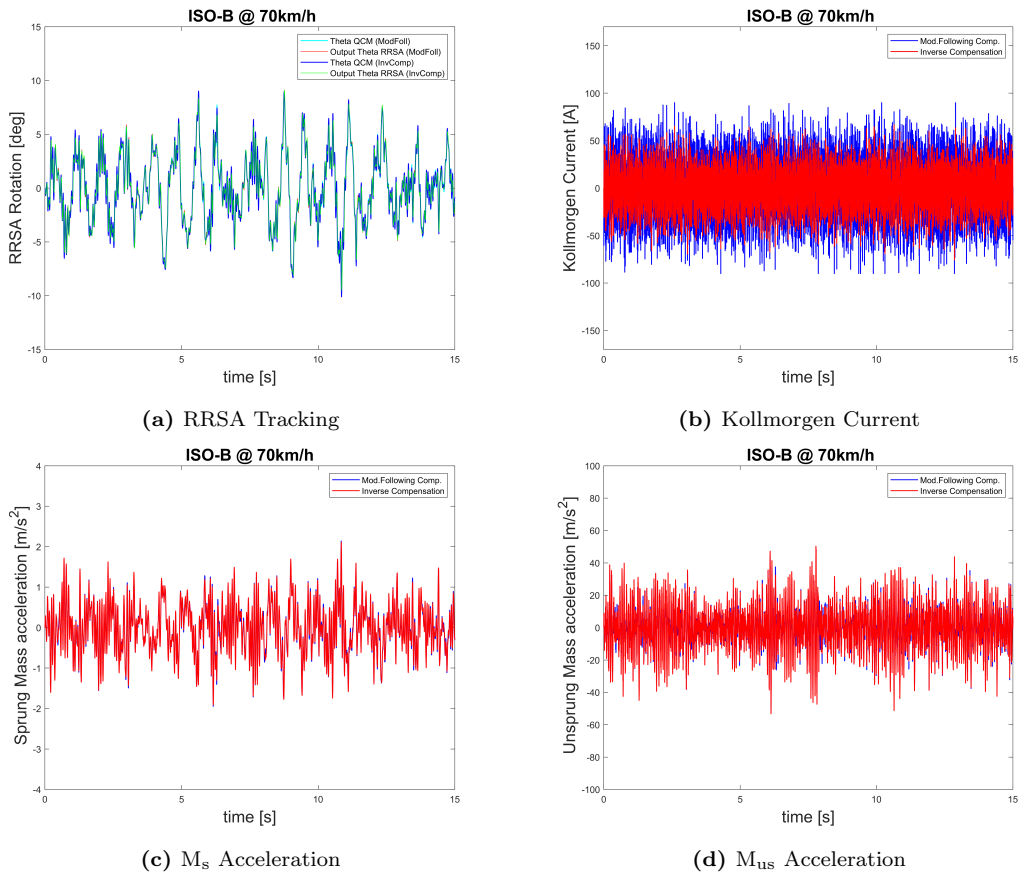


Figure 3.63: Time domain results comparison between **Model Following with Bessel Filter** ($f_{cut}=500\text{Hz}$) and **Inverse Compensation Method** ($f_{cut}=500\text{Hz}$) for ISO-B profile @ 70km/h, with Testbench **RRSA damping=1000Ns/m** and Compensator **RRSA damping=0Ns/m**

These outputs are grouped in Figure 3.63 in comparison with the corresponding results obtained with *Inverse Compensation Method*.

As expected, considering the differences between the two methods (quite relevant only at high frequencies), the obtained results do not diverge significantly between each other, just showing some differences in the Kollmorgen Current signal, with slightly higher local peaks closer to the saturation limit. On the other hand, QC performance and RRSA tracking do not show relevant deviations, overall providing quite overlapped behaviours.

3.5.3 Final considerations

Overall, the performed analysis concerning the *Model Following Method* has demonstrated its validity as alternative Compensation approach to the *Inverse Method*. Not only it has proved to properly work in increasing the Testbench bandwidth and providing reliable results at the HIL level, but it has also clearly shown to be able to improve the overall required performance. With respect to the *Inverse Compensation Method*, in fact, it increases the frequency range within which no relevant attenuations in Magnitude or Phase occur, for the same designed conditions (i.e, *cut-off frequency*). However, it shows the same expected limit in compensating whenever the Testbench has a RRSA damping value different from the Compensation Scheme one (i.e, 0Ns/m), which mathematically implies the impossibility to perfectly compensate the Testbed dynamics.

Overall considering, in simulation the *Model Following Method* has numerically proved to enhance the compensating performance with respect to the *Inverse Method*, hence leading to possibly design it for the experimental test in Hardware-In-the-Loop.

RRSA Control Strategy: Numerical Modelling

4.1 Sky-Hook Control

4.1.1 Sky-Hook Theory

Ideal Sky-Hook

The analysis can start considering a simple quarter car with two degrees of freedom, like the one shown in Fig. 4.1. A damper placed not between the two masses but between the sprung mass and a fixed point would be needed to damp the motion of the vehicle body in an optimal way, as described in detail in [3]. A model with this configuration, usually referred to as *skyhook*, is shown in Figure 4.1. The considered point to which the damper is attached is fixed in an inertial frame, while the designed damper can substitute or not the traditional suspension shock absorber, according to the scheme.

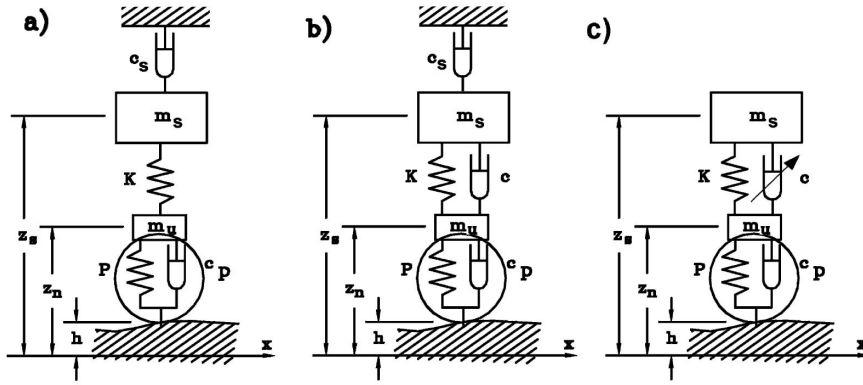


Figure 4.1: Skyhook application on two degrees of freedom QC: a) and b) with and without suspension shock absorber, c) practical implementation with controlled damper between the two masses, [3]

With reference to Figure 4.1 a), the resulting equation of motion is expressed in 4.1, modified in 4.3 with the introduction of some important dimensionless parameters, shown in 4.2, according to [3].

$$\begin{aligned} & \begin{bmatrix} m_s & 0 \\ 0 & m_u \end{bmatrix} \begin{Bmatrix} \ddot{z}_s \\ \ddot{z}_u \end{Bmatrix} + \begin{bmatrix} c_s & 0 \\ 0 & c_p \end{bmatrix} \begin{Bmatrix} \dot{z}_s \\ \dot{z}_u \end{Bmatrix} + \\ & + \begin{bmatrix} K & -K \\ -K & K + P \end{bmatrix} \begin{Bmatrix} z_s \\ z_u \end{Bmatrix} = \begin{Bmatrix} 0 \\ c_p \dot{h} + Ph \end{Bmatrix} \end{aligned} \quad (4.1)$$

$$a = \frac{m_u}{m_s}, \quad b = \frac{P}{K}, \quad \zeta_s = \frac{c_s}{2\sqrt{m_s K}}, \quad \zeta_p = \frac{c_p}{2\sqrt{m_s K}}, \quad (4.2)$$

$$\begin{aligned} & m_s \begin{bmatrix} 1 & 0 \\ 0 & a \end{bmatrix} \begin{Bmatrix} \ddot{z}_s \\ \ddot{z}_u \end{Bmatrix} + 2\sqrt{m_s K} \begin{bmatrix} \zeta_s & 0 \\ 0 & \zeta_p \end{bmatrix} \begin{Bmatrix} \dot{z}_s \\ \dot{z}_u \end{Bmatrix} + \\ & + K \begin{bmatrix} 1 & -1 \\ -1 & 1 + b \end{bmatrix} \begin{Bmatrix} z_s \\ z_u \end{Bmatrix} = \begin{Bmatrix} 0 \\ c_p \dot{h} + Ph \end{Bmatrix}. \end{aligned} \quad (4.3)$$

If the tire damping is neglected (as it often happens in this Thesis Work), the obtained *amplification factor* is:

$$\frac{|z_{s0}|}{|h_0|} = PK \sqrt{\frac{1}{f^2(\omega) + c_s^2 \omega^2 g^2(\omega)}} \quad (4.4)$$

If, instead, the shock absorber between masses is still present, as it happens in Figure 4.1, the new equation of motion is:

$$\begin{aligned} & \begin{bmatrix} m_s & 0 \\ 0 & m_u \end{bmatrix} \begin{Bmatrix} \ddot{z}_s \\ \ddot{z}_u \end{Bmatrix} + \begin{bmatrix} c+c_s & -c \\ -c & c+c_p \end{bmatrix} \begin{Bmatrix} \dot{z}_s \\ \dot{z}_u \end{Bmatrix} + \\ & + \begin{bmatrix} K & -K \\ -K & K+P \end{bmatrix} \begin{Bmatrix} z_s \\ z_u \end{Bmatrix} = \begin{Bmatrix} 0 \\ c_p \dot{h} + Ph \end{Bmatrix}, \end{aligned} \quad (4.5)$$

i.e:

$$\begin{aligned} & m_s \begin{bmatrix} 1 & 0 \\ 0 & a \end{bmatrix} \begin{Bmatrix} \ddot{z}_s \\ \ddot{z}_u \end{Bmatrix} + 2\sqrt{m_s K} \begin{bmatrix} \zeta_s + \zeta & -\zeta \\ -\zeta & \zeta_p + \zeta \end{bmatrix} \begin{Bmatrix} \dot{z}_s \\ \dot{z}_u \end{Bmatrix} + \\ & + K \begin{bmatrix} 1 & -1 \\ -1 & 1+b \end{bmatrix} \begin{Bmatrix} z_s \\ z_u \end{Bmatrix} = \begin{Bmatrix} 0 \\ c_p \dot{h} + Ph \end{Bmatrix}. \end{aligned} \quad (4.6)$$

Once obtained these results, it is possible to plot the frequency response of the quarter car 2dof *sprung mass* with skyhook implementation, represented in Figure 4.2, in which is shown the amplification factor and the inertance.

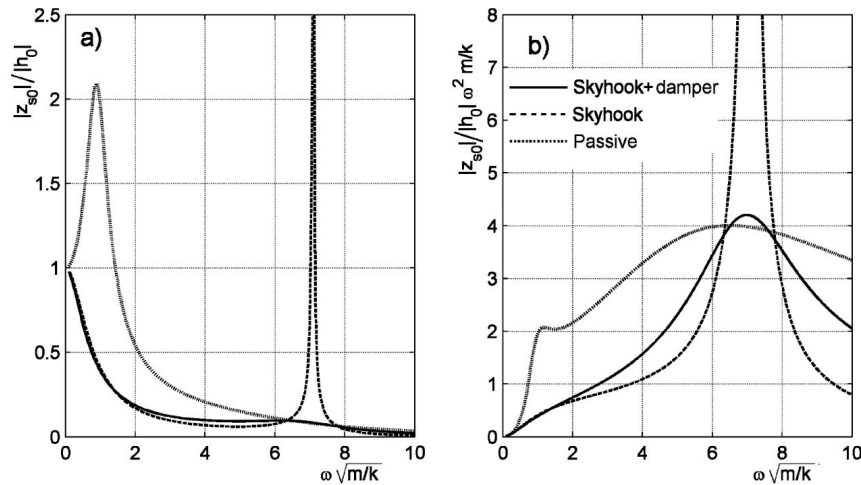


Figure 4.2: Non-dimensional frequency response of the sprung mass of a quarter car with two degrees of freedom. Dimensionless parameters: $b=P/K=4$ and $a=m_u/m_s=0.1$. Passive system with optimum damping (ratio 0.433), simple skyhook (ratio 1) and skyhook with same ratio plus a damper between the two masses with damping equal to 1/3 of the optimum (0.1443), [3]

The presence of the skyhook greatly reduces the displacement and the acceleration at low frequency, while causing a very high, although not infinite, resonance peak at the resonant frequency characterizing the unsprung mass. However, as it can be observed, the addition of even a small damper between the two masses strongly reduces

this peak, cancelling it without affecting the response at low frequency.

This type of system is, hence, capable of controlling the sprung mass motion in a quite effective way but, unfortunately, is completely unsatisfactory from what concerns the control of the *unsprung mass*, whose frequency response is shown in Figure 4.3. The skyhook system has basically no effect on the unsprung mass motion in the frequency range of its resonance. However, the introduction of a conventional damper between the two masses, even small as the one used here, strongly reduces the unsprung mass displacement and acceleration; hence, with an increased damping value, the resonance peak disappears with just a slight increase at low frequency.

The ideal skyhook is, then, a theoretical solution for particularly controlling the low frequency motions of the sprung mass, remaining however just an ideal solution, without the possibility to implement it in practice.

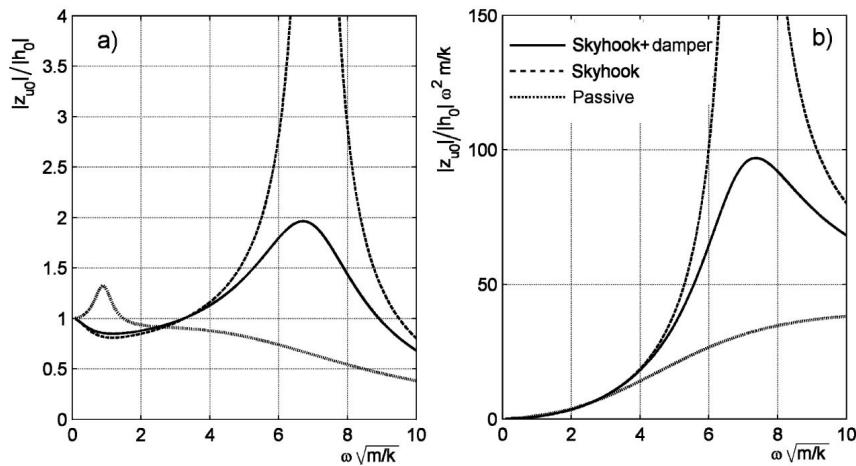


Figure 4.3: Non-dimensional frequency response of the unsprung mass of a quarter car with two degrees of freedom, [3]

Semi-active quarter car with real skyhook

The fixed point (the "sky") where the skyhook damper is attached does not exist in the real implementation. This system must therefore be designed using a device located between the sprung and the unsprung masses of the Quarter Car, [3]. The semi-active solution, based on a damper with controllable damping coefficient, is shown in Figure 4.1 c) and must provide a force, defined in [3], given by:

$$F = -c_s \dot{z}_s - c(\dot{z}_s - \dot{z}_u) \quad (4.7)$$

that can be re-arranged in:

$$F = - \left(c_s \frac{\dot{z}_s}{\dot{z}_s - \dot{z}_u} + c \right) (\dot{z}_s - \dot{z}_u) \quad (4.8)$$

As it can be observed, it should be possible to implement a device able to simulate the skyhook simply by modulating the damping coefficient of the damper, so that it is, in each instant, equal to:

$$c_{eq} = c_s \frac{\dot{z}_s}{\dot{z}_s - \dot{z}_u} + c \quad (4.9)$$

Even considering this formulation, however, the ideal skyhook can only be approximated by this semi-active design, since the forces exerted on the unsprung mass are different with respect to the ideal system, while the ones provided to the sprung mass are those defined by the ideal skyhook.

Most important, a passive system can not replicate the behaviour shown in Equation 4.9. In fact, when the equivalent damping coefficient is positive, the device dissipates energy and the working principle is the same of a conventional shock absorber, but when this coefficient is negative the damper should introduce energy into the system, i.e requiring an *active device*.

Active quarter car with real skyhook

The active system, able to transfer energy to the system, is hence required to follow the law 4.8. For this purpose must be used a device usually defined as operating on *four quadrants*, expression that comes from the force-velocity plot of the damper. With the usually adopted sign convention, the conditions in which a passive system can operate lie in the second and fourth quadrants, i.e. in the quadrants where force and velocity have opposite signs and the resulting power is dissipated (if the force is that exerted by the damper to one of its end points and the velocity is that of the same point while

the other is constrained).

An active system, instead, may also exert forces with the same sign of the velocity, in which case it works in all four quadrants. Considering a traditional two-degrees of freedom QCM, [3], where the shock absorber between the masses is substituted by an actuator operating on four quadrants, and neglecting the tire-damping, the resulting equation of motion is:

$$\begin{bmatrix} m_s & 0 \\ 0 & m_u \end{bmatrix} \begin{Bmatrix} \ddot{z}_s \\ \ddot{z}_u \end{Bmatrix} + \begin{bmatrix} K & -K \\ -K & K + P \end{bmatrix} \begin{Bmatrix} z_s \\ z_u \end{Bmatrix} = \begin{Bmatrix} F \\ -F \end{Bmatrix} + \begin{Bmatrix} 0 \\ Ph \end{Bmatrix} \quad (4.10)$$

in which F is the force provided by the actuator on the sprung mass. By re-arranging it, it becomes:

$$m_s \begin{bmatrix} 1 & 0 \\ 0 & a \end{bmatrix} \begin{Bmatrix} \ddot{z}_s \\ \ddot{z}_u \end{Bmatrix} + K \begin{bmatrix} 1 & -1 \\ -1 & 1 + b \end{bmatrix} \begin{Bmatrix} z_s \\ z_u \end{Bmatrix} = \begin{Bmatrix} F \\ -F \end{Bmatrix} + \begin{Bmatrix} 0 \\ Ph \end{Bmatrix} \quad (4.11)$$

In order to simulate the skyhook behaviour, this force, previously defined in 4.7, must be equal to:

$$F = -c_s \dot{z}_s - c(\dot{z}_s - \dot{z}_u) = -(c_s + c)\dot{z}_s + c\dot{z}_u \quad (4.12)$$

With this new equation of motion the overall frequency response of the system is changed. Assuming the same Quarter Car Model used in Figures 4.2 - 4.3, the frequency response of the sprung mass (in terms of vertical displacement and acceleration) is shown in Figure 4.4. As can be observed, the quarter car with a skyhook of this type does not differ from the ideal one. The main effect of the actual skyhook, in fact, is related to the frequency response of the unsprung mass, shown in Figure 4.5. The resulting response of the system is quite different from the ideal one, still remaining unsatisfactory. This limit is actually improved by setting a higher damping value of the suspension shock absorber, which in the considered analysis is 1/3 of the optimum one. With this suspension damping increase, therefore, the frequency response at higher frequencies improves and the amplitude peaks can be easily reduced, obtaining an overall optimization even for the *unsprung mass* performance.

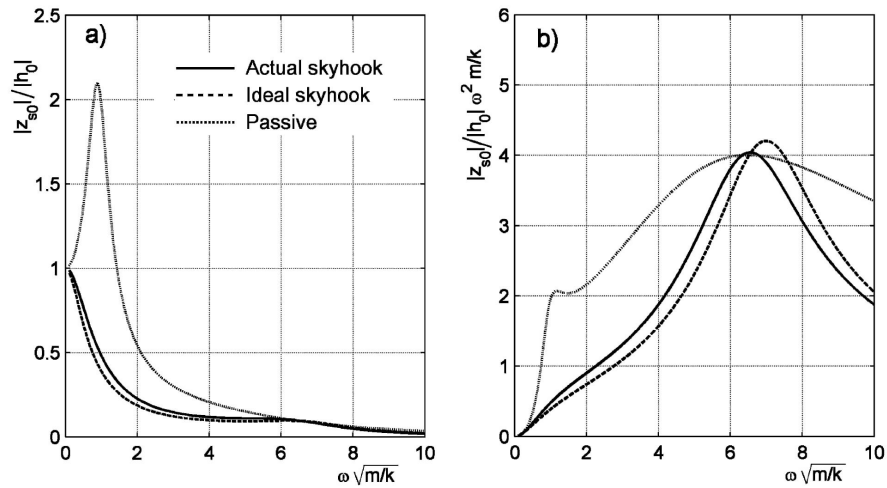


Figure 4.4: Non-dimensional frequency response of the sprung mass of a quarter car with two degrees of freedom with $b=P/K=4$ and $a=\mu/m_s=0.1$. Passive system with optimum damping (ratio 0.433), skyhook (ratio 1 and suspension damping ratio equal to 1/3 of the optimum) and actual skyhook with same values of the parameters, [3].

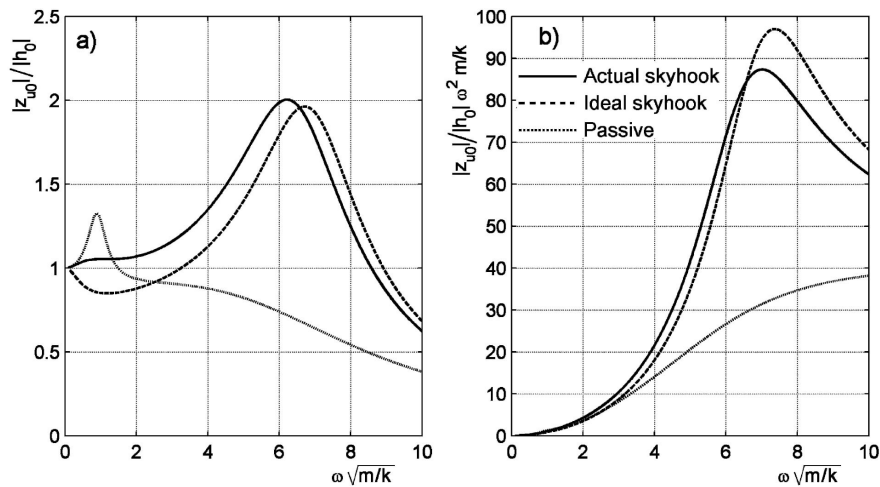


Figure 4.5: Non-dimensional frequency response of the unsprung mass of a quarter car with two degrees of freedom (with actual skyhook), [3].

4.1.2 QC and Sky-Hook Control Model

The study focuses now on the Numerical Modelling of the system with *Sky-Hook Controller*. Once evaluated the benefits and the limits of this Control Strategy, it is applied on a MATLAB/SimulinkTM numerical model which takes into account the QC previously described.

Without considering the HIL model implementation, the QCM is directly linked to the Sky-Hook Controller and to the RRSA System, as visible in Figure 4.6.

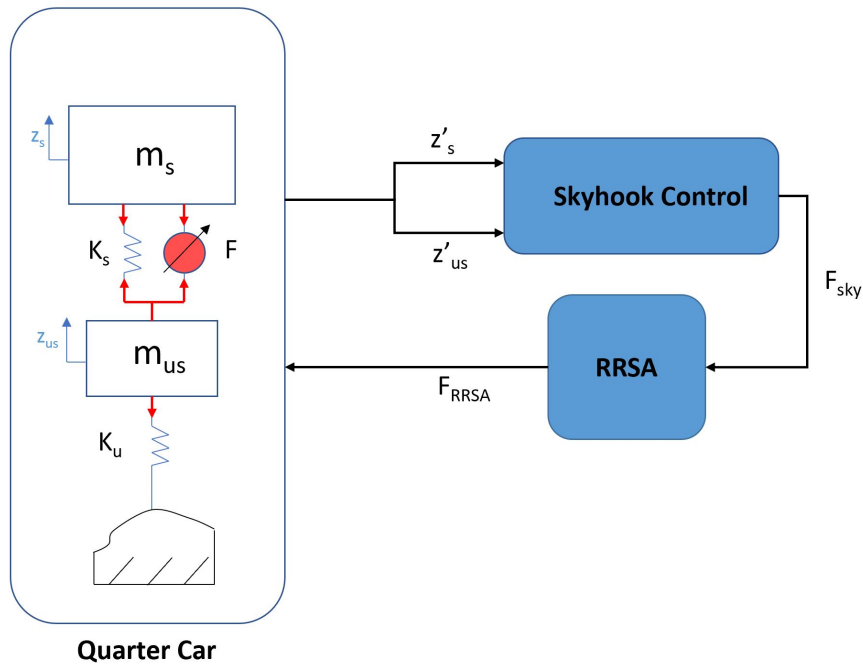


Figure 4.6: Working principle of Sky-Hook Controller applied to the RRSA system in the Quarter Car Model implementation (the static weights of the QC masses are not shown)

In order to follow the Equation 4.12, the Control System receives the absolute vertical velocity signals of the both masses, computes the relative speed and provides a force, completely dependent on the used coefficients, as shown in the SimulinkTM scheme in Figure 4.9.

Once generated such force on the SH Controller, it becomes the input signal to the RRSA System, which in turns provides it directly to the QCM, always passing through the transmission lever characterizing this vehicle implementation. In Figure 4.7 is shown the overall corresponding SimulinkTM Model, with the three main blocks of the simulation.

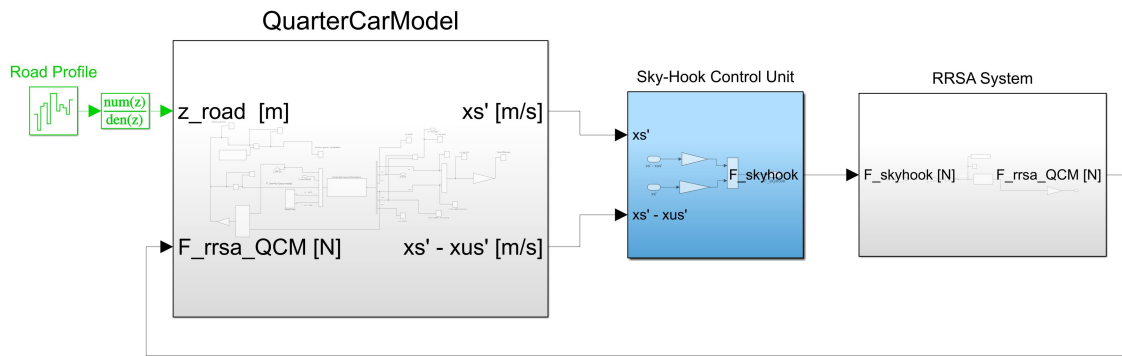


Figure 4.7: SimulinkTM Model of Quarter Car with Sky-Hook controlling the RRSA system

The Quarter Car Model is implemented with the same starting features of the one used in HIL Simulation 3.4.3 but with some additional modifications. First of all, in order to increase the accuracy level of the modelling process, the static conditions are properly taken into account by evaluating the effects of the weight forces of the sprung and unsprung masses. Due to these time-invariant actions, in fact, is computed the achieved equilibrium condition for the whole QC, expressed in terms of vertical displacements of both masses and, consequently, in terms of pre-compression of the springs. For these reasons, hence, in the State Space Model two new input signals are introduced, representing the *constant weight forces*.

The second important modification that is here implemented concerns the force exchanged between tire and road. Even if with standard ISO road profile this can hardly happen, it is important to take into account the "detachment event" of the tire from the ground. Strictly speaking, the reaction *from* the ground to the tire can be directed only towards the tire itself, i.e *up*, while the opposite would imply the detachment of the tire from the ground level. For this reason, hence, the *tire-road force* (defined by $F_t = k_t(z_u - z_g)$, in which $z_u = \text{unsprung mass displacement}$, $z_g = \text{road displacement}$) is no more computed at the output of the state space model, but is introduced as input (considering both vertical displacements) and passed through a *Saturation Block* in order to consider only the negative part of the signal, as can be overall observed in Figure 4.8. In fact, taking into account the chosen sign convention visible in Figure 4.6, this force must always be negative (directed up), while the opposite would give the described *detachment problem*.

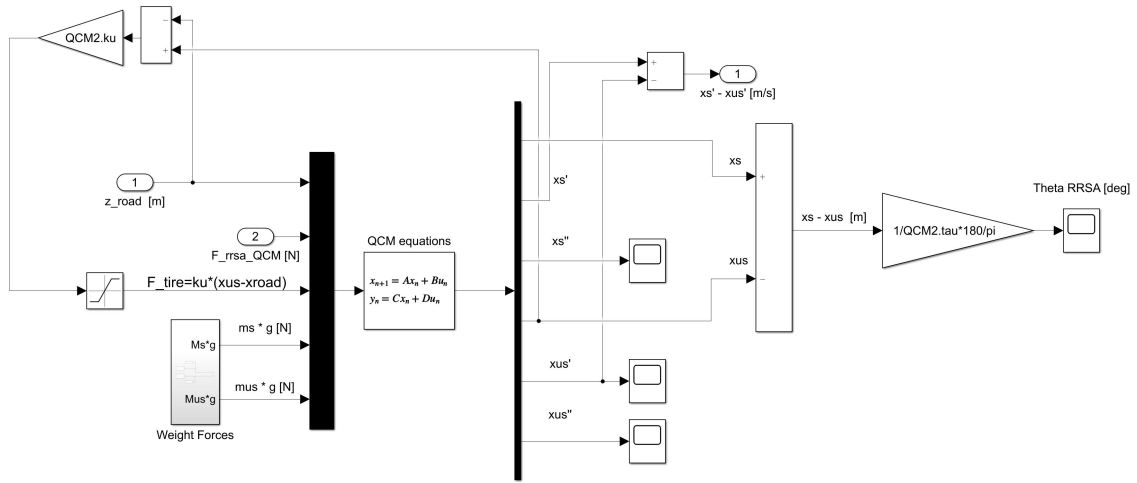


Figure 4.8: Quarter Car Simulink Model detail

As mentioned, the Sky-Hook Controller model, here shown in Figure 4.9, receives the signals carrying information about vertical velocities of both masses and, combining them according to 4.12, provides the Sky-Hook Force. This force is not, then, directly introduced in the QCM, since its function it's that of controlling the RRSA active damper.

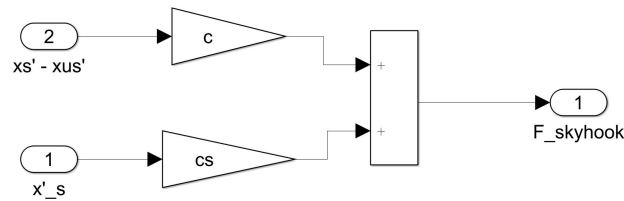


Figure 4.9: Sky-Hook Simulink Model

The RRSA system, which is represented in detail in Figure 4.10, is substantially modelled with the same logic of 3.1.3. The desired force computed by the SH Controller is first converted into the torque available at the output of the planetary gearbox, i.e. passing through the transmission ratio of the connecting leverage, and then into the current required from the RRSA Electric machine. Once obtained the current signal, the RRSA modelling process is basically over, since the current is re-introduced in a

RRSA *sub-block* which replicates the performed transformations in order to get the torque at the output of the gearbox as unique output. At this point, the signal is converted again into the force on the suspension (clearly coinciding with the signal computed by the SH Controller) and finally introduced in the QCM.

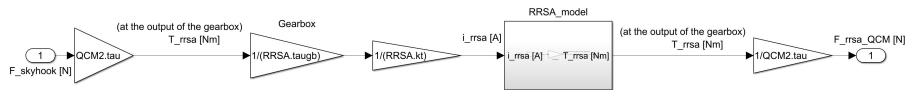


Figure 4.10: RRSA Simulink Model

4.1.3 Methodology

Once described the implemented model for *SkyHook Control Strategy*, a brief introduction to the simulation set up and to the followed procedure is required. The realized QCM, first of all, does not use the same data presented in the previous section, referred to a JeepTM Renegade, but the ones related to the Alfa RomeoTM Stelvio, the actual car model for which is designed the final electro-mechanical RRSA prototype, whose characteristic data are summed up in Table 4.1 (the suspension passive damping is considered null since it is applied the Control Strategy).

Sprung Mass [kg] \longrightarrow m_s	521.75
Unsprung Mass [kg] \longrightarrow m_{us}	55
Susp.Stiffness [N/m] \longrightarrow k_s	43900
Susp.Passive damping [Ns/m] \longrightarrow c_s	0
Tire Stiffness [N/m] \longrightarrow k_u	255e3
Tire Damping [Ns/m] \longrightarrow c_u	50

Table 4.1: Quarter Car Model Data (Alfa RomeoTM Stelvio)

The first performed analyses, as shown in the scheme of Figure 4.10, do not take into

account the inertial and dissipative contributions of the RRSA device. The controlled damping force, in fact, is just provided by the Sky-Hook Strategy without considering the actual characteristics of the system composed by the gearbox and the electric machine. Moreover, the RRSA is first assumed to ideally work with maximum efficiency of *100%*, independently on the working point of its *Torque-Speed Conversion Efficiency Map*, ensuring power transmissions without any kind of losses.

After this first ideal analysis, the overall model will be simulated taking into account both the energy conversion efficiency and the inertial and dissipative contributions, for providing even more realistic results.

Passing to the implemented control system, the SH Control Strategy is analyzed with a variable range of its main factors, c and c_s , for evaluating the optimal performance that can be achieved for the considered QCM. The MATLABTM code, in fact, has been organized with several *loops* for generating an overall matrix collecting all possible combinations of *damping parameters*, in order to provide the desired simulation outputs in the considered range.

This analysis, devoted to study some possible strategies for controlling the active damper, has focused on a specific set of fundamental outputs, referred to two different subgroups:

- *QCM Performance Indicators*
 - Human Acceleration RMS (for Comfort analysis)
 - Tire-Road Holding Coefficient

- *Damper Indicators*
 - RRSA Current
 - Damping Force
 - Damping Speed
 - Regenerable Power

In the QCM Indicators, the Human Acceleration RMS represents the fundamental signal for evaluating the comfort level of the QCM over a specific road profile. It is directly obtained from the *Sprung Mass Acceleration*, output of the QCM, passing through a defined filter, in this case imposed by the standard ISO 2631 for *evaluation of human exposure to whole-body vibration*, defined by [9]:

$$H = \frac{80.03s^2 + 989s + 0.02108}{s^3 + 78.92s^2 + 2412s + 5614} \quad (4.13)$$

Based on this standardized legislation, the output measurement of this filter must be evaluated according to the following specific ranges, in order to provide the actual achieved comfort level:

- Less than 0.315 m/s²: *not uncomfortable*
- 0.315m/s² to 0.63m/s²: *a little uncomfortable*
- 0.5m/s² to 1m/s²: *fairly uncomfortable*
- 0.8m/s² to 1.6m/s²: *uncomfortable*
- 1.25m/s² to 2.5m/s²: *very uncomfortable*
- Greater than 2m/s²: *extremely uncomfortable*

For what concerns the Road Holding indicator, instead, its computation is based on the *actual tire variable vertical force* compared to the *static vertical force*, explained by the following mathematical steps:

$$TireForce = k_u(z_{us} - z_{road}) \quad (4.14)$$

$$\frac{\Delta F_{tireRMS}}{F_{z.static}} = \frac{rms[TireForce - k_u \Delta Z_{mus}]}{(m_s + m_{us})g} = \eta_{rh} \quad (4.15)$$

In which η_{rh} is the Road-Holding indicator, k_u is the *tire stiffness*, the subscript *us* and *s* represent the *unsprung mass* and the *sprung mass*, respectively, and ΔZ_{mus} is the static vertical displacement affecting the unsprung mass due to the overall weight, defined by:

$$\Delta Z_{mus} = -\frac{(m_s + m_{us})g}{k_u} = -0.022m \quad (4.16)$$

The resulting expression in 4.15 provides useful information regarding the tire capability of keeping contact with the ground, ensuring different levels of traction and control according to the assumed value: the *higher* the ratio, the worse the *performance* of tire-ground contact.

Since the *RMS* calculation, the ratio expressed by 4.15 is, in the following, computed for each simulated Sky-Hook configuration, meaning that every tested condition will be characterized by a *single* value of η_{rh} , as well as the *Human Acceleration RMS*. In this way, each considered simulation, identified by specific damping values, will be characterized by just two fundamental performance parameters.

Considering, instead, the indicators related to the RRSA device, they are evaluated over the simulation time just to provide useful references and *root-mean-square values*, for assessing the actual working conditions of the simulated actuator.

Taking into account, for example, both damping coefficients, i.e c and c_s , set to 1000Ns/m, and an input road profile given by the standard *ISO-B @ 70km/h*, some of the resulting plots in time domain are shown in Figure 4.11, providing an RMS value of the perceived human acceleration equal to 0.4225 m/s², placing this specific configuration, used as example, in the *little uncomfortable* range.

It is important to highlight that the *electrical power*, i.e the *damping power*, is obtained by the product between the relative speed of the two masses of the QCM (computed with the expression: *Relative Speed*= $\dot{x}_s - \dot{x}_{us}$) and the computed Sky-Hook Control Force. With reference to Figure 4.6, taking into account the orientation of the relative speed and the one of the damping force acting on the *Sprung Mass*, the resulting *RRSA power* is a *dissipative power* when its sign is > 0 , while it is a *required power* when it is < 0 . The positive values, in particular, represent *potential regenerable power* by the RRSA System, while the negative values represent power that must be introduced in the suspension system, i.e *active power*, provided by the actuator itself. Considering the specific case shown in Figure 4.11, it is evident that, over a ISO-B profile at 70km/h, and with the imposed damping values, the active suspension works

mainly only on *damping mode*, requiring energy from the battery in a very reduced number of instants.

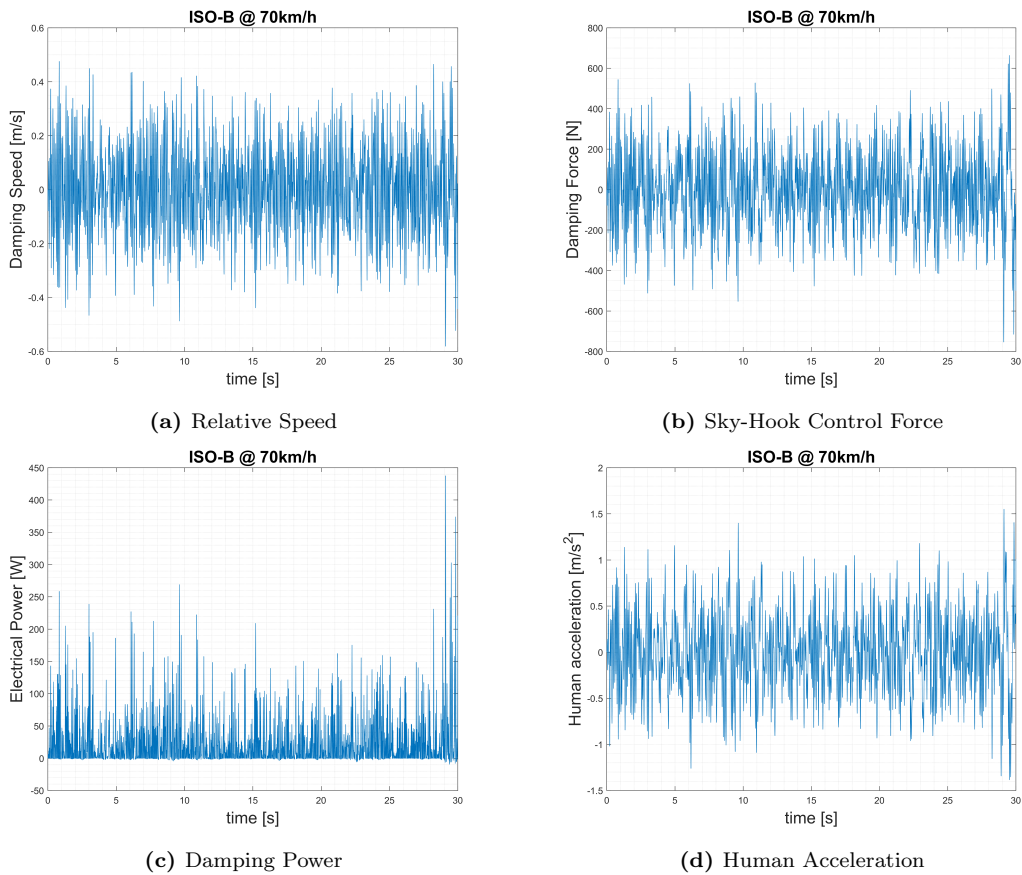


Figure 4.11: Output results for QCM with Sky-Hook Control Strategy with ISO-B @ 70km/h ($c=1kNs/m$, $c_s=1kNs/m$)

4.1.4 QCM Results

This Section focuses on the study of the Sky-Hook Control Strategy applied to the QCM described in 4.1, whose numerical characteristics have been introduced in 4.1.2. The SH parameters have been set as variable coefficients in the MATLAB/SimulinkTM Simulation, according to specific range suggested by MarelliTM analysis on SH Control, [8]. In particular:

$$\begin{aligned}
 c &= [100 \ 200 \ 500 \ 1000 \ 1200 \ 1500 \ 2000 \ 2500 \ 3000] \text{ Ns/m} \\
 c_s &= [1000 \ 2000 \ 3000 \ 5000 \ 10000 \ 20000] \text{ Ns/m}
 \end{aligned}
 \tag{4.17}$$

Taking into account these values, it has been performed a certain number of analyses concerning the performance indicators and the energetical aspect of the active suspension RRSA, evaluating their dependences on the SH damping values.

Moreover, both standard road profiles *ISO-B at 70km/h* and *ISO-C at 35km/h* have been analyzed.

Comfort Analysis

The first factor that is taken into account is the *Comfort level* provided by the suspension system, according to the ISO 2631 filter defined in Equation 4.13. This indicator has been introduced in a MATLABTM colour map as a function of the variable damping coefficients, for an optimized visualization of the achieved level.

In order to provide relevant considerations concerning the obtained comfort result with SH Control, it is useful to consider the achieved comfort level with a standard *passive shock absorber*, modelled on the same QCM, without any active device, with a constant damping value of 2500Ns/m for both tested road profiles, as shown in Figure 4.12.

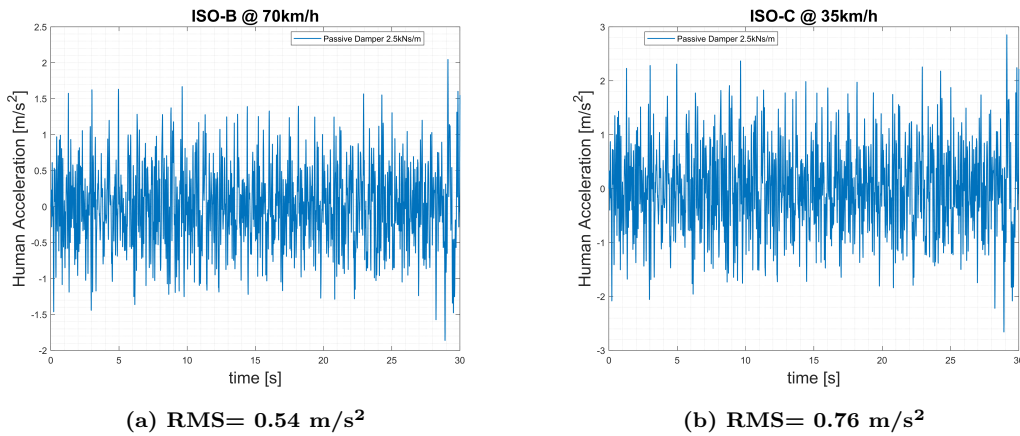


Figure 4.12: *Perceived Human Acceleration with passive damper $c=2.5kNs/m$*

In particular, with these RMS values, the Comfort performance obtained with this constant-damping passive suspension for ISO-B and ISO-C profiles are, respectively, included in the *fairly uncomfortable* range.

ISO-B @ 70km/h

In Figure 4.13 can be observed the resulting map for the ISO-B road profile at 70km/h. The achieved comfort level shows a clear dependency on the SH coefficients, being generally optimized for high values of *Sky-Hook damping* c_s (for a fixed c), while a significant worsening occurs for increased values of c (for a fixed c_s). Moreover, the overall perceived *Human Acceleration* is included in the first two classes of highest comfort (respectively, *not uncomfortable* and *a little uncomfortable*), since maximum and minimum accelerations are just over 0.5m/s^2 and below 0.3m/s^2 . The optimal performance offered by the SH Control Strategy for this specific road profile, moreover, can be further appreciated by considering the resulting comfort of passive shock absorber, shown in Figure 4.12 a), whose obtained RMS value (0.54 m/s^2) can be just compared with the worst possible acquired Sky-Hook result in Figure 4.13.

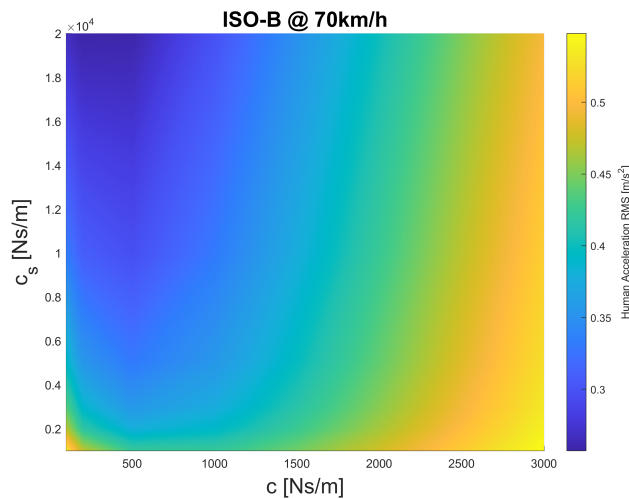


Figure 4.13: Comfort Map for ISO-B at 70km/h

ISO-C @ 35km/h

Passing to the ISO-C road profile, the same trend has been obtained, as shown in Figure 4.14. Due to the fact that the ISO-C profile represents more critical road conditions, the resulting comfort is clearly reduced in the same range of damping variation, i.e the *perceived human acceleration* is evidently increased. The comfort level, in fact, is partially included in the *third comfort class*, i.e *fairly uncomfortable*, overcoming 0.75m/s^2 for very high values of c and low values of c_s . However, even with the increased irreg-

ularity of the road, the SH Control achieves greatly improved result with respect to a simple passive shock absorber, as shown in Figure 4.12 b). The worse obtained results, in fact, are just slightly higher than 0.75m/s^2 , the same order of magnitude achieved without any control strategy with the constant-damping passive suspension.

The obtained colour maps in Figures 4.13 and 4.14, provide a significant amount of working conditions in which the comfort level is greatly improved, with respect to the capacity offered by the traditional shock absorber. The Sky-Hook control demonstrates, hence, to be particularly suited for considerably improving the human comfort performance, according to the imposed damping and electrical parameters of the RRSA active device.

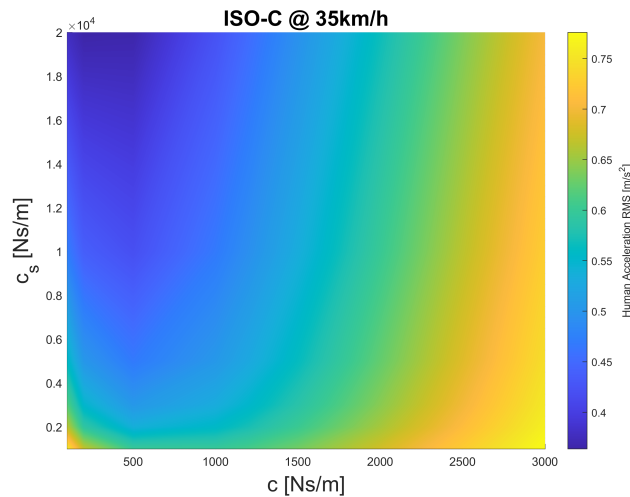


Figure 4.14: *Comfort Map for ISO-C at 35km/h*

Road Holding Analysis

The second considered performance index is the *Road Holding*, evaluated for each considered simulation according to the Equation 4.15. As it has been done for the Comfort analysis, described in 4.1.4, this analysis has been carried out by using a similar MatlabTM *for-loop* code containing the mathematical expressions from 4.14 to 4.16, then graphical represented in a colour map depending on the SH damping values defined in 4.17. Also in this study is fundamental to compare the obtained results with SH Control Strategy with the ones characterizing the passive damper with $c=2500\text{Ns/m}$,

shown in Figure 4.15, for both tested ISO road profiles.

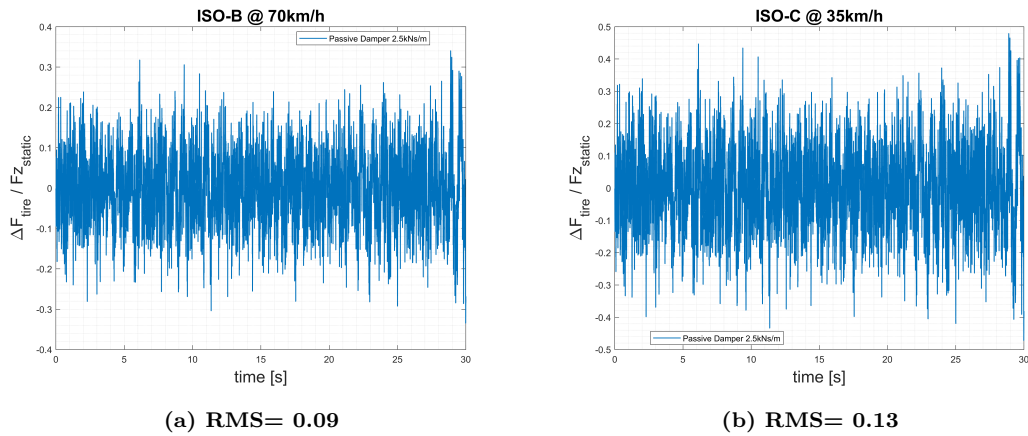


Figure 4.15: Road-Holding Coefficient with passive damper $c=2.5\text{kNs/m}$

ISO-B @ 70km/h

The results of the first tested input road profile can be observed in the obtained colour map in Figure 4.16. With respect to the perceived Comfort level, the resulting chart shows quite a different trend. In fact, the increase of Sky-Hook damping c causes a reduction in η_{rh} , hence an improvement in road-holding capacity, opposite to the observed corresponding comfort level reduction experienced for the same variation range, visible in Figure 4.13. On the contrary, the worst obtained conditions can be found for reduced values of both SH coefficients, with overall RMS ratio higher than 0.22.

Compared to the road-holding performance offered by the passive damper in Figure 4.15, the Sky-Hook Strategy appears to be able to provide quite equivalent results for a relatively narrow range of damping values, particularly similar if significant increases can be sustained from the point of view of the electric machine performance.

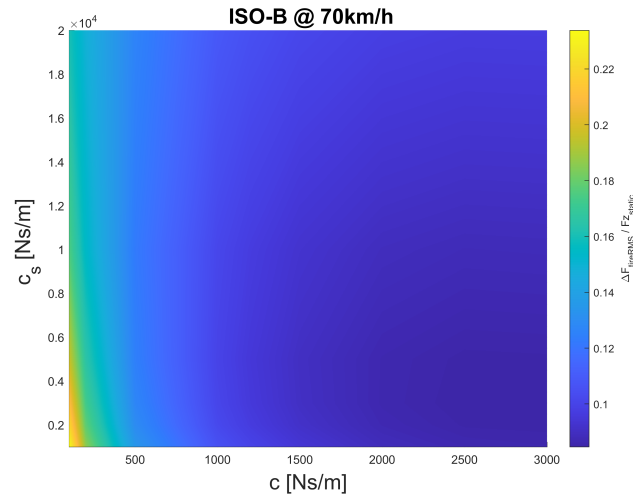


Figure 4.16: Road Holding Map for ISO-B at 35km/h

ISO-C @ 35km/h

Passing to the second tested ISO road profile, the same colour map is obtained, as shown in Figure 4.17. As expected, due to the increased roughness of the road, the resulting η_{rh} covers a range of higher values, as observed in the Comfort study. Even compared to the passive damper, the obtained SH performance can be considered of the same order of magnitude only for a reduced range of variation.

Overall, from this initial analysis, it clearly appears that the *Sky-Hook Control Strategy* provides great performance in terms of *perceived Comfort* with respect to a traditional passive suspension, having a wide range of possible configurations in which the system can properly work with significant improvements. However, corresponding to these good results, the *Road-Holding Coefficient* experiences an opposite trend, being optimized in the working conditions that do not ensure totally satisfying comfort levels. Moreover, the Sky-Hook Control is particularly designed for enhancing vehicle comfort performance rather than road-holding capacities, which are instead on the same order of magnitude of the ones offered by the considered passive damper.

Hence, this Control Law must be properly managed in order to find the best trade-off between both performance indexes, as will be done later in this study.

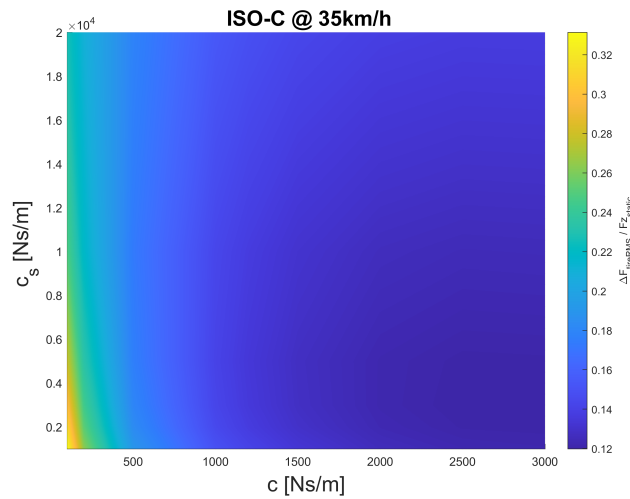


Figure 4.17: Road Holding Map for ISO-C at 35km/h

Sky-Hook damping lines

Once described the road-holding and comfort simulation outputs, the study proceeds by considering both performance indexes in a single analysis, to provide an overall view of the possibilities offered by the SH Control strategy. The perceived human acceleration and the η_{rh} coefficient have been plot on the same chart depending on the imposed *damping values*, i.e c and c_s , in order to acquire the RRSA characteristics that can maximize both performances. This purpose implies the achievement of two kinds of graphical representations, complementary between each other, according to the considered *constant SH damping value*: lines at *constant c* and lines at *constant c_s*.

Moreover, these representations have been performed for both considered ISO road profiles.

Damping Lines: constant c

In Figures 4.18 and 4.19 can be observed the resulting charts with iso- c lines, for both ISO-B and ISO-C road profile respectively, in which the simulated damping conditions are the ones described in Equation 4.17. Considering the direction of increase of the curves, it is clear that some values of c provide better overall results than others, while, instead, some other working conditions optimize just one performance index. For both

road profiles, for example, the third curve from the right, representing $c=500\text{Ns/m}$, optimize the perceived Comfort if combined with the highest c_s , i.e 20kNs/m , while the same can not be said about the road-holding performance, which are certainly improved for higher values of c , contrasting with a progressive reduction in comfort level.

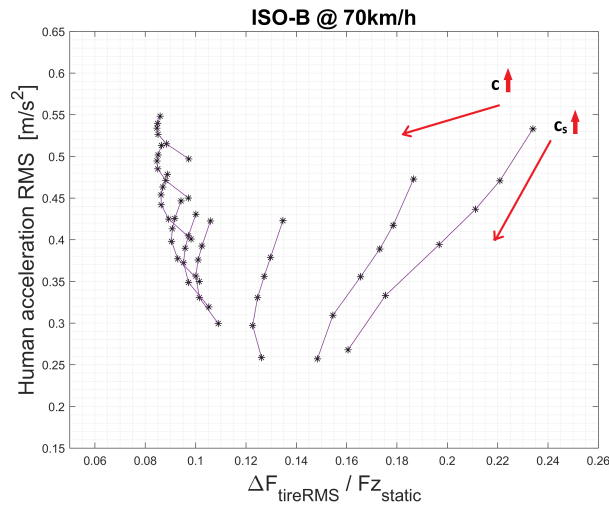


Figure 4.18: Comfort Coefficient and Road Holding Coefficient with lines at constant c for ISO-B at 70km/h

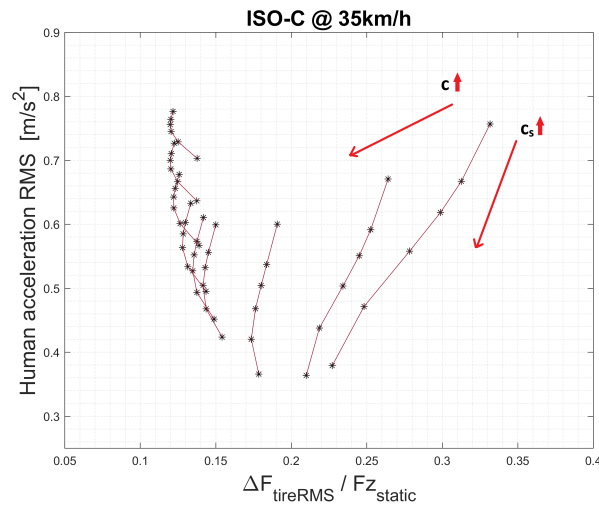


Figure 4.19: Comfort Coefficient and Road Holding Coefficient with lines at constant c for ISO-C at 35km/h

Damping Lines: constant c_s

The complementary charts to the ones represented in Figures 4.18-4.19 are obtained

by simply connecting the same points but according to the corresponding constant values of c_s , as shown in Figures 4.20 - 4.21 for both profiles. Even with this different points arrangement it is possible to observe the dependency between Comfort and Road-Holding coefficient, previously individually described by the corresponding colour maps. In fact, considering the increment of c_s , the observed behaviour in 4.1.4 is here validated, showing minimum perceived human acceleration for increased SH c_s , for a fixed c .

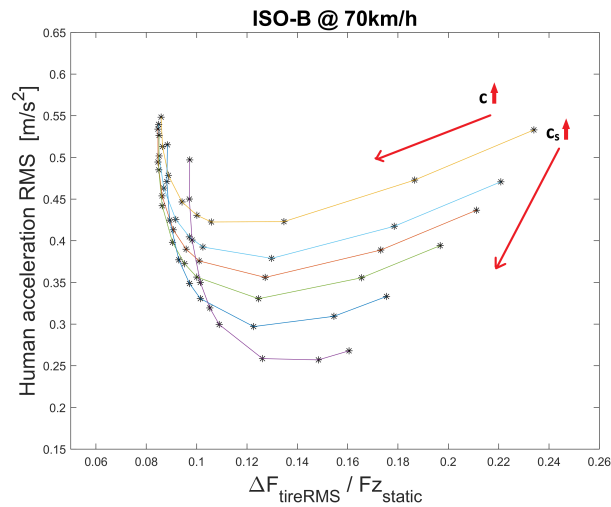


Figure 4.20: Comfort Coefficient and Road Holding Coefficient with lines at constant c_s for ISO-B at 70km/h

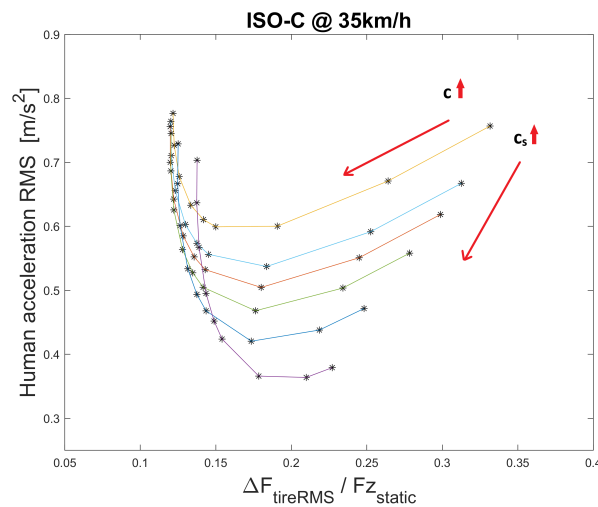


Figure 4.21: Comfort Coefficient and Road Holding Coefficient with lines at constant c_s for ISO-C at 35km/h

RRSA Regenerable Power

Once analyzed the dependence of both performance indicators on the defined SH damping values, the study focuses on the energetical analysis of the active suspension. As described in 4.1.3, the RRSA device can work in two different conditions, according to the actual power flow: damping power, i.e. *regenerable mode*, and active/consumed power, i.e. *active mode*. As mentioned, the considered power is computed as the product between the relative speed of the suspension (between sprung and unsprung mass) and the obtained Sky-Hook control force, providing, for each tested SH condition, a certain time history of the *Power signal*, as the one shown in Figure 4.11 c). Considering, for instance, the previously described passive damper with constant $c=2500\text{Ns/m}$, implemented on the same QCM, it provides the Power output signals visible in Figure 4.22, for both ISO road profiles.

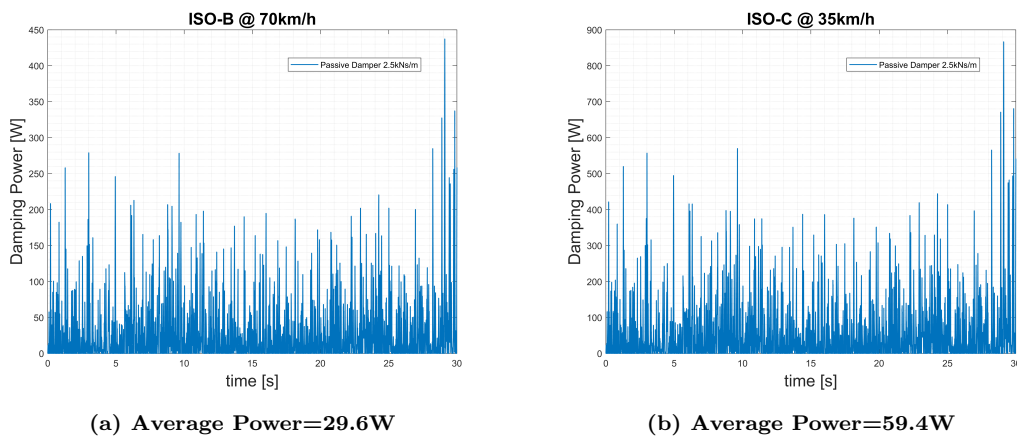


Figure 4.22: Damping Power with passive damper $c=2.5\text{kNs/m}$

As expected, the obtained power signal is placed on the *positive quadrant*, since a traditional passive damper can only dissipate the suspension energy, with no possibilities of introducing energy in the system. Based on the acquired signal, a specific MATLABTM code is used for computing the *Mean Power* value, to provide an approximated value of the average potentially regenerable power (in this case, considering a passive damper, the power *can be only* regenerated). In Figure 4.11 c), in fact, by implementing the RRSA device together with the Sky-Hook Control, the resulting signal partially covers negative values, meaning that the suspension is receiving *active power*

from the actuator.

In the following is shown the MATLABTM code used for the Mean Power computation. The first step is to load on the MATLABTM Workspace the required signals from the Simulink Model, by means of the *to Workspace* Simulink Block. Considering the described mathematical expression of the Power, is just required to load the *Relative Speed* and the *Damping Force* signals, and computing then on MATLABTM the resulting product. Having performed this calculation, the obtained signal is called *Power*, while its time vector is defined as *time_{Power}*. Then, to compute the integral signal of the Power, i.e the signal *Energy Content*, is used the *trapz* MATLABTM command, shown in Equations 4.18-4.19. Finally, once obtained the Energy content of the time-signal, it is simply divided by the considered simulation time, i.e *t_{sim}*=30s, hence getting the desired *Mean Power* value.

$$integral_{Power} = trapz(time_{Power}, Power) \quad (4.18)$$

$$Mean_{Power} = \frac{1}{t_{sim}}(integral_{Power}) \quad (4.19)$$

ISO-B @ 70km/h

Similarly to what has been done in 4.1.4 and in 4.1.4, this study provides a MATLABTM colour map for representing the Average Power characterizing each specific tested condition, depending on the SH damping values. Its representation can be seen in Figure 4.23 for ISO-B road profile. Considering what has been described in the previous sections, the higher is the positive value of the Average Power, the higher is the contribution of the *damping mode* along the time simulation, i.e the lower is the one of the *active mode*. This first analysis is obtained without accounting for the *efficiency map* of the RRSA, hence not affected by the actual working point of its electric machine, and without considering the *inertial* and *dissipative* contributions of the RRSA itself. It clearly represents an idealized modelling process, being the energy conversion efficiency of the EM fixed to 100%, but anyway useful for evaluating the maximum ideally available performance of the overall system.

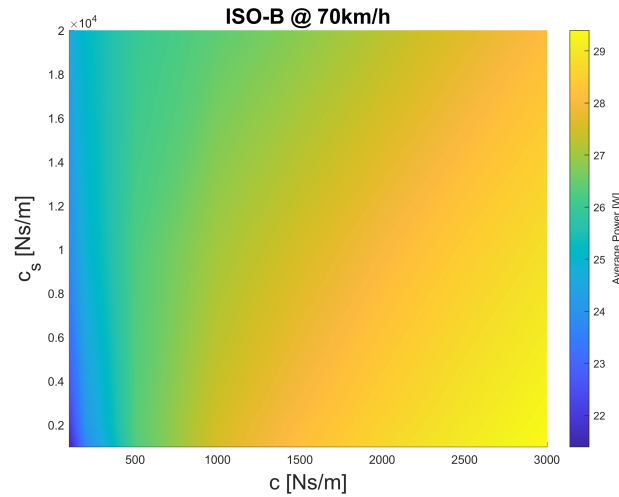


Figure 4.23: Average Power for ISO-B at 70km/h (with 100% energy efficiency)

Considering the obtained trend, the SH Control seems to provide augmented damping power levels (potentially, *regenerated power*) by increasing, for a certain SH c_s value, the SH c coefficient. Moreover, the obtained range of variability results to be quite close to the performance offered by the passive damper shown in Figure 4.22 a). Even considering the useful amount of information carried out by this type of graphical representation, this study has developed an even more important detailed description. In Figure 4.24, in fact, are represented the *Sprung Mass Acceleration RMS* and the η_{rh} , with lines at constant c_s and with corresponding *Average Power* levels. This type of chart has been inspired by the performed analysis by MarelliTM, [8], capable of summing up the most important QC information over a specific road profile, in this case ISO-B at 70km/h, with reference to the SH damping range previously defined in 4.17. Combining, in fact, the Power colour map in Figure 4.23 with the iso- c_s lines in Figures 4.20-4.21, the resulting chart allows to perform a complete energetical analysis taking into account two key parameters. As can be observed, the average power rises for increased SH damping c , for a certain c_s , meaning that the system is intensifying the *damping mode* and reducing the *active mode*, hence potentially regenerating more power and providing less power to the suspension system.

Simultaneously, this described SH configuration (very high values of c with relatively low values of c_s) correspond to increased Sprung Mass acceleration and reduced η_{rh} , i.e improving road-holding performance while worsening comfort level (the sprung mass

acceleration is directly connected to the Comfort by means of the ISO 2631 filter).

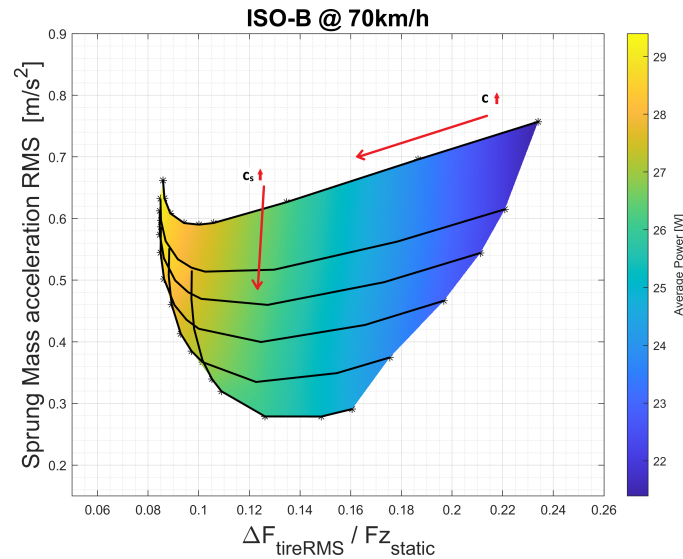


Figure 4.24: Sprung Mass Acceleration and Road Holding Coefficient with Average Power for ISO-B at 70km/h with lines at constant c_s (with 100% energy efficiency)

In Figure 4.25, to expand the analysis, is reproduced the same chart but with an extended *SH range of variation*, defined as follows:

$$\begin{aligned} c &= [100 \ 200 \ 500 \ 1000 \ 1200 \ 1500 \ 2000 \ 2500 \ 3000] \text{ Ns/m} \\ c_s &= [1000 \ 2000 \ 3000 \ 5000 \ 10000 \ 20000 \ 30000 \ 40000 \ 50000] \text{ Ns/m} \end{aligned} \quad (4.20)$$

Three values of c_s , i.e 30-40-50kNs/m, have been added in order to evaluate the simulated behaviour for an even wider range of working conditions. It is observed that, as partially visible with the reduced range, by further increasing damping c_s , the resulting curve tends to move to the right, providing reduced sprung mass accelerations but worsened road-holding performance. Moreover, with the highest tested values of c_s , the actual distance between each iso- c_s lines reduces, providing no more significantly different overall performance.

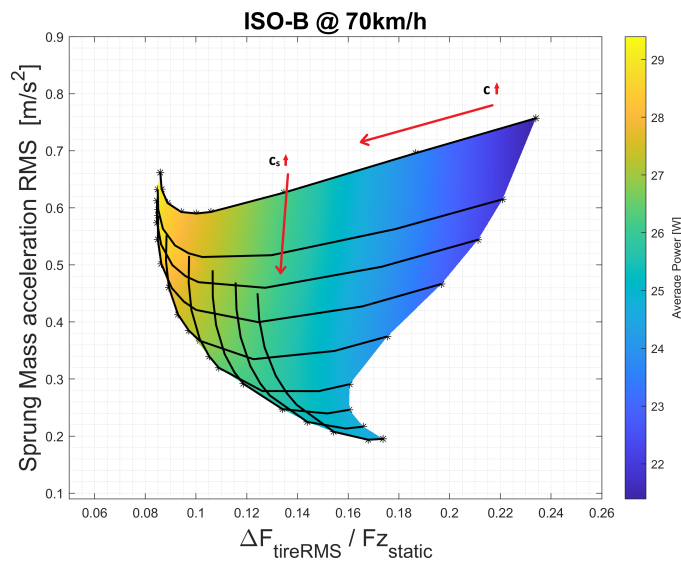


Figure 4.25: Sprung Mass Acceleration and Road Holding Coefficient with Average Power for ISO-B at 70km/h with lines at constant c_s (with 100% energy efficiency and extended range of variation of c_s)

Finally, to complete the energetical analysis about the idealized modelling process, the chart in Figure 4.25 is modified into the one shown in Figure 4.26, obtained by considering the *Human Acceleration RMS* instead of the vehicle body acceleration, in order to visualize both performance indicators combined with the power flow information, depending on the SH damping values.

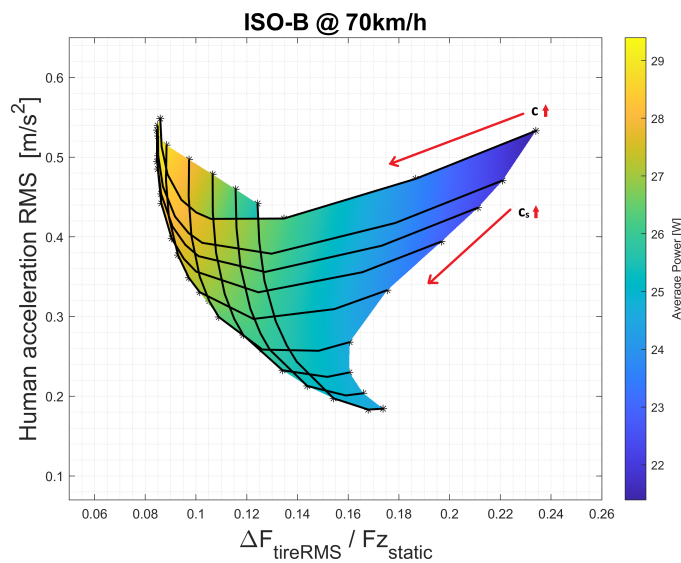


Figure 4.26: Comfort Coefficient and Road Holding Coefficient with Average Power for ISO-B at 70km/h with lines at constant c_s (with 100% energy efficiency and extended range of variation of c_s)

ISO-C @ 35km/h

In this section the study performs the same analysis described for *ISO-B @ 70km/h* road profile with ideal RRSA modelling, but applied to the ISO-C road profile.

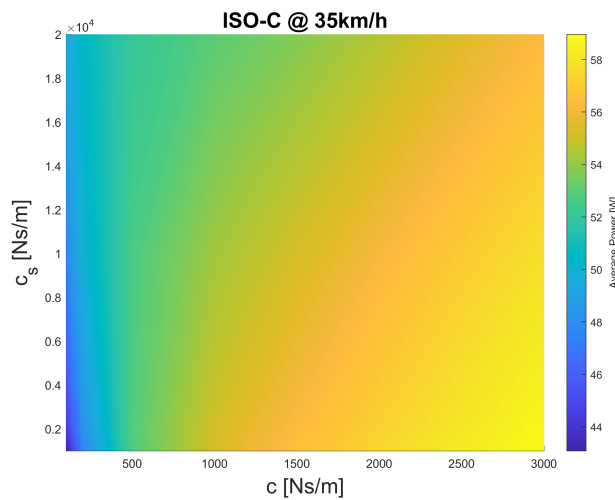


Figure 4.27: Average Power for ISO-C at 35km/h with 100% energy efficiency

The trend observed in Figure 4.27 and 4.28 is just the same but, as expected, with significantly higher values of average power, due to the fact that the more demanding conditions of the road profile (at the considered speed of 35 km/h) imply increased force and relative velocity. The maximum and minimum power, in fact, are doubled with respect to the ISO-B case.

Then, the colour maps with extended range of variation, similarly to the case with ISO-B, are realized and shown in Figures 4.29-4.30

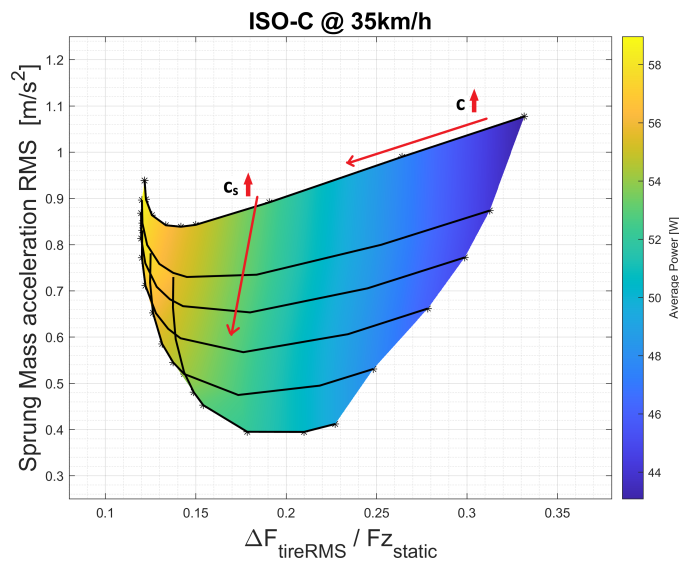


Figure 4.28: Sprung Mass Acceleration and Road Holding Coefficient with Average Power for ISO-C at 35km/h with lines at constant c_s (with 100% energy efficiency)

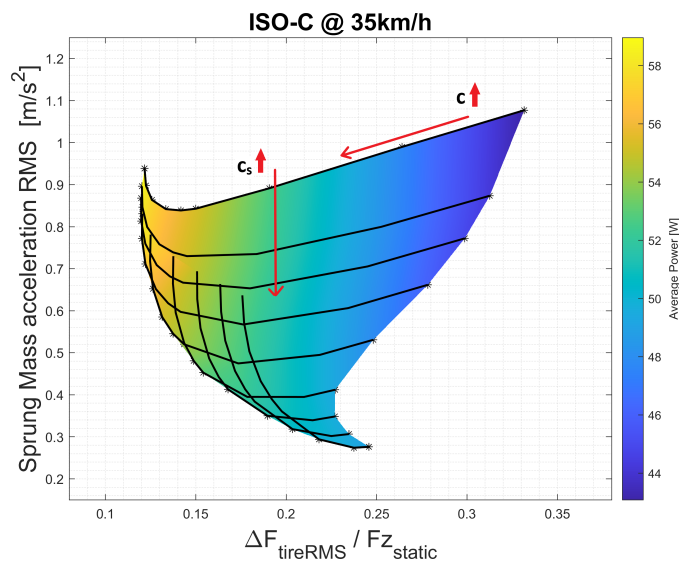


Figure 4.29: Sprung Mass Acceleration and Road Holding Coefficient with Average Power for ISO-C at 35km/h with lines at constant c_s (with 100% energy efficiency and extended range of variation of c_s)

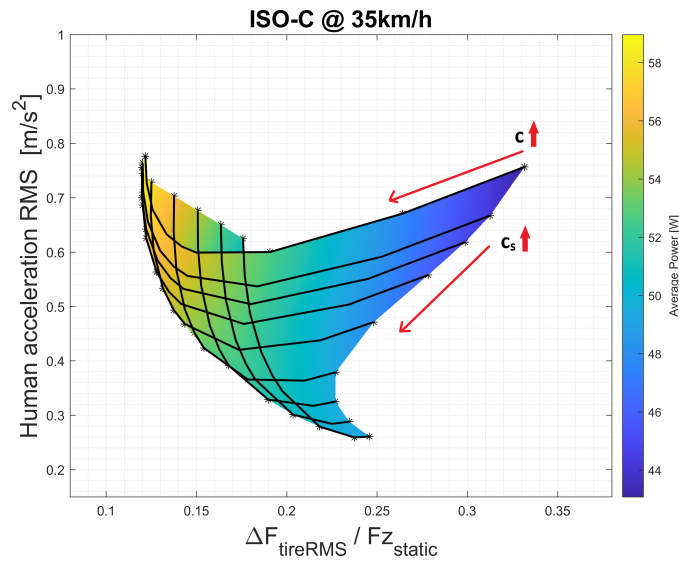


Figure 4.30: Comfort Coefficient and Road Holding Coefficient with Average Power for ISO-C at 35km/h with lines at constant c_s (with 100% energy efficiency and extended range of variation of c_s)

Trade-Off Sky-Hook configuration

Once described the simulation results obtained with variable Sky-Hook damping, the study provides some numerical outputs for a specific working configuration of the system. Based on Figure 4.26, in order to obtain an overall acceptable behaviour in terms of perceived Comfort and Road-Holding performance, the considered SH coefficients are set to $c=1.2\text{kNs/m}$ and $c_s=10\text{kNs/m}$, as visible in Figure 4.31. This working condition has been defined according to the values assumed by both Performance Indicators, with the purpose of finding an optimal trade-off, and taking into account the Average Power Map, that here provides relatively high values of *damping/regenerated power*.

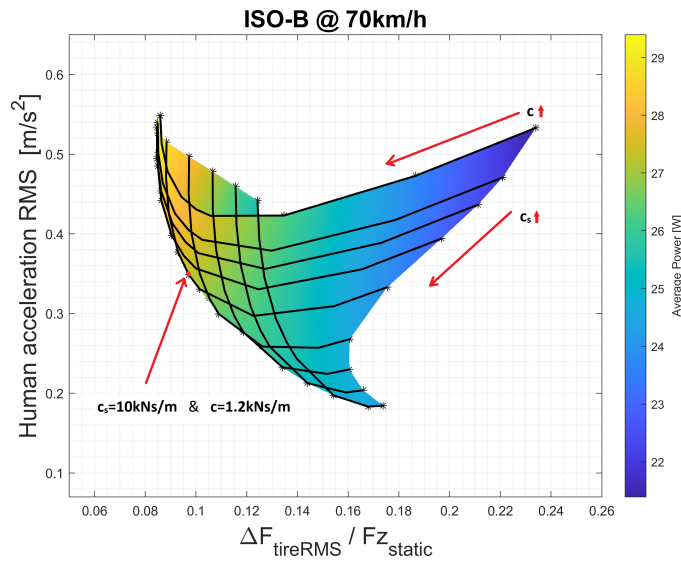


Figure 4.31: Comfort Coefficient and Road Holding Coefficient with Average Power Map for ISO-B at 70km/h with highlighted SH configuration $c=1.2\text{kNs/m}$ and $c_s=10\text{kNs/m}$

ISO-B @ 70km/h

With the set up Sky-Hook configuration, the first simulation takes into account the ISO-B road profile, the same described in the previous analyses. Fixed both damping coefficients, the MATLAB/SimulinkTM time domain analysis is performed, providing four main outputs: *Performance Indicators*, *Power flow* and *RRSA current*.

As can be seen in Figure 4.32 a), this SH configuration allows to reach really improved comfort performance with respect to the passive damper considered in Figure 4.12, with the RMS value reduced from 0.54m/s^2 to 0.356m/s^2 , hence included in the "a little uncomfortable" range, just slightly higher than the best standardized available range of values.

Considering the *Road-Holding coefficient*, the result shows a RMS value quite close to the passive damper one (0.09), practically minimized (0.098) if is taken into account the available range in Figure 4.31, not able to go below 0.08.

In Figure 4.33, instead, can be seen that the *Electrical Power* signal provides a RMS (28.21W) just slightly lower than the damping power resulting from the Passive Damper (29.6W) and with evident *active mode operations*. Moreover, taking into consideration the Colour Map in Figure 4.31, this Power value is close to the maximum available with the Sky-Hook Strategy adopted according to the fixed damping range.

4.1. Sky-Hook Control

Finally, the current flowing in the RRSA Electric Machine, shown in Figure 4.33 b), has a time history which locally can reach almost 30A, far from the maximum possible value achievable by the EM, and a RMS value quite low (8.14A), making this SH Configuration feasible even from the point of view of the RRSA active damper.

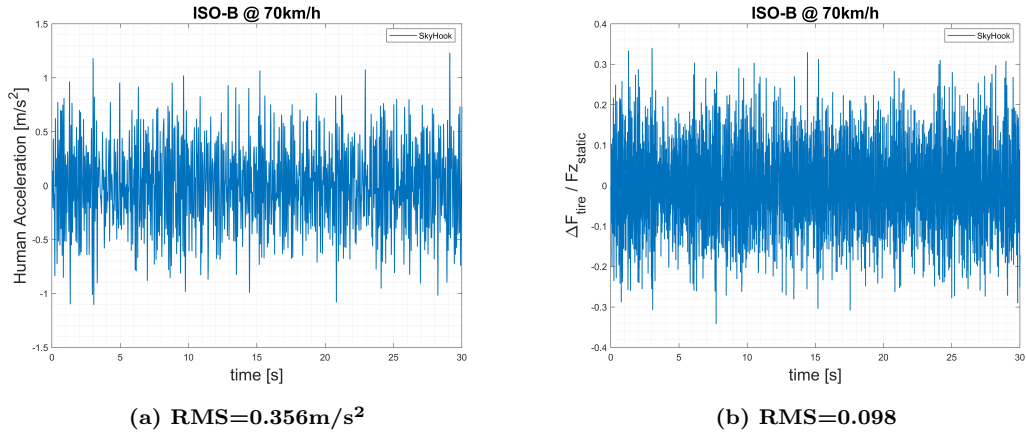


Figure 4.32: Performance Indicators with Sky-Hook Control with $c=1.2kNs/m$ and c_s10kNs/m for ISO-B at 70kph

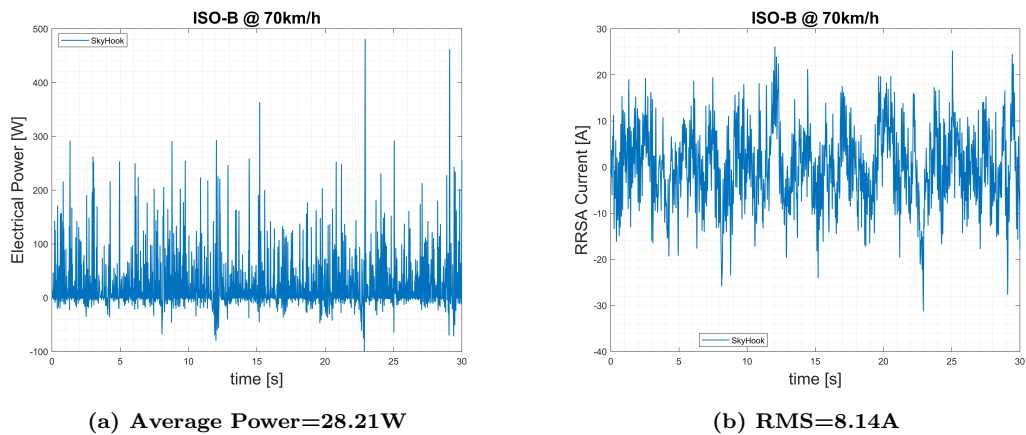


Figure 4.33: Electrical Power and RRSA Current with Sky-Hook Control with $c=1.2kNs/m$ and $c_s=10kNs/m$ for ISO-B at 70kph

Bump 30mm @ 50km/h

The second case study with the described SH configuration regards the QCM crossing a sequence of road *bump profiles*. Each of them reaches a maximum depth of 30mm and the approaching speed is fixed to 50km/h, as can be seen in Figure 4.34. The considered outputs are the same as described in the previous subsection, and in order to provide a significant analysis, the Sky-Hook Strategy has been compared again with

the resulting behaviour of the passive damper taken into account, whose simulation results can be observed in Figure 4.35.

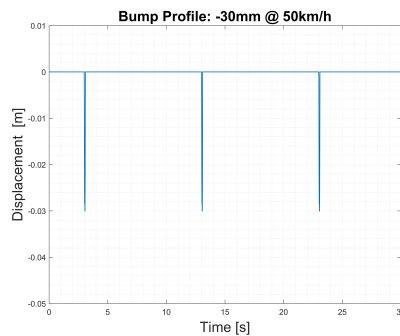
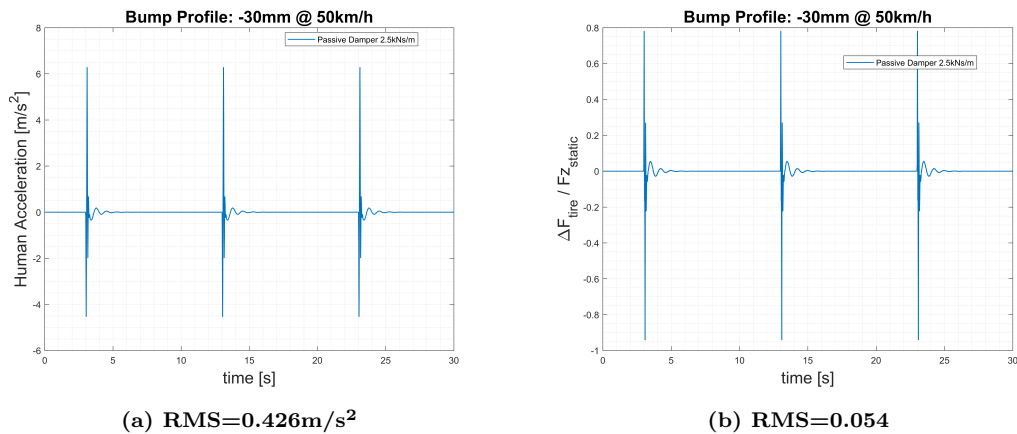
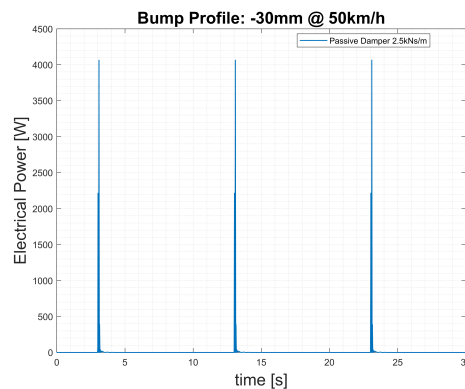


Figure 4.34: Sequence of three bump profiles



(a) RMS=0.426m/s²

(b) RMS=0.054



(c) Average Power=16.91W

Figure 4.35: Bump Profile results with passive damper $c=2500\text{Ns/m}$

The resulting signals with Sky-Hook Control are shown in Figure 4.36 and 4.37. If compared to the passive shock-absorber performance, is significant the improvement in *perceived Comfort*, since with the SH Control is achieved a lower peak and a reduced

RMS value (from 0.426m/s^2 to 0.303m/s^2), hence further demonstrating the relevant performance offered by the Sky-Hook strategy in particularly enhancing the comfort level.

For what concerns the *road-holding* capacity, the results do not show an improvement with respect to the passive damper case, but indeed a slight worsening (from 0.054 to 0.066). This behaviour, however, was quite expected, considering that it has been just noted in the performed analysis in 4.1.4.

The *power flow*, instead, is very similar between the two systems, obviously not showing negative values for the passive damper. Moreover, the maximum and minimum reached peaks with SH Control are significantly higher than the maximum value obtained by the passive damper (8kW and -6kW, for the SkyHook, while 4kW for the Passive SA). Finally, the current flowing in the RRSA Electric Machine locally reaches maximum value of almost 60A, while providing a RMS value quite low, i.e 4.65A. Both values, anyway, are perfectly in line with the maximum feasible electrical characteristics of the Rotary Regenerative Shock Absorber.

Validating what has been analyzed in the previous sections for the ISO road profiles, the implemented Sky-Hook Strategy seems to be particularly suitable, even in the considered *Bump profile sequence*, in significantly improving the traditional damper *Comfort* level, keeping the *Road-Holding* coefficient in a good range of acceptability, and providing good results in terms of *Available Power* and *RRSA Electrical Current*.

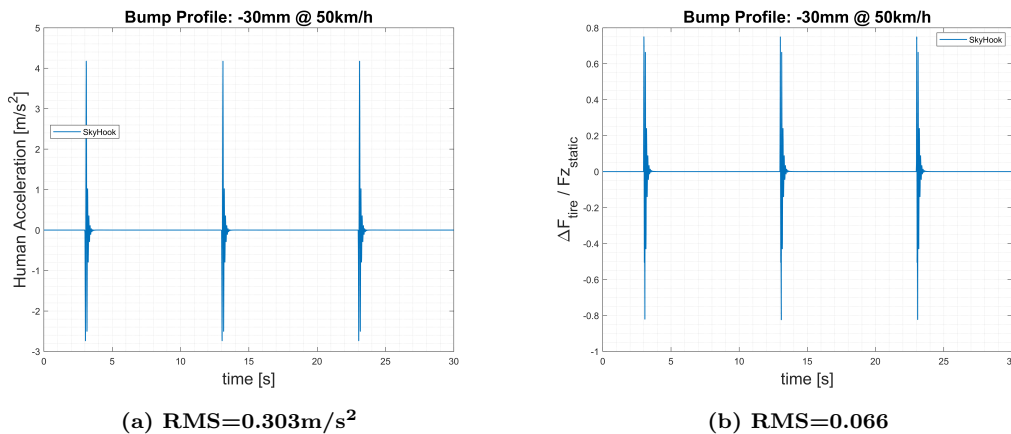


Figure 4.36: Electrical Power and RRSA Current with Sky-Hook Control with $c=1.2\text{kNs/m}$ and $c_s=10\text{kNs/m}$ for ISO-B at 70kph

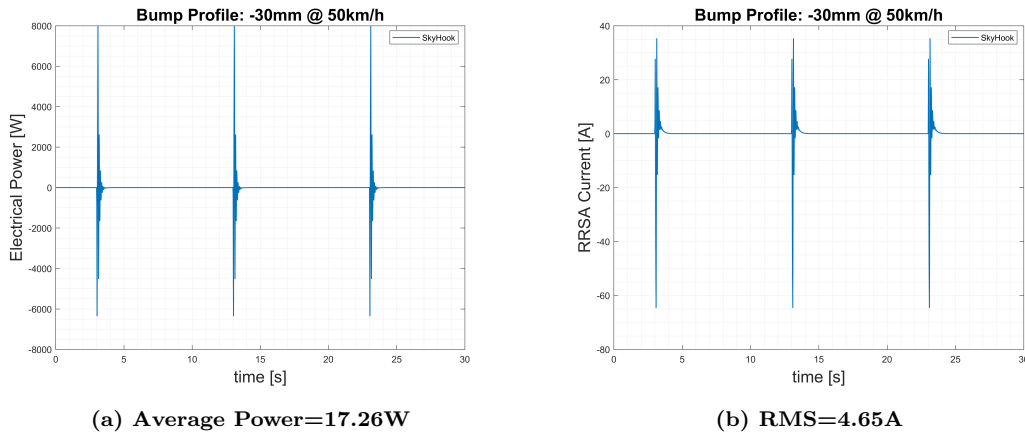


Figure 4.37: Electrical Power and RRSA Current with Sky-Hook Control with $c=1.2\text{kNs/m}$ and $c_s=10\text{kNs/m}$ for ISO-B at 70kph

RRSA working regions: 4 quadrants map

In this short section the study provides a quite useful overview of the actual working conditions of the Active Damper, considering the same SH Configuration introduced in 4.1.4. It has been developed for both ISO-road profiles, with a dedicated MATLABTM code, a *four quadrants map* with Damping Force (considering the vector acting on the *Sprung Mass*) and Relative Speed (defined as $\dot{x}_s - \dot{x}_{us}$) in order to visualize the working regions during the entire time of simulation (30s), as shown in Figure 4.38. In this representation, both RRSA operative conditions can be found: the *damping Mode* and the *active Mode*.

The *damping mode*, in which the dissipated power can be regenerated (in this ideal case, 100% of it is regenerated), is related to the quadrants where force and speed have the *same sign*, with reference to Figure 4.6, meaning that the considered power flow is *dissipated* (since force and speed, according to the adopted scheme, would have opposite verses). This type of behaviour is related to the 1st and 3rd quadrants (red regions).

The *active mode*, instead, is the condition in which damping force and speed have *opposite sign*, meaning that the actual considered vectors have the same verse, hence resulting in a power flow introduced in the suspension system, observable instead in the 2nd and 4th quadrants (green regions). As can be seen, during the whole duration of the simulation, for both road profiles, the suspension passes from one mode to the other

one, reflecting what has been represented in Figure 4.33 a) about the power flow of the system. A traditional passive damper, instead, can't provide the same performance, since the suspension relative speed and the damping force have *always* opposite verses, just providing dissipative power. Moreover, as expected, due to the more demanding characteristics of the road profile, the ISO-C results provide higher damping force in both operating conditions.

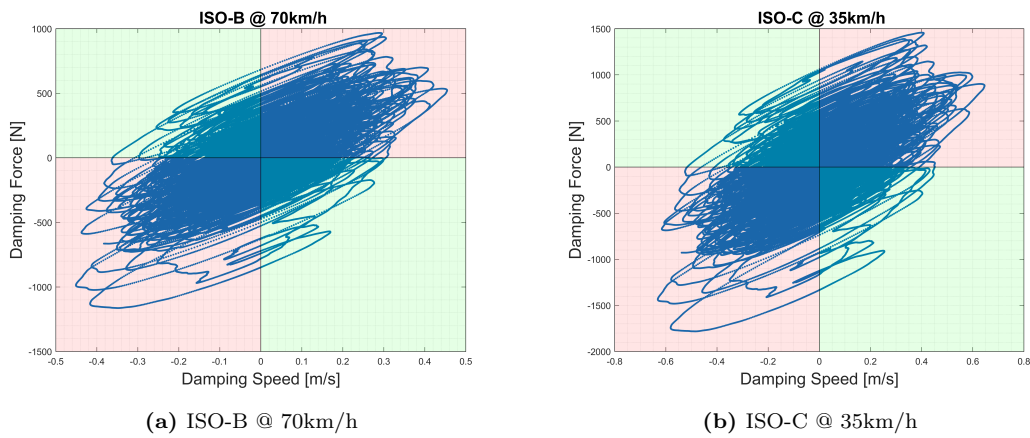


Figure 4.38: RRSA working region with $c_s=10$ kNs/m and $c=1.2$ kNs/m with ISO road profiles for 30s.

Experimental RRSA efficiency map

Methodology

Once analyzed the *Sky-Hook Control Strategy* with a simplified modelling process, the study focuses now on a more complete kind of numerical simulation. In this Section, in fact, the RRSA device is modelled in MATLAB/SimulinkTM taking into account its *Efficiency Map*, that has been experimentally obtained by Eng. Salvatore Circosta and represented in Figure 4.39.

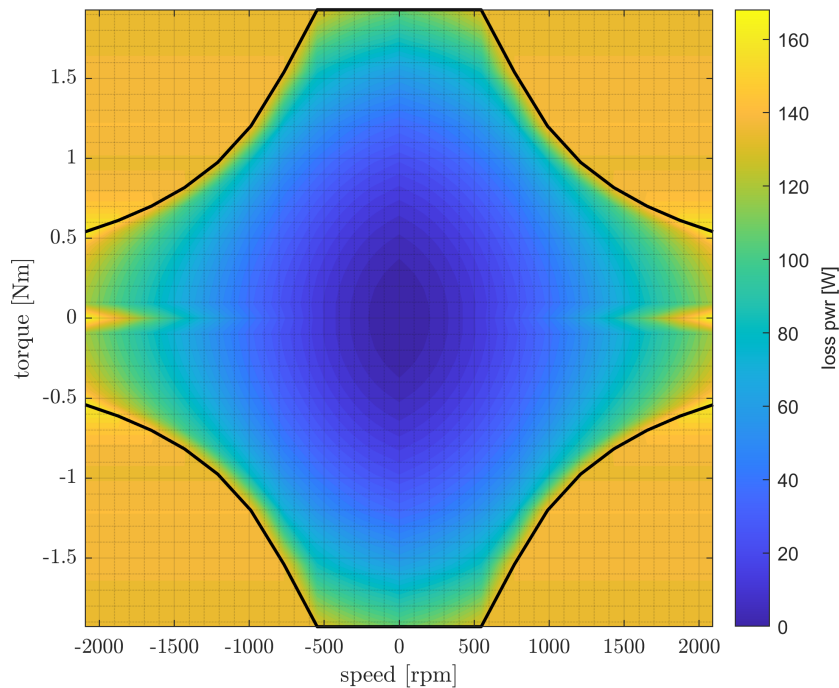


Figure 4.39: RRSA Efficiency Map with Loss Power

In this representation, as can be seen, according to the working point of the RRSA electric machine in terms of *Torque* and *rotational speed*, the power losses significantly change. In particular, the *maximum torque curve* (the black one in the graph), defined as *defluxing curve* of the electric machine, can be considered the limit above which the losses significantly increases.

In this model, moreover, the *planetary gearbox* efficiency, usually characterized by very high values for wide range of torques and speed, has been considered equal to 100%, a slight modelling idealization that keeps the analyses valid and reliable in any case.

In addition to the efficiency map, this Section also includes the *inertial* and *dissipative* RRSA contribution to be accounted in the final energetical balance. The resulting Damper SimulinkTM Model can be observed in Figure 4.40. As can be seen, similarly to what has been done in 4.1.2, two different Subsystems identify the actual RRSA device and its Control Unit, that can be properly set to provide Sky-Hook force or any other designed strategies. Moreover, together with the *Damper Block*, the entire model is completed by the block model referred to the *QC sprung mass* and *unsprung*

4.1. Sky-Hook Control

mass, and to the *suspension spring system*, grouped in Figure 4.41, receiving anyway the traditional road input signal.

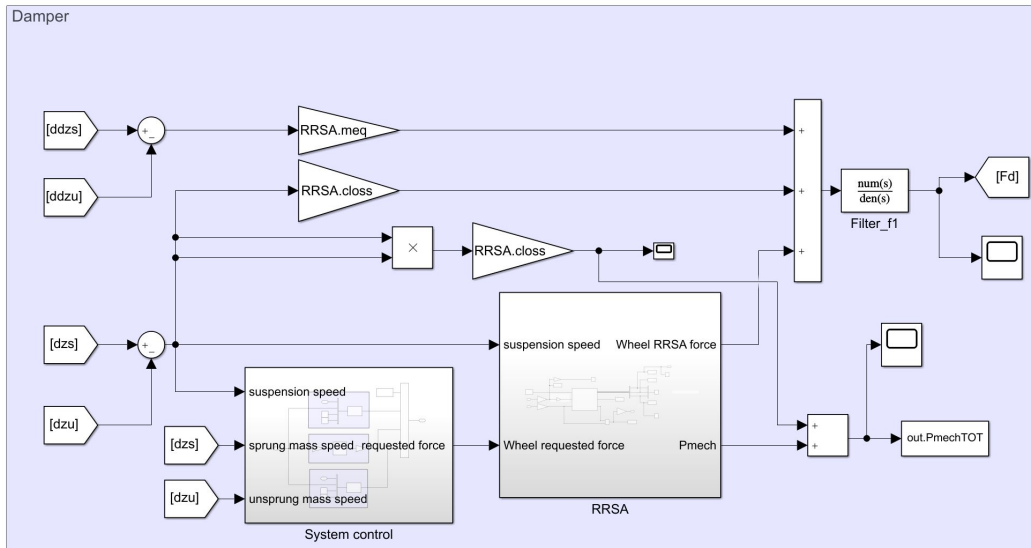


Figure 4.40: Damper SimulinkTM Model with RRSA Efficiency Map&Losses implemented

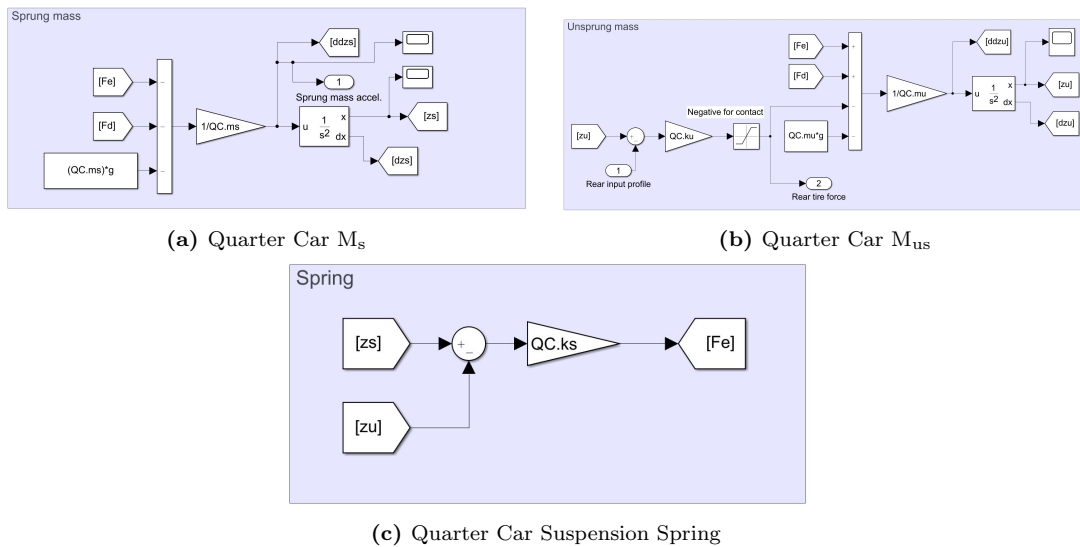


Figure 4.41: Main blocks SimulinkTM Model of QC with RRSA Efficiency Map&Losses implemented

In the *Damper Layout*, inside the *System Control* Block, shown in detail in Figure 4.42, is implemented the *Electric Motor Map*, receiving force and velocity signals and providing battery signals (current) and Power flows information.

The obtained *Mechanical Power*, strongly defined by the QC dynamics, is added to the

RRSA dissipative contribution in order to get the *overall Mechanical Power*, defined as *PmechTOT* signal in the Simulink™ layout of Figure 4.40. Together with the mechanical power flow, the *Electric Power* passing through the EM is monitored and acquired in the Mapped Motor model.

In order to provide significative analyses concerning the energetical balance of the active suspension, a specific sign convention is fixed:

- positive power \longrightarrow power flow *in* the electric machine
- negative power \longrightarrow power flow *out* of the electric machine

Some considerations are required for better evaluating the energetical results obtained in the following sections. A positive value of *mechanical power* represents a *dissipative power flow*, as it has been described in 4.1.4, meaning that the suspension is dissipating energy, hence acting as traditional passive damper. However, since the QC is equipped with the RRSA device, such mechanical power available at the entry of the RRSA electric machine is converted into *electric power*, directly transferred to the car battery pack. This second power flow, moreover, since coming out from the electric machine for reaching the car battery, assumes a *negative value*. This working condition, in which the *mechanical power* is *positive* and the *electric power* is negative, corresponds to what has been described as *damping/regenerative mode*.

However, differently from the analyses performed in 4.1.4 in which the *conversion efficiency* was assumed equal to 100%, this updated model takes into account the power losses depending on the working conditions of the electric machine. As a consequence, not all the mechanical power dissipated in the suspension system can be regenerated in the battery pack. In fact, the third important *energetical information* carried out by the *Mapped Motor* model is the *Power Loss*, strictly defined on the experimental motor map, which constitutes the real-time difference between the two power signals. The other operating condition, instead, is defined by having a negative value of *mechanical power*, which represents a *consumed power flow*, with the same definition of 4.1.4. In this case the electric power is retrieved from the battery pack (hence *entering in the RRSA electric machine*) and converted into *mechanical power* (which, in turns, goes out of the electric machine), clearly affected by the conversion efficiency,

for providing *active forces* to the QCM. This other working condition, in which the *mechanical power* is *negative* and the *electric power* is *positive*, corresponds to the previously described *active mode*, where *Sprung Mass Actuator Force* and its *Relative Velocity* have the same orientation.

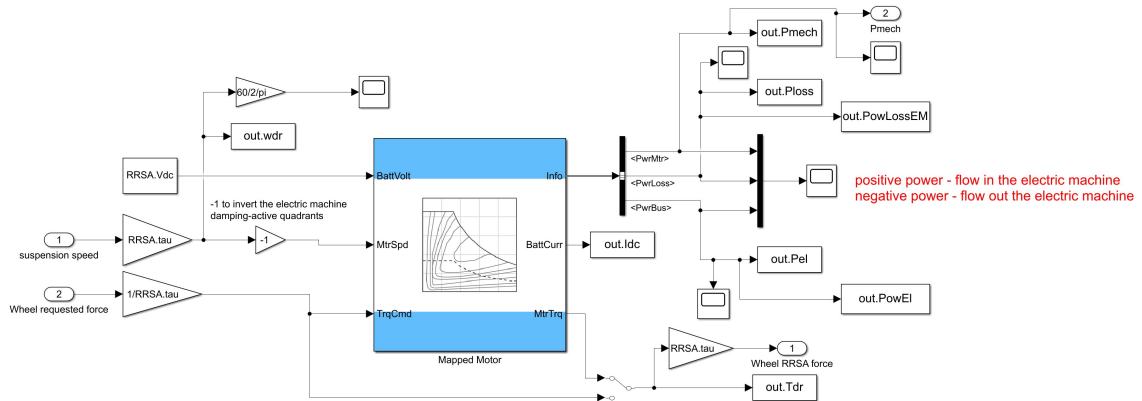


Figure 4.42: RRSA Simulink™ Model with RRSA Efficiency Map&Losses implemented

The analyses performed with this updated Simulink™ Model have been focused just on the *ISO-B @ 70km/h input road profile*, analyzed with both the *SH damping variable ranges* and the *Trade-Off SH configuration*, introduced in 4.1.4, for providing a complete and effective comparison between the two implemented models.

ISO-B @ 70km/h: SH Damping Range

Once described the implemented model, the first analysis is focused on the evaluation of the effects of the *RRSA Efficiency Map and losses* that have been introduced in the modelling process.

In particular, the same ranges of SH Damping values defined in 4.17 and 4.20 are considered, for providing a useful comparison with the previous cases. In the following Figure 4.43 the resulting lines at constant c and c_s for both considered Sky-Hook ranges are represented, following the same MATLAB™ code used in the former model. As can be seen, with respect to the plots obtained in 4.1.4, the effects of the implemented *RRSA Efficiency Map* and its *inertial and dissipative contribution* can be found in a different trend of the iso-lines, particularly visible at the lowest values of SH damping c . Due to these differences, the $\eta_{\text{roadholding}}$ range is quite reduced, reaching maximum

values around 0.17 (instead of 0.24), while the *ISO-2631 Human Perceived Comfort* is maintained substantially in the same range, despite the modified behaviour at low damping c .

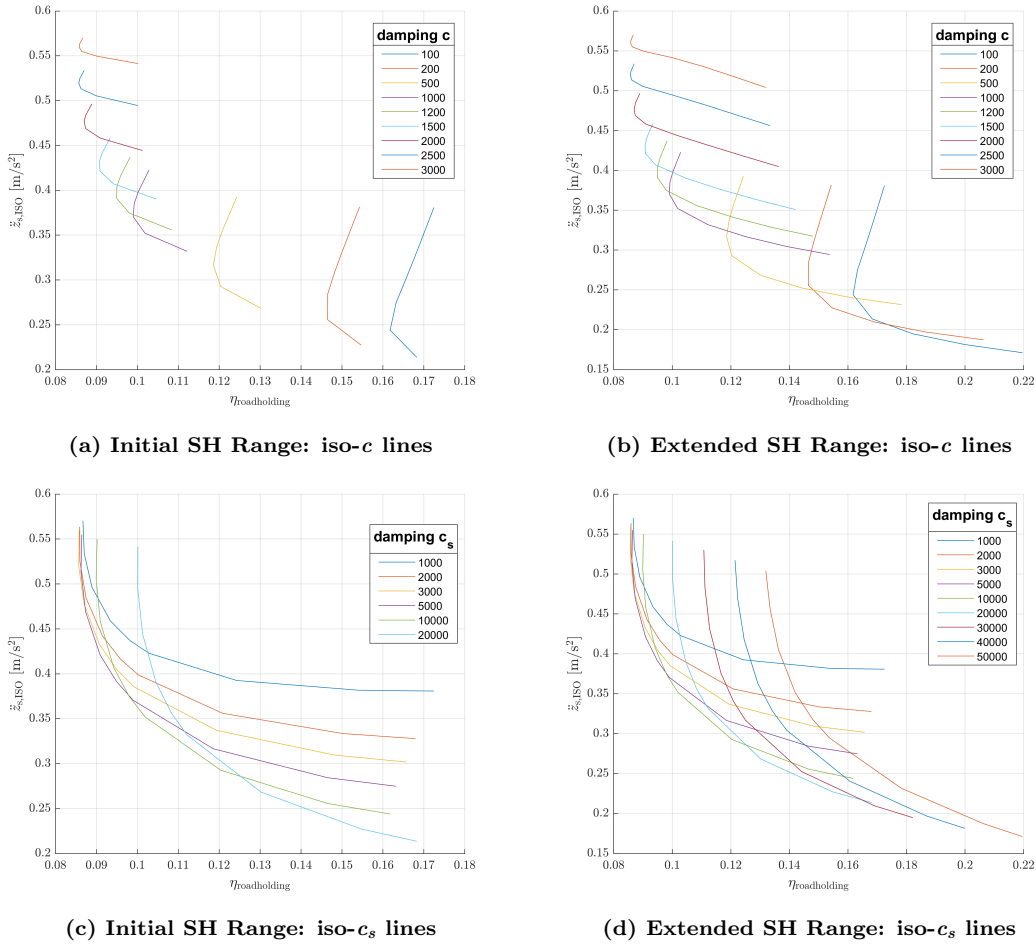
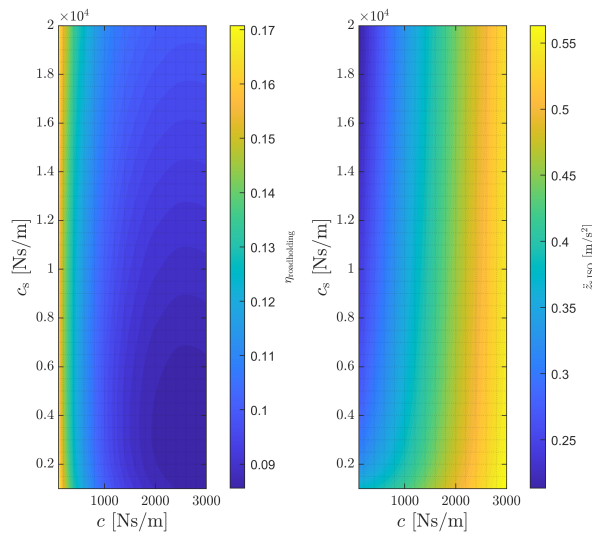
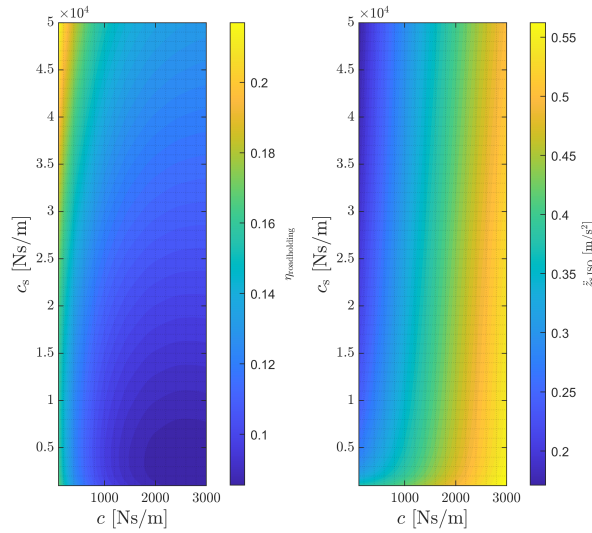


Figure 4.43: Lines at constant c and c_s with RRSA Efficiency Map&Losses implemented for ISO-B @ 70km/h

The same experienced effects can be observed in the *Comfort and Road-Holding Color Maps*, shown in Figure 4.44 for both SH ranges. By comparing them with the results obtained in Figure 4.1.4 and 4.1.4, in fact, it is quite evident the modified color trend of the $\eta_{roadholding}$, being characterized by a different variation range. Anyway, the resulting behaviour is still acceptable from the point of view of both *Performance Indicators*. In fact, the *RRSA dissipations and inertial effects*, combined with its *Energy Efficiency Map*, despite the modifications on the low damping behaviour, lead in any case to quite good results in *Comfort Level*, with maximum RMS acceleration values of around 0.55 m/s^2 , in line with the ones observed in 4.1.4.



(a) Initial SH Range



(b) Extended SH Range

Figure 4.44: Comfort and Road-Holding Coefficients Map with RRSA Efficiency Map&Losses implemented

Together with the analyses concerning the *Comfort* and *Road Holding Performances*, the *energy estimate* of the overall implemented system is carried out. In particular, taking into account what has been described in the previous sections, the focus of this study is towards the three fundamental power flows: the mechanical power, *dissipated* or *introduced* in the suspension system, the electric power, *stored* or *extracted* from the car battery, and the RRSA Electric-Machine Loss Power, which depends on the working condition of the implemented *electric motor model*. Starting with

the *initial SH range*, i.e 4.17, and always considering the *ISO-B @ 70km/h* input road profile, the resulting *Color Power Maps* have been computed and grouped in Figure 4.45. In particular, similarly to what has been performed in 4.1.4, it is here evaluated the *average value* of the considered power signal by using the described Equation 4.19. By observing the obtained representations, some important considerations can be carried out. The *Total Mechanical Power*, which includes the output of the EM but also the friction-dissipations of the RRSA itself, provides a *maximum average value* of more than 29.5W for very high damping c combined with low values of damping c_s , i.e the bottom-right corner of the map. Corresponding to these damping conditions, the *Electric Power* provides its *maximum average value* (in absolute terms), around 22W. Considering both signs, these results indicate that the dissipated mechanical power *entering* in the RRSA is, on average, 29.5W, while the electric power *going out* from the RRSA, towards the car battery, is on average 22W. The difference between them is due to the fact that not all the mechanical available power can be regenerated. The *EM Loss Power*, in fact, provides an average value of 4.5W of loss power, due to the working point of the electric machine. As a consequence, the remaining power in this damping configuration, i.e around 3W, is lost in the RRSA friction dissipations.

For what concerns, instead, the *minimum average power loss in the RRSA Electric Machine*, the color map indicates that the corresponding SH damping condition can be identified by the SH damping c between 500Ns/m and 1000Ns/m, combined with very low values of SH damping c_s . In this range, in fact, the *average mechanical power* is around 28W, the *average regenerated electric power* is more or less 20W and the *power loss in the EM* is less than 3W, the minimum value reached with ISO-B road profile with this SH range.

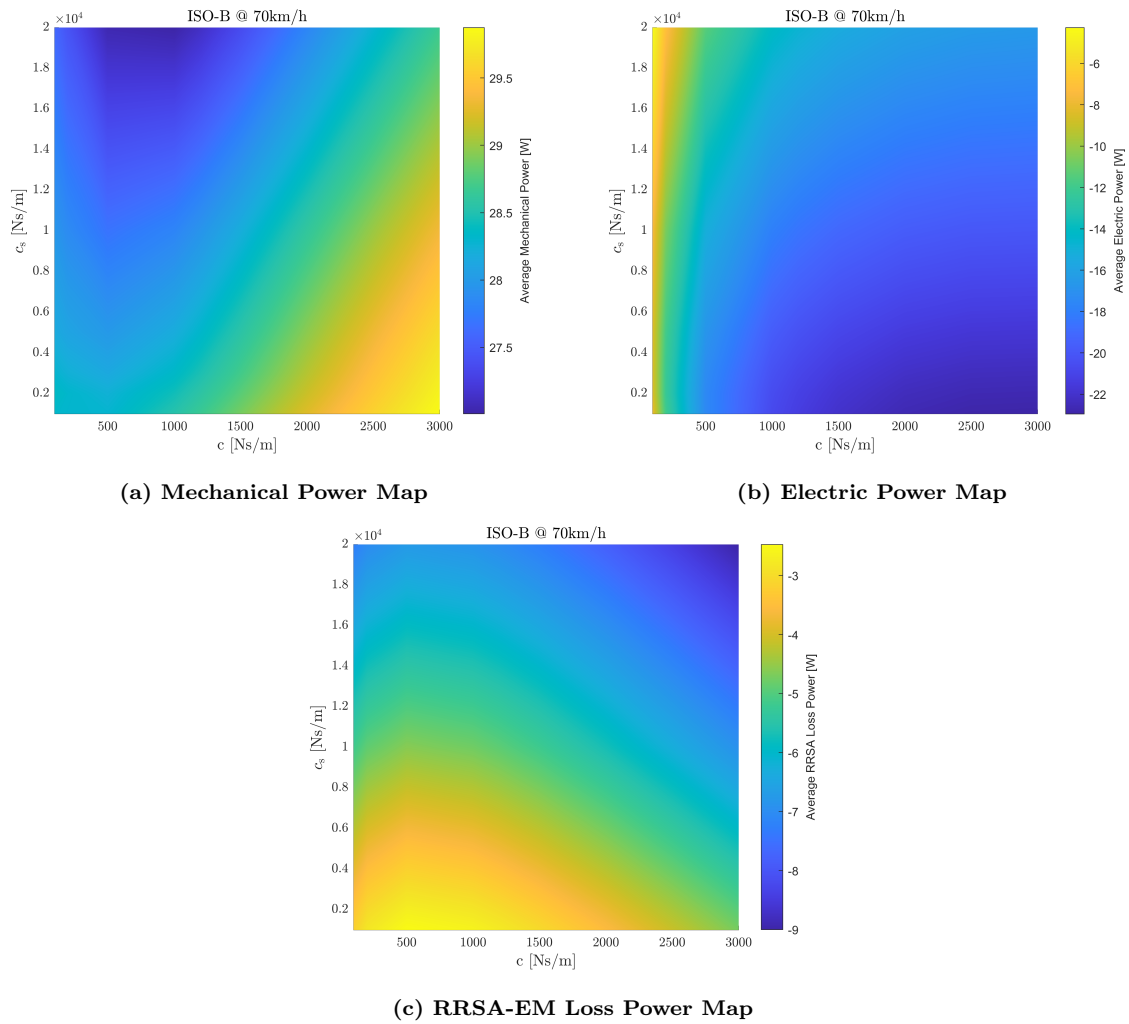


Figure 4.45: Power Color Maps with RRSA Efficiency Map&Losses implemented for ISO-B @ 70km/h

By increasing the SH damping range, using the one introduced in Equation 4.20, equivalent considerations can be performed. In particular, with the additional values of SH damping c_s , a different behaviour can be observed for very high SH damping c_s combined with low SH damping c . In this condition, in fact, despite the average mechanical power is positive (hence, dissipated by the suspension) with a value around 27W, the average electric power is positive, with a value slightly higher than 10W. This fact is explained by considering the obtained *Efficiency Conversion Map* represented in Figure 4.47.

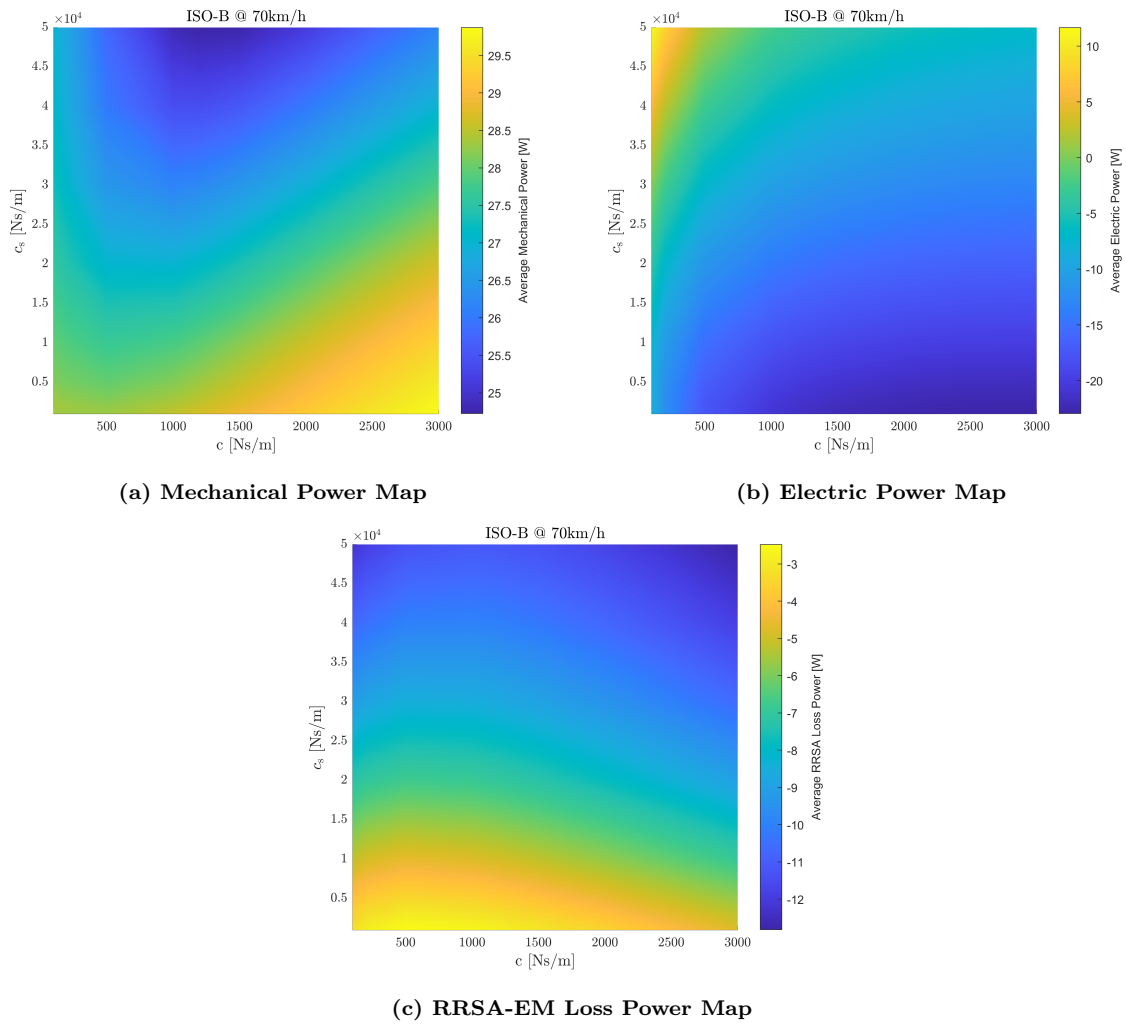


Figure 4.46: Power Color Maps with RRSA Efficiency Map&Losses implemented for ISO-B @ 70km/h, with SH extended range

In this color map, as a matter of fact, can be observed the energy conversion efficiency of the RRSA device according to the considered SH damping conditions. In particular, this efficiency has been computed taking into account, for both mechanical and electric power, the energy content of their *time signal*, performing the ratio between them. With the *trapz* MATLABTM command is computed the integral of the power signal, i.e the *energy content*:

$$Energy = trapz(time, Power) \quad (4.21)$$

in which, *time* is the SimulinkTM time vector of the simulation, while *Power* is the

Simulink™ signal vector of the considered power flow. By applying this code to both power flows, the following condition is imposed for the calculation of the *RRSA energy conversion efficiency*:

$$\begin{aligned}
 &\text{if } \longrightarrow \text{abs}(Energy_{elect}) < \text{abs}(Energy_{mech}) \\
 &\quad Efficiency = \frac{-(Energy_{elect})}{(Energy_{mech})} \\
 &\quad \text{else} \\
 &\quad Efficiency = \frac{-(Energy_{mech})}{(Energy_{elect})}
 \end{aligned} \tag{4.22}$$

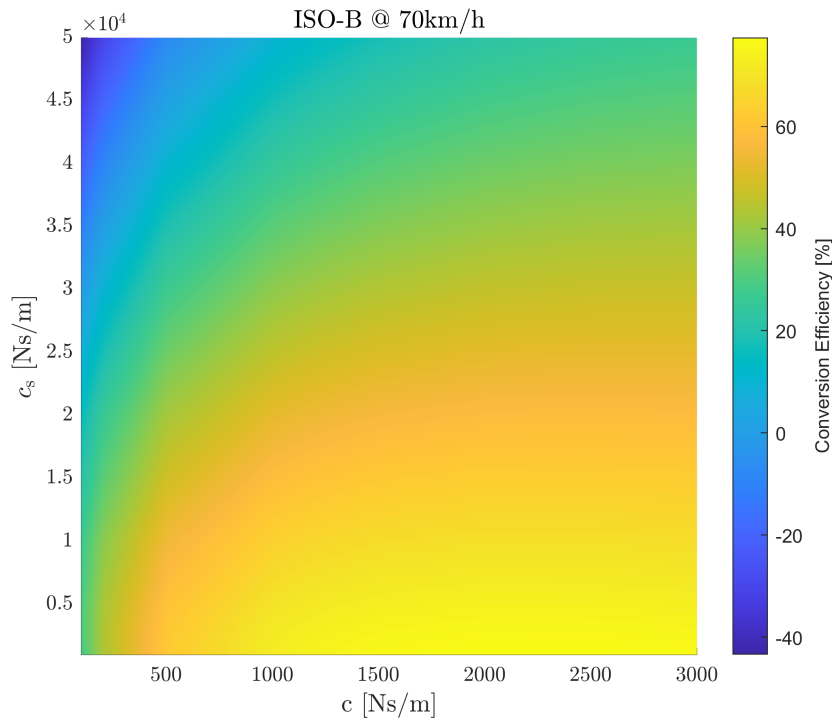


Figure 4.47: *RRSA Conversion Efficiency Map for ISO-B @ 70km/h*

In the resulting map, then, considering the described condition with positive average electric power, can be clearly noted a region with negative values of *conversion efficiency*. In particular, for very low values of c and very high values of c_s , the RRSA conversion efficiency is close to -40%. In this damping configuration, despite the dissipated mechanical power, the RRSA is operating, for a relatively long time, on some

low efficiency working points of its characteristic map and, as a consequence, it must provide electric energy (retrivied from the car battery) for compensating the power losses.

On the other hand, considering a Sky-Hook configuration with high values of damping c and very low values of damping c_s , always in Figure 4.46-4.47, the RRSA is mainly operating as a traditional damper (i.e dissipating energy) and regenerating maximum power and absorbing very reduced amount of power from the battery, minimizing its working operations in *active mode*.

ISO-B @ 70km/h: SH Trade-Off Configuration

Having described and analyzed the overall performance depending on the variable SH Damping range, the study proceeds considering the *optimal Sky-Hook trade-off* described in 4.1.4 for evaluating the updated results with the introduced RRSA features. Hence, the model shown in Figure 4.40 - 4.41 is simulated with Sky-Hook $c=1.2\text{kNs/m}$ and $c_s=10\text{kNs/m}$, maintaining the *ISO-B @ 70km/h* as main road input profile and running SimulinkTM simulations of 30s. These tested conditions do not correspond exactly to the best trade-off available with the new updated model, but they are anyway simulated in order to provide a useful comparison between the models.

The QCM time domain results are grouped together in the following Figure 4.48, showing the road input profile displacement z_{in} , the tire force F_{tire} and both *Performance Indicators*, i.e the *ISO₂₆₃₁ Human Comfort* and the $\eta_{roadholding}$.

The force exerted by the tire is correctly varying in the negative values range, since the saturation limit imposed to 0 for ensuring tire-ground contact, visible in the Simulink representation in Figure 4.41 b) (according to the sign convention, this force must not be positive, otherwise the tire is detached from the ground).

For what concerns the *Performance Indicators*, the resulting signals are combined with their corresponding RMS values, showing quite satisfying correspondences with the outputs described in 4.1.4. The *Human Acceleration ISO₂₆₃₁*, in fact, provides a RMS of 0.37m/s^2 , very close to the 0.356m/s^2 in Figure 4.32 a), obtained without RRSA Efficiency Map, losses and inertial contributions implemented, while the $\eta_{roadholding}$ is even closer, with a RMS of 0.1 compared to 0.098, visible in Figure 4.32 b).

Considering these outcomes, it is clear that the overall system with the imposed Sky-Hook damping conditions ($c=1.2\text{kNs/m}$ and $c_s=10\text{kNs/m}$) seems to be not significantly affected by the implemented modifications concerning the RRSA Efficiency, losses and inertial contributions, fact that can be easily appreciated by observing Figure 4.43 c). Taking into account the *green line* of 10kNs/m , in fact, it is evident that the corresponding *Performance Indicators* are close to the previous results, obtained in 4.1.4, for relatively high values of damping c , while the same can not be said for lower values, due to the different trend of the curves.

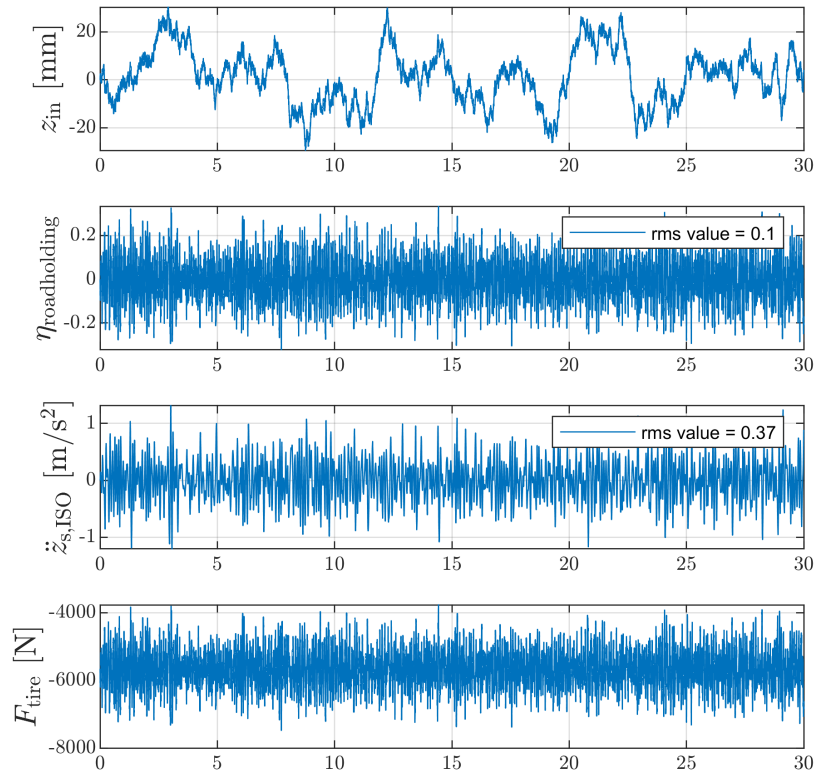
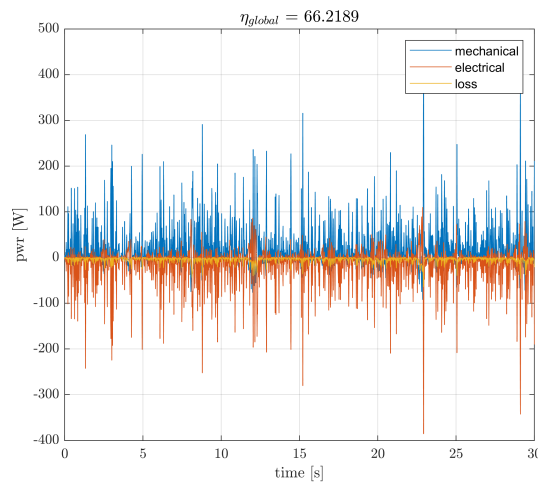


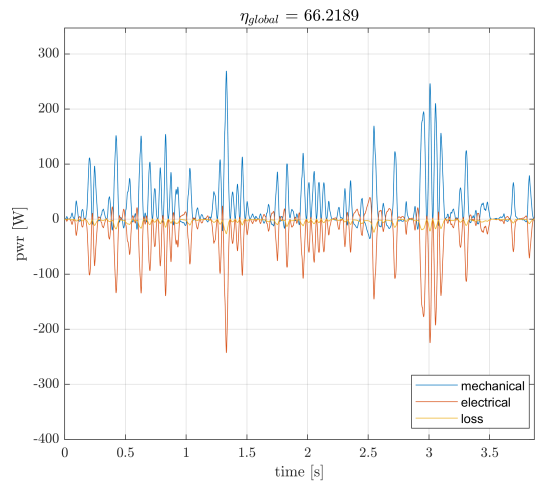
Figure 4.48: QCM Time domain results with SH $c=1.2\text{kNs/m}$, $c_s=10\text{kNs/m}$ and with RRSA Efficiency Map and losses taken into account, for ISO-B @ 70km/h

Moving to the *Power flows analysis*, in the following Figure 4.49 a) are represented all the time signals characterizing the modelled RRSA device with its Efficiency Motor Map, implemented in the QC system. Moreover, in Figure 4.49 b), is shown a detail of the Figure a), in order to focus the attention on the differences between the *available*

mechanical power and the electric power, certainly not perfectly symmetrical between each other due to the power lost in the Electric Machine. In this case, the resulting power conversion efficiency is slightly higher than 66%, a relatively high value obtained if it is considered the reduction imposed by the introduced RRSA losses. Moreover, this obtained conversion efficiency, among the highest achievable values, was just available by considering this SH Trade-Off condition in the Efficiency Map in Figure 4.47.



(a) Complete Simulation



(b) Simulation Detail

Figure 4.49: Power Signals with RRSA Efficiency Map&Losses with SH $c=1.2kNs/m$, $c_s=10kNs/m$ for ISO-B @ 70km/h

Finally, similarly to what has been done without implementing the Electric Motor Map, i.e represented in Figure 4.38, the ISO-B road profile analysis is concluded with the equivalent RRSA four quadrants map, shown in Figure 4.50 and in this case repre-

senting the torque and rotational speed of the input shaft to the RRSA. Passing from one quadrant, with same sign for both dimensions, to another one, with opposite signs, the device is showing its dual behaviour, i.e. the *active* and *regenerative* operational modes.

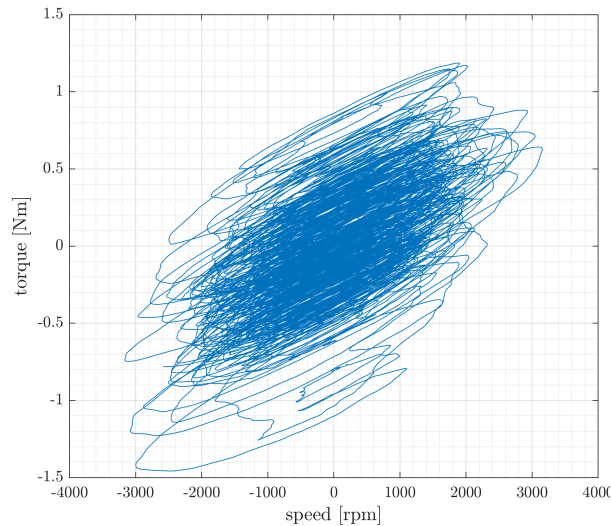


Figure 4.50: RRSA Torque-Speed Map with $SH\ c=1.2\text{kNs/m}$, $c_s=10\text{kNs/m}$ and RRSA Efficiency Map&Losses, for ISO-B @ 70km/h

4.2 Spring-Negation Control

4.2.1 Methodology

In order to control the RRSA device, once described the Sky-Hook Strategy, another type of Control is considered: the *Spring-Negation* (SN). This method, also defined as *Spring-Nulling*, consists in providing an overall control force constantly equal and opposite to the force generated by the *suspension spring*, hence *nulling* the spring action. This theory certainly implies that the overall resulting force acting on the *sprung mass* is zero (since the actuator force is equal to the sum of the suspension spring force and the QC static weight, and no extra damping is considered) while the *unsprung mass* is no more affected by an actual damping force (i.e. a force with 90° phase shift with respect to the displacement), hence causing very bad QC road-holding performance. In order to improve this condition, which is quite good if considered only Comfort

performance (since the Sprung Mass is basically fixed in space while running a certain road profile), the Control Strategy is modified including not only a dynamic contribution in phase with the displacement, i.e a *displacement/spring contribution*, but also a component with 90° of phase shift with respect to it, i.e a *damping contribution*. In Figure 4.51 can be observed the Subsystem Simulink™ Model representing the *SN Control Unit*. It receives both relative displacement and speed information from the QCM and, based on the computation shown in the detail Figure 4.52 and in Equation 4.23 (where k_{susp} is the *suspension spring stiffness* and c_{RRSA} is the *RRSA damping*), computes a control force to be transmitted to the QCM. Before directly introducing this signal in the QCM, as it has been described in 4.1.2, it passes through the *RRSA Subsystem* in order to compute the required electrical current to produce the control force. After that, the RRSA Current is re-converted in torque and again in force, as it has been described in Figure 4.10, to be finally introduced in the QCM.

$$F_{SN} = -(x_s - x_{us})k_{susp} - (m_s g) + (\dot{x}_s - \dot{x}_{us})c_{RRSA} \quad (4.23)$$

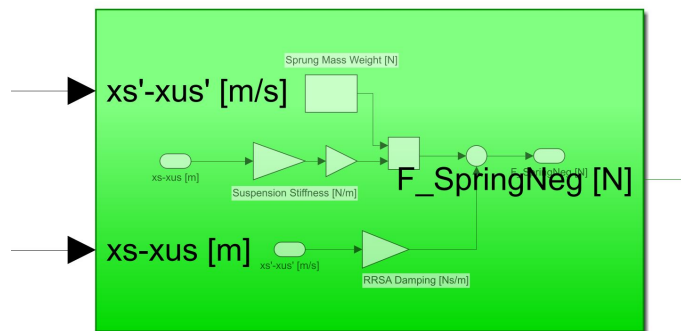


Figure 4.51: Simulink™ Block for Spring-Negation RRSA Control

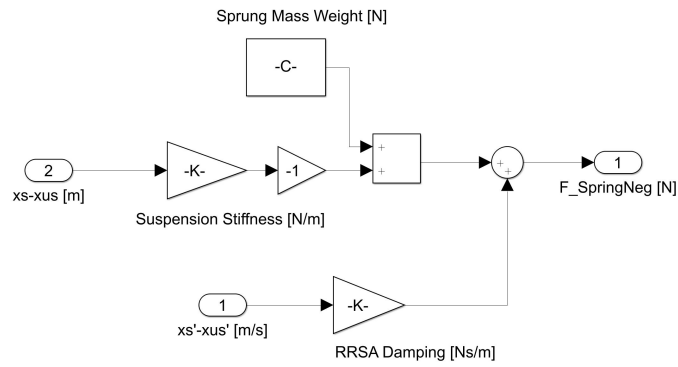


Figure 4.52: SimulinkTM Block for Spring-Negation RRSA Control: detail

4.2.2 QCM results

ISO-B @ 70km/h

The followed Modelling Process replicates what has been done, initially, for the Sky-Hook Theory, hence providing a *SimulinkTM* Model not affected by the *inertial and dissipative RRSA contribution* and neither by the *efficiency map* of the electric machine.

Considering the introduction of the damping contribution in the control unit, a certain damping range has been considered:

$$c_{SN}=[0 \ 50 \ 100 \ 200 \ 500 \ 1000 \ 1200 \ 1500 \ 2000 \ 2500 \ 3000 \ 5000] \text{ Ns/m} \quad (4.24)$$

and, with a MATLABTM code similar to that used for the SH, it has been computed the chart with Comfort and Road-Holding Coefficient for the *ISO-B road profile @ 70km/h*, as a function of the imposed RRSA damping. Moreover, as can be observed in Figure 4.53, the resulting yellow curve is placed on the same space of the *SH lines at constant c_s* . In order to properly compare these two control strategies, the considered damping range is reduced to just *three* values:

$$c_{SN}=[500 \ 1000 \ 2000] \text{ Ns/m} \quad (4.25)$$

for providing the same working conditions to both strategies, in terms of Comfort and Road-Holding.

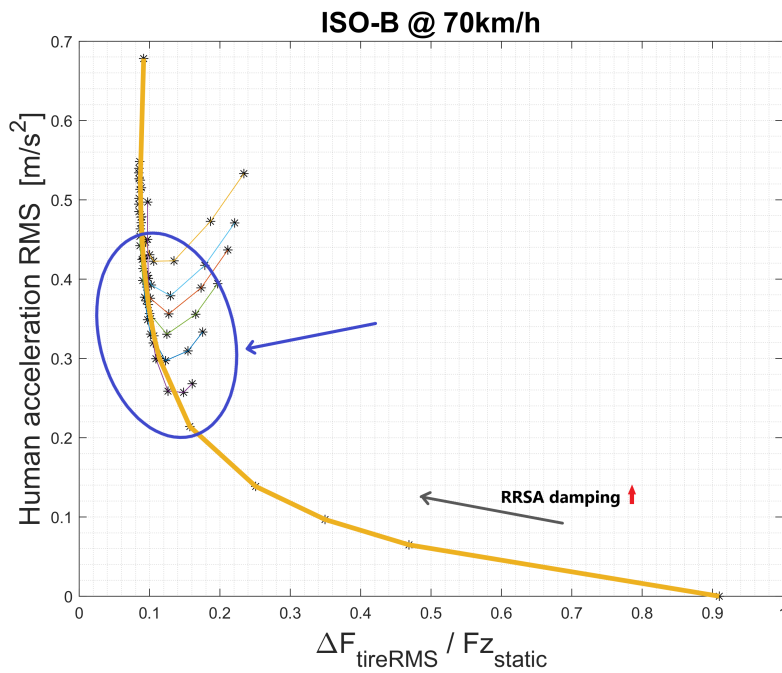


Figure 4.53: Comfort and Road-Holding Coefficient with comparison between Sky-Hook initial range (lines at constant c_s) and Spring-Negation variable damping, for ISO-B @ 70km/h.

The same four simulation outputs have been computed, as shown in Figure 4.54 and 4.55, by plotting on the same chart all of the damping configurations characterizing the SN Control. Most important, each simulation is analyzed with the corresponding significant measurement, i.e the RMS and Mean values, grouped in Table 4.2, for comparing the obtained results with both Control Strategies (with SH $c=1.2\text{kNs/m}$ and $c_s=10\text{kNs/m}$) and the ones achieved with Passive SA.

4.2. Spring-Negation Control

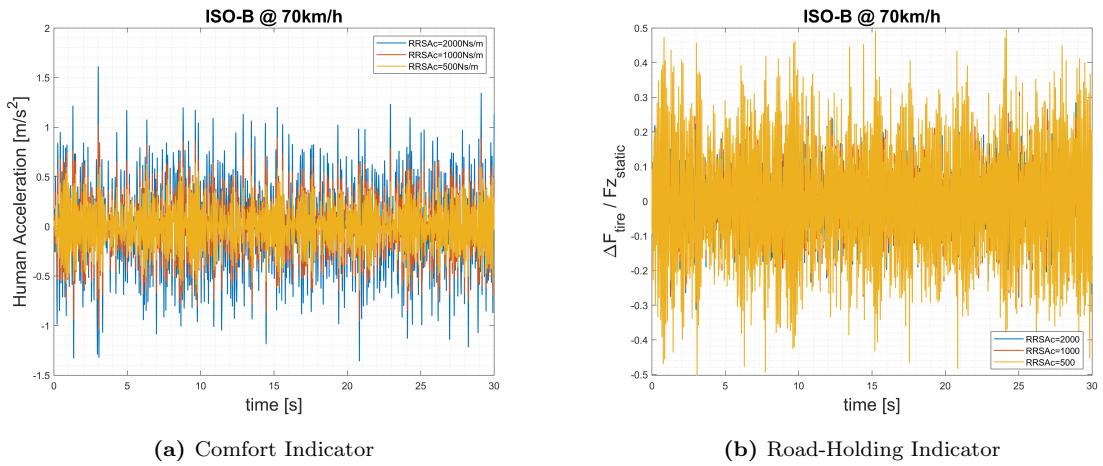


Figure 4.54: Comfort and Road-Holding Performance with Spring-Negation Control variable-damping, for ISO-B @ 70km/h

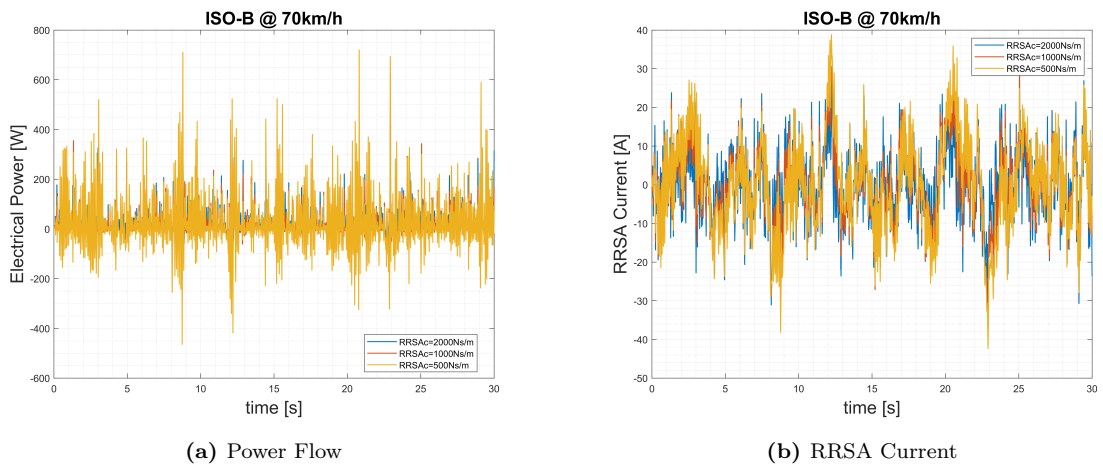


Figure 4.55: Power Flow and RRSA Current with Spring-Negation Control variable-damping, for ISO-B @ 70km/h

As can be seen in the time domain plots and, more evident, in Table 4.2, the QC Comfort Performance offered by the Spring-Negation can be considered slightly improved with respect to the considered Sky-Hook if the *damping coefficient is reduced*. This trend was certainly expected, since the reduction in *damping contribution* tends to lead the SN Control to its theoretical configuration, i.e. *without damping*, which ideally optimizes the perceived comfort.

However, as expected by the dynamic behaviour of the QCM, a reduction in damping, which improves the Comfort level, causes on the other hand a not negligible worsen-

ing in Road-Holding performance, which shows its best behaviour with the traditional Passive Shock-Absorber (which, in turns, does not provide good results in Comfort). For what concerns the *Average Power*, instead, all of the considered damping configurations give almost the same result, in the order of 28W for the simulation time of 30s taken into account.

The RRSA current, instead, has a slightly lower RMS value for SH Control, while the reduction in damping performed with SN causes a progressive increase in its RMS value. Anyway, the time domain results shown in Figure 4.55 b) do not provide significantly high local peaks, being always far from the maximum feasible limits, hence proving reasonable results for the RRSA Electric performance.

<i>ISO-B @ 70km/h</i>	Passive SA	SH	SN		
			<i>2kNs/m</i>	<i>1kNs/m</i>	<i>0.5kNs/m</i>
H_{RMS} [m/s ²]	0.54	0.356	0.43	0.3	0.215
η_{rh}	0.09	0.098	0.09	0.114	0.157
$\text{Power}_{\text{Mean}}$ [W]	29.6	28.21	28.6	27.52	27.62
$\text{Current}_{\text{RMS}}$ [A]	nd	8.14	9.4	9.9	11.8

Table 4.2: Performance Comparison for ***ISO-B @ 70km/h*** with Passive Shock-Absorber ($c=2.5\text{kNs/m}$), Sky-Hook ($c=1.2\text{kNs/m}$ and $c_s=10\text{kNs/m}$) and Spring-Negation with damping ($c=0.5, 1, 2\text{kNs/m}$)

Bump 30mm @ 50km/h

The same Modelling Process and numerical analyses, performed for the ISO-B @ 70km/h, have been followed for the *Bump Road Profile 30mm @ 50km/h*, using the same sequence of three bumps described in 4.1.4. With reference to the same adopted damping range variability, the obtained time domain results are grouped together in Figure 4.56. Moreover, Table 4.3 sums up the Performance comparison between the implemented and tested systems, i.e *Passive SA*, *Sky-Hook* and *Spring-Negation*.

4.2. Spring-Negation Control

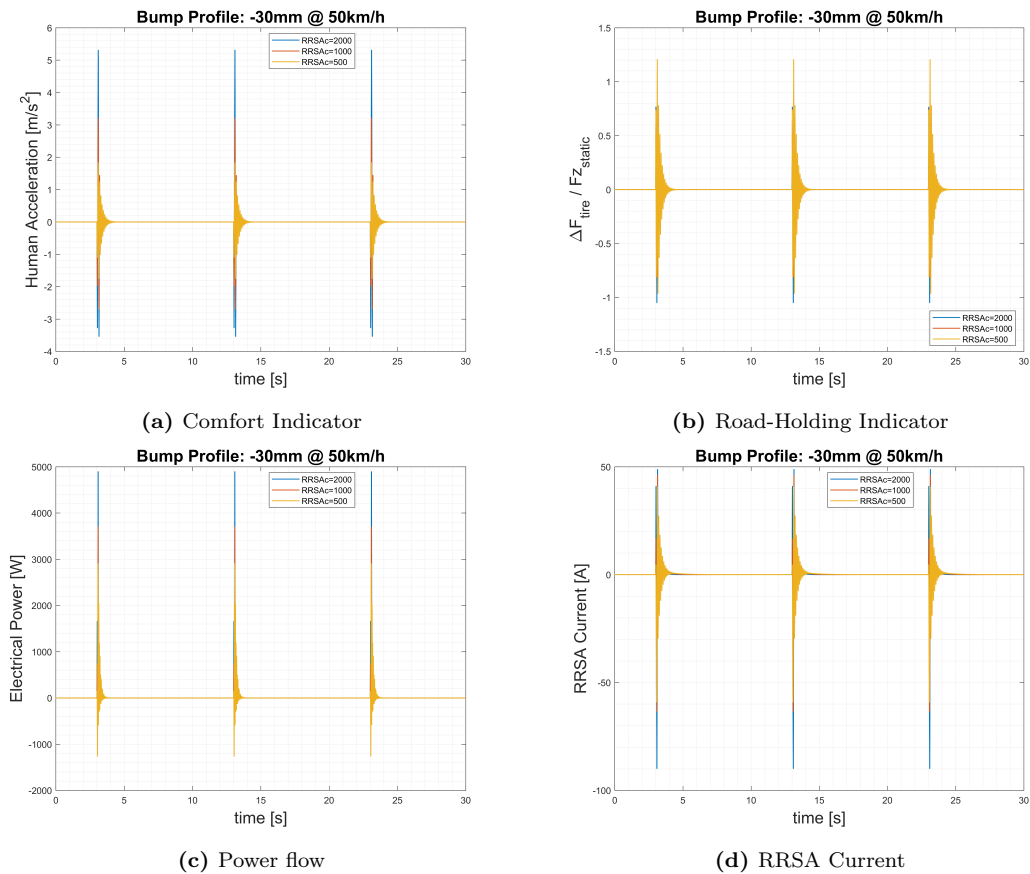


Figure 4.56: QCM Time Domain results with *Spring-Negation Control* variable-damping, for Bump Profile 30mm @ 50km/h

In overcoming the sequence of three bumps, the QC has provided similar trends, observable in Table 4.3, with respect to those observed in Table 4.2 for the ISO-B profile. The Passive SA, in fact, seems to be the best choice for what concerns the *Road-Holding Performance*, reaching the minimum result, while the worst in terms of *Perceived Comfort*. Moreover, the observed trend in the Spring-Negation Control is here still present, since the improvement in *Comfort level* by reducing the damping coefficient is strictly coupled with a significant worsening in road-holding capacity. The Average Power assumes similar values for all the considered configurations, being this time the Passive SA slightly below all the others. For what concerns the current flowing in the EM of the RRSA model, the Sky-Hook Control still provides the minimum RMS value, even though the observed trend for the Spring-Negation is inverted with respect to the ISO-B case, since it decreases by reducing damping coefficient.

Moreover, considering the time domain plots in Figure 4.56 d), the maximum peaks reached with the Spring-Negation Control Strategy are still within the possible range imposed by the characteristics of the RRSA electric machine, further demonstrating the feasibility of the simulated conditions.

Bump Sequence <i>30mm @ 50km/h</i>	Passive SA	SH	SN		
			<i>2kNs/m</i>	<i>1kNs/m</i>	<i>0.5kNs/m</i>
H_{RMS} [m/s ²]	0.43	0.303	0.386	0.262	0.176
η_{rh}	0.054	0.066	0.067	0.082	0.115
Power _{Mean} [W]	16.91	17.26	19.85	18.28	17.05
Current _{RMS} [A]	nd	4.65	6.12	5.06	4.92

Table 4.3: Performance Comparison for **Bump Sequence 30mm @ 70km/h** with Passive Shock-Absorber ($c=2.5kNs/m$), Sky-Hook ($c=1.2kNs/m$ and $c_s=10kNs/m$) and Spring-Negation with damping ($c=0.5, 1, 2kNs/m$)

In addition to the considered range of variation of the damping value for the Spring-Negation Control, the study has performed a further analysis on the *Sequence of Bump 30mm @ 50km/h* by using a reduced variation range, defined as *reduced variable-damping range* in 4.26, for investigating some other conditions closer to the *ideal SN Control*:

$$c_{SNred}=[50 \ 100 \ 300] \text{ Ns/m} \quad (4.26)$$

With these new values the study has obtained the same four outputs, visible in Figure 4.57, and the overall Performance Comparison with the other two configurations, that can be seen in Table 4.4.

As expected, the reduction in damping leads to a relevant improvement in perceived Comfort (with a minimum RMS value of 0.05m/s²), while causing a dramatic increase in η_{rh} coefficient, i.e a not sustainable worsening in QC road-holding performance (which, in turns, reaches 0.38, corresponding to the condition that offers best Comfort level).

The average power, instead, is slightly below the Sky-Hook and Passive SA references,

4.2. Spring-Negation Control

while the current flowing in the RRSA Electric Machine provides RMS values higher than the ones obtained through SH, and with different trend with respect to the case observed in Table 4.3. In addition, the RRSA Time signal, shown in Figure 4.57 d), even with the more demanding conditions characterizing the lower damping (50Ns/m), provide maximum peaks still inside the EM working range.

Taking into account both Performance Indicators, moreover, it can be observed that the oscillations, due to the decreased damping contribution, tend to be particularly extended, even arriving to the next *bump profile*. This condition provides negligible effects for what concerns the human comfort, since the reached peaks are quite low and the RMS calculation provides very small values, but particularly complex outcomes for η_{th} signal. The reached peaks are higher than 1.5 and, most relevant, each bump causes very prolonged oscillations, probably not sustainable from the point of the view of the *QC tire-road contact performance*.

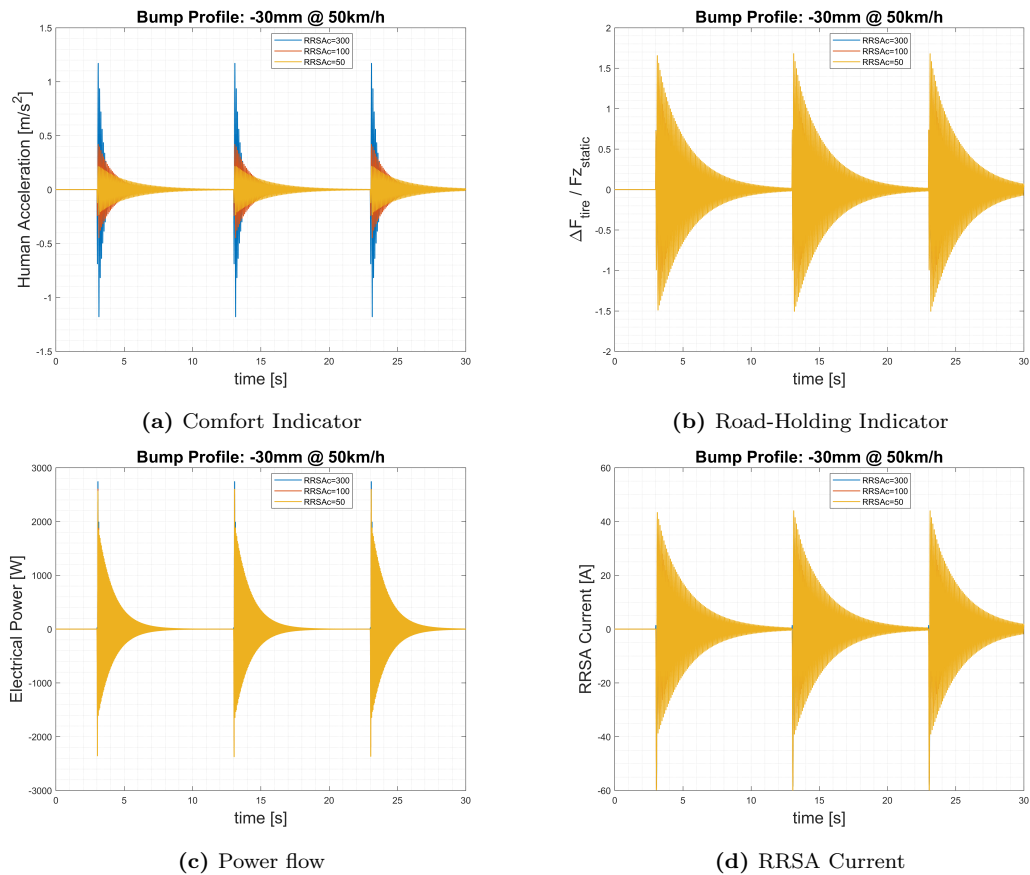


Figure 4.57: QCM Time Domain results with **Spring-Negation Control** reduced variable-damping, for Bump Profile 30mm @ 50km/h

<i>Bump Sequence</i> <i>30mm @ 50km/h</i>	Passive SA	SH	SN		
			<i>0.3kNs/m</i>	<i>0.1kNs/m</i>	<i>0.05kNs/m</i>
H_{RMS} [m/s ²]	0.43	0.303	0.133	0.07	0.05
η_{rh}	0.054	0.066	0.15	0.265	0.38
Power _{Mean} [W]	16.91	17.26	16.44	15.77	15.79
Current _{RMS} [A]	nd	4.65	5.33	7.66	10.4

Table 4.4: Performance Comparison for **Bump Sequence 30mm @ 70km/h** with Passive Shock-Absorber ($c=2.5\text{kNs/m}$), Sky-Hook ($c=1.2\text{kNs/m}$ and $c_s=10\text{kNs/m}$) and Spring-Negation with damping ($c=300, 100, 50\text{Ns/m}$)

4.3 Final considerations

The analyses carried out in this Chapter have provided significant results in terms of *Control Strategies* to be implemented with the RRSA device. The modelling process in MATLAB/SimulinkTM, focused on the Quarter-Car of the Alfa RomeoTM Stelvio, has been first developed around the *Sky-Hook* Control Theory according to the known benefits described in literature.

The first considered model has been produced without reference, within the dynamics of the overall system, neither to the actual *Efficiency Map* characterizing the RRSA device, nor to its dissipative and inertial contributions. The resulting outputs obtained with a defined *trade-off Sky-Hook Configuration*, imposed as ideally achievable, have shown relevant improvements in terms of *ISO₂₆₃₁ Human Comfort* with respect to the performance offered by a traditional passive damper with constant damping coefficient (2.5kNs/m), considering an ISO-B road profile at 70km/h and a sequence of three bumps of -30mm at 50km/h.

The Sky-Hook Control Strategy, then, has been included in a more accurate modelling process, taking into account the experimentally-obtained *Energy Conversion Efficiency* of the RRSA electric machine and its dissipative and inertial contributions. The equivalent analyses have been done even for this new SimulinkTM model and, most important, the main differences have been highlighted. In particular, the introduction of the *EM Efficiency Map*, depending on the RRSA working conditions, combined with the new

considered dynamic contributions, has led to low modifications in terms of simulated *Comfort* and *Road-Holding* performance, but to significant differences in the *Energy Balance* of the whole system.

The regenerative capacity of the modelled RRSA, in fact, strongly depends on its actual operating conditions. The fundamental *Conversion Efficiency Map* shown in Figure 4.47, obtained with an extended SH damping range, has proved that the energy conversion efficiency of this active device can be particularly high when operating in efficient region of its characteristic map (with conversion efficiency even $>70\%$), but also significantly *negative* when the RRSA is operating in *low efficient conditions* of its map. In these last conditions, in fact, the actuator requires electric energy from the car battery in order to compensate the produced power loss, while in the former condition a relevant amount of dissipated mechanical energy is regenerated and stored in the battery itself.

The energy analysis performed with the second implemented model has overall provided positive results with satisfactory achievable conversion efficiencies in specific operating and damping conditions.

Finally, the *Spring Negation Control Strategy* has been described and modelled in the same SimulinkTM space, with reference to the simplified RRSA model, for producing a useful comparison between control schemes. Overall considered, the performance offered by the SN Control can be judged as acceptable and possibly improved with respect to those achieved by the traditional passive damper (with constant $c=2500\text{Ns/m}$), for both *ISO-B* and *Bump Sequence* profile. However, the overall performances obtained with the Sky-Hook Control can be indicated as the most suitable ones, providing satisfactory behaviour in Comfort level and, especially, in Road-Holding capacity for both types of input road profile.

Experimental Tests

5.1 HIL Testing: Model-Following Compensation

5.1.1 Methodology

In this final chapter of the Thesis Work is described the experimental implementation of the designed *Compensation Approach* in the physical Testbench described in Chapter 2.

In particular, the *Model Following Method* analyzed in 3.5 has been tested in the physical Hardware-In-the-Loop installation for evaluating the resulting *compensating performance*, taking into account the satisfactory numerical results and the limits obtained in simulation.

Considering the modelling features of this method, deeply described in 3.5.2, the HIL Testing procedure has been developed with a variable *RRSA damping value* imposed to the active device by the MPPM Unit, properly set in the User-interface. In particular, two RRSA damping values in the Testbench have been considered for assessing the desired performance:

- 0Ns/m
- 500Ns/m

Both of them have been tested in *HIL Configuration* with a QCM, the same described

and used in this Thesis Work with the additional *tire damping* coefficient that has been set to 10Ns/m, for providing a minimum damping to the QCM itself. Moreover, two possible road input profiles have been analyzed, for carrying out useful reference outcomes:

- ISO-B @ 70km/h
- ISO-C @ 35km/h

For what concerns the *Compensation Scheme*, the $TF_{following}$ has been modelled by taking into account the RRSA damping = 0Ns/m, in order to evaluate the results with a fixed Compensator not affected by the damping value itself. Moreover, the *Desired Testbench Behaviour*, expressed in the Control Scheme by the transfer function TF_{des} , has been implemented by means of the described *Bessel Filter*, with a filter order $n_{des}=4$ and with a cut-off frequency $f_{cut}=500\text{Hz}$.

5.1.2 Results

Testbench with RRSA damping=0Ns/m

ISO-B @ 70km/h

The first simulated condition is characterized by the physical Testbench without RRSA damping and with a ISO-B road profile with a vehicle speed of 70km/h. By means of the User-Interface, the current imposed by the MPPM Unit, which provides the desired *damping coefficient* to the RRSA device, is null, hence producing 0Ns/m in the testbench.

This damping value, moreover, coincides with the one characterizing the Compensator Scheme, in particular defined in the $TF_{following}$. The numerical results coming from this correspondence have been evaluated in 3.5.2 in the frequency domain, showing perfectly ideal overlapping behaviour between the *desired* and the *actual* bench response; the remaining step is to compare them with the acquired experimental signals.

In Figure 5.1 are grouped together the attained results concerning the *Testbench measured signals*, which can be summed up as:

- Hydraulic Piston stroke

- Hydraulic Piston speed
- Load Cell force
- Hydraulic Pressure (left and right side of the Gerotor Pump)
- Tracking of the RRSA rotation
- Kollmorgen current

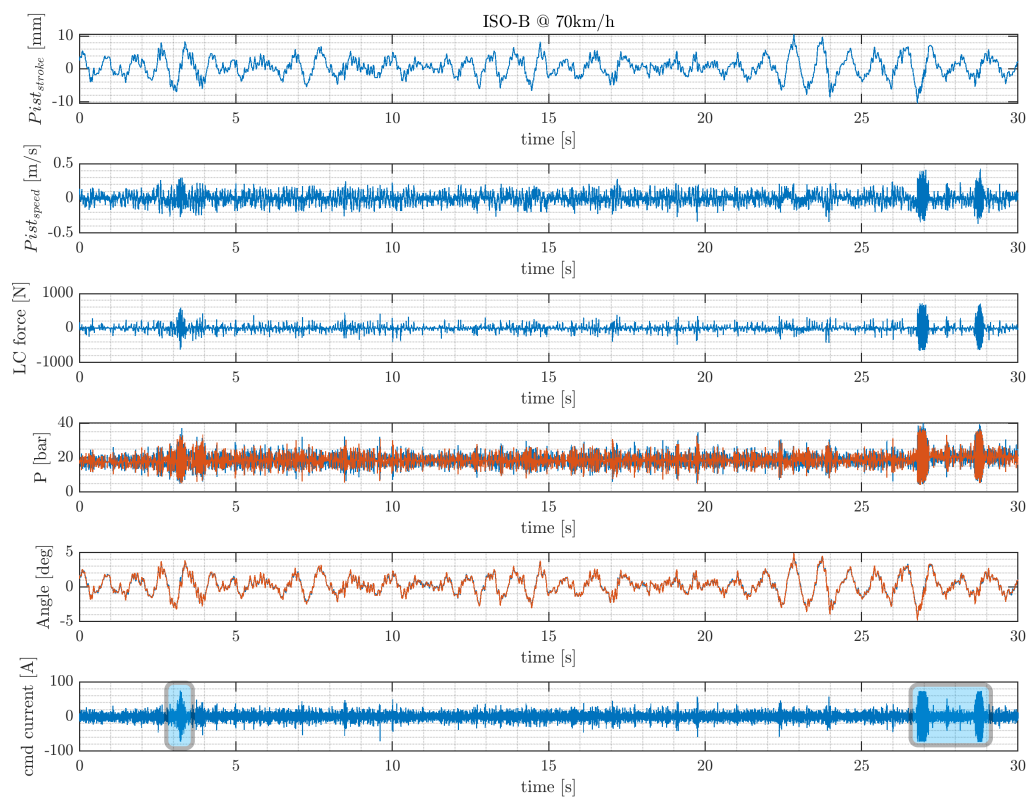


Figure 5.1: HIL Testing: TestBench measured signals, for ISO-B @ 70km/h without RRSA damping.

Among them, in particular, the *Kollmorgen current* represents the easiest way to evaluate, as a first attempt, the stability of the overall HIL System. The Saturation limit of the Kollmorgen unit has been fixed to 70A in the User-Interface, and whenever the measured current reaches this limit, it means that the HIL System is characterized by an *unstable behaviour*. As described in Chapter 3, in fact, the Kollmorgen Current

strictly depends on the error introduced in the PID Controller and, when it is significantly high, the saturated current is a key indicator of the experienced instability.

The acquired Kollmorgen Current signal results in an *overall stable behaviour* for the entire duration of the test (around 30s), with just three isolated instability points, highlighted in the blue squares in Figure 5.1. These unstable working conditions can be observed, simultaneously, in all the other measured signals, particularly visible in the increased *Hydraulic pressure* and *Load Cell force* signals.

Despite these local instabilities experienced by the Testbench in the HIL Configuration, the obtained results are certainly *remarkable*. Without a Compensation Method applied to the Bench, in fact, none of these results could have been acquired, since the Testbench unstable behaviour (related to its *limited bandwidth*) was completely predominant, without allowing any kind of data acquisition or HIL Testing processes. For what concerns, instead, the obtained *tracking performance*, the reference and the measured rotations appear to be overall superimposed, providing a further satisfactory result with the tested *Model Following Compensation method*. Moreover, in Figure 5.2 has been included a detail of the measured tracking in order to better appreciate the achieved results.

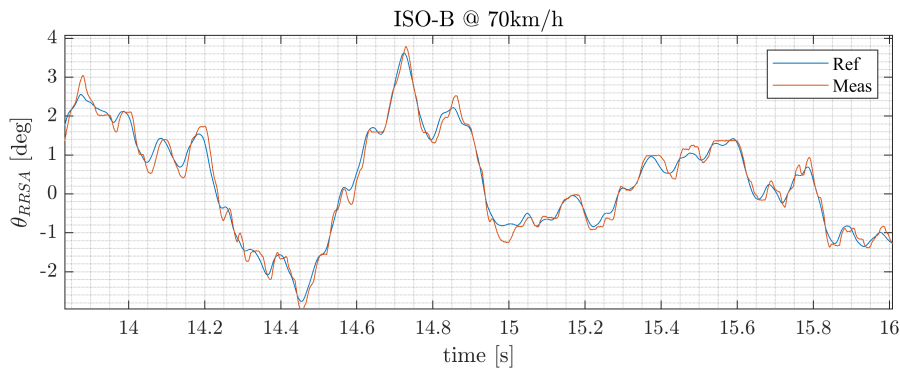


Figure 5.2: HIL Testing: RRSA Angle Tracking detail, for ISO-B @ 70km/h without RRSA damping.

From the point of view of the amplitude of the rotation, the two signals show very close results, suggesting that the applied Compensation Method is correctly operating. However, as it can be observed, the measured RRSA rotation is affected by a slight *phase shift* with respect to the reference one. This fact indicates that the physical Testbench may be characterized by some non-linearities that have not been consid-

ered during its experimental characterization and, consequently, not included in the numerical model and in the *Compensation Scheme*, i.e without the possibility of being tested. To improve this condition, additional analyses and Compensation Methods can be investigated both in simulation and in physical HIL Testing, in future developments to this Thesis Work.

Together with the measured signals characterizing the Testbench, during the HIL Testing process the Quarter Car Model signals have also been acquired and grouped in Figure 5.3. Not only the sprung and unsprung masses *displacement* and *speed*, but also the input road profile *ISO-B* and the *RRSA force* have been measured. Even in this case, corresponding to the local experienced instabilities, the signals are variably affected by them, particularly evident in the *RRSA force signal*.

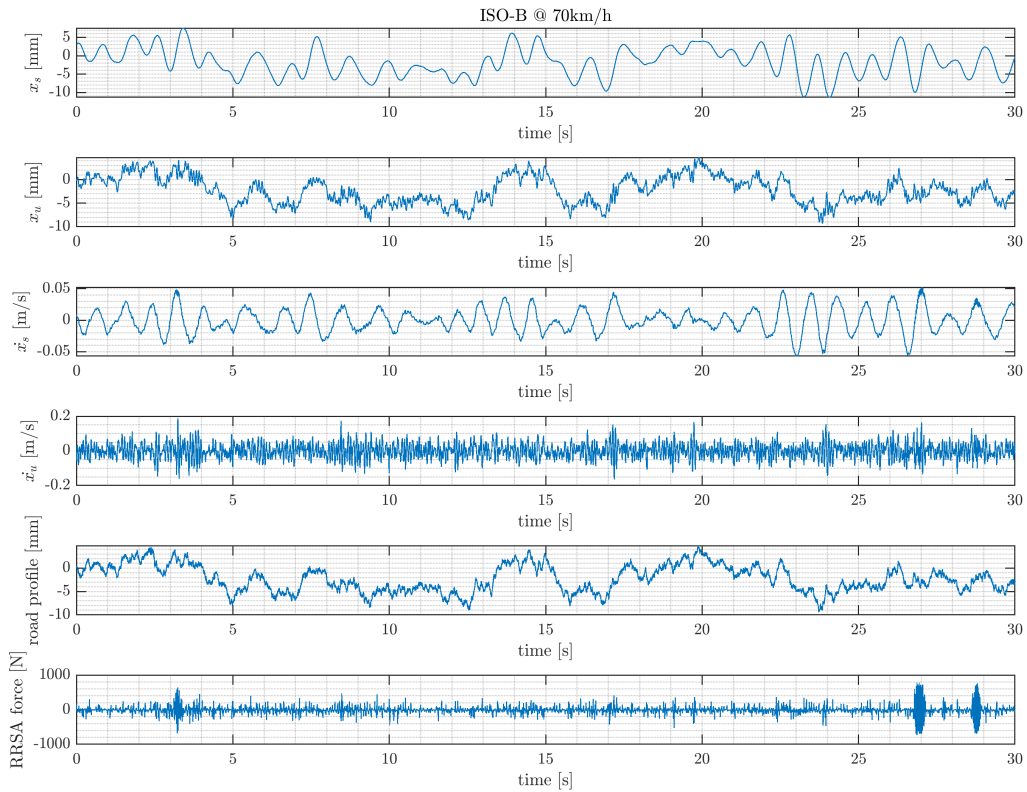


Figure 5.3: HIL Testing: Quarter Car Model results for ISO-B @ 70km/h without RRSA damping.

In Figure 5.4, instead, the *Performance Indicators* of *ISO₂₆₃₁ Human Comfort* and η_{rh} have been measured, considering their definitions introduced in 4.1.4, with the

additional corresponding RMS value placed in the chart legend. The road-holding coefficient has a rms value of 0.13, quite high if compared to the results obtained in 4.1.4, while the Human acceleration has an overall rms of 0.01g, i.e. 0.1m/s^2 . Both results must be valued and weighed considering that, in this test, the damping coefficient characterizing the Bench and, consequently, the QCM, is equal to 0Ns/m , hence resulting in a QC with just 10Ns/m of damping contribution provided by the *tire*.

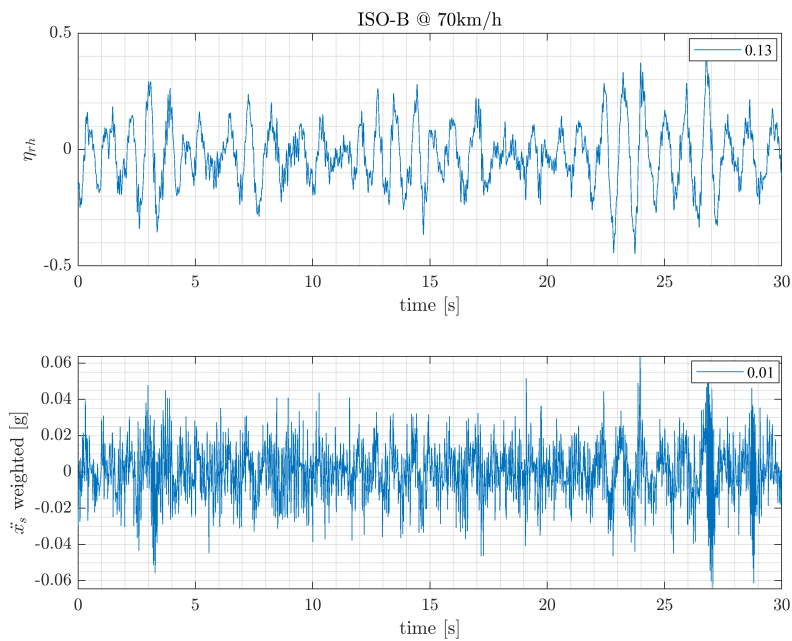


Figure 5.4: *HIL Testing: Human Acceleration ISO₂₆₃₁ (Comfort coefficient) and Road-Holding Coefficient, for ISO-B @ 70km/h without RRSA damping.*

Finally, the power flows and the electric current flowing in the Battery (in the *Battery Management System*) have been measured and acquired in Figure 5.5. In particular, the *mechanical power*, resulting from the QCM operating conditions, and the *electric power*, extracted or stored in the battery, have been plotted and compared with the same sign convention described in 4.1.4. The mechanical power, in fact, results to be a signal with mainly positive values, hence providing the *damping mode* of the active suspension, i.e. dissipating energy, while the electric power is mainly negative, providing energy to the battery pack to be stored, i.e. *regenerated*. Moreover, considering the RRSA *Efficiency Map* depending on its operating conditions, previously described in 4.1.4 for the numerical model, the overall electric power signal is characterized by

a visibly lower average value, meaning that the *regenerated power* is lower than the available *dissipated mechanical power* due to all the existing losses.

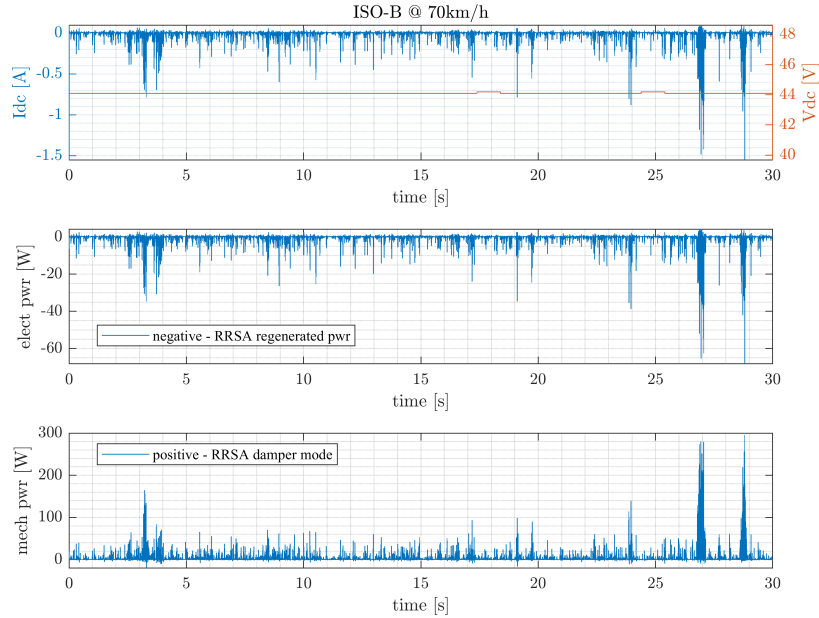


Figure 5.5: HIL Testing: Mechanical Power, Electric Power and Electric Current signals, for ISO-B @ 70km/h without RRSA damping.

ISO-C @ 35km/h

In this subsection are grouped the same acquired signals of the previous one but obtained with the *ISO-C @ 35km/h* road profile. In Figure 5.6, first of all, can be observed the resulting signals characterizing the Testbed. As can be seen, the Kollmorgen current appears to be much more saturated (at 70A) along the entire simulation, with a significative saturation within the first 5 seconds of HIL Testing. This fact, as previously described, represents the achieved instability of the overall Testbench, perfectly visible in the corresponding increased Hydraulic Pressure, Load Cell Force and Piston speed signals. Considering that in this HIL Configuration the damping settings have not been modified with respect to the previous results (neither for the Compensator nor for the Bench), i.e the numerical compensating correlation is still valid, it is likely that one of causes of the resulting increased instabilities is due to the fact that the Bench, at the time of ISO-C profile Testing, had been used for a prolonged time causing the increase in hydraulic oil temperature, which in turns has led to a visible

increase in hydraulic pressure (with average value around 40bar instead of 20/25bar) and modifications in the behaviour of the overall system.

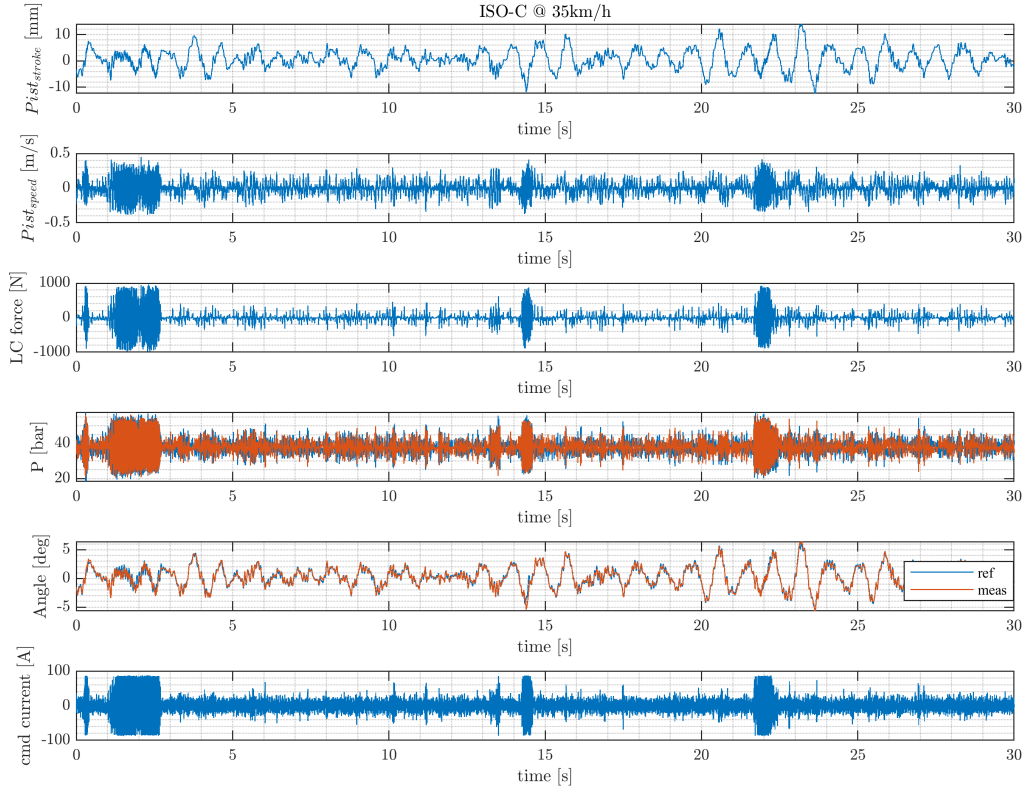


Figure 5.6: HIL Testing: TestBench measured signals, for ISO-C @ 35km/h without RRSA damping.

In Figure 5.7, instead, can be observed the Performance Indicators of *Comfort* and *Road-Holding* resulting from this HIL Testing. Due to the more demanding characteristics of the ISO-C road profile, the η_{rh} has achieved a rms value of 0.18 with respect to the ISO-B 0.13, while the rms of the Comfort coefficient has increased to 0.02g, i.e. 0.196m/s^2 , double with respect to the ISO-B case. Moreover, the experienced instability within the first 5 seconds of testing is particularly visible in the acceleration plot. Finally, to complete the analyses related to the ISO-C profile with no RRSA damping, the resulting power flow signals have been acquired and collected together in Figure 5.8. As previously described, even these results show the effects of the RRSA dissipations, observable in the differences between the dissipated mechanical power and the actual regenerated one, strictly dependent on the working condition of the electric machine.

5.1. HIL Testing: Model-Following Compensation

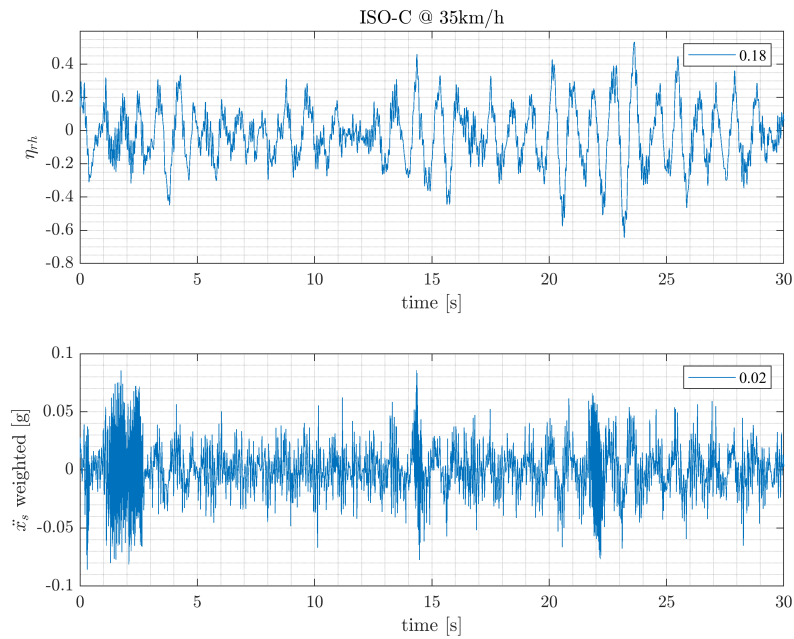


Figure 5.7: HIL Testing: Human Acceleration ISO_{2631} (Comfort coefficient) and Road-Holding Coefficient, for ISO-C @ 35km/h in HIL Testing.

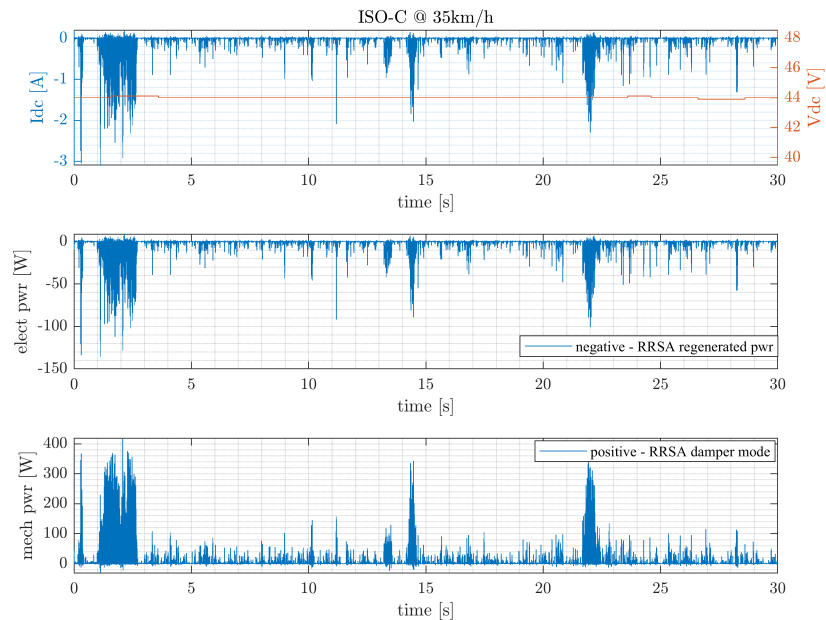


Figure 5.8: HIL Testing: Mechanical Power, Electric Power and Electric Current signals, for ISO-C @ 35km/h without RRSA damping.

Testbench with RRSA damping=500Ns/m**ISO-B @ 70km/h**

In this section are collected all the results acquired in the HIL Testing by setting the Testbed with a RRSA damping equal to 500Ns/m, with the only *ISO-B @ 70km/h* road profile. The ISO-C road profile results have not been included, in this second bench configuration, since their main characteristics have been described in 5.1.2. Moreover, in the present HIL testing, their acquisitions have not provided any additional information with respect to the ISO-B profile.

Differently from the case with no damping, the Compensator is now *decoupled* from the Testbench. In fact, the $TF_{following}$, characterizing the Compensation Scheme, is constantly modelled with reference to a *numerical bench* without RRSA damping, while the physical Testbench is now identified by a RRSA damping equal to 500Ns/m, set in the MPPM Unit by operating on the User-interface program. As described in 3.5 in the evaluation of the numerical results, whenever the Compensator and the Testbench are characterized by different RRSA damping coefficients, the Modell-Following Compensation method does not operate properly with the same effectiveness with respect to the case with same damping coefficient. If this is true from the mathematical point of view and the numerical results have proved it (in the different frequency response functions), the actual HIL Testing have done the same.

In Figure 5.9, indeed, the Testbench results acquired for the ISO-B road profile are grouped together. This testing procedure has been performed just after the previous ISO-B test shown in 5.1.2, ensuring in this way to have the hydraulic circuit almost at its nominal temperature and average pressure. The resulting Hydraulic Pressure signal, in fact, is oscillating around a mean value of about 25bar, defined as the nominal one for the testing procedure, while in 5.1.2, when the hydraulic oil was overheated in the ISO-C test, the mean value was around 40bar.

As can be observed in the Kollmorgen Current signal, the saturation value of 70A is reached quite often during the entire duration of the test, meaning that the HIL System has experienced many relatively prolonged instabilities.

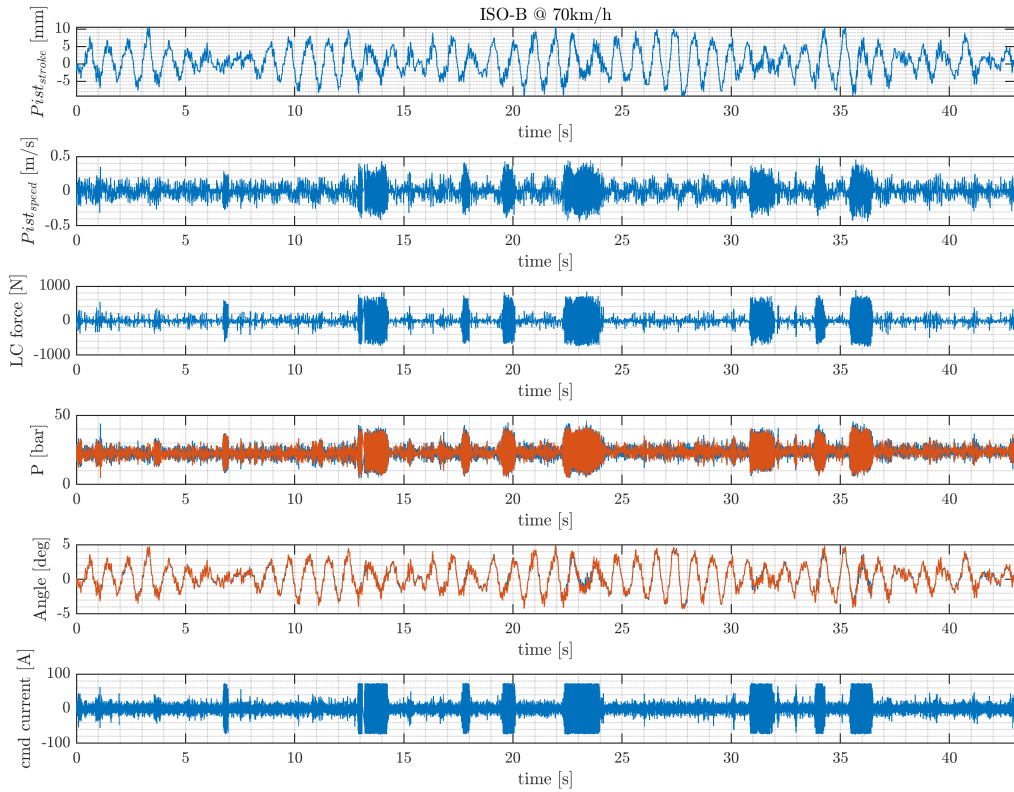


Figure 5.9: HIL Testing: TestBench measured signals, for ISO-B @ 70km/h with Testbench RRSA damping=500Ns/m.

This fact was somehow expected, considering the numerical results concerning the frequency response function of the *Compensated Testbench*, whenever a certain difference in damping exists between the Compensation Scheme and Testbench, as shown in Figure 3.61. The Model Following Scheme can not properly compensate the Testbed dynamics related to the RRSA, due to the fact that its damping features are not included in the $TF_{\text{following}}$, hence resulting in a more diffused local unstable behaviours. Moreover, in Figure 5.10 has been included a detail of the RRSA Tracking and Kollmorgen current signals centered in the interval of the most relevant experienced instability (around after 22s from the start of the test), showing the actual transition from the *stable* behaviour to the *unstable* one, clearly indicated by the electric current saturation and by the minimized tracking performance.

In any case, the experienced phase shift observed in 5.1.2 between the reference and

the measured signal is here still evident in the tracking acquisition.

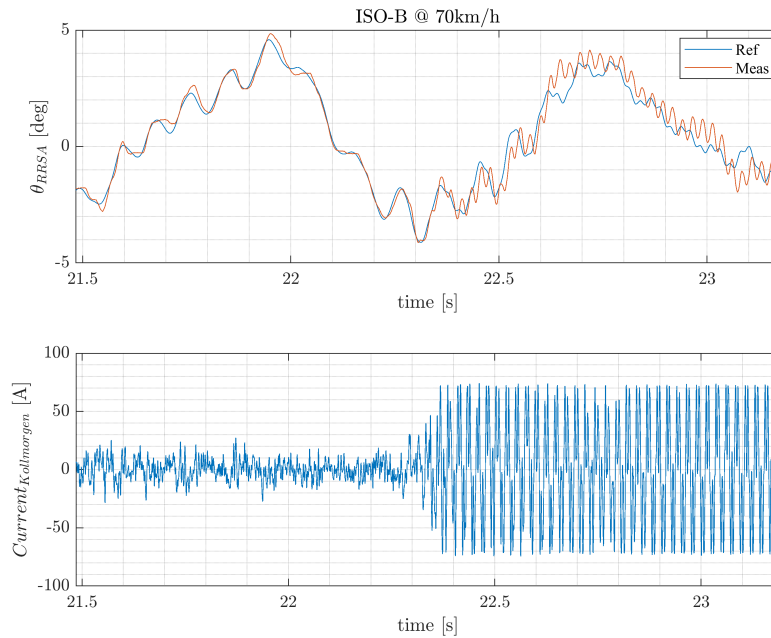


Figure 5.10: HIL Testing: RRSA Angle Tracking detail, for ISO-B @ 70km/h with Testbench RRSA damping=500Ns/m.

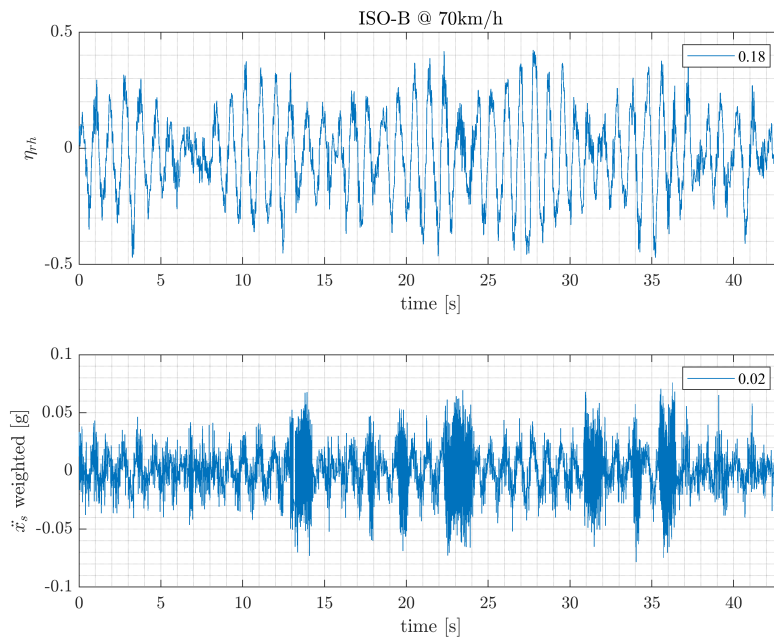


Figure 5.11: HIL Testing: Human Acceleration ISO₂₆₃₁ (Comfort coefficient) and Road-Holding Coefficient, for ISO-B @ 70km/h with Testbench RRSA damping=500Ns/m.

Then, the *Comfort* and the *Road-Holding* coefficients are measured and represented in Figure 5.11. Despite the test has been performed with ISO-B road profile, the resulting rms values coincide with the ones obtained in 5.1.2 with ISO-C profile, significantly higher with respect to the corresponding ISO-B results (for Comfort level, 0.02g instead of 0.01g, while for η_{rh} , 0.18 instead of 0.13). If, on one hand, the obtained increase in road-holding rms is due to the fact that the QCM suspension damping is increased (from 0Ns/m to 500Ns/m), the increase experienced by the Comfort coefficient (doubled with respect to the previous ISO-B test) is instead mainly caused by the repeated local instabilities, clearly observable in Figure 5.11.

Finally, the *power flows* and the *battery current* are measured and collected in Figure 5.12. The previously described characteristics regarding the *conversion efficiency effects*, on the dissipated and regenerated power, are perfectly extended to these acquired signals, furthermore taking into account the increased number of instabilities.

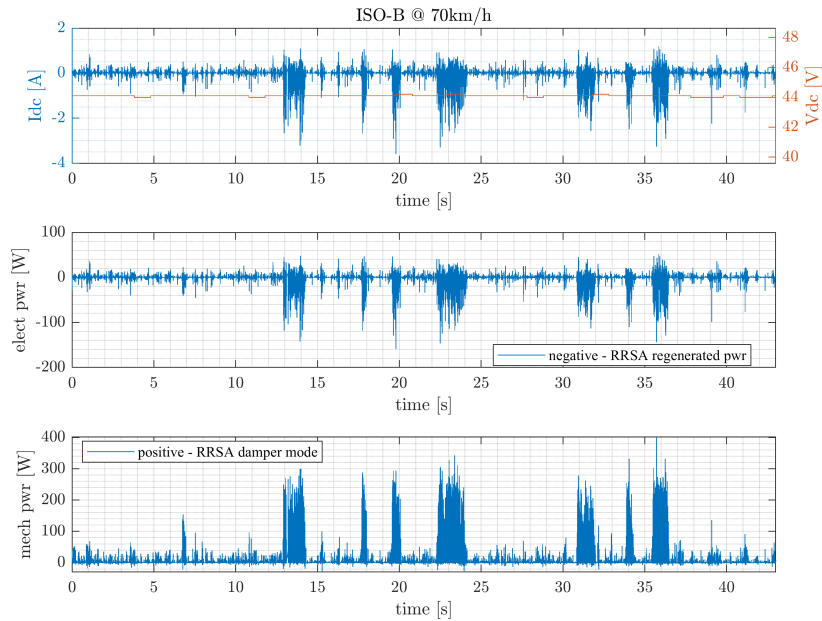


Figure 5.12: HIL Testing: Mechanical Power, Electric Power and Electric Current signals, for ISO-B @ 70km/h with Testbench RRSA damping=500Ns/m.

Conclusions and future developments

A concise introduction to the active and semi active suspension technologies has been outlined, pointing out the most relevant advantages and limits, together with a brief description of the Hardware-In-the-Loop testing procedure. This Thesis Work, then, has focused on the modelling process of a Rotary Regenerative Shock Absorber prototype, previously realized, in a simulated HIL environment.

The starting goal of this study has been the *compensation* of the real testbed dynamics, which had not allowed, before the development of this Work, to perform HIL Tests due to the instability of the entire physical system.

Chapter 2 provides a description of the physical RRSA prototype considering its main design aspects, and an overview of the actual Testbed installed in the Laboratory of the *Politecnico di Torino* in Verrès (AO), Italy. The main components and their functions are briefly described, focusing then on the explanation of the working principle of the entire Testbench in HIL configuration. Each included component plays a specific function strictly related to the others, and the overall operations chain is illustrated.

Once provided the main information concerning the RRSA device and the Testbench, the whole Chapter 3 focuses on the actual Numerical Modelling process performed in MATLAB/SimulinkTM environment. The first implemented model, with *block representation*, has been accurately analyzed with proper references to the physical system.

After that, the other two implementations, *state-space* and *transfer-function* representations have been described and compared, and both of them have been positively validated for ensuring effective analyses. Then, the overall HIL Model has been evaluated in the first Simulink™ test, numerically demonstrating the *unstable* behaviour characterizing the actual bench. Analyzing the obtained results and demonstrating it with further tests, the cause of the instability has been identified in the *limited frequency bandwidth* available in the Testbed itself, which does not include the Quarter-Car-Model frequency characterizing the *unsprung mass*, around 13Hz. Consequently, the *Inverse Compensation Method* has been introduced, described and numerically implemented, providing satisfactory results in HIL configuration. Different input road profiles have been tested and useful obtained outputs have been acquired. Furthermore, two types of *robustness test* have been introduced and implemented for proving the actual stability of the numerical model and increasing the accuracy level of the modelling process. At the end, the model has positively passed the designed tests. Finally, another compensation approach, the *Model Following Method*, has been introduced, described and implemented, providing satisfactory results and improving the performance offered by the *Inverse Compensation Method*. However, both approaches can not be used with high effectiveness when a certain damping difference is imposed between the Testbench model and the Compensation Scheme, since the latter is nominally defined with no RRSA damping.

Chapter 4, then, focuses on the possible Control Strategies to be used to command the RRSA in a QC from the numerical point of view. A brief introduction to one of the most used strategies is carried out, i.e the *sky-hook theory*, pointing out main benefits and limits. The Sky-Hook control has been modelled and implemented in MATLAB/Simulink™ environment considering a two degrees of freedom QCM. Assuming a simplified model for the RRSA, specific analyses have been carried out for ISO profiles and *road bump sequence*, to provide useful outputs about *Comfort* and *Road Holding* Performance, with reference to the ISO₂₆₃₁ standardization, and about the energetical performance of the RRSA in regenerating and consuming power. After that, the RRSA model has been updated with the introduction of its inertial and dissipative contributions and, most important, its *Efficiency Map*, experimentally obtained

by Eng. Salvatore Circosta. The resulting model has been tested and quite interesting and positive results have been obtained, pointing out, in particular, the regenerative performance of the active damper in a more realistic perspective. To conclude this Chapter, another Control Strategy, defined as *Spring-Negation Control*, has been introduced, described and numerically implemented. The obtained results have been considered quite satisfactory compared with the performance offered by a traditional passive shock absorber. However, overall evaluating, the designed Sky-Hook Control has provided better performance in the considered QC implementation.

Finally, Chapter 5 includes the experimental results obtained in the Laboratory of the *Politecnico di Torino* in Verrès (AO). In particular, the *Model Following Method* has been implemented in the software part of the physical installation to evaluate its compensating performance in HIL Configuration. With great success, the designed control scheme has allowed to perform a certain number of tests running the Testbench over a simulated ISO-B and ISO-C road profile. The system, overall considered, has been defined as stable, fact demonstrated by the presence of the signal acquisitions that were not physically available before the Compensation introduction, due to the significant instability of the Testbed in HIL. However, the experienced limits in the numerical model concerning the damping difference between Compensation Scheme and Testbench, has been highlighted and amplified in the actual HIL Testing, providing a signal in some instants locally unstable, despite the overall achieved stability.

Future development

The present Thesis Work has provided satisfactory numerical results for the HIL Model and for the designed controlled strategies of the active damper. Once implemented in the physical HIL Testing, the designed Compensation Method has positively solved the instability affecting the Testbench, extending the limited testbench-bandwidth. However, the stability has not been established in every possible working configurations of the testbed, due to the numerical damping difference between the control scheme and bench itself.

Consequently, further investigations should be taken into account for future develop-

ments. In particular, the following list briefly sums up some possible considerations to be practically implemented:

- First, for increasing the accuracy of the modelling process, a further experimental characterization of the entire testbed may be performed. Possible non-linearities not considered in the actual model may be detected and properly implemented.
- Sensor measuring performances may be evaluated and eventually improved if it is demonstrated that they are introducing a significative bandwidth limitation.
- New *Compensation Schemes*, based or not on the ones described in this Thesis Work, may be designed and numerical tested for enhancing the compensation performance on the Testbench. If positively validated, further HIL Testing may be conducted.

List of Figures

1.1	Examples of semi-active damper with variable controlled damping	3
1.2	Example: Hardware-In-the-Loop with semi-active suspension [5]	6
1.3	Example: Hardware-In-the-Loop with MR damper [7]	6
2.1	Rotary Regenerative Shock Absorber working principle diagram	10
2.2	RRSA prototype	10
2.3	RRSA gearbox scheme	12
2.4	RRSA linkage position	14
2.5	Inverter and Control PC with User-Interface for HIL Testing	16
2.6	Hydraulic Pump and Kollmorgen Motor	17
2.7	Driving actuator with Load Cell and connection to the rotary damper	18
2.8	RRSA Prototype installed in the Testbench (without electric connections to the phases)	18
2.9	Battery Management System	19
2.10	MPPM and dSpace TM	19
2.11	Dedicated box for sensor supply	20
3.1	HIL block model	22
3.2	Road Profile White Noise	22
3.3	Quarter Car with two degrees of freedom	23
3.4	QCM force diagrams	24
3.5	Testbench block model	26
3.6	KPG model	27
3.7	Piston-RRSA Interface model with 1 degree of freedom	29
3.8	PRI block model	29
3.9	RRSA Controller and System model	31
3.10	HIL State Space Model: overall layout	33
3.11	HIL State Space Model: QCM layout	33
3.12	HIL State Space Model: Testbench layout	34
3.13	HIL Transfer Function Model: overall layout	35
3.14	TestBench frequency response without RRSA damping	37
3.15	HIL Model: HIL RootLocus (sprung mass displacement=output, road profile=input) .	38
3.16	HIL Model: Instability results with Sinewave input=1Hz/0.01m and RRSA damp- ing=1kNs/m	39
3.17	HIL Model: Rootlocus Stable results with unsprung mass=320kg and RRSA damp- ing=1000Ns/m	40
3.18	HIL Model: Stable results with unsprung mass=320kg and RRSA damping=1000Ns/m	40
3.19	Application scheme of Inverse Compensation Method	42
3.20	Bode Diagram of Compensator Transfer Function with cut-off frequency=500Hz . . .	45

3.21	Bode Diagram of Compensated Testbench TF with cut-off frequency=500Hz and with testbench RRSA damping=0kNs/m	46
3.22	Bode Diagram of Compensated Testbench TF with cut-off frequency=500Hz and with testbench RRSA damping=1kNs/m	47
3.23	Simulink™ Model of Compensated Testbench	48
3.24	Compensated Testbench results with no damping and input rotation of 10Hz-2deg	48
3.25	Compensated Testbench results with testbench RRSA damping=1kNs/m and input rotation of 10Hz-2deg	50
3.26	Frequency Domain results of HIL with Compensation and $f_{cut}=250\text{Hz}$	52
3.27	HIL Compensated Simulink™ Model	53
3.28	Compensation Results with ISO-B and ISO-C inputs and $f_{cut}=250\text{Hz}$: Tracking of RRSA rotation	55
3.29	Compensation Results with ISO-B and ISO-C inputs and $f_{cut}=250\text{Hz}$: Load Cell Force	56
3.30	Compensation Results with ISO-B and ISO-C inputs and $f_{cut}=250\text{Hz}$: KollMorgen Current	57
3.31	Compensation Results with ISO-B and ISO-C inputs and $f_{cut}=250\text{Hz}$: Unsprung Mass Acceleration	59
3.32	Compensation Results with ISO-B and ISO-C inputs and $f_{cut}=250\text{Hz}$: Sprung Mass Acceleration	61
3.33	HIL Compensation Results with ISO-B input, $f_{cut}=500\text{Hz}$ and RRSA damping=1kNs/m: comparison between different implementations	64
3.34	Piston Mass and Dissipation Robustness Test: Testbench Bode Diagram ($\frac{\theta_{out}}{\theta_{ref}}$)	66
3.35	Piston Mass and Dissipation Robustness Test: Testbench Root Locus ($\frac{\theta_{out}}{\theta_{ref}}$)	67
3.36	OFAT Robustness Test: HIL Root Locus without Compensation (<i>Sprung Mass displacement =output, road displacement=input</i>)	68
3.37	Piston Mass and Dissipations Robustness Test: Compensator-Testbench Bode Diagram ($\frac{\theta_{out}}{\theta_{ref}}$, with RRSA current=0)	69
3.38	Piston Mass and Dissipations Robustness Test: Compensator-Testbench Bode Diagram ($\frac{\theta_{out}}{\theta_{ref}}$) with RRSA current ($c=1\text{kNs/m}$)	70
3.39	OFAT Robustness Test: HIL Compensated Bode Diagram (<i>Sprung Mass displacement =output, Road displacement=input</i>) with RRSA current ($c=1\text{kNs/m}$)	71
3.40	OFAT Robustness Test: HIL Compensated Root Locus (<i>Sprung Mass displacement =output, Road displacement=input</i>) with RRSA current ($c=1\text{kNs/m}$)	72
3.41	OFAT Robustness Test: Tracking of RRSA rotation	74
3.42	OFAT Robustness Test: Load Cell Force	75
3.43	OFAT Robustness Test (-10%): KollMorgen Current	77
3.44	OFAT Robustness Test (-10%): Unsprung Mass Acceleration	79
3.45	OFAT Robustness Test (-10%): Sprung Mass Acceleration	82
3.46	Load Cell Noise added at the output of the Testbench block model	86
3.47	Load Cell Noise signal	86
3.48	Piston Position Noise added inside the Testbench block model	86
3.49	Piston Position Noise signal	87
3.50	Noise Disturbance Robustness Test: Tracking of RRSA rotation	88
3.51	Noise Disturbance Robustness Test: Load Cell Force	88
3.52	Noise Disturbance Robustness Test: KollMorgen Current	89
3.53	Noise Disturbance Robustness Test: Unsprung Mass Acceleration	90
3.54	Noise Disturbance Robustness Test: Sprung Mass Acceleration	91
3.55	Bode Diagram of TF_{des} (Bessel filter)	93
3.56	Model Following Scheme applied to the Testbench system.	94
3.57	Model Following Control Scheme implemented in Simulink™	94
3.58	Model Following Scheme applied to the HIL system.	95
3.59	Bode Diagram comparison between Bench TF with Compensation and Desired TF (Bessel Filter), with Testbench&Compensator RRSA damping=0Ns/m	96

3.60	Bode Diagram comparison between Model Following Method (with Bessel filter and $f_{cut}=500\text{Hz}$), Inverse Compensation Method (with $f_{cut}=500\text{Hz}$) and Bench without Compensation , with Testbench&Compensator RRSA damping=0Ns/m	96
3.61	Bode Diagram comparison between Bench TF with Model Following Method (with Bessel Filter and $f_{cut}=500\text{Hz}$), Desired TF (Bessel Filter) and Bench TF without Compensation , with Testbench RRSA damping=1000Ns/m and Compensator RRSA damping=0Ns/m	98
3.62	Bode Diagram comparison between Bench TF with Model Following Method (with Bessel Filter and $f_{cut}=500\text{Hz}$) and Bench TF with Inverse Compensation (with $f_{cut}=500\text{Hz}$), with Testbench RRSA damping=1000Ns/m and Compensator RRSA damping=0Ns/m	98
3.63	Time domain results comparison between Model Following with Bessel Filter ($f_{cut}=500\text{Hz}$) and Inverse Compensation Method ($f_{cut}=500\text{Hz}$) for ISO-B profile @ 70km/h, with Testbench RRSA damping=1000Ns/m and Compensator RRSA damping=0Ns/m	99
4.1	Skyhook application on two degrees of freedom QC: a) and b) with and without suspension shock absorber, c) practical implementation with controlled damper between the two masses, [3]	102
4.2	Non-dimensional frequency response of the sprung mass of a quarter car with two degrees of freedom. Dimensionless parameters: $b=P/K=4$ and $a=m_u/m_s=0.1$. Passive system with optimum damping (ratio 0.433), simple skyhook (ratio 1) and skyhook with same ratio plus a damper between the two masses with damping equal to 1/3 of the optimum (0.1443), [3]	103
4.3	Non-dimensional frequency response of the unsprung mass of a quarter car with two degrees of freedom, [3]	104
4.4	Non-dimensional frequency response of the sprung mass of a quarter car with two degrees of freedom with $b=P/K=4$ and $a=mu/ms=0.1$. Passive system with optimum damping (ratio 0.433), skyhook (ratio 1 and suspension damping ratio equal to 1/3 of the optimum) and actual skyhook with same values of the parameters, [3].	107
4.5	Non-dimensional frequency response of the unsprung mass of a quarter car with two degrees of freedom (with actual skyhook), [3].	107
4.6	Working principle of Sky-Hook Controller applied to the RRSA system in the Quarter Car Model implementation (the static weights of the QC masses are not shown)	108
4.7	Simulink™ Model of Quarter Car with Sky-Hook controlling the RRSA system	109
4.8	Quarter Car Simulink Model detail	110
4.9	Sky-Hook Simulink Model	110
4.10	RRSA Simulink Model	111
4.11	Output results for QCM with Sky-Hook Control Strategy with ISO-B @ 70km/h ($c=1\text{kNs/m}$, $c_s=1\text{kNs/m}$)	115
4.12	Perceived Human Acceleration with passive damper $c=2.5\text{kNs/m}$	116
4.13	Comfort Map for ISO-B at 70km/h	117
4.14	Comfort Map for ISO-C at 35km/h	118
4.15	Road-Holding Coefficient with passive damper $c=2.5\text{kNs/m}$	119
4.16	Road Holding Map for ISO-B at 35km/h	120
4.17	Road Holding Map for ISO-C at 35km/h	121
4.18	Comfort Coefficient and Road Holding Coefficient with lines at constant c for ISO-B at 70km/h	122
4.19	Comfort Coefficient and Road Holding Coefficient with lines at constant c for ISO-C at 35km/h	122
4.20	Comfort Coefficient and Road Holding Coefficient with lines at constant c_s for ISO-B at 70km/h	123
4.21	Comfort Coefficient and Road Holding Coefficient with lines at constant c_s for ISO-C at 35km/h	123
4.22	Damping Power with passive damper $c=2.5\text{kNs/m}$	124
4.23	Average Power for ISO-B at 70km/h (with 100% energy efficiency)	126

4.24	Sprung Mass Acceleration and Road Holding Coefficient with Average Power for ISO-B at 70km/h with lines at constant \mathbf{c}_s (with 100% energy efficiency)	127
4.25	Sprung Mass Acceleration and Road Holding Coefficient with Average Power for ISO-B at 70km/h with lines at constant \mathbf{c}_s (with 100% energy efficiency and extended range of variation of \mathbf{c}_s)	128
4.26	Comfort Coefficient and Road Holding Coefficient with Average Power for ISO-B at 70km/h with lines at constant \mathbf{c}_s (with 100% energy efficiency and extended range of variation of \mathbf{c}_s)	128
4.27	Average Power for ISO-C at 35km/h with 100% energy efficiency	129
4.28	Sprung Mass Acceleration and Road Holding Coefficient with Average Power for ISO-C at 35km/h with lines at constant \mathbf{c}_s (with 100% energy efficiency)	130
4.29	Sprung Mass Acceleration and Road Holding Coefficient with Average Power for ISO-C at 35km/h with lines at constant \mathbf{c}_s (with 100% energy efficiency and extended range of variation of \mathbf{c}_s)	130
4.30	Comfort Coefficient and Road Holding Coefficient with Average Power for ISO-C at 35km/h with lines at constant \mathbf{c}_s (with 100% energy efficiency and extended range of variation of \mathbf{c}_s)	131
4.31	Comfort Coefficient and Road Holding Coefficient with Average Power Map for ISO-B at 70km/h with highlighted SH configuration $\mathbf{c}=1.2\mathbf{kNs/m}$ and $\mathbf{c}_s=10\mathbf{kNs/m}$	132
4.32	Performance Indicators with Sky-Hook Control with $\mathbf{c}=1.2\mathbf{kNs/m}$ and $\mathbf{c}_s=10\mathbf{kNs/m}$ for ISO-B at 70kph	133
4.33	Electrical Power and RRSA Current with Sky-Hook Control with $\mathbf{c}=1.2\mathbf{kNs/m}$ and $\mathbf{c}_s=10\mathbf{kNs/m}$ for ISO-B at 70kph	133
4.34	Sequence of three bump profiles	134
4.35	Bump Profile results with passive damper $\mathbf{c}=2500\mathbf{Ns/m}$	134
4.36	Electrical Power and RRSA Current with Sky-Hook Control with $\mathbf{c}=1.2\mathbf{kNs/m}$ and $\mathbf{c}_s=10\mathbf{kNs/m}$ for ISO-B at 70kph	135
4.37	Electrical Power and RRSA Current with Sky-Hook Control with $\mathbf{c}=1.2\mathbf{kNs/m}$ and $\mathbf{c}_s=10\mathbf{kNs/m}$ for ISO-B at 70kph	136
4.38	RRSA working region with $\mathbf{c}_s=10\mathbf{kNs/m}$ and $\mathbf{c}=1.2\mathbf{kNs/m}$ with ISO road profiles for 30s.	137
4.39	RRSA Efficiency Map with Loss Power	138
4.40	Damper Simulink TM Model with RRSA Efficiency Map&Losses implemented	139
4.41	Main blocks Simulink TM Model of QC with RRSA Efficiency Map&Losses implemented	139
4.42	RRSA Simulink TM Model with RRSA Efficiency Map&Losses implemented	141
4.43	Lines at constant \mathbf{c} and \mathbf{c}_s with RRSA Efficiency Map&Losses implemented for ISO-B @ 70km/h	142
4.44	Comfort and Road-Holding Coefficients Map with RRSA Efficiency Map&Losses implemented	143
4.45	Power Color Maps with RRSA Efficiency Map&Losses implemented for ISO-B @ 70km/h	145
4.46	Power Color Maps with RRSA Efficiency Map&Losses implemented for ISO-B @ 70km/h, with SH extended range	146
4.47	RRSA Conversion Efficiency Map for ISO-B @ 70km/h	147
4.48	QCM Time domain results with SH $\mathbf{c}=1.2\mathbf{kNs/m}$, $\mathbf{c}_s=10\mathbf{kNs/m}$ and with RRSA Efficiency Map and losses taken into account, for ISO-B @ 70km/h	149
4.49	Power Signals with RRSA Efficiency Map&Losses with SH $\mathbf{c}=1.2\mathbf{kNs/m}$, $\mathbf{c}_s=10\mathbf{kNs/m}$ for ISO-B @ 70km/h	150
4.50	RRSA Torque-Speed Map with SH $\mathbf{c}=1.2\mathbf{kNs/m}$, $\mathbf{c}_s=10\mathbf{kNs/m}$ and RRSA Efficiency Map&Losses, for ISO-B @ 70km/h	151
4.51	Simulink TM Block for Spring-Negation RRSA Control	152
4.52	Simulink TM Block for Spring-Negation RRSA Control: detail	153
4.53	Comfort and Road-Holding Coefficient with comparison between Sky-Hook initial range (lines at constant \mathbf{c}_s) and Spring-Negation variable damping, for ISO-B @ 70km/h.	154
4.54	Comfort and Road-Holding Performance with Spring-Negation Control variable-damping, for ISO-B @ 70km/h	155

4.55	Power Flow and RRSA Current with Spring-Negation Control variable-damping, for ISO-B @ 70km/h	155
4.56	QCM Time Domain results with Spring-Negation Control variable-damping, for Bump Profile 30mm @ 50km/h	157
4.57	QCM Time Domain results with Spring-Negation Control reduced variable-damping, for Bump Profile 30mm @ 50km/h	159
5.1	HIL Testing: TestBench measured signals, for ISO-B @ 70km/h without RRSA damping.	165
5.2	HIL Testing: RRSA Angle Tracking detail, for ISO-B @ 70km/h without RRSA damping.	166
5.3	HIL Testing: Quarter Car Model results for ISO-B @ 70km/h without RRSA damping.	167
5.4	HIL Testing: Human Acceleration ISO ₂₆₃₁ (Comfort coefficient) and Road-Holding Coefficient, for ISO-B @ 70km/h without RRSA damping.	168
5.5	HIL Testing: Mechanical Power, Electric Power and Electric Current signals, for ISO-B @ 70km/h without RRSA damping.	169
5.6	HIL Testing: TestBench measured signals, for ISO-C @ 35km/h without RRSA damping.	170
5.7	HIL Testing: Human Acceleration ISO ₂₆₃₁ (Comfort coefficient) and Road-Holding Coefficient, for ISO-C @ 35km/h in HIL Testing.	171
5.8	HIL Testing: Mechanical Power, Electric Power and Electric Current signals, for ISO-C @ 35km/h without RRSA damping.	171
5.9	HIL Testing: TestBench measured signals, for ISO-B @ 70km/h with Testbench RRSA damping=500Ns/m.	173
5.10	HIL Testing: RRSA Angle Tracking detail, for ISO-B @ 70km/h with Testbench RRSA damping=500Ns/m.	174
5.11	HIL Testing: Human Acceleration ISO ₂₆₃₁ (Comfort coefficient) and Road-Holding Coefficient, for ISO-B @ 70km/h with Testbench RRSA damping=500Ns/m.	174
5.12	HIL Testing: Mechanical Power, Electric Power and Electric Current signals, for ISO-B @ 70km/h with Testbench RRSA damping=500Ns/m.	175

List of Tables

3.1	Quarter Car Model Data (Jeep Renegade)	24
3.2	PID coefficients	27
3.3	KollMorgen Pump Group Data	28
3.4	Piston-RRSA-Interface Data	30
3.5	RRSA Data	32
3.6	Simulation Data of Compensation Analysis	51
3.7	Compensation Results ISO-B with $f_{cut}=250\text{Hz}$: Kollmorgen Current RMS	57
3.8	Compensation Results ISO-B with $f_{cut}=250\text{Hz}$ with relative deviation: Kollmorgen Current RMS	58
3.9	Compensation Results ISO-C with $f_{cut}=250\text{Hz}$ with relative deviation: KollMorgen Current RMS	58
3.10	Compensation Results ISO-B with $f_{cut}=250\text{Hz}$: Unsprung Mass Acceleration RMS	59
3.11	Compensation Results ISO-B with $f_{cut}=250\text{Hz}$ with relative deviation: Unsprung Mass Acceleration RMS	59
3.12	Compensation Results ISO-C with $f_{cut}=250\text{Hz}$ with relative deviation: Unsprung Mass Acceleration RMS	60
3.13	Compensation Results ISO-B with $f_{cut}=250\text{Hz}$: Sprung Mass Acceleration RMS	61
3.14	Compensation Results ISO-B with $f_{cut}=250\text{Hz}$ with relative deviation: Sprung Mass Acceleration RMS	61
3.15	Compensation Results ISO-C with $f_{cut}=250\text{Hz}$ with relative deviation: Sprung Mass Acceleration RMS	62
3.16	Simulation Data	73
3.17	OFAT Robustness Test (-10%): Kollmorgen Current RMS	78
3.18	OFAT Robustness Test (-10%) relative deviation: Kollmorgen Current RMS	78
3.19	OFAT Robustness Test (+10%): Kollmorgen Current RMS	78
3.20	OFAT Robustness Test (+10%) relative deviation: Kollmorgen Current RMS	78
3.21	OFAT Robustness Test (-10%): Unsprung Mass Acceleration RMS	80
3.22	OFAT Robustness Test (-10%) relative deviation: Unsprung Mass Acceleration RMS	80
3.23	OFAT Robustness Test (+10%): Unsprung Mass Acceleration RMS	81
3.24	OFAT Robustness Test (+10%) relative deviation: Unsprung Mass Acceleration RMS	81
3.25	OFAT Robustness Test (-10%): Sprung Mass Acceleration RMS	83
3.26	OFAT Robustness Test (-10%) with relative deviation: Sprung Mass Acceleration RMS	83
3.27	OFAT Robustness Test (+10%): Sprung Mass Acceleration RMS	83
3.28	OFAT Robustness Test (+10%) with relative deviation: Sprung Mass Acceleration RMS	83
3.29	Noise Disturbance Testing: Simulation Data	85
3.30	Noise Disturbance Robustness Test: Kollmorgen Current RMS	89
3.31	Noise Disturbance Robustness Test with relative deviation: Kollmorgen Current RMS	89
3.32	Noise Disturbance Robustness Test: Unsprung Mass Acceleration RMS	90

3.33	Noise Disturbance Robustness Test with relative deviation: Unsprung Mass Acceleration RMS	90
3.34	Noise Disturbance Robustness Test: Sprung Mass Acceleration RMS	91
3.35	Noise Disturbance Robustness Test with relative deviation: Sprung Mass Acceleration RMS	91
4.1	Quarter Car Model Data (Alfa Romeo TM Stelvio)	111
4.2	Performance Comparison for ISO-B @ 70km/h with Passive Shock-Absorber (c=2.5kNs/m), Sky-Hook (c=1.2kNs/m and c_s=10kNs/m) and Spring-Negation with damping (c=0.5, 1, 2kNs/m)	156
4.3	Performance Comparison for Bump Sequence 30mm @ 70km/h with Passive Shock-Absorber (c=2.5kNs/m), Sky-Hook (c=1.2kNs/m and c_s=10kNs/m) and Spring-Negation with damping (c=0.5, 1, 2kNs/m)	158
4.4	Performance Comparison for Bump Sequence 30mm @ 70km/h with Passive Shock-Absorber (c=2.5kNs/m), Sky-Hook (c=1.2kNs/m and c_s=10kNs/m) and Spring-Negation with damping (c=300, 100, 50Ns/m)	160

Bibliography

- [1] Cheng Chen and James M.icles. “Analysis of actuator delay compensation methods for real-time testing”. In: *Engineering Structures* 31 (2009). Ed. by SAGE Institution of Mechanical Engineers, pp. 2643–2655.
- [2] Renato Galluzzi et al. “Rotary regenerative shock absorbers for automotive suspensions”. In: *Mechatronics* 77 (2021), p. 102580. ISSN: 0957-4158. DOI: <https://doi.org/10.1016/j.mechatronics.2021.102580>. URL: <https://www.sciencedirect.com/science/article/pii/S0957415821000672>.
- [3] Lorenzo Morello Giancarlo Genta. *The Automotive Chassis. Vol. 2: System Design*. Mechanical Engineering Series. Springer, Dordrecht, 2009. DOI: <https://doi.org/10.1007/978-1-4020-8675-5>.
- [4] SR Hashemi, M Montazeri, and M Nasiri. “The compensation of actuator delay for hardware-in-the-loop simulation of a jet engine fuel control unit”. In: *SIMULATION* 90 (2014). Ed. by SAGE Institution of Mechanical Engineers, pp. 745–755.
- [5] SUNG-HO HWANG et al. “Vehicle Dynamic Analysis and Evaluation of Continuously Controlled Semi-Active Suspensions Using Hardware-in-the-loop Simulation”. In: *Vehicle System Dynamics* 27 (1997). Ed. by Taylor Francis, pp. 423–434.

-
- [6] S.J. Hwang, S.H. Heo and K. Park. “Design and evaluations of semi-active suspension control algorithms using hardware-in-the-loop simulations”. In: *Vehicle System Dynamics* 19 (1998). Ed. by Belgium European Commission Brussels, pp. 540–551.
- [7] Ruben Morales-Menendez Jorge de-J Lozoya-Santos and Ricardo A Ramirez-Mendoza. “Evaluation of on-off semi-active vehicle suspension systems by using the hardware-in-the-loop approach and the software-in-the-loop approach”. In: *Journal of AUTOMOBILE ENGINEERING* 229(I) (2015). Ed. by SAGE Institution of Mechanical Engineers, pp. 52–69.
- [8] MarelliTM. “Rotary sim Toyota demo car MARELLI”. 2020.
- [9] BSI Standards Publication. *Mechanical vibration and shock — Evaluation of human exposure to whole-body vibration. Part 1*. 1997.